

*Cytoskeletal control of B cell receptor dynamics and signaling*

by

Spencer Alexander Freeman

A THESIS SUBMITTED IN PARTIAL FULFILLMENT OF  
THE REQUIREMENTS FOR THE DEGREE OF

DOCTOR OF PHILOSOPHY

in

The Faculty of Graduate and Postdoctoral Studies

(Cell and Developmental Biology)

THE UNIVERSITY OF BRITISH COLUMBIA

(Vancouver)

April 2014

© Spencer Alexander Freeman, 2014

## **Abstract**

The nucleation, polymerization, and depolymerization of actin filaments is spatially and temporally controlled in order to regulate cell motility, cell morphology, and protein organization within the plasma membrane. By limiting receptor diffusion, the submembrane actin cytoskeleton modulates the signaling output of receptors such as the B-cell antigen (Ag) receptor (BCR) that are activated by clustering. Restricting BCR mobility limits BCR-BCR collisions and the resultant ‘tonic’ signaling. Conversely, more dynamic actin filaments or F-actin clearance promotes BCR-BCR collisions and leads to a ‘primed’ state where the threshold for Ag-induced activation is reduced. In chapter 2, I show a mechanism of receptor cross-talk where microbial danger signals (TLR ligands) prime B cells for Ag-induced activation by enhancing actin dynamics. TLR signaling reduced BCR confinement, promoted BCR-BCR collisions and potentiated responses to low densities of membrane-associated Ags.

The interaction of B-cells with antigen-presenting cells displaying membrane-Ags results in initial BCR signaling that promotes cell spreading and increases the probability of BCRs encountering Ag. This is coupled with increased BCR mobility and the formation of BCR microclusters that recruit and activate signaling enzymes. Cell spreading and BCR microcluster mobility require severing of cortical submembrane actin, a precursor to F-actin branching that drives cell spreading. In chapter 3, I show that BCR signaling increases actin dynamics and BCR microcluster formation by activating the actin-severing protein cofilin via a signaling pathway involving Rap GTPases.

Because Rap is a central regulator of actin dynamics and adhesion, I hypothesized that Rap activation, elevated in many tumor types, is important in metastatic progression. I focused on circulating tumor cells (CTCs) and in chapter 4, I show that Rap plays a critical role in the formation of adhesive contacts between CTCs and vascular endothelium by promoting the clustering, activation, and turnover of integrin. Blocking Rap activation and preventing the cycling of Rap between active and inactive forms reduced transendothelial migration, thereby limiting metastatic colonization of secondary sites.

Together, this work shows that Rap-dependent regulation of actin dynamics controls the organization of membrane proteins such as the BCR and integrins, exerting control over processes that include B-cell activation and tumor metastasis.

## **Preface**

### **Status of data chapters and my contributions to them**

The material contained in this thesis is derived from the following publications or manuscripts:

#### **Chapter 2**

- Manuscript to be submitted January 2014: TLR ligands increase the sensitivity of BCR signalling by increasing cytoskeletal dynamics and reducing BCR spatial confinement
- I performed all of the experiments contained in this chapter with the exception of Fig. 8B, S1, S8. Fig. 8B and S1 were analyses completed by Dr. Raibatak Das. Fig S8 were experiments completed by Kate Choi.

#### **Chapter 3**

- Published article: Cofilin-mediated F-actin severing is regulated by the Rap GTPase and controls the cytoskeletal dynamics that drive lymphocyte spreading and BCR microcluster formation. Freeman SA, Lei V, Dang-Lawson M, Mizuno K, Roskelley CD, Gold MR.

J Immunol. 2011 Dec 1;187(11):5887-900.

- I performed all of the experiments contained in this chapter with the exception of Fig. 2C-E and Fig. 4A-D . These experiments were completed by Victor Lei and May Dang-Lawson.

## **Chapter 4**

- Published article: Preventing the activation or cycling of the Rap1 GTPase alters adhesion and cytoskeletal dynamics and blocks metastatic melanoma cell extravasation into the lungs. Freeman SA, McLeod SJ, Dukowski J, Austin P, Lee CC, Millen-Martin B, Kubes P, McCafferty DM, Gold MR, Roskelley CD. Cancer Res. 2010 Jun 1;70(11):4590-601.

- I performed all of the experiments contained in this chapter with the exception of Fig. 1A, S1, and S3. These experiments were completed by Dr. Sarah McLeod. Fig. 2 was performed by myself and Dr. McLeod. Experiments in Fig. 6 were performed by myself and Brandie Millen-Martin.

## **Appendix A**

- Manuscript to be submitted: Force activation of Rap GTPases regulates adhesion dynamics.

Spencer A. Freeman, Irene Iu, Dan Coombs, Michael R. Gold, Calvin D. Roskelley

- I supervised or performed all of the experiments contained in this appendix with the help of Irene Iu.

## **Appendix B**

- Manuscript to be submitted: Inflammation in the lung primes the premetastatic niche via hyaluronic acid

Megan Gilmour\*, Spencer A. Freeman\*, Grace F. Poon, Matthew J. Gold, Jeff Dong, Paul Kubes, Donna-Marie McCafferty, Marie-Renee Blanchet, Kelly M. McNagny, Pauline Johnson, Michael R. Gold, Calvin D. Roskelley

\* both authors contributed equally

• I supervised or performed all of the experiments contained in this appendix with the help of Megan Gilmour.

I also made significant contributions to the following publications:

Control of the hippo pathway by Set7-dependent methylation of Yap.

Oudhoff MJ, Freeman SA, Couzens AL, Antignano F, Kuznetsova E, Min PH, Northrop JP, Lehnertz B, Baryte-Lovejoy D, Vedadi M, Arrowsmith CH, Nishina H, Gold MR, Rossi FM, Gingras AC, Zaph C.

Dev Cell. 2013 Jul 29;26(2):188-94.

The invasion inhibitor sarasinamide A1 reverses mesenchymal tumor transformation in an E-cadherin-independent manner.

Austin P\*, Freeman SA\*, Gray CA, Gold MR, Vogl AW, Andersen RJ, Roberge M, Roskelley CD.

Mol Cancer Res. 2013 May;11(5):530-40.

\* both authors contributed equally

Opposing roles for CD34 in B16 melanoma tumor growth alter early stage vasculature and late stage immune cell infiltration.

Maltby S, Freeman S, Gold MJ, Baker JH, Minchinton AI, Gold MR, Roskelley CD, McNagny KM.

PLoS One. 2011 Apr 11;6(4):e18160.

Rap GTPase-mediated adhesion and migration: A target for limiting the dissemination of B-cell lymphomas?

Lin KB\*, Freeman SA\*, Gold MR.

Cell Adh Migr. 2010 Jul-Sep;4(3):327-32.

\* both authors contributed equally

## Table of Contents

<b>Abstract.....</b>	<b>ii</b>
<b>Preface.....</b>	<b>iv</b>
<b>Table of contents .....</b>	<b>viii</b>
<b>List of tables.....</b>	<b>xiii</b>
<b>List of figures.....</b>	<b>xiv</b>
<b>List of abbreviations .....</b>	<b>xviii</b>
<b>Acknowledgements .....</b>	<b>xxiii</b>
<b>Introduction.....</b>	<b>1</b>
<b>1.1 The immune system .....</b>	<b>1</b>
<b>1.2 The BCR in B cell development and survival.....</b>	<b>3</b>
1.2.1 Overview .....	3
1.2.2 B cell development .....	5
1.2.3 BCR tonic signaling.....	9
1.2.4 BAFF and BCR interplay for B cell survival.....	18
<b>1.3 B cell encounters with antigen presenting cells.....</b>	<b>18</b>
1.3.1 Overview.....	18
1.3.2 APCs in SLOs.....	19
1.3.3 BCR triggering and kinetic segregation.....	23
1.3.4 Thresholds and BCR microclusters .....	26
1.3.5 The germinal center reaction .....	28
<b>1.4 Integrating B cell responses through Toll-like receptors and the BCR.....</b>	<b>30</b>
<b>1.5 Molecular diffusion, single particle tracking, and models of diffusion in the plasma membrane.....</b>	<b>32</b>
1.5.1 Molecular diffusion.....	32
1.5.2 Single particle tracking .....	35
1.5.3 Models of membrane diffusion: from the fluid mosaic model to hop diffusion .....	37
1.5.4 BCR organization in the PM.....	44
<b>1.6 Actin .....</b>	<b>45</b>
1.6.1 Overview.....	45
1.6.2 Actin polymerization .....	46
1.6.3 Actin nucleators .....	47
1.6.4 Nucleation promoting factors .....	51
1.6.5 Reconstitution of actin-based motility .....	54
1.6.6 Cofilin .....	56

<b>1.7 Rap GTPases: regulators of actin dynamics and adhesion</b> .....	<b>60</b>
1.7.1 Control of Rap GTPase activation .....	60
1.7.2 Rap activation in cell polarity .....	65
1.7.3 Rap activation in cell migration .....	70
1.7.4 Rap activation in cell spreading and adhesion on membranes .....	74
<b>1.8 Tumor cell metastasis</b> .....	<b>76</b>
1.8.1 Overview .....	76
1.8.2 Inflammation and metastasis.....	78
1.8.3 The tensional phenotype, Rap activation, and metastasis.....	81
<b>1.9 Thesis aims</b> .....	<b>87</b>
<b>Chapter 2 – TLR ligands increase the sensitivity of BCR signalling by increasing cytoskeletal dynamics and reducing BCR spatial confinement</b> .....	<b>88</b>
<b>2.1 Introduction</b> .....	<b>88</b>
<b>2.2 Results</b> .....	<b>91</b>
2.2.1 TLR ligands prime B cells to respond to low densities of membrane-bound antigen.....	91
2.2.2 TLR signalling reduces BCR confinement and increases BCR diffusion .....	92
2.2.3 BCR confinement and diffusion are controlled by the actin cytoskeleton .....	94
2.2.4 TLR signalling increases actin cytoskeleton dynamics and activates cofilin ..	94
2.2.5 TLR enhancement of BCR mobility is dependent on actin severing .....	97
2.2.6 TLR engagement increases BCR-BCR collisions and tonic BCR signaling... ..	98
2.2.7 TLR enhancement of antigen-induced BCR signaling depends on actin dynamics .....	100
2.2.8 Naturally primed B cell populations have an elevated level of active cofilin .....	100
<b>2.3 Discussion</b> .....	<b>101</b>
<b>2.4 Figures</b> .....	<b>106</b>
<b>2.5 Experimental procedures</b> .....	<b>130</b>
2.5.1 B cell isolation and culture .....	130
2.5.2 Analysis of BCR microcluster formation and signalling on antigen-presenting cells (APCs).....	130
2.5.3 F-actin staining and confocal microscopy .....	131
2.5.4 Single-particle tracking (SPT) and merge-split analysis .....	132
2.5.5 Scanning electron microscopy .....	135
2.5.6 Determination of G-actin/F-actin ratio .....	136
2.5.7 <i>In vitro</i> actin-polymerization activity in cell extracts .....	136
2.5.8 <i>In vivo</i> F-actin severing activity.....	136
2.5.9 Actin polymerization at barbed ends of actin filaments in permeabilized cells .....	137
2.5.10 Cell stimulation, preparation of cell extracts, and immunoblotting.....	138

2.5.11 Cofilin peptides, RhoA-activating peptide, and Syk inhibitor.....	138
2.5.12 RhoA activation assay.....	139
2.5.13 Statistical analysis.....	139

<b>Chapter 3 – Cofilin-mediated F-actin severing is regulated by the Rap GTPase and controls the cytoskeletal dynamics that drive lymphocyte spreading and BCR microcluster formation.....</b>	<b>140</b>
<b>3.1 Introduction.....</b>	<b>140</b>
<b>3.2 Results .....</b>	<b>143</b>
3.2.1 AgR-induced cell spreading is associated with increased actin dynamics. ...	143
3.2.2 AgR signaling stimulates cofilin-mediated F-actin severing.....	145
3.2.3 The Rap GTPases control peripheral actin dynamics, F-actin severing, and cofilin activation .....	146
3.2.4 Cofilin activation is required for lymphocyte spreading and actin dynamics	148
3.2.5 The Rap-cofilin pathway is required for B cells to spread across APCs and gather Ag into microclusters.....	149
3.2.6 The Rap-cofilin pathway controls the mobility of BCR microclusters .....	151
<b>3.3 Discussion .....</b>	<b>153</b>
<b>3.4 Figures.....</b>	<b>158</b>
<b>3.5 Supplemental videos .....</b>	<b>180</b>
<b>3.6 Experimental procedures .....</b>	<b>180</b>
3.6.1 Cell preparation and culture.....	180
3.6.2 Plasmids and transient transfections .....	181
3.6.3 Antibodies.....	181
3.6.4 Cell spreading .....	182
3.6.5 Cell stimulation and immunoblotting .....	182
3.6.6 Assays for G-actin/F-actin and in vitro actin-polymerizing activity .....	183
3.6.7 Fluorescence recovery after photobleaching (FRAP).....	184
3.6.8 Labeling of actin filament barbed ends.....	184
3.6.9 Immunofluorescence.....	185
3.6.10 <i>In vitro</i> F-actin severing.....	185
3.6.11 <i>In vivo</i> F-actin severing.....	186
3.6.12 BCR microcluster formation on surrogate APCs.....	186
3.6.13 BCR microcluster mobility .....	187
3.6.14 Statistical analysis.....	187
<b>Chapter 4 – Preventing the activation or cycling of the Rap1 GTPase alters adhesion and cytoskeletal dynamics and blocks the extravasation of metastatic melanoma cells into the lungs .....</b>	<b>188</b>
<b>4.1 Introduction.....</b>	<b>188</b>
<b>4.2 Results .....</b>	<b>190</b>

4.2.1 Modulating Rap1 activation alters focal adhesion formation by tumor cells	191
4.2.2 Modulating Rap1 activation impairs adhesion dynamics, cytoskeletal dynamics, cell polarization, and cell motility	192
4.2.3 Modulating Rap1 activity inhibits the metastatic extravasation of B16F1 cells from the lung microvasculature	192
4.2.4 Modulating Rap1 activation inhibits transendothelial migration (TEM) by tumor cells	193
4.2.5 Modulating Rap1 activation alters adhesion dynamics in tumor cells interacting with endothelial cells	194
4.2.6 Modulating Rap1 activation inhibits the formation of polarized protrusions by tumor cells lodged within capillaries <i>in vivo</i>	195
<b>4.3 Discussion</b>	<b>196</b>
<b>4.4 Figures</b>	<b>200</b>
<b>4.5 Experimental procedures</b>	<b>218</b>
4.5.1 Cells	218
4.5.2 Reagents	218
4.5.3 Transfection	218
4.5.4 Rap1 activation	219
4.5.5 Immunofluorescence	219
4.5.6 Cell motility	219
4.5.7 Tumor assays	219
4.5.8 Arrest and extravasation assays	220
4.5.9 Adhesion under flow	220
4.5.10 Transendothelial migration	220
4.5.11 Collagen invasion	220
4.5.12 Adhesion dynamics at tumor cell-endothelial cell interfaces	221
4.5.13 Intravital microscopy	221
4.5.14 Statistics	221
<b>Chapter 5 – Concluding chapter</b>	<b>222</b>
<b>5.1 Summary of main findings</b>	<b>222</b>
<b>5.2 Discussion</b>	<b>225</b>
5.2.1 The Rap/cofilin pathway and receptor diffusion	225
5.2.2 Clearance of F-actin, a porous elastic solid material	229
5.2.3 The IS as a diffusion barrier	231
5.2.4 Immune cell populations, receptor organization and response thresholds	232
5.2.5 Closing remarks	235
<b>References</b>	<b>237</b>
<b>Appendix A: Force activation of Rap GTPases regulates adhesion dynamics</b>	<b>260</b>
<b>A.1 Introduction</b>	<b>260</b>
<b>A.2 Figures</b>	<b>262</b>

<b>A.3 Conclusions .....</b>	<b>268</b>
<b>A.4 Experimental procedures .....</b>	<b>269</b>
A.4.1 Cell lines .....	269
A.4.2 Plasmids, transfections, FRAP .....	270
A.4.3 Collagen gel contraction assays .....	270
A.4.4 3D collagen growth assay .....	270
A.4.5 Equibiaxial stretch of cells in 2D .....	271
A.4.6 Uniaxial stretch of cells in 3D .....	272
A.4.7 Immunofluorescence staining in 2D/3D .....	273
A.4.8 Rac1/RhoA activation assays and phospho-p130cas .....	273
A.4.9 Western blotting and antibodies .....	274
<b>Appendix B: Inflammation in the lung primes the premetastatic niche via hyaluronic acid .....</b>	<b>275</b>
<b>B.1 Introduction .....</b>	<b>275</b>
<b>B.2 Figures .....</b>	<b>278</b>
<b>B.3 Conclusions .....</b>	<b>286</b>
<b>B.4 Experimental procedures .....</b>	<b>287</b>
B.4.1 Induction of asthma and assessment of alveolar inflammation .....	287
B.4.2 Induction of HP and assessment of lung inflammation .....	288
B.4.3 Cells .....	288
B.4.4 FACS of bronchoalveolar lavage fluid and tumor cells .....	288
B.4.5 Tracking B16F0 colonization of the lung .....	289
B.4.6 Immunostaining .....	289
B.4.7 <i>In vitro</i> transendothelial migration .....	290
B.4.8 2D fibronectin migration .....	290
B.4.9 MatriGel invasion .....	291
B.4.10 Intravital microscopy .....	291
B.4.11 Statistics .....	291

## List of tables

Table 1.1 Single particle tracking studies .....	39
Table 1.2 Rap GTPase activity in cancers .....	83

## List of figures

1.1 B cell development in the bone marrow .....	8
1.2 A continuum model of BCR signaling in development, survival, and activation .....	10
1.3 Ag presentation to B cells in the LN.....	21
1.4 Ag encounter on APCs by B cells leads to F-actin remodeling and BCR microcluster formation.....	24
1.5 Theoretical MSD plots.....	34
1.6 F-actin branching regulation.....	50
1.7 Rap activation at cell membranes .....	62
1.8 Establishing cell polarity.....	69
2.1 TLR priming increases the sensitivity of B cells to membrane-bound Ags .....	106
2.2 Single-state and two-state analysis of BCR mobility.....	108
2.3 TLR ligands decrease BCR confinement and increase BCR mobility.....	109
2.4 BCR confinement and diffusion are controlled by the actin cytoskeleton.....	110
2.5 TLR signaling enhances actin dynamics and activates cofilin.....	111
2.6 TLR enhancement of BCR mobility is dependent on actin severing.....	113
2.7 TLR ligands increase BCR-BCR collisions and tonic BCR signalling.....	114
2.8 B cell responses to APC-bound Ags are dependent on actin dynamics that are correlated with cofilin activation .....	116
2.9 Single particle labeling of the BCR on B cells adhered to anti-MHCII-coated coverslips .....	118
2.10 Representative distributions of BCR confinement diameters .....	120
2.11 Syk and PI3K regulate BCR mobility.....	122
2.12 Cofilin-blocking peptides inhibit the <i>in vitro</i> severing of actin filaments by cell extracts.....	123
2.13 Disrupting the actin cytoskeleton increases Ag-independent BCR signalling in both resting and TLR-activated B cells .....	124
2.14 Model for TLR-induced transition of B cells from a resting state to an activated state .....	125
2.15 TIRF imaging of mIgM yields similar particle motion behavior as confocal	

microscopy .....	126
3.1 B and T cell spreading is associated with increased actin dynamics and actin reorganization .....	158
3.2 AgR signaling induces cofilin-mediated F-actin severing and cofilin dephosphorylation.....	160
3.3 Rap activation is required for peripheral actin dynamics, F-actin severing, and actin incorporation at barbed ends .....	162
3.4 AgR-induced cofilin dephosphorylation depends on Rap activation .....	164
3.5 Rap-dependent cofilin dephosphorylation is required for cell spreading and actin dynamics .....	165
3.6 Surrogate APCs expressing a single-chain anti-Igκ Ab induce B cell spreading, BCR microcluster formation, and BCR signaling .....	167
3.7 Rap activation is important for B cell spreading, Ag gathering, and BCR signaling during B cell–APC interactions.....	169
3.8 Cofilin dephosphorylation is important for B cell spreading, Ag gathering, and BCR signaling during B cell–APC interactions.....	171
3.9 The Rap–cofilin module acts independently of ezrin .....	172
3.10 The Rap–cofilin pathway controls BCR microcluster mobility .....	173
3.11 The Rap–cofilin pathway promotes B cell spreading and BCR microcluster formation.....	174
3.12 Rap activation is required for Ag receptor-induced increases in cytoskeletal dynamics .....	175
3.13 Expression of cofilin-mCherry fusion proteins.....	176
3.14 The Rap-cofilin pathway regulates B cell spreading, Ag gathering, and BCR signaling during B cell-APC interactions, acting independently of ezrin .....	177
3.15 The magnitude of p-Tyr signaling is related to the amount of Ag gathered into microclusters at the B cell-APC contact .....	179
4.1 Rap1 regulates focal adhesion formation.....	200
4.2 Rap1 regulates adhesion and cytoskeletal dynamics, cell polarization, and tumor cell motility .....	202
4.3 Modulating Rap1 activity alters melanoma growth and metastasis <i>in vivo</i> .....	204

4.4 Modulating Rap1 activity impairs melanoma cell extravasation.....	205
4.5 Modulating Rap1 activity inhibits tumor cell TEM and alters adhesion dynamics in tumor cells interacting with endothelial cells .....	207
4.6 Modulating Rap1 activity reduces the ability of melanoma cells to form protrusions that cross capillary walls <i>in vivo</i> .....	209
4.7 Expression of Rap1V12 and Rap1GAPII alters Rap1-GTP levels in B16F1 melanoma cells.....	210
4.8 Rap1-GTP levels regulate total adhesive strength .....	211
4.9 Rap1-GTP levels regulate the amount of active human beta-1 integrin in clusters at the cell-ECM interface (i.e. focal adhesions).....	212
4.10 Rap1 activation and cycling are required for establishing a polarized distribution of F-actin cytoskeleton and PIP <sub>3</sub> .....	213
4.11 FRAP analysis of beta-1 integrin-GFP exchange in adhesions .....	215
4.12 The exchange of beta-1 integrin-GFP in adhesions is limited by the actin cytoskeleton .....	216
A.1 Applied stretch induces vinculin binding at focal adhesions in B16F1 cells.....	262
A.2 Applied stretch activates Rap1 and results in phosphorylation of the p130Cas cryptic tyrosine in tumor cells in a positive feedback loop .....	263
A.3 Vinculin enrichment at focal adhesions in response to stretch in 2-D requires Rap activation and cycling .....	264
A.4 Vinculin enrichment at focal adhesions in 3-D requires Rap activation and cycling.....	265
A.5 Shear flow activates Rap1 to stabilize integrin and increase turnover of paxillin at established focal adhesions .....	266
A.6 Rap1-GTP regulates growth in 3D and <i>in vivo</i> .....	267
B.1 Hypersensitivity pneumonitis and asthma models of inflammation in the lung .....	278
B.2 Hypersensitivity pneumonitis and asthma models of inflammation increase pulmonary metastasis.....	280
B.3 The inflammatory niche does not alter or select for enhanced tumor cell motility .	281
B.4 B16F0 cells show enhanced extravasation under inflammatory conditions <i>in vitro</i> but not <i>in vivo</i> .....	282

B.5 B16 cells arrest in small capillaries of the closed vasculature in the cremaster muscle .....	283
B.6 Initial cell divisions and metastases show close association with hyaluronic acid more abundant in inflamed lungs.....	284
B.7 The intrinsic ability of tumor cells to bind HA augments lung metastases.....	285

## **List of abbreviations**

Ab – antibody

ADF – actin depolymerization factor

Ag – antigen

AID – activation-induced deaminase

APC – antigen presenting cell or adenomatous polyposis coli

ADP – adenosine diphosphate

Arp – actin related protein

ATP – adenosine triphosphate

BAFF – B-cell activating factor

BAFF-R – B-cell activating factor receptor

BCR – B-cell receptor

BCAP – B-cell adaptor protein

BiFC – bifluorescence complementation

BNPA - bromo-(2-nitrophenyl) acetic acid

CAM – cell adhesion molecule

Cbl – cordon-bleu

Cc – critical concentration

CLP – common lymphoid progenitor

CR – complement receptor

CTC – circulating tumor cell

CTL – cytotoxic T lymphocyte

DAG – diacylglycerol

DC – dendritic cell

DNA – deoxyribonucleic acid

ECM – extracellular matrix

EHEC – Enterohaemorrhagic *E. coli*

ER – endoplasmic reticulum

F-actin – filamentous actin

FAK – focal adhesion kinase

FDC – follicular dendritic cell

FH – fomin homology

FRAP – fluorescence recovery after photobleaching

FRET – fluorescence resonance energy transfer

G-actin – globular actin

GAP – GTPase activating protein

GBD – GTPases binding domain

GCR – germinal center reaction

GEF – Guanine nucleotide exchange factor

GFP – green fluorescent protein

GMF – glia maturation factor

GOF – gain of function

GPI – glycosylphosphatidylinositol

GDP – guanosine diphosphate

GTP – guanosine triphosphate

HA – hyaluronic acid

HVR - hypervariable region

IC – immune complex

ICAM – intercellular adhesion molecule

IP(3) – inositol triphosphate

IL – interleukin

INF – interferon

IRF – interferon regulatory factor

IS – immune synapse

ITAM – immunoreceptor tyrosine-based activation motif

ITIM – immunoreceptor tyrosine-based inactivation motif

LEGI - local excitation, global inhibition

LINC - linker of nucleoskeleton and cytoskeleton

LLC – Lewis lung carcinoma

Lmod - leiomodin

LN – lymph node

LOF – loss of function

MAC1 – macrophage receptor-1

MAMP – microbe-associated molecular pattern

MSD – mean square displacement

MSK – membrane-associated actin cytoskeleton

MTOC – microtubules organization center

NF- $\kappa$ B - nuclear factor  $\kappa$ B

NF-AT - nuclear factor of activated T cells

NHE – Na<sup>+</sup>/H<sup>+</sup> exchanger

NHEJ – nonhomologous end-joining

NOD – nonobese diabetes

NPF – nucleation promoting factor

PALM - photoactivation localization microscopy

PAMP – pathogen associated molecular pattern

PDK1 – phosphoinositide-dependent kinase 1

PE – phosphatidylethanolamine

PKA – protein kinase A

PKC – protein kinase C

PI3K – phosphoinositide-3 kinase

(PI(3,4,5)P<sub>3</sub>) - phosphatidylinositol (3,4,5)-trisphosphate

(PI(3,4)P<sub>2</sub>) - phosphatidylinositol (3,4)-bisphosphate

(PI(3)P) - phosphatidylinositol 3-phosphate

PLC – phospholipase C

PM – plasma membrane

PRR – pattern-recognition receptor

PTK – protein tyrosine kinase

PTM - post-translational modification

PTP – protein tyrosine phosphatase

Qdots – quantum dots

RA - Ras/Rap association

RAG – recombination activating gene

RNA – ribonucleic acid

SCF – stem-cell factor

SCID – severe combined immunodeficiency

SCS – subcapsular sinus

SFK – Src family kinase

SHRC - WASH regulatory complex

SLO – secondary lymphoid organ

SPT – single particle tracking

STED - stimulated emission depletion

TAM – tumor associated macrophage

TCR – T-cell receptor

TEM - transmission electron microscopy or transendothelial migration

TLR – Toll-like receptor

TIR - Toll-IL-1 receptor

TIRF – total internal refractive fluorescence

TNF – tumor necrosis factor

VCA – verprolin, central, acidic domain

WASp – Wiskott-Aldrich Syndrome protein

WH – WASp homology

WRC – WAVE regulatory complex

YFP – yellow fluorescent protein

## Acknowledgements

I would like to first acknowledge my supervisors Drs Michael Gold and Calvin Roskelley for their unwavering support. Their contributions to this work have been immeasurable. They have led by example in how to conduct successful scientific research while being a positive and encouraging colleague. We have pooled and shaped a lot of ideas together and brought many to fruition. Throughout my time as their student, I have looked forward to getting in every day. I have been given the incredible scientific freedom to pursue questions in other labs and work with other investigators at UBC and beyond. This has been largely possible because of all the relationships they have cultivated within the community. The respect they have gained from their colleagues is enormous and I will forever be thankful that they have trusted me as an extension of them.

I would like to acknowledge the supervisors that took me into their labs in order to pursue specific techniques. Drs. Paul Kubes and Donna-Marie McCafferty were generous enough to allow me to learn intravital microscopy and explore interactions between tumor cells and endothelial *in vivo*. This was a major contribution to at least one publication, but also to how we continue to think about these interactions. Within the I3 group at the University of Calgary, I would like to particularly thank Brandie Millen-Martin. Brandie's patience and expertise was remarkable. I was also able to spend five months at the University of Toronto in the lab of Dr. Sergio Grinstein. Sergio has been an incredible mentor. His intensity and love for Science reverberates beyond SickKids and through all trainees he has touched. Though the number of people he has trained is in

the triple digits, he continues to approach mentoring with vigor. From the Grinstein lab, I would like to particularly thank Dr. Valentin Jaumoullie. Val's knowledge of experiments and the literature is vast and he is always willing to share it. Sitting with Val and discussing Science has been a real source of enjoyment for me. Without him, I would not have been able to complete the work on BCR diffusion.

Within the Life Science Institute, I have forged many meaningful relationships that have been a great source of support and scientific inspiration. Dr. Linda Matsuuchi has been a great mentor and friend. I appreciate all the work Linda has done to refine manuscripts and help guide me through the past several years. Dr. Robert Nabi has given me great advice and has also been a keen mentor. Dr. John Church has always kept me on track and looked out for my best interests. Drs. Chris Loewen, Douglas Allan, Don Moerman and Shernaz Bamji have been wonderful teachers and have done tremendous things for students, including me, in the Cell and Developmental Biology Program. I would like to particularly acknowledge Dr. Loewen for all of his support in putting together the student led seminar series with Stephanie Ellis and myself. Stephanie, Dr. Jacky Goetz, Dr. Marcia Graves, Dr. Menno Oudoff and Dr. Pascal St. Pierre have kept Science from something that takes place within a building and woven it into the fabric of our friendships that I hope will continue for a long time in ways our lives allow. Outside of the LSI, I have been fortunate to have incredible friends that kept me from living and breathing experiments all the time. Christopher Carrique, Joshua Cox, Anders Hemmingsen, and Dr. Damian Murray have been the source of much needed breaths of fresh air.

I would like to thank members of the Gold and Roskelley labs that have made major contributions to this work and have been part of a vibrant scientific culture. May Dang-Lawson is the rock-solid foundation of the Gold lab and has been a wonderful person to work with. Megan Gilmour has been a huge help with many experiments and has always been a source of great support. Past members of the Gold and Roskelley labs, in particular, Dr. Raibatak Das, Dr. Kevin Lin, Dr. Sarah McLeod, Jane Iwanyshan, Janet Dukowski, and Victor Lei have been fantastic colleagues and friends. I would like to thank current Gold and Roskelley lab members, in particular, Sonja Christian, Jia Wang, and Kate Choi.

Finally, I would like to thank my parents. To my Mom, Dr. Sheryl Freeman, you are the magnet of my moral compass. To my Dad, you keep me running.

# 1. Introduction

## 1.1 The immune system

Cellular immunity developed as far back in evolutionary time as multicellularity (i.e. in all vertebrates, invertebrates, and plants) [1] whereas molecular defense mechanisms against attacks by infectious agents occur even in the most simple cell types [2]. Indeed, host-pathogen interactions have shaped many aspects of evolution from chemical secretions in saliva to social group size and personality in humans [3, 4]. While physical barriers and avoidance of infection via socio-cultural mechanisms limit pathogen encounter and attack, the body's immune system is poised to eliminate pathogenic challenges that overcome this first line of defense. All immune systems perform three functions: 1) recognize a diverse array of pathogens, 2) eliminate or neutralize recognized pathogens, and 3) avoid damaging self-tissues [1]. The human immune system has two arms, both geared for these functions. With respect to recognition, one arm, the innate immune system, recognizes and responds to infectious non-self or altered-self whereas the adaptive immune system recognizes and responds to all non-self antigens [5].

The innate immune system consists of cells with non-clonally distributed receptors that recognize patterns on a pathogen's surface as well as the plasma membranes of apoptotic cells and indicators of cellular damage [6, 7]. The receptors that recognize these danger signals include pattern-recognition receptors (PRRs: Toll-like receptors, Nod-like receptors) and scavenger receptors that evolved to not recognize common indicators of infection or damage and which were likely selected to not recognize self, which could lead to autoimmunity, death or low fitness of the organism [8]. The recognition of altered-self, including oxidized glycoproteins and glycolipids or self components that are not usually exposed to cells of the innate immune system

for example phosphatidylserine, DNA, endoplasmic reticulum (ER)-resident proteins, or F-actin, is required for tissue homeostasis.

The cells of the innate immune system, which include monocytes, macrophages, neutrophils, mast cells, basophils, natural killer cells, and dendritic cells, coordinate the recognition of infectious targets with the mounting of an effector response [1]. Normally, the sensing of damaged cells or their contents, as well as oxidized lipids and proteins targeted for destruction, leads only to phagocytic clearance without mounting an effector response. However, if a ‘danger’ signal is sensed via PRRs, innate immune cells will mount effector responses [9] that can clear an infection via the secretion of antimicrobial peptides and cytokines that stimulate acute phase responses, or by the trapping of pathogens via DNA-based ‘nets’ [10-12]. At the same time, phagocytes can clear many infections by internalizing pathogens through the process of phagocytosis or macropinocytosis and killing them. Both humoral and cellular responses can orchestrate the induction of the adaptive arm of the immune system by secreting cytokines and presenting surface peptides/immune complexes along with adhesion and co-stimulatory molecules.

The adaptive immune system evolved in jawed fish vertebrates and is distinguished from the innate system by the diversification of clonal Ag receptors and by the generation of immunological memory [13]. Its cellular constituents are lymphocytes, which are divided into two families named for their organ of origin: T cells (thymus-derived) and B cells (bursa- or bone-marrow-derived) [13]. The diversification of Ag receptors is achieved through programmed somatic recombination of random germline variable (V), diversity (D) and joining (J) gene segments within Ag receptor genes, termed V(D)J recombination [5]. This process is random, giving rise to a vast number of combinatorial possibilities and Ag receptors. Importantly,

once successful rearrangement of Ag receptor genes is complete, further rearrangement is blocked. This results in the clonal nature of the TCR or BCR on individual lymphocytes (this is not absolute for T cells) and the vast number of these clones. Random recombination will result in some of these clones recognizing self. The self-tolerance mechanisms of the adaptive immune system, unlike that of the innate immune system, are established within the organism. The encounter of self-Ag by immature T and B cells leads to cell death, a process called negative selection, or other possible outcomes in which the cells are rendered non-functional (anergy; see next section on B cell development). Encounter of self-Ag in the periphery results also results in clonal anergy unless the Ag is encountered in the context of co-stimulatory molecules that are induced by the recognition of danger signals by innate immune cells. In this case, clonal expansion and differentiation occurs, giving rise to effector T and B cells as well as immunological memory [14].

## **1.2 The BCR in B cell development and survival**

### **1.2.1 Overview**

B cell receptor (BCR) signaling is fundamental to B cell development, survival, and responses to Ag. Signaling by the BCR and its precursor, the pre-BCR, is required for B cells to transit developmental checkpoints during development, mediates negative selection, and provides Ag-independent signals (i.e. tonic signaling) that are required for B cell survival in the periphery. These selection processes limit the development of B cells that recognize self but determine a setpoint for tonic BCR signaling. A second round of BCR-mediated selection occurs when B cells enter a germinal center reaction (GCR) after encountering cognate Ag in

secondary lymphoid organs (SLOs). This reaction is a Darwinian process, where highly proliferative but pro-apoptotic activated B cells compete for limiting amounts of Ag and T cell help that will allow further proliferation and differentiation.

The BCR is a protein complex comprised of non-signaling membrane-bound Ig (mIg) containing heavy and light chains linked via disulfide bonds to a transmembrane signaling competent heterodimer of two polypeptides, Ig $\alpha$  and Ig $\beta$ . Ig $\alpha$  and Ig $\beta$  contain Immunoreceptor Tyrosine-based Activation Motifs (ITAMs) that can be phosphorylated by protein tyrosine kinases (PTKs) Lyn, Fyn, and Blk at the plasma membrane [15]. Phosphorylated tyrosines of Ig $\alpha$  and Ig $\beta$  recruit SH2 domain containing PTKs including Syk and additional Src family kinases, amplifying the signal [15, 16]. Syk in particular can phosphorylate adaptor proteins that initiate signaling complexes leading to the activation of the phosphoinositide-3 kinase (PI3K) pathway, the phospholipase C gamma (PLC $\gamma$ ) pathway, the Ras-Raf-Erk pathway, Rap GTPases, and small Rho-GTPases [17, 18].

Syk phosphorylates CD19, a member of the BCR coreceptor complex, as well as the B cell adaptor protein (BCAP). Once phosphorylated, CD19 and BCAP can recruit the p85 subunit of PI3K via an SH2 interaction with the Y(P)XXM motif [19, 20]. PI3K can then phosphorylate phosphatidylinositols to phosphatidylinositol 3-phosphate (PI(3)P), phosphatidylinositol (3,4)-bisphosphate (PI(3,4)P2), and phosphatidylinositol (3,4,5)-trisphosphate (PI(3,4,5)P3). PI(3,4,5)P3 recruits phosphoinositide-dependent kinase (PDK1), Akt, Btk, and PLC $\gamma$ 2 via their Pleckstrin-homology (PH) domains [17]. Importantly, Akt activates the pro-survival nuclear factor  $\kappa$ B (NF- $\kappa$ B) pathway and inactivates pro-apoptotic pathways by phosphorylation of Bcl-2 family members and caspase 9 [21, 22]. Syk also phosphorylates the adaptor BLNK that recruits

PLC $\gamma$ 2 to the plasma membrane. PLC $\gamma$ 2 recruitment results in its phosphorylation and activation by Syk and Btk. The lipase can then cleave phospholipids, giving rise to second messengers IP $_3$  and DAG. IP $_3$  causes the release of Ca $^{2+}$  from intracellular stores and the activation of the nuclear factor of activated T cells (NF-AT) transcription factor, while DAG activates Ras guanyl nucleotide-releasing protein (RasGRP), CalDAG-GEFI (RasGRP2), and protein kinase C (PKC) enzymes. These enzymes modulate the activity of other targets in the Ras-Raf-MEK-ERK pathway, NF- $\kappa$ B, the JNK and p38 MAPKs, and the Rap GTPases [18]. Collectively, these pathways regulate B cell differentiation, proliferation, and survival discussed in this section.

### **1.2.2 B cell development**

B cells develop from a common lymphoid progenitor (CLP) in the fetal liver of embryos and the bone marrow of adults (see Figure 1). Stromal cells in the bone marrow set up the niche for B cell development by providing adhesion molecules as well as cytokines such as IL-7 and stem-cell factor (SCF) [5]. Stromal cells also secrete the chemokine CXCL12 (SDF-1), which plays a major role in the retention of pro- and pre-B cells within the stromal microenvironment [23, 24]. As B cells progress through developmental steps (outlined below and in Figure 1) they migrate from the inner bone surface (endosteum) towards the sinuses, which located in the center of the marrow cavity and are sites at which B cells exit the bone marrow and enter into circulation [5].

Discrete steps in B cell development are characterized by stages of BCR rearrangement along with the expression of other B cell-specific membrane proteins such as CD19 [5]. The BCR, in turn, orchestrates B cell development by providing checkpoint signals at different stages. First, early pro-B cells, which do not yet express the pre-BCR or surface Ig, undergo Ig

heavy chain rearrangement that joins a  $D_H$  gene segment to a  $J_H$  gene segment. This is followed by a late pro-B cell stage where  $V_H$  to  $DJ_H$  joining occurs. The complex process of V(D)J rearrangement was discovered by Susumu Tonegawa in 1978 [25], for which he won a Nobel prize in 1987, and the mechanism of recombination was discovered by David Baltimore in 1989 [26, 27]. Briefly, the somatic DNA recombination requires double-strand DNA breaks at gene segment borders mediated by the recombination activating genes (RAGs), which encode for an endonuclease. The endonuclease is composed of the RAG1 and RAG2 proteins, whose expression is tightly controlled in lymphocyte development. The accessibility of the Ag receptor gene segments to RAG is also controlled by DNA methylation, localization of the Ig and TCR loci within the nucleus, and the chromatin ultrastructure of these regions [28]. Additional Ig diversification by mechanisms other than V(D)J recombination is generated by terminal deoxynucleotidyl transferase, which can add nontemplate nucleotides to the V, D, and J exons [5]. The joining step of the reaction is mediated by a common double-strand DNA break repair mechanism involving proteins of the nonhomologous end-joining (NHEJ) pathway [29].

Pro-B cells that undergo successful Ig heavy chain rearrangements (~ 55% of the cells) undergo selection at a pre-BCR checkpoint [5]. The pre-BCR is composed of a complete  $Ig\mu$  heavy chain (i.e. variable and constant regions) and a surrogate light chain composed of the  $\lambda 5$  and VpreB polypeptides (see Figure 1). Expression of the pre-BCR on the cell surface, and the resulting BCR signaling, prevents further rearrangement of the heavy chain (termed allelic exclusion) and provides proliferation signals for large Pre-B cells to undergo considerable expansion [5]. How the pre-BCR initiates signals that drive proliferation is not completely understood. The pre-BCR may be clustered by extracellular ligands present in the bone marrow stroma such as galectin-1 [30, 31], or may provide signals via ligand-independent clustering or

collisions in the plasma membrane (PM) (i.e. tonic signaling, see next section) [32]. Pro-B cells that do not successfully rearrange their IgH chain genes and do not express a pre-BCR on their surface do not receive these signals and instead undergo cell death. Similarly, B cell progenitors lacking the proximal pre-BCR signaling kinases Blk, Fyn, and Lyn, or the co-receptor CD19, do not pass this checkpoint [33, 34]. At the subsequent small pre-B-cell stage, rearrangements of the light-chain loci occur in a similar manner as for the Ig heavy chain. Once a light chain gene is successfully rearranged, Ig light chain polypeptides form disulfide-bonded complexes with the Ig heavy chain in the ER to make a complete membrane IgM (mIgM), which associates with the,  $Ig\alpha/Ig\beta$  signaling subunit to form a functional BCR complex that is trafficked to the plasma membrane (Figure 1) [5].

Figure 1

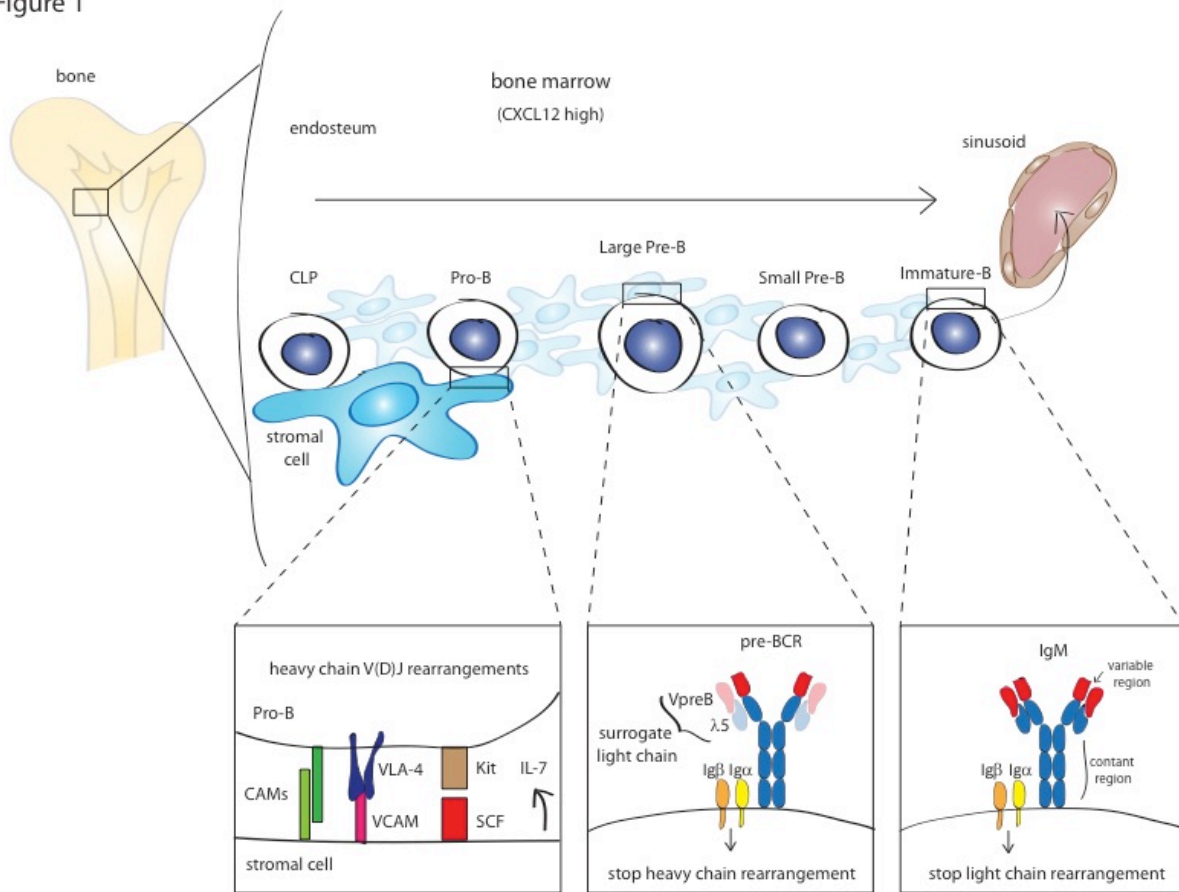


**Figure 1.1.** *B cell development in the bone marrow.* Early pro-B cells arise from a common lymphoid progenitor (CLP) in the endosteum of the bone. Stromal cells provide B cells with cell adhesion molecules (CAMs, specifically VCAM), stem cell factor (SCF), and IL-7, all partly required throughout their development. Discrete steps in B cell development are characterized by stages of BCR rearrangement. The pre-BCR is formed after successful Ig heavy chain rearrangements and provides proliferative signals and prevents further rearrangement of the heavy chain. A complete mIgM BCR in immature B cells that does not recognize self will result in preventing light chain rearrangement and the trafficking into circulation via sinusoids.

Immature B cells expressing mIgM undergo negative selection where recognition of self in the bone marrow results in either 1) apoptosis/clonal deletion, 2) receptor editing where they

undergo further light chain rearrangement in order to generate BCRs with a different Ag specificity, 3) ignorance, in the case of weak-binding to self, or 4) anergy. Anergic B cells constitute more than half the immature B cell compartment [35, 36] and cannot be activated by their specific ligand even in the presence of T cell help. Although the mechanisms of B cell anergy are still not fully understood, it is clear that anergic B cells have much shorter half-lives than their naïve counterparts (5 days versus 40 days). This is the result of an impaired ability to compete for niche in the periphery where survival cytokines such as B cell activating factor (BAFF) are produced [37] and expression of FAS (CD95), a cell surface protein that can initiate apoptosis [36]. Additionally, anergic B cells do not localize to B cell follicles but instead remain in the T cell zones of SLOs which may also limit exposure to pro-survival cytokines [36]. Anergic B cells also exhibit decreased cell surface expression of the BCR, owing to its selective retention in the ER. However, the BCR that does get to the PM is in a state of chronic auto-Ag induced signaling, which leads to both receptor desensitization and anergy as the level of BCR signaling is sufficient to ensure B cell survival but maintained at a level below what would trigger B cell activation [36].

### **1.2.3 BCR tonic signaling**

Once B cells exit the bone marrow and enter circulation, they continue to require signals from surface BCR. Such ligand-independent signaling is termed tonic signaling and also plays a significant role in pre-BCR signaling [38]. BCR signaling was first demonstrated to be necessary for B cell survival in the periphery by selectively deleting surface Ig in mature B cells, which shortened their half-life from 40 days to 3-6 days [39, 40]. The presumed tonic BCR signals that promoted B cell survival was shown to be ligand-independent as truncations of the extracellular Ig domains that prevent Ag binding did not impact B cell development or survival

[41, 42]. This tonic BCR signaling is mediated by the immune tyrosine activation motifs (ITAM) found in the Ig $\alpha$  and Ig $\beta$  components of the BCR [40, 43]. Tonic BCR signaling can be thought of as the equivalent of a low Ag-induced signal (i.e. as part of a continuum) that exceeds the threshold for B cell survival, but is below the threshold for activation (see Figure 2, left side) [38].

Figure 2

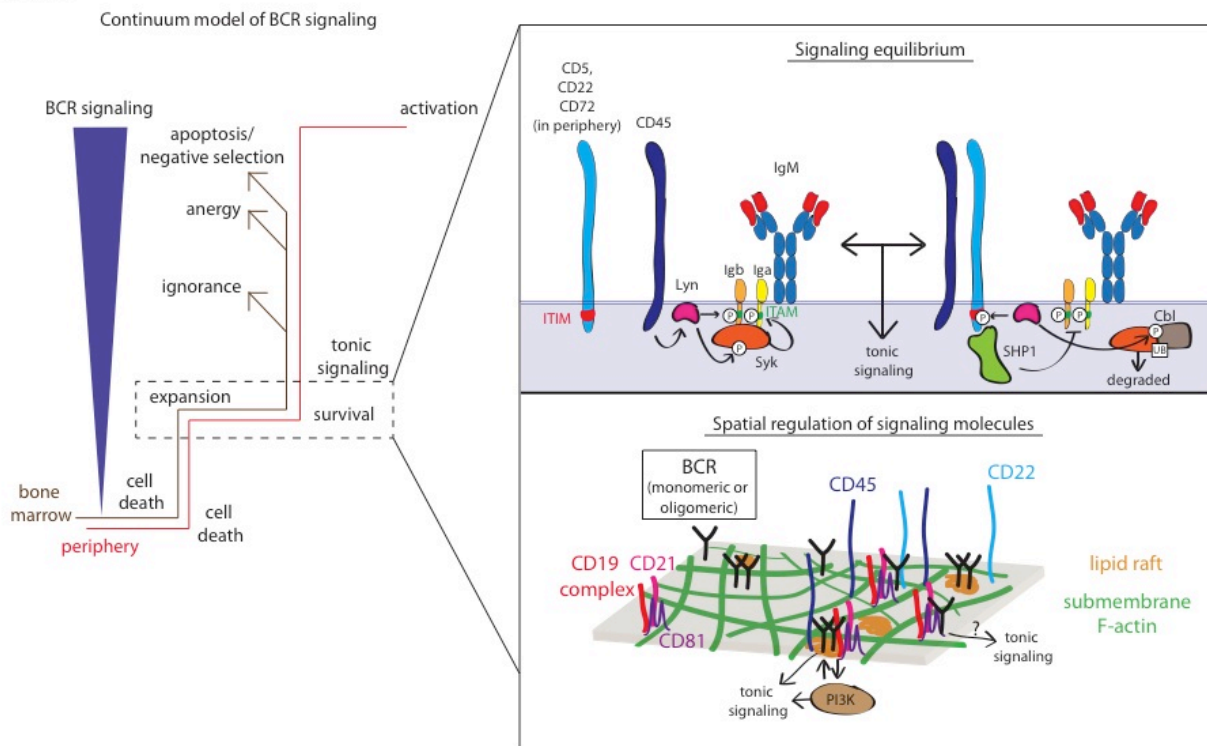


**Figure 1.2.** A continuum model of BCR signaling in development, survival, and activation. Signaling by the pre-BCR in the bone marrow is required for the survival and expansion of pre-B cells. Too much signaling results in ignorance or anergy of these cells if they enter circulation or negative selection in the bone marrow. Once in the periphery, tonic BCR signaling is required for cell survival. Tonic signaling is mediated by the dynamic equilibrium of PTKs (e.g. Lyn, Syk) and PTPs (e.g. SHP1). PTK and PTP activities are partly controlled by transmembrane ITIM containing proteins (CD5, CD22, CD72) and transmembrane phosphatases (CD45) as well as degradation by ubiquitination. An important consideration for tonic signaling is the spatial organization of the BCR, coreceptor

complex (CD19/CD21/CD81), and PTKs/PTPs in the plasma membrane. BCR mediated tonic signaling appears to be largely PI3K dependent.

The mechanisms controlling tonic signaling are not entirely understood, but it likely involves a dynamic equilibrium between the kinase and phosphatase activities that regulate BCR signaling (Figure 2, upper right). In line with this idea, global inhibition of protein tyrosine phosphatases (PTPs) using pervanadate leads to strong ligand-independent BCR signaling [44]. More targeted experiments have shown that mice lacking the SHP-1 phosphatase that directly dephosphorylates tyrosine residues in the Ig $\alpha$  and Ig $\beta$  ITAMs [45] have a lower threshold for negative selection in development and activation in the periphery [46, 47]. This results in substantial defects in peripheral B cell numbers, but also the production of autoantibodies and severe autoimmunity in adults [46, 47]. On the other side of the equation, tonic signaling is dependent on the Syk protein tyrosine kinase [16, 48, 49]. Syk is negatively controlled by PTPs and appears to be positively controlled by redox potential [16]. Indeed, treating B cells with either pervanadate or hydrogen peroxide results in rapid activation of Syk [16]. How Syk might be activated in this way to promote tonic signals from the BCR has been postulated to stem from the BCR itself or possibly TNF family receptors like BAFF-R [16, 50, 51].

The Src family kinase (SFK) Lyn plays both positive and negative roles in BCR signaling. Lyn, can phosphorylate Ig $\alpha$  and Ig $\beta$ , CD19, and protein tyrosine kinases Syk and Btk, thereby promoting signaling downstream of the BCR, however, Lyn $^{-/-}$  B cells are hyperresponsive to BCR cross-linking [7]. Lyn $^{-/-}$  mice have phenotypes similar to SHP-1 $^{-/-}$  mice: defects in selection during development, decreased peripheral B cells, and the production

of autoantibodies. In a negative regulatory role, Lyn can phosphorylate CD22 to recruit SHP-1 and also phosphorylates Syk to recruit the E3 ubiquitin ligase Cbl, leading to its degradation (Figure 2, upper right).

The paradoxical immunodeficiency that is accompanied by eventual autoimmunity in both SHP-1 and Lyn knock-out mice suggests a paradigm in which regulators that control tonic BCR signaling during B cell development act to tune thresholds for Ag-stimulated responses in the periphery. In this way, tonic signaling serves as a setpoint, similar to a setpoint in the design of a thermostat [52]. A thermostat is a simple technology in which the device measures temperature, compares the temperature to a setpoint and then uses what is called the ‘feedback error’ between the two to adjust the heat accordingly (turn heat on when the building temperature is too low and turn it off when it is too high) [52]. In the same way, the B cell compartment compares the periphery to the sterile bone marrow, using BCR signaling as an organizing principle (i.e. unit of measure). That regulators overlap in positive and negative propagation of the signal likely acts to aid in sensing discontinuity of BCR signaling and possibly discriminate the physical form of presented Ag. This also allows B lymphocytes to act on a population basis, eventually leading to the production of the best protective antibodies.

A major mechanism governing tonic signaling in B cells is the spatial organization of BCR complexes in the PM in relation to the PTKs and PTPs that control proximal BCR signaling, and the CD19/CD21/CD81 co-receptor complex that amplifies BCR signaling (Figure 2 right side, lower right). This organization has been probed by three investigators, Michael Reth, Facundo Batista, and Susan Pierce, using microscopy approaches such as fluorescence resonance energy transfer (FRET), super resolution microscopy (e.g. STORM), single particle tracking (SPT), and bifluorescence complementation (BiFC) [53-55]. Michael Reth proposed in

2000 that the BCR exists in the PM as an autoinhibited oligomer, stably interacting with other BCRs, based upon biochemical evidence [56]. It was postulated that an oligomeric conformation of the BCR could confer responses to diverse antigenic structures where the Ag drives apart the BCR to make Ig $\alpha$ /Ig $\beta$  ITAMs accessible to phosphorylation by Syk. This was later called the ‘dissociation model’ for BCR activation. Ten years later, the Reth group used BiFC where YFP was separated into two domains, each fused to the cytoplasmic tail of a subset of Ig $\alpha$  molecules in the cell, such that BCR dimerization would result in a complete YFP and fluorescence [53]. Indeed, IgM and IgD BCR complexes were shown to undergo homo-oligomerization at the PM. These studies by Michael Reth challenge the BCR cross-linking hypothesis: that the B cell PM contains inert monomeric BCR that is activated by random collisions (tonic signaling) or Ag-induced clustering [6]. Instead, a dissociation model postulates that monomeric BCR is active, turns over readily, and is the source of tonic signaling [53]. Concerns with these studies are that 1) they were carried out in either the J558 plasmacytoma and the S2 *Drosophila* cell lines, which may have altered membrane compartmentalization and lack transmembrane proteins such as CD19, CD22 and CD45 that regulate BCR activity and/or organization and 2) they use an overexpression system to describe BCR oligomers. Moreover, in the BiFC experiments, once YFP is complemented, the dissociation is very low, which could contribute to the observed stability of the dimer. More generally, it is not clear from this model how Ag affinity would be distinguished, as the dissociation-induced triggering of BCR signaling would be a binary switch.

Very different ideas have been proposed by Susan Pierce to support of a ‘conformation model’ for BCR triggering and presumably tonic signaling. In resting B cells, Pierce and colleagues have shown using FRET that the BCR is a monomer that is not in close enough proximity to achieve FRET via homotypic interactions [57]. In order to determine the diffusion

behavior of single BCRs, they used SPT. The median diffusion coefficient of single BCRs was  $0.1 \mu\text{m}^2/\text{s}$  and they considered single BCRs with diffusion coefficients below  $0.01 \mu\text{m}^2/\text{s}$  to be immobile. Using these parameters they determined that 80% of the BCR monomers show short range movement consistent with free diffusion while 20% of the BCRs spontaneously form immobile oligomers [58]. The addition of either multivalent or monovalent Ag in a lipid bilayer increased the population of immobile receptors to 50%. The arrest of engaged BCRs resulted in the accumulation of Syk-GFP but was independent of SFK activity and did not require the association with Ig $\alpha$  and Ig $\beta$  [58]. Deletions within the Ig  $\mu$  heavy chain showed that the arrest of BCR mobility caused by monovalent Ag required a single ectodomain (C $\mu$ 4) and the N-terminal part of the transmembrane of mIgM, neither of which are involved in Ag recognition [58]. Based on previous experiments, the transmembrane domain of the mIgM is thought to mediate an interaction with membrane lipids that contributes to Ag induced oligomerization [46]. However, tonic signaling mediated by the pre-BCR does not seem to require lipid raft localization [59]. Nevertheless, the model based on these observations proposes that a small number of transient BCR oligomers in resting mature B cells are the source of tonic BCR signaling.

The structural changes that may occur in the BCR when it is immobilized in the PM are not known. In fact, the ectodomain structure of a complete BCR with associated Ig $\alpha$  and Ig $\beta$  has yet to be solved. Initial studies employing FRET by the Pierce lab have shown that upon immobilization induced by monovalent Ag, the ectodomains of the mIg subunit and the Ig $\alpha$ / $\beta$  subunit of the BCR come closer together while the cytoplasmic tails of Ig $\alpha$  and Ig $\beta$  move further apart [6, 55]. The lipid microdomain environment has been proposed to regulate these conformational changes [6]. One idea is that the ITAM containing cytoplasmic tails of Ig $\alpha$  and

Ig $\beta$  are shielded from kinases through an interaction with the inner leaflet of the PM [6]. This type of “safety” on the receptor trigger has been shown for the cytoplasmic tails of TCR in CD3 $\zeta$  and  $\epsilon$  chains [3, 4]. The interactions that embed ITAMs of these CD3 chains requires the cytoplasmic tail to have a number of basic residues that interact with negatively charged lipids like phosphatidylserine and phosphatidylglycerol [3]. CD3 $\zeta$ , for example, contains 14 basic residues (~30% of total amino acids) and only 4 acidic residues. Ig $\alpha$  and Ig $\beta$ , on the other hand, have an inverse ratio, with 4 and 3 basic residues, respectively (less than 7%), and 14 and 12 acidic residues, respectively. It seems unlikely that the ITAMs of Ig $\alpha$  and Ig $\beta$  are buried in the lipid membrane via the charge-based interaction with lipids that is observed for CD3 $\zeta$ . Another possibility is that entering lipid rafts containing unsaturated lipids, which are thicker regions of the lipid bilayer, may result in a conformational change of the cytoplasmic tail [6]. This may coincide with lipid raft resident SFK binding, an interaction that has been shown to disrupt the spatial proximity of Ig $\alpha$  and Ig $\beta$  cytoplasmic tails [6, 57]. Generally, the conformation model put forward by the Pierce group for BCR triggering postulates that 1) immobile BCRs are the source of tonic signaling in a resting state and that 2) engagement by membrane-bound Ags, even if monovalent, provides an opposing force upon receptors, increases the fraction of immobile BCR, and may alter local lipid microenvironments to increase BCR signaling.

The best evidence that spatial organization of the BCR contributes to tonic signaling comes from work carried out by Facundo Batista’s group, which demonstrates that the membrane-associated actin cytoskeleton (MSK) limits BCR diffusion and signaling [60]. This work followed up on previous studies demonstrating that the signal strength of the BCR is limited by F-actin [61]. By using SPT of the BCR, Bebhinn Treanor in the Batista lab demonstrated that the receptor was largely mobile but compartmentalized by MSK networks (i.e.

confined-mobile). The median diffusion coefficient for mIgM was  $0.03 \mu\text{m}^2/\text{s}$ , could be substantially increased by disrupting the MSK or the connection between the MSK and the membrane, and this correlated with elevated BCR signaling [60, 62].

Additional work from Batista and colleagues showed that the BCR co-receptor CD19 was necessary for the increase in BCR signaling observed upon dissolution of the actin MSK and that the diffusion of CD19 was itself limited by tetraspanins and the MSK [63]. Batista and colleagues used STORM to show that the BCR formed nanoclusters or protein islands in resting B cells and postulated that CD19 entered these preformed clusters upon disruption of tetraspanins and F-actin as the BCR clusters did not change in size in these experiments [63]. While STORM based experiments can oversample individual particles and give the appearance of clustering, these experiments demonstrated heterogeneity of clustering between the IgM (40% clustered) and IgD (70% clustered) isotypes, suggesting this was likely not the case [63]. Moreover, previous experiments demonstrated that IgM and IgD do not localize to the same nanoclusters in resting B cells, suggesting some active process or preference for BCR isotypes in organizing into these islands [64]. The radii of clusters were 60-80 nm and estimated to contain 20-150 BCRs per cluster [63]. While BCRs may be pre-assembled in protein islands within regions defined by the MSK, how these islands interact with the MSK is not well understood. In T cells, for example, protein islands containing just 7-20 TCRs are both corralled and directly interact with F-actin to maintain the LAT signaling adaptor spatially segregated from the TCR [65, 66]. The disruption of the MSK in B cells by Latrunulin may increase confinement zones but also the diffusion of the BCR within these regions and diffusion of CD19 into these regions. This is very similar to super-resolution based experiments where the addition of TCR

agonists resulted in the concatenation of TCR and LAT protein islands leading to TCR signaling ‘hotspots’[65].

CD19 is a major regulator of PI3K in B cells [64] whose signaling alone is sufficient to rescue tonic signaling in B cells lacking a BCR [67], but is dispensable for BCR signaling in response to soluble Ags [64]. CD19 is also expressed early in B cell development and is required for B cells to pass pre-BCR checkpoints [34, 68]. Interestingly, variants of the DT40 chicken B cell line in which the gene encoding the p85 subunit of PI3K has been disrupted still exhibit elevated Ag-independent BCR signaling, as measured by ERK phosphorylation, in response to disruption of F-actin by latrunculin. In contrast, DT40 cells lacking proximal BCR signaling components such as the Lyn SFK, the Btk tyrosine kinase, or CD19 do not show increased BCR signaling when the MSK is disrupted [60, 63]. When the tyrosines in the cytoplasmic domain of CD19 that act as binding sites for Vav and PLC $\gamma$ -2 are mutated, this also abrogated ligand-independent signaling [63]. This suggests that CD19 recruits other signaling molecules (i.e. Vav, PLC $\gamma$ -2, Grb2, SFKs) to the BCR to mediate signaling in response to latrunculin.

While the resting state organization of the BCR is still up for debate, (i.e. monomeric, clustered, or oligomeric), it seems apparent that the control of BCR tonic signals requires the CD19 co-receptor complex and other transmembrane proteins such as CD22, CD5, and CD72 that can recruit PTPases. If these negative regulators, which are expressed more highly in the periphery, interacted transiently with BCR complexes, it would lower tonic signaling, further limiting auto-activation. While a clear picture of the enzymatic control of BCR signaling has emerged over the past few decades, how these interactions are spatially regulated is an important

topic of future investigation. For a more detailed discussion of molecular diffusion with a focus on the BCR, see the section on *Molecular Diffusion*.

#### **1.2.4 BAFF and BCR interplay for B cell survival**

B cells require two signals for survival in the periphery: 1) BCR tonic signaling and 2) the TNF family cytokine, BAFF [38, 69]. The amount of BAFF also determines the size of the B cell compartment. Elevation of BAFF levels in transgenic animals can dramatically expand B cell populations and lead to autoimmunity [70]. Recently it has been shown that survival signals from BAFF are entirely dependent on the activation of Syk, which resulted in phosphorylation of Ig $\alpha$  as well as the activation of downstream BCR signaling pathways [41]. These results indicate that one function of this pro-survival cytokine is to co-opt the BCR itself to mediate tonic signaling. It should be noted, however, that B cells lacking the BCR rescued from cell death with an active form of PI3K still require BAFF for survival *in vitro*, suggesting that the BAFF-R likely initiates both BCR-dependent and –independent survival signals [67].

### **1.3 B cell encounters with antigen presenting cells**

#### **1.3.1 Overview**

The high diversity of BCRs/clonal B cells confers the ability for the peripheral B cell compartment to recognize a huge range of potential Ags but would also make these encounters impossibly rare in an open system. For this reason, Ags become concentrated within (SLOs) including lymph nodes, spleen, Peyer's patches, and other mucosal lymphoid tissues. Ags are further concentrated on the PMs of Ag presenting cells (APCs) such as subcapsular macrophages

and dendritic cells [71]. In circulation, B cells undergo rapid amoeboid migration (6  $\mu\text{m}/\text{min}$ ) in these SLOs. This limits B cell adhesion but maximizes the number of contacts they make with potential APCs [72]. B cells home to SLOs, migrate within them, and exit within 24 hours to then repeat the process, effectively scanning the body for cognate Ag. B cell trafficking is orchestrated by chemokines. CXCL13 is produced by follicular stromal cells and promotes B cell migration within SLOs. The egress of B cells from SLOs occurs via the lymphatic sinuses and is dependent on sphingosine 1-phosphate [73]. Upon encountering cognate Ag, triggering of the BCR results in the formation of a *de novo* cell-cell contact termed the immunological synapse, the biophysical principles of which augment B cell activation [74, 75]. In this section, I describe the lymph node (LN) architecture, as an example of a SLO, with a focus on B cell:APC interactions. I then discuss the triggering of the BCR, microcluster/immune synapse (IS) formation, and the subsequent signaling reactions that promote B cell activation and differentiation.

### **1.3.2 APCs in SLOs**

During an infection, small soluble Ags that are present in the tissues enter the lymph fluid, which drains into the nearest LN via an afferent lymph vessel that fuses with the subcapsular sinus that is located between a collagen-rich capsule and the cortex of the LN (Figure 3) [72]. Very small Ags (< 10 nm diameter) such as toxins or peptides can pulse through the LN via a conduit network that can be sampled by dendritic cells or directly by B cells [72, 76]. Virus-sized antigenic particles that are 20-200 nm in diameter, as well as opsonized antigenic particles and immune complexes (ICs), are captured by subcapsular sinus (SCS) macrophages via a variety of receptors. Complement-opsonized Ags are bound by complement receptor 1/macrophage receptor 1 (CR1/MAC1), antibody-opsonized Ags are engaged by

Fc $\gamma$ RIIB, and carbohydrate-containing Ags are engaged by DC-SIGN and other lectins (Figure 3). All of these receptors can present the intact Ag to B cells by either retaining them at the PM (e.g. MAC1) or by internalizing and recycling them via non-degradative vesicular compartments (e.g. Fc $\gamma$ RIIB, DC-SIGN). Larger bacteria-sized Ags of 500-2000 nm are phagocytosed, delivered and presented to B cells by immigrant DCs. Although Ag size can determine how it will reach the LN, exceptions have been observed in skin-draining LNs and some large pathogens can reach the lymph node intact resulting from their own invasive capacity [72].

Figure 3

lymph node

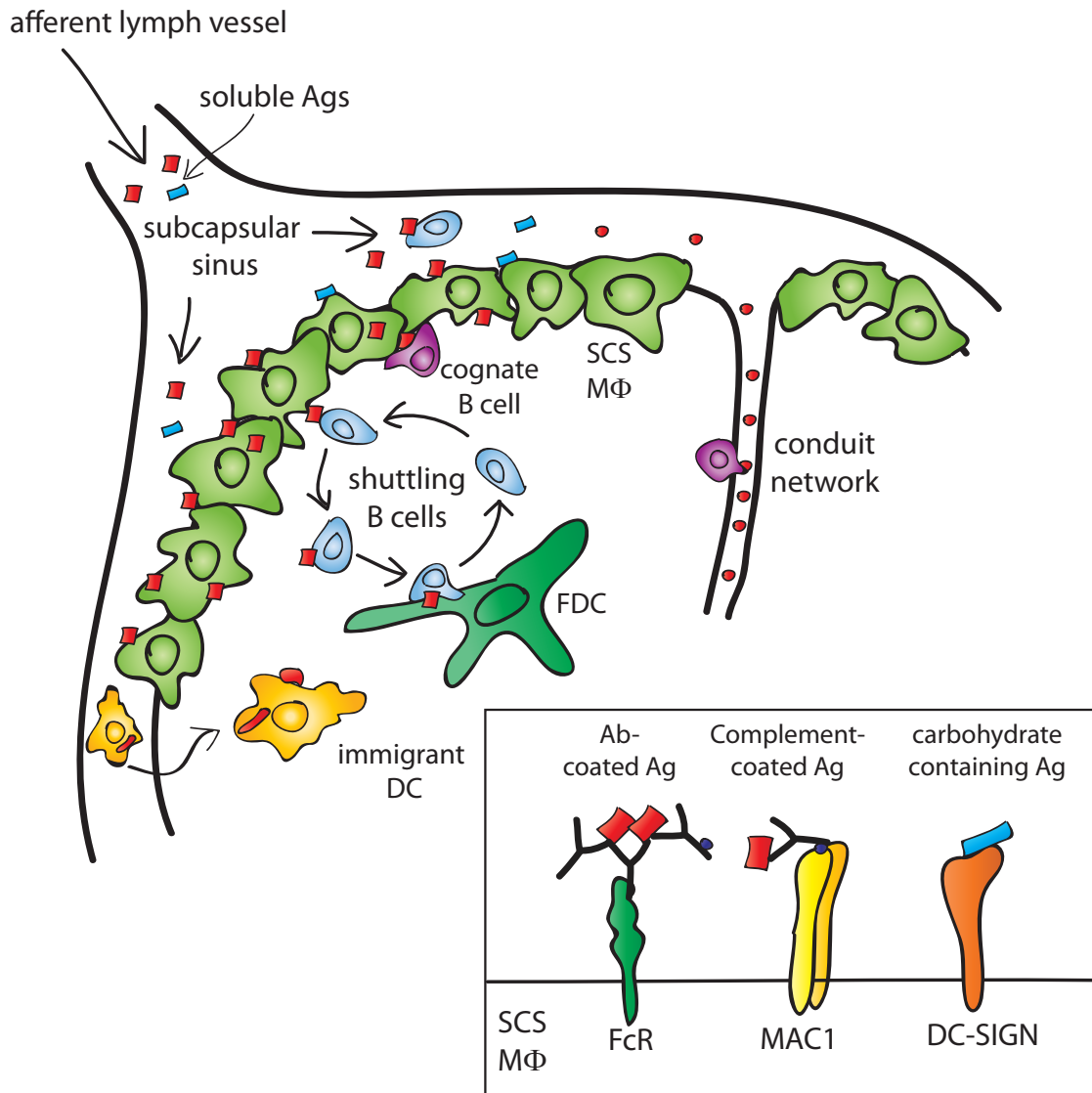


**Figure 1.3.** *Ag presentation to B cells in the LN.* Ags enter the draining LN via the afferent lymph vessel and are either bound by subcapsular sinus macrophages (SCS) or enter the conduit network. Alternatively, Ags are presented to B cells by immigrant DCs that enter the LN from the site of infection. SCS macrophages bind and present Ags via Fc receptors, complement receptors (e.g. Mac-1), and carbohydrate receptors (e.g. DC-SIGN) (inset). B cells recognizing cognate Ag on the surface of APCs can rapidly respond by spreading upon the APC surface. Non-cognate B cells can also shuttle Ags via Fc or complement receptors to follicular dendritic cells (FDCs) where these Ags can be long-lasting reservoirs during the germinal center reaction.

SCS macrophages are positioned to dynamically probe the draining lymphatic fluid while maintaining contact with B cells in the B cell follicle [72]. They act as “flypaper” in the lymphatic system to limit the systemic spread of soluble Ags through the body [77] and require lymphatic flow as well as the B cell-expressed cytokine lymphotoxin- $\alpha$ 1 $\beta$ 2 for their maintenance at these sites [72, 78]. SCS macrophages have a lower propensity for lysosomal mediated destruction of Ags than classical macrophages, highlighted by the fact that they can become reservoirs for viral infection [72]. The maintenance of Ags in native conformations makes SCS macrophages ‘professional’ APCs for B cells as well as iNKT cells that are specific for lipid Ags [79]. Immigrant DCs, on the other hand, enter the draining lymph node after internalizing Ags at the peripheral site of infection. Although much of the Ag will be presented in the form of peptide-MHC to T cells, DCs also have a lower destruction capacity than classical macrophages and can recycle intact Ags to the PM for presentation to B cells [72]. In order for B cells to continually see Ag in germinal center reactions, they require a sustained source after an infection is cleared. Resident follicular DCs can become these antigenic hubs for B cells, readily trafficking Ag to-and-from their surfaces for long periods of time [71, 80]. This unique property of FDCs shape the GCR as B cells are selected for high Ag affinity by these APCs (see below) [81]. Finally, B cells can play a role in shuttling ICs from SCS macrophages or the blood to FDCs. Because B cells express Fc $\gamma$ RIIB and the CR2 complement receptor, they can bind IgG- or complement-bound particles during homeostatic trafficking [72]. FDCs may have more of these receptors, allowing them to extract ICs from the surface of non-cognate B cells [82]. FDCs may also actively bind and internalize ICs via actin-driven processes from the surface of non-cognate B cells in order to re-present the Ag for cognate B cells [80].

### 1.3.4 BCR triggering and kinetic segregation

Encounter of Ag on the surface of APCs by cognate B cells leads to their integrin-mediated adhesion to the APC, which is followed by rapid cell spreading, and subsequently by membrane contraction and IS formation (Figure 4) [83]. These early events in B cell activation maximize Ag gathering [84] as well as force-mediated extraction of Ag from the APC membrane [85], which is required for B cells to present Ag to T cells and elicit T cell help. The more Ag gathered and acquired, the more T cell help they will receive. The magnitude of adhesion, spreading, Ag gathering, and Ag extraction is controlled by BCR signal strength. Consequently, morphological responses to APCs can be described as a means of discriminating BCR affinity for the Ag. The triggering of the BCR by Ag, which may involve spatial changes (i.e. cross-linking or dissociation) or conformational changes that were discussed earlier, results in the phosphorylation of Ig $\alpha$ / $\beta$  ITAMs by Lyn and Syk [15]. This initiates the assembly of a macromolecular signalosome that is comprised of PLC $\gamma$ 2, PI3K, Btk, and Vav. The signalosome assembly leads to the production of second messengers including Ca<sup>2+</sup>, DAG, and PIP<sub>3</sub>. Collectively, this enhances cytoskeletal dynamics via the activation and recruitment of GTPases and also induces transcriptional programs that are important for B cell activation.

## Figure 4

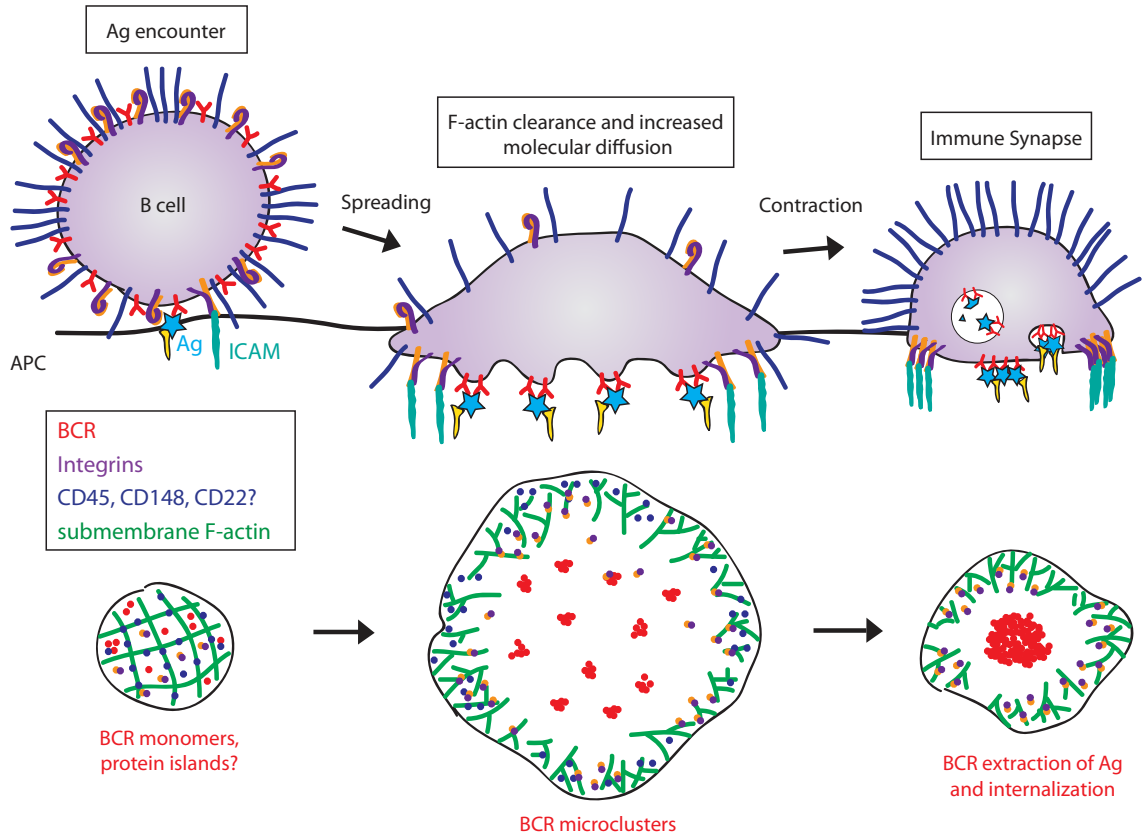


**Figure 1.4.** *Ag encounter on APCs by B cells leads to F-actin remodeling and BCR microcluster formation.* In a resting state, the actin cytoskeleton of B cells maintains the BCR in compartments in the plasma membrane and limits BCR-BCR collisions and interactions with co-receptor complexes. Upon encounter of Ag on the surface of an APC, B cells rapidly (1-2 min) undergo integrin mediated cell spreading. Spreading increases the chances of unligated BCR encountering Ag while also breaking down submembrane F-actin networks to release transmembrane pickets like CD45 and the BCR itself. F-actin networks become more branched and turnover more rapidly, providing the protrusive force on the plasma membrane that underlies spreading. Collectively, spreading and increased receptor diffusion promotes BCR microcluster formation, sites of signalosome assembly. Within 5-10 min, B cells contract on the surface of APCs and may either form an immune synapse and/or extract Ags from the APC membrane to later present to T cells.

Biophysical processes at the B cell PM in these cell-cell contacts can limit BCR signaling. Highly expressed transmembrane phosphatases with large extracellular domains such as CD45 and CD148 extend well beyond the Ag-binding site of the BCR, preventing the receptor from contacting Ags that are on the surface of APCs (Figure 4). The ectodomain of CD45 has been estimated to extend 30-50 nm from the cell surface depending on the splice variant [86] and CD148 has an ectodomain of ~50 nm [87], whereas an antibody molecule extends ~10 nm from the cell surface [88]. While the enzymatic activities of these transmembrane phosphatases may in fact have positive roles in triggering the BCR [89], the low flexibility of their fibronectin ectodomains may limit Ag engagement and triggering of the receptor.

In addition to the MSK limiting the mobility of the BCR within the plane of the PM, the segregation of CD45 from the BCR, which has been observed during IS formation, is also limited by the MSK. The interaction between CD45 and F-actin via spectrin and ankyrin may also restrain BCR diffusion in the PM and limit BCR clustering. In this sense CD45 acts as a picket in the picket fence model of membrane diffusion. A focus on transmembrane phosphatases has pervaded these biophysical questions based on models where the exclusion of the phosphatases from Ag receptors would result in their triggering [90]. This model is termed 'kinetic segregation' and was borne out of observations that CD45 is excluded from the T cell IS [91] and CD45 and CD148 are excluded from the B cell IS [92] and macrophage phagocytic synapse [93]. Indeed, experiments by Anton van der Merwe's group and Ron Vale's group demonstrated that removing the ectodomains of these phosphatases alone could set off Ag receptor triggering [87, 94]. Whether these transmembrane proteins are part of a larger group of "pickets", bridging F-actin to the membrane and limiting molecular diffusion, is unknown. Moreover, the regulation of the diffusion of such proteins by actin is largely undetermined.

Undoubtedly, the physical restraints on BCR engagement and clustering set by CD45/CD148 and F-actin must be released in order to form signalosomes.

### **1.3.5 Thresholds and BCR microclusters**

The response of B cells to APCs with cognate Ag on their surface occurs through a series of morphological steps that are largely identical to those that occur during T cell IS formation (Figure 4). First, B cells move in a highly adherent/elongated fashion on APC membranes as a result of LFA-1 integrin-ICAM interactions. This contact may increase the chances of BCR-Ag encounter. Increased actin dynamics (stimulated by Ag receptor signaling) drives membrane ruffling at the leading edge of these cells, which increases the ability of the B cell to scan the APC membrane, further increasing the chances of BCR encountering Ag, as has been shown in T cells [1]. These invadopodia-like structures extend deeply (0.4 – 2  $\mu\text{m}$ ) and rapidly (<10 s) into APCs and can be stabilized by Ag or ICAM to form podo-synapses at least in effector and memory T cells [9, 13]. Should B cells encounter cognate Ag, this further increases integrin activation and leads to a rapid spreading response that requires the coordination of adhesion and cytoskeletal dynamics [84, 95, 96]. The spreading response is initiated by small microclusters comprised of engaged BCRs as well as the coreceptor CD19, which may have similar adaptor functions as Lat in T cells [83]. Not surprisingly, actin-based spreading [74], integrin adhesion [97], and CD19 expression [64] lower the cellular threshold for B cell activation by membrane-bound Ags.

Underlying the cellular threshold for B cell activation is a triggering threshold operating at the microcluster level. The formation of small microclusters precedes the development of an IS in T and B cells and these microclusters are the functional units that nucleate the assembly of

microsignalosomes which initiate downstream signaling pathways [83, 98]. Extensive work dissecting the number of peptide-MHC agonists required for T cell activation (as measured by  $\text{Ca}^{2+}$  flux) has shown that a ratio of 4 pMHC complexes per TCR cluster was sufficient to induce maximal  $\text{Ca}^{2+}$  signaling [14]. Importantly, the critical triggering threshold did not decrease when more TCR microclusters were engaged, suggesting that the critical consideration is a ratio of Ag:TCR cluster rather than Ag:T cell [14]. In contrast, the addition of CD80-CD28 costimulation, which can activate PI3K and enhance actin dynamics, did lower triggering thresholds [14]. Because p-MHC mobility was limited in these experiments by using metal grids underlying a lipid bilayer, it argues that when Ags are spatially separated, a triggering threshold at a microcluster/protein island level then sets the cellular threshold for activation. Thus the mobility and spatial organization of Ag within the PM of the APC can also set the threshold for initiating Ag receptor signaling. Although little is known about Ag pre-clustering, viral infection can lead to pMHCI clustering. As well, artificially clustering pMHCI complexes lowers the threshold for T cell activation [25, 27]. If the TCR and BCR are indeed pre-clustered in protein islands in the lymphocyte PM [63, 65, 66], then pre-clustering of Ag may facilitate the alignment of complementary Ag:Ag receptor clusters.

A final threshold consideration is whether microclusters coalesce into a stable IS with an APC. For T cells, this can be determined on the APC population level [26]. In the context of an infection, T cells transition between three phases of migration in the LN characterized by 1) migration and serial contacts with multiple APCs, 2) stable IS contacts with single APCs, and 3) a return to a migratory phenotype [26]. The transition kinetics between phase I and phase II varies (2 to 12 hrs) depending on the quantity and quality of Ag in the LN [26]. Importantly, T cells can integrate signals from the TCR between serial contacts with different APCs. The signal

integration is not well understood, but may involve NFAT, which rapidly enters the nucleus but is exported at a much slower rate [29]. It is becoming increasingly clear that the transition to a stable synaptic state is not required for lymphocytes to become activated or mount an effector response [28, 99]. Instead, the IS may have a specialized function in the development of memory [28, 99] and the effector function of T cells, in particular CTLs [31, 36]. In the case of B cells, their interactions with APCs *in vivo* appear to be too fast for stable synapses to form [38, 44]. They rapidly respond to a population of APCs, extract and process Ag, and then present pMHC to T cells, all within minutes. Despite this observation *in vivo*, it has been determined that B cells can form an IS with APCs or particulate Ags *in vitro*. These synapses can persist for up to an hour and have been proposed as a mechanism for the directed secretion of lysosomal contents so as to promote Ag extraction [33, 34]. The B cell IS may also be important in subsequent B cell-T cell interactions, where a reciprocal synaptic state has been observed *in vitro* [37]. The docking of the MTOC at the IS, as well as the clearance of F-actin at the contact [75, 100], can promote the reorientation of the Golgi apparatus to the IS allowing the directed secretion of cytokines [35, 41].

### **1.3.6 The germinal center reaction**

After encountering cognate Ag, B cells enter a GCR in which they expand and differentiate into long-lived Ab secreting plasma cells and memory B cells. Germinal centers are secondary follicles within B cell follicles of SLOs and largely contain activated B cells. They consist of light and dark zones containing FDCs and T cells respectively. Within GCs, activated B cells remain highly migratory and undergo somatic hypermutation of lower affinity germline VDJ regions and Ig gene switch regions. This process is mediated by the induced expression of the enzyme activation-induced deaminase (AID). A number of characteristic markers of GC B

cells coincide with AID including Bcl-6 and Fas (a death receptor). This results in pro-apoptotic state of activated B cells and allows DNA damage tolerance by suppression of p53 for example. Bcl-6 also desensitizes BCR signaling. Collectively, this results in GC B cells that rapidly undergo cell death without pro-survival signals from either Ag on the surface of FDCs or T cell help.

Clonal B cells with resultant mutated/class-switched BCRs are selected through a “Darwinian” process of affinity maturation [69]. A significant amount of recent evidence suggests that this selection is shaped by interactions with follicular helper T cells, which provide co-stimulation through CD40L-CD40 interaction and pro-survival cytokines like IL-21 [42, 47, 69]. Artificially bridging follicular T helper cells to all activated B cells irrespective of the amount of p-MHCII on their surface results in impaired affinity maturation for example [42]. Blocking CD40L [40] or IL-21 [43, 56] also terminates the GCR. Whether or not IL-21 is directionally secreted to an IS as is the case for cytokines like IL-2 and INF $\gamma$  [101] has not been determined, but that physical interaction between T and B cells augments selection in the GCR suggests this may be the case. Because the amount of pMHCII on the surface of activated B cells is coupled to Ag acquisition from APCs such as FDCs, contacts between B cells and APCs as well as T cells underlie the GCR. Indeed, mutations in DOCK8 or CD19 that abrogate B cell contacts and Ag acquisition from APCs lead to impaired affinity maturation [47, 102]. How *de novo* immune contacts in the GCR may be tuned in an immune response is an interesting area for future work [41].

## 1.4 Integrating B cell responses through Toll-like receptors and the BCR

Within the adaptive immune system, B cells are unique in that they express both a clonally rearranged BCR as well as germline-encoded Toll-like receptors (TLRs) [103]. TLRs are germline encoded pattern recognition receptors (PRRs) that recognize a wide range of microbe-associated molecular patterns (MAMPs) [9]. Recognition of MAMPs by TLRs results in signaling cascades initiated by the recruitment of one or more adaptors to the Toll-IL-1 receptor (TIR) domain in the intracellular tail of TLRs [9]. This leads to the activation of NF- $\kappa$ B and/or IRF3, IRF7 transcriptional programs and the secretion of inflammatory cytokines, type I IFN, chemokines, and antimicrobial peptides [9]. Responding to microbial components via TLRs is well recognized as essential for the activation of innate immune cells. However TLRs also play a critical, less appreciated role in directly influencing adaptive B cell responses [103]. In mice, TLR2, 4, 6, 7, and 9 are highly expressed in all B cell subtypes, all of which are upregulated during activation through the BCR, CD40 ligation, or exposure to MAMPs [46, 50, 104-106].

Optimal antibody responses are thought to require three signals: BCR signaling induced by cognate antigen, co-stimulatory signaling through CD40 ligand-induced clustering of CD40 (T cell help), and a third "danger" signal provided by TLR signaling, which may also be required for the survival and differentiation of B lymphocytes [105]. Consistent with this, TLR agonists serve as potent adjuvants for certain clinical and experimental vaccines [107, 108]. B-cell-deficient mice reconstituted with B cells lacking TLR signaling (TLR4 knockout or MyD88 knockout B cells; MyD88 is an important TIR adaptor for all TLRs with the exception of TLR3) show impaired Ag-specific IgM and IgG responses compared to wildtype reconstituted control

mice [107]. Vaccination models for H1N1 influenza using virus-sized nanoparticles that contain Ag and TLR ligands also induce synergistic increases in Ag-specific, neutralizing antibodies compared to those with just Ag [109]. These results were corroborated in studies comparing the delivery of TLR ligands in soluble versus particulate forms, which showed that when TLR ligands are incorporated in the particle, B cell-intrinsic TLR signaling is required to mount a robust antibody response [107, 110]. Conversely, when TLR ligands are delivered in a soluble form, or a strong soluble adjuvant is used along with antigen in experimental vaccinations, the requirement TLR signaling in B cells is no longer necessary [107, 111]. Taken together, B cells seem to be able to discriminate between Ags based on their physical form, which determines the requirement for TLR signaling in order to mount a humoral response.

Even in the absence of Ag, B cells can proliferate, secrete cytokines, express co-stimulatory molecules, and secrete antibodies in response to TLR ligands [105, 106, 112]. While optimum antibody secretion requires additional signals from Ag, CD40 ligation, and BAFF, the recognition of TLR ligands may lower the amount of cognate Ag concentration that is required for naive B cells to be fully activated [105] (see also Chapter 2). Consistent with this idea, TLR signaling often plays a role in the production of autoantibodies in systemic autoimmune diseases [113]. In many autoimmune pathologies, autoantibodies against DNA and RNA are generated and the production of these autoantibodies is augmented by signals through TLR9 or TLR7 [113]. Similarly, production of autoreactive B cells specific for self-IgG produced antibodies, commonly referred to as rheumatoid factor, requires the synergistic engagement of the BCR and TLR9 (ICs) [114]. While TLR ligands play a direct and critical role in B cell activation, the molecular mechanisms through which TLR signaling either synergizes with BCR signaling or primes and even directly stimulates B cell activation are not fully understood. Chapter 2 of this

dissertation describes a novel mechanism of receptor crosstalk in which TLR signaling primes the BCR for encounter with membrane-bound Ags by increasing the diffusion of the BCR in the PM.

## **1.5 Molecular diffusion, single particle tracking, and models of diffusion in the plasma membrane**

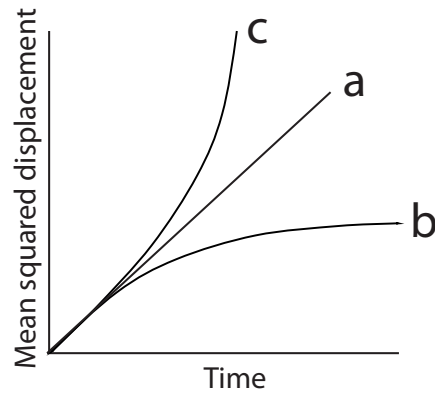
### **1.5.1 Molecular diffusion**

Brownian motion, named after the botanist Robert Brown in 1827, was used to describe the purely physical nature of the erratic motion of small pollen grain particles and other granular or glassy materials on water when observed under the microscope [115]. Subsequent experimental and theoretical work in the late 19<sup>th</sup> and early 20<sup>th</sup> century demonstrated that Brownian motion arises from the permanent motion of the surrounding molecules of the liquid, and that the motion of the particles could be accelerated if the liquid viscosity is lowered, for example [115]. In 1905, the same year Albert Einstein explained Brownian motion in this way, the term “random walk” was used by Karl Pearson to statistically describe migrating insects, where the path of the insect consists of a succession of random steps [115]. The Brownian motion of a particle in a membrane can be described in the same way, where for each observable step the particle moves in a random direction, independent of previous positions.

In order to describe the motion of particles in a membrane, a measure of the mean square displacement (MSD) is often used. The calculation of the MSD of a particle’s trajectory may be taken at each recorded time point, such that each particle trajectory will have  $n-1$  MSD

calculations, and a running average of the MSD is calculated for the total number of time intervals for which observations are made, i.e.  $n\Delta t$ . For true unrestricted Brownian motion, the MSD increases linearly with time such that the total  $\text{MSD} = 2xDt$ , where  $x$  is the number of dimensions in which the particle is moving (i.e.  $x=2$  for 2D) and  $t$  is the total observation time (i.e.  $n\Delta t$ ) (Figure 5). Therefore, for a particle in a 2-dimensional fluid like a membrane, the Brownian motion follows the equation  $\text{MSD} = 4Dt$ , where  $D$  is the diffusion coefficient. Often, diffusion coefficients ( $D = \text{MSD}/4t$ ) are derived from the first few data points of MSD over time as the error in measuring the MSD increases with time [60, 116]. The diffusion coefficient, which represents the area probed by the particle per unit time, is the parameter that is most commonly used to describe a particle's motion.

Figure 5



a  $MSD = 4D\Delta t$

b  $(x^2)(t) = L_x^2/6 - 16L_x^2/\pi^4 \sum_{n=1(\text{odd})}^{\infty} 1/n^4 \exp \{1/2 \cdot (n\pi\sigma_x/L_x)^2 t\}$

c  $MSD = 4D\Delta t + v^2(\Delta t)^2$

**Figure 1.5.** Theoretical MSD plots. A) Pure Brownian motion. B) Confined Brownian motion ( $L_x$  = length of the corral along the x-axis,  $\sigma_x = 2Dx$ , the diffusion coefficient along the x-axis. Similar derivation is used to the y-axis). C) Flow/directed component ( $v$  = the flow speed).

Simple diffusion/Brownian motion can exist within compartments or can be influenced by drift or flow forces. If a flow force directs the motion of the particle, the MSD will increase exponentially in the running average graph of MSD over time (Figure 5). Directed motion of a particle results in an increase in the distance travelled with each time point and given that the displacement calculation is already a squared value, the relationship with time becomes

parabolic. If a particle is restricted within a compartment, the probability of the MSD becoming less over time increases, such that the MSD will deviate from the linear relationship with time, and curve towards the horizontal  $\Delta t$  axis, i.e. the total displacement will asymptotically reach a maximal value that corresponds to the size of the confinement zone (Figure 5). In a compartment, the particle has a maximum value of displacement independent of time, and therefore the MSD is limited to this distance. Determining the relationship between the MSD and time, as outlined, can lead to a spatial description of particle trajectories [116]. Although Brownian motion is not observed for proteins or lipids in the PM (see next section), observing a linear relationship between the MSD and time indicates that a particle's movement is not restricted by barriers for the time period for which it has been observed (I refer to these particles as being *free* in Chapter 2). If a particle's trajectory results in decreased  $\Delta$ MSD over time, this suggests the particle is restricted in its motion by a barrier (e.g. a physical barrier such as the actin MSK or a region of reduced viscosity) in the PM and therefore experiences confinement (I refer to these particles as being *confined*). If flow forces act on a particle, as would be the case for motor proteins moving along microtubules, these particles could be referred to as having *directed* motion. See the Methods section in Chapter 2 for more details.

### **1.5.2 Single Particle Tracking**

The diffusion of proteins or lipids in cells can be determined using fluorescence recovery after photobleaching (FRAP), fluorescence correlation spectroscopy (FCS), or single particle tracking. Both FRAP and FCS have spatial resolution of a few hundred nanometers and therefore rely on an ensemble average of the diffusion behavior of the molecules within a region of interest. These bulk experiments yield average diffusion coefficients for the protein, but mask

the individual trajectories of single particles and their interactions within their microenvironments.

The spatial resolution for single particle detection can be less than 10 nm, an order of magnitude lower than for FRAP, provided that the center of a Gaussian curve is fit to the point-spread function of light from a single particle [116]. The resolution limit for an optical system is calculated by Rayleigh's criteria as:

$$R = 1.22 \times \lambda / 2NA \quad (\lambda \text{ is light wavelength, NA is numerical aperture of the lens})$$

If quantum dots (semi-conductive nanocrystals, from here on referred to as Qdots) with emission maxima of 655nm are used in experiments, then  $R = 276$  nm. Upon fitting a Gaussian curve to this point spread function or "airy disc", resolution below 10 nm can be achieved depending upon the detection camera used (i.e. pixel size). Once Gaussians are fit to particles in each frame of a video, each point needs to be linked to the subsequent point representing the same particle. This is achieved using a global nearest neighbor cost matrix, described in Jaqaman *et al.* [117].

If Gaussian curves for two particles come together and overlap such that each particle cannot be resolved and the fluorescence intensity doubles, it can be considered that the two particles have "merged". Similarly, if two Gaussian curves emerge from a single Gaussian curve of twice the intensity, this can be considered a "splitting" event. The merging and splitting of particles in a membrane may reflect collisions of like particles, which can be of significant biological consequence when bearing in mind receptors which signal by cross-phosphorylation or those that require dimerization for signal transduction.

Tracking can become more complex if the fluorophore used is not continuously excited or undergoes “blinking”, as is the case for quantum dots (Qdots). Blinking behavior of the particles can be taken into account by the cost matrix where a particle may be expected to be lost for a frame, for example. The trajectories, generated from linking the position of Gaussians for each frame of a video, become more detailed and reliable at high frame rates, although high frame rates may result in the bleaching of certain fluorophores (i.e. Cy3). This presents a trade-off in the advantages of using fluorophores that blink but do not bleach (Qdots) and those that do not blink, but can bleach (Cy3). Performing the same experiments using different fluorophores leads to more robust data sets. Finally, the type of microscopy used can determine whether a fluorophore stays within the field of detection. Confocal microscopy can detect a fluorophore at a greater depth along the z axis than total internal refractive fluorescence (TIRF) microscopy. Again, using multiple excitation techniques yields more robust SPT data.

### **1.5.3 Models of membrane diffusion: from the fluid mosaic model to hop diffusion**

Although ideas have evolved over the past 40 years [118], the 1972 *Science* paper in which Singer and Nicholson proposed the fluid mosaic model of the PM was indeed a quantum step in understanding the *structure* of the two dimensional PM (i.e. a phospholipid bilayer) [119]. This paper explained the requirement for membrane-embedded proteins to exhibit the same type of motion as particles within a *fluid* such that aggregation could occur in response to stimuli such as the clustering of membrane proteins by the lectin, concanavalin A, and the clustering of the BCR in B lymphocytes [119]. The fluid mosaic model, however, predicted that embedded proteins and lipids should undergo simple or Brownian diffusion in the 2D fluid. This prediction was not borne out in experiments using either FRAP or SPT [118, 120].

Instead, the fluid nature of the lipid bilayer is now appreciated as a foundation on which a hierarchical complexity of architecture is built [118]. The first indications that the fluid mosaic model could not account for the observed dynamics of lipids and proteins in the PM came from experiments measuring the diffusion coefficients of these PM constituents in artificial membranes versus cellular membranes. Depending on the technique used (i.e. FRAP versus SPT), and the acquisition frame rate of live membranes, it was generally found that the same proteins or lipids moved an order of magnitude slower in cells than in artificial lipid bilayers [118, 120]. Using sophisticated microscopes equipped with very fast cameras, Kusumi and colleagues showed that even the most abundant phospholipids, like phosphatidylethanolamine (PE), when imaged singly did not move as would be predicted by pure Brownian motion (Table 1) [121]. Instead, phospholipids and sphingolipids imaged at >10,000 frames/s, underwent “hop” diffusion, where they moved within compartmentalized regions of the PM and occasionally (every 1-20 ms) switched to neighboring compartments [121, 122]. As subsequent experiments were carried out with ligand-bound transmembrane proteins (transferrin receptors, EGFR, LFA-1), non-ligated single receptors (CD36, BCR, FcR $\epsilon$ ), or glycosylphosphatidylinositol (GPI)-anchored proteins (MHC-II GPI-I-E<sup>k</sup>), an emerging trend showed that most, if not all, proteins associated with the PM are also compartmentalized (see Table 1).

**Table 1.1**

Single Particle Tracking Studies

Cell Type	Proteins	Methods	Trajectory/Diffusion related data	Reference
<b>Immune Cells</b>				
<b>B cells</b>	BCR (IgM, IgD)	Alexa633 and Cy3 labelled Fab fragments	Diffusion of IgM and IgD is limited by the actin cytoskeleton, IgM has faster diffusion than IgD, disruption of actin results in BCR signaling	Treanor <i>et al.</i> ( <i>Immunity</i> , 2010)
<b>B cells</b>	CD19, BCR co-receptor	Alexa 633 conjugate Fab fragments	Diffusion of CD19 is controlled by the tetraspanin CD81 and is only increased by the disruption of actin networks in CD81 <sup>-/-</sup> cells	Mattila <i>et al.</i> ( <i>Immunity</i> , 2013)
<b>Macrophages</b>	CD36, scavenger receptor	Qdots, Cy3 labelled Fab fragments	Different populations of trajectories defined spatially as confined and unconfined. Found that some confined receptors moved linearly (i.e. linear confinement zones) and this increased chances of ligand binding. Linear confinement required actin and microtubules, the disruption of which lowered ligand binding.	Jaqaman <i>et al.</i> ( <i>Cell</i> , 2010)
<b>Mast cells</b>	FcR <sub>ε</sub>	Hyperspectral microscopy of many Qdots to investigate oligomerization	Demonstrated that small clusters of FcR <sub>ε</sub> (trimers) remain mobile and activate Syk, immobilization required higher order oligomers formed using multivalent Ag. The SFK inhibitor PP2 had no effect on immobilization or internalization of receptor clusters.	Andrews <i>et al.</i> ( <i>Immunity</i> , 2009)
<b>Mast cells</b>	FcR <sub>ε</sub>	Qdots with Fab fragments	Using actin-GFP, demonstrated that FcR <sub>ε</sub> is mobile within regions of low actin-GFP density which is rapidly remodelled (i.e. seconds); cross-linking of FcR <sub>ε</sub> immobilizes the receptor; disruption of actin increases diffusion of cross-linked clusters of FcR <sub>ε</sub> .	Andrews <i>et al.</i> ( <i>Nat Cell Biol.</i> , 2008)
<b>T cells, PBLs</b>	CD45	1 μm polystyrene microspheres labelled with anti-CD45 Fab fragments. The center of the bead is detected and tracked.	CD45 showed slow and fast diffusion with median diffusion coefficients of 0.04 μm <sup>2</sup> /s and 0.003 μm <sup>2</sup> /s. Both populations increased in their diffusion coefficients with disruption of the cytoskeleton, while both decreased in response to PMA. A role of actin binding by using spectrin and ankyrin peptides was inferred.	Cairo <i>et al.</i> ( <i>J Biol Chem.</i> , 2010)
<b>T cells</b>	LFA-1	1 μm polystyrene microspheres labelled with anti-LFA-1 Fab fragments against different conformations of the integrin or ICAM coated (i.e. ligated). The center of the bead is detected and tracked.	Conformational states of the integrin showed different diffusion behaviours. Open and ligated conformations of LFA-1 were more slowly diffusing in activated cells while intermediate conformations of LFA-1 were fast diffusing. All conformational states were sensitive to disruption of F-actin.	Cairo <i>et al.</i> ( <i>Immunity</i> , 2006)
<b>Non-immune Cells</b>				
<b>CHO cells</b>	MHC-II (TM-I-E <sup>h</sup> ), transmembrane form	Fluorescent probes Cy3-MCC 95-103 or Alex594-Fab fragments or colloidal gold particles coated in Fab fragments	Rapid hop diffusion between 40-nm compartments was observed, with an average dwell time of 1–3 ms in each compartment. Disruption of actin by latrunculin A increased the compartment sizes, which led to an ~50% increase in the diffusion coefficient	Umemura <i>et al.</i> ( <i>Biophysical J.</i> , 2008)
<b>CHO cells</b>	MHC-II (GPI-I-E <sup>h</sup> ), GPI-anchored form	Fluorescent probes Cy3-MCC 95-103 or Alex594-Fab fragments or colloidal gold particles coated in Fab fragments	Rapid hop diffusion between 40-nm compartments was observed, with an average dwell time of 1–3 ms in each compartment. Disruption of actin by latrunculin A increased the compartment sizes, which led to an ~50% increase in the diffusion coefficient	Umemura <i>et al.</i> ( <i>Biophysical J.</i> , 2008)
<b>epidermoid carcinoma cells</b>	EGFR, ErbB1	Two color Qdots to investigate dimerization	Ligand-bound dimers were long-lived, independent of kinase activity; unligated dimers were relatively short-lived. Disrupting actin increased the diffusion of receptor dimers.	Low-Nam <i>et al.</i> ( <i>Nat Struct Mol Biol.</i> , 2011)

**Table 1.1**

## Single Particle Tracking Studies

Cell Type	Proteins	Methods	Trajectory/Diffusion related data	Reference
mouse keratinocyte	Transferrin receptor	Transferrin attached to colloidal gold particles	TfR showed confined, directed, and unconfined trajectories. Confinement was, on average 500 nm and could persist for 30 s (30 frames/s acquisition rates). Trajectory type was somewhat dependent on Ca <sup>2+</sup> , where TfR became less restricted in low Ca <sup>2+</sup> .	Kusumi <i>et al.</i> ( <i>Biophysical J.</i> , 1993)
mouse keratinocyte	E-cadherin	Anti-E-cadherin antibodies attached to colloidal gold particles	E-cadherin showed confined, directed, and unconfined trajectories. Confinement was, on average 300 nm and could persist for 30 s. Trajectory type was highly dependent on Ca <sup>2+</sup> , where E-cadherin became more directed in low Ca <sup>2+</sup> .	Kusumi <i>et al.</i> ( <i>Biophysical J.</i> , 1993)
mouse keratinocyte	EGFR	EGF attached to colloidal gold particles	EGFR showed confined, directed, and unconfined trajectories. Confinement was, on average 600 nm and could persist for 30 s. Trajectory type was somewhat dependent on Ca <sup>2+</sup> , where EGFR became more directed in low Ca <sup>2+</sup> .	Kusumi <i>et al.</i> ( <i>Biophysical J.</i> , 1993)
Cell Type	Lipids	Methods	Trajectory/Diffusion related data	Reference
Ptk2 epithelial cells	phosphoethanolamine	Cells were incubated with BSA-lipid-complexes containing Atto647N-labelled phospholipids on ice before imaging	PE underwent hop diffusion with very short (< 4 ms) trapping times	Sahl <i>et al.</i> , ( <i>PNAS</i> , 2010)
NRK fibroblasts	DHPTE	Qdots were conjugated to the phospholipid and incorporated into plasma membranes by vesicle fusion	At 1000 frames/s, a diffusion of 0.85 $\mu\text{m}^2/\text{s}$ was observed and could be described as hop-diffusion within compartments ranging from tens to a few hundred nm in size	Murcia <i>et al.</i> , ( <i>JACS</i> , 2008)
Ptk2 epithelial cells	sphingomyelin	Cells were incubated with BSA-lipid-complexes containing Atto647N-labelled phospholipids on ice before imaging	PG underwent hop diffusion with trapping times longer than PE (15 ms) which required cholesterol.	Sahl <i>et al.</i> , ( <i>PNAS</i> , 2010)

The compartments that confine lipids, transmembrane proteins and non-transmembrane proteins vary in size depending on the cell type used and range from 40-300 nm. There are several possible explanations for the compartmentalization of the PM. The first is that lipids self-organize into microdomains (e.g. lipid rafts) and that these domains restrict the mobility of the constituent lipids and proteins. Lipid rafts form via the preferential association of sphingolipids, sterols, and specific proteins such as GPI-anchored proteins [123]. The formation of lipid rafts that have distinct properties from the surrounding lipid bilayer requires cholesterol-dependent lipid partitioning in which rigid sterols interact more readily with the more extended

hydrocarbon chains of saturated lipids and collectively exclude unsaturated lipids that cannot undergo such close packing due to rigid double bond structures. Biochemically, a number of proteins fractionate with lipid raft markers, however, it has been more challenging to observe rafts in living cells (see later). Another basis for the compartmentalization of the PM is that networks of transmembrane proteins form “pickets” within the PM, which are organized by intracellular (e.g. actin filaments) or extracellular polymers (e.g. galectin lattices) that form “fences”. This hypothesis was termed by Kusumi and colleagues as the “picket-fence” model. Kusumi proposes that the MSK acts as a fence or barrier that compartmentalizes PM components including proteins, lipids, and lipid rafts [121, 122]. Finally, in regions of high proteins density (e.g. protein islands) crowding in the PM may contribute to the decreased diffusion of proteins. However, this would not explain lipid confinement or compartmentalization [124]. Instead, both rafts and polymer networks (i.e. the MSK) likely exhibit a dynamic interplay that control membrane protein and membrane lipid dynamics.

Experiments carried out by Michael Sheetz in 1980 implicated the MSK in restricting protein mobility. Using FRAP to compare protein mobility in normal mouse erythrocytes to spherocytic erythrocytes which are devoid of spectrin and actin networks, Sheetz showed the mobility of integral membrane proteins was 50-times greater in the absence of spectin/actin meshworks [125]. Subsequent experiments using chemicals or actin-specific drugs to induce membrane blebs showed that these F-actin-free blebs do not exhibit compartmentalization and the diffusion coefficients for proteins was increased 4- to 20-fold as compared to the intact PM [121, 122]. Importantly, membrane blebs contain similar protein densities and membrane composition as intact cells, arguing against protein crowding effects [126]. Further experiments used atomic force microscopy to bind, drag, and deform exposed membrane-associated actin

while acquiring trajectory information of proximal particles residing in different compartments [127]. These experiments demonstrated that dragging the MSK shifted particles in surrounding compartments of the membrane, illustrating the elasticity and interconnectivity of the MSK network and its ability to compartmentalize proteins.

In the last 10 years, advances in imaging techniques such as stimulated emission depletion (STED) microscopy and photoactivation localization microscopy (PALM) have brought a greater understanding of the size of membrane domains, including lipid rafts [123]. At the same time, developments in electron tomography and transmission electron microscopy (TEM) have allowed the sizes of compartments within the MSK and protein islands to be determined [66, 128]. Using these techniques, lipid rafts have been consistently observed with high spatial and temporal resolution and shown to have diameters of ranging from 10-20 nm to 120 nm. This is generally smaller than the diameter of MSK compartments, which range from 50 nm to 600 nm [123, 128]. Trapping of GPI-anchored proteins, sphingomyelin, and the ganglioside GM1 has been independently confirmed by Stefen Hell's group using STED based SPT to last for 10-20 ms [129] and Kusumi's group using SPT [121, 130]. The slowed diffusion of GPI-anchored proteins within rafts has been attributed to differences in non-covalent bonding within the raft, membrane order, or actin [123]. Work from Mark Davis's lab using TEM of the inner leaflet of PMs has also shown the presence of rafts, however, these rafts once formed, did not require actin for their maintenance [66]. This work instead put forward the idea that all proteins in the PM form protein islands, that actin associates with these islands, and that protein islands require F-actin for their formation.

Although the interplay between the MSK and lipid rafts is still not entirely understood, it appears that both have a role in slowing the diffusion of different membrane constituents. Raft

components become briefly trapped within rafts, which helps to explain their formation. Cholesterol, a raft organizer, has been postulated to be excluded from transmembrane protein pickets due to a structural incompatibility, thus making the picket-fence a raft “unfriendly” environment, though this has yet to be directly observed in live cells. While rafts have been shown to slow the diffusion of lipids and GPI-anchored proteins, the MSK has been shown by several groups to control the diffusion of many different proteins in multiple cell types (see Table 1). For transmembrane proteins, there is often an interaction between cytoplasmic tails and actin filaments but no apparent binding. In the picket-fence model, the MSK and the pickets, which bind filaments either directly or via scaffolding proteins such as ezrin, ankyrin, spectrin, are speculated to limit “hop” diffusion by creating direct barriers. Similarly, actin-driven clustering of proteins [131] represents another mechanism by which actin filaments can limit protein diffusion. As well, the formation and mobility of protein islands [66] may also depend on the actin MSK. Thus all of these mechanisms, along with lipid rafts, may define the spatial organization of the PM and determine the diffusion rates of proteins within different domains.

In recent years, additional types of barriers to protein diffusion have been discovered in mammalian cells as well as in yeast and bacteria. For example, septins partition proteins between the primary cilium and apical microvilli of epithelial cells [132]. This septin-based barrier is thought to partition macro-membrane domains that have specialized function in signaling. For example, the loss of Septin2 results in decreased ciliogenesis and abrogated Sonic hedgehog signaling that is normally transduced from cilia [132]. Septin-based diffusion barriers were originally identified in budding yeast where they mediate asymmetric distribution of mRNAs between mother and daughter cells at the bud neck [133]. Subsequent work has also

shown that septins can maintain positioning of whole organelles [134]. Similar to the role of septins in yeast and in ciliated cells, in the Gram-negative bacterium *Caulobacter crescentus*, multi-protein complexes comprised of *Stalk* proteins (StpA-D) create a diffusion barrier separating the stalk and the cell body [135]. These barriers extend through the cytoplasm of the bacterium and restrict the mobility of both cytoplasmic and membrane-bound proteins. It was postulated that controlling molecular diffusion in this way provides the bacteria with a fitness advantage by maintaining newly synthesized cellular constituents within the cell body where they are most needed for adaptation to environmental changes [135]. In general, matrices used by cells to create diffusion barriers at the plasma membrane or within the cytoplasm are thought to act as barriers that either concentrate or prevent the aggregation of cellular constituents. How diffusion barriers are remodeled to free or limit diffusion is a major question going forward.

#### **1.5.4 BCR organization in the PM**

In a primary murine B cell, there is an estimated 250,000 BCRs. Kusumi and colleagues have predicted that fibroblasts with MSK compartments of 60 nm x 60 nm will have approximately 2 million compartments [118]. Given cell size differences, this might translate to 200,000 or so compartments in a B cell, which on average would result in 1 BCR per compartment. While BCRs in the PM may form oligomers [8] or clusters [63], the mobility of these are restricted by the MSK and disrupting F-actin networks leads to robust BCR signaling [60]. How submembrane F-actin networks are regulated in resting B cells so as to allow tonic BCR signaling that promotes survival but not activation is not understood, nor are the mechanisms by which the cytoskeleton is remodeled during Ag-induced BCR clustering.

## 1.6 Actin

### 1.6.1 Overview

Actin, along with myosins A and B, were first discovered in striated muscle cells in the 1940s as proteins that constitute more than half the protein content of the cells. Using an Ostwald viscometer and ground muscle tissue, the Nobel Prize winning physiologist Albert Szent-Gyorgyi and colleagues differentiated myosin A from myosin B (later called actomyosin) based on viscosity [136]. Myosin B was of a higher viscosity than myosin A, which could be reduced with the addition of ATP and this correlated with the contraction of threads appearing in the myosin B preparation. Work done by the biochemist Bruno Ferenc Straub in Szent-Gyorgyi's lab demonstrated that the reason for the differential viscosity of myosin A and B preparations and the appearance of threads was the presence of a third protein in the myosin B preparation, which they called actin [137]. Straub went on to describe actin as existing in two forms: filamentous actin (F-actin), which was abundant in physiological conditions that contained salt and ATP in the solution, and globular actin (G-actin), which was present when salts were removed [138].

Twenty years later, actin and myosins were discovered to be abundant in other (and now all) eukaryotic cell types and it is increasingly appreciated that actin-based filaments and the meshworks they comprise are fundamental to many cellular processes. The actin cytoskeleton is required for cellular homeostasis. It provides a structural integrity to the cell to maintain cell shape [139, 140], organizes proteins and membrane domains in the PM [122], orchestrates vesicular trafficking and endocytosis [141], underpins multiple steps in cell division [142], and regulates transcription [143]. In cellular responses to extracellular stimuli, dynamic

rearrangements of the actin cytoskeleton are required to change cell shape, remodel or form adhesions, migrate, and reorganize proteins in the PM. From the first experiments with actin filaments *in vitro*, two fundamental understandings of actin polymerization have been appreciated: 1) the polymerization of actin can occur in a very simple system (i.e. pure actin, salt, and ATP) and 2) the generation of mechanical forces by actin polymers requires other proteins such as myosin.

### 1.6.2 Actin polymerization

Actin polymerization occurs in three phases: an initial nucleation or lag phase, a filament elongation phase in which growth is linear with time and a steady state phase in which polymerization and depolymerization rates are balanced. Actin can self-assemble into polymers *in vitro* under physiological buffer conditions when G-actin monomers exceed the critical concentration ( $C_c$ ) of 0.1  $\mu\text{M}$ . Although nucleation, can occur spontaneously at these concentrations, this reaction is energetically unfavorable owing to the instability of actin dimers and trimers. This slow nucleation reaction contributes to the lag phase of polymerization that is observed *in vitro*. Once nucleation occurs, elongation of the filament occurs rapidly at the barbed end and 5- to 10-times more slowly at the pointed end [144]. The relative rate of monomer addition during the nucleation phase versus the elongation phase can be understood by considering the dissociation equilibrium constants ( $K_D$ ) for these reactions. The reaction of two actin monomers to form a dimer has a  $K_D$  of 4.6 M, for monomer addition to a dimer the  $K_D$  is 0.6 mM, for monomer addition to a trimer the  $K_D$  is 0.14  $\mu\text{M}$ , and for monomer addition to a tetramer the  $K_D$  is 0.12  $\mu\text{M}$  [145]. From these values, it can be appreciated that the addition of

monomers to the critical nucleus of a trimer is orders of magnitude more favorable than the initial two reactions of dimerization and trimerization.

Because actin monomers within an actin filament have the same orientation, the polymer has distinct polarity, which can be observed structurally by transmission electron microscopy (TEM). In 1986, Thomas Pollard used TEM to show that at physiological concentrations of actin ranging from 1  $\mu\text{M}$  to 20  $\mu\text{M}$  the elongation rate at barbed ends is 5 to 10 times faster than at pointed ends and that elongation at both ends involves the addition of ATP-bound actin [144]. Nucleotide exchange in which ATP displaces ADP is only observed for monomeric actin. Because 50% of the ATP bound to an actin monomer is hydrolyzed to ADP within 2 s of the monomer's addition to an existing filament, ATP-bound actin is primarily found at the growing ends of actin filaments. Additionally, because the  $C_c$  is much lower for monomer addition at barbed ends (0.1  $\mu\text{M}$ ) than at pointed ends (0.7  $\mu\text{M}$ ), actin filaments undergo subunit flux or treadmilling in which subunits that dissociate from the pointed end are then incorporated at the barbed end [146]. This effect, as described, occurs very slowly (0.1 subunits/s) and is of little physiological consequence. However, treadmilling of actin filaments can be dynamically controlled by proteins that accelerate filament turnover, the nucleation of filaments, or the incorporation of monomers into filaments [147].

### **1.6.3 Actin nucleators**

While actin can polymerize and turn over in the absence of actin-binding proteins, coordinating actin polymerization to external stimuli or with cellular processes such as vesicular trafficking and endocytosis requires the spatially-restricted stimulation of actin nucleation and elongation [148]. With a new understanding of the thermodynamics of actin polymerization,

Thomas Pollard used profilin-coated Sepharose beads in an attempt to precipitate proteins that could nucleate actin filaments from amoeba lysates. In 1994, his group published the discovery of 2 actin-like proteins of 47 kDa and 44 kDa that co-precipitated in a highly stable complex with 5 smaller proteins and shared amino acid sequence homology with non-conventional actins that had been discovered in *C. elegans* (act d and act c), bovines (act2), and yeast (act2 and ACT2) [149]. They referred to these non-conventional actins as actin-related proteins (later called Arp2 and Arp3) and the complex they discovered is now termed the Arp2/3 complex whereas the other 5 proteins in the complex are referred to as Arp2/3 complex proteins 1-5 (ARPC1-5). Although the amino acid sequences of these actin-related proteins have less than 50% homology to actin from the same species, the Arp2 and Arp3 proteins have been shown to nucleate actin filaments by forming a trimer complex with actin that is structurally similar to actin that self-assembles into a trimer [150]. Because Arp2 and Arp3 spontaneously form a stable complex, this overcomes the initial low efficiency of actin monomer dimerization that is the rate-limiting step in actin self-assembly. Four years after the discovery of the Arp2/3 complex, Dyche Mullins in Thomas Pollard's lab determined that the Arp2/3 complex bound actin dimers within existing "mother" filaments and nucleated filaments that branched from the mother filament at a 70° angle [151]. They termed this action of the Arp2/3 complex a "dendritic nucleation model for actin polymerization", which continues to be the prevailing model for the action of Arp2/3. There is considerable evidence that the Arp2/3 complex binds at barbed ends, nucleates branch points from rapidly growing filaments, and remains bound to the mother filament until debranching occurs (Figure 5) [147]. However a detailed molecular mechanism of the Arp2/3 complex binding and unbinding F-actin, the mechanism by which it

nucleates the formation of branched filaments, and the function of Arp2/3 in cellular processes such as motility is still an area of intense investigation...

In the 20 years since the finding that the Arp2/3 complex nucleates actin polymerization, a growing number of modular actin binding proteins have been found to form a critical nucleus with actin monomers including formins, spire, adenomatous polyposis coli (APC), cordon-bleu (Cobl), leiomodin (Lmod), and JMY (Figure 6) [152]. At high enough concentrations the actin-binding protein cofilin may also nucleate actin filaments, though it should be borne in mind that these concentrations are likely not observed in cells [153]. In 2002, formins were identified as a second major class of actin nucleators that acted independently of Arp2/3 to nucleate unbranched filaments [154, 155]. Like the Arp2/3 complex, formins are highly conserved through evolution, particularly in the formin homology 1 and 2 (FH1 and FH2) domains. Interestingly, a considerable expansion of formin genes appears to have occurred over evolution as fungal species express 2 to 3 formin proteins while mammalian cells express up to 15 different formins [156]. A general architecture based on solved 3D structures of formin domains and interaction studies suggests that formins dimerize via the trans-binding of the FH2 domain. The dimerized FH2 domain can bind with high affinity to barbed ends of filaments or is sufficient to catalyse nucleation without a preexisting filament. Each half of the FH2 domain dimer can bind two actin subunits within an F-actin polymer while the C-terminal FH1 domains can each bind a profilin-bound actin monomer. The region between the FH2 and FH1 domains is considered to be highly flexible, allowing for FH1 domains to deliver actin monomers to the growing filament. As new subunits of actin are added to the actin filament, the formin dimer moves step-wise towards the growing end. Because of this mechanism, formins are considered to be processive actin nucleation proteins [156]. The added effect of binding to the barbed end is that formins act

to prevent the binding of capping proteins that would otherwise stop the polymerization reaction [157].

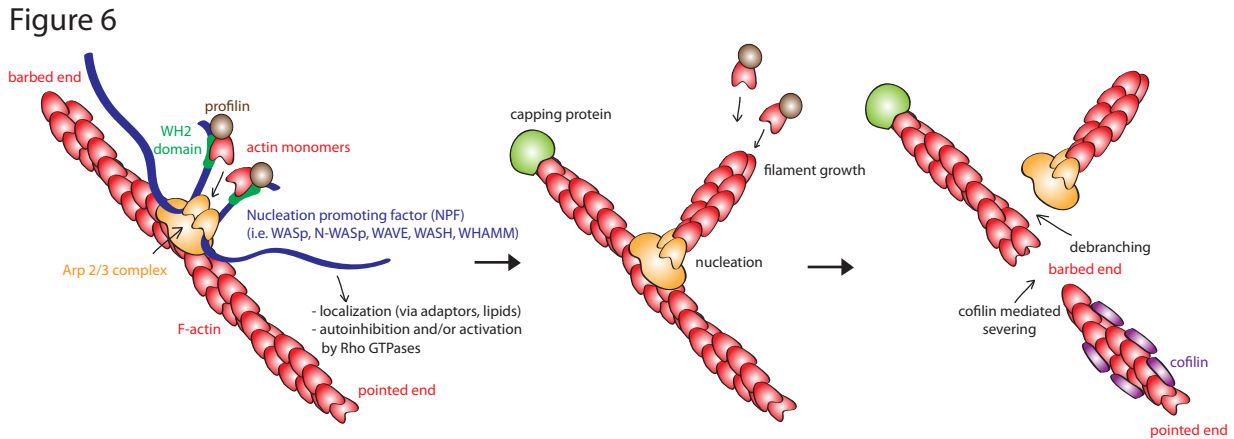


**Figure 1.6.** *F-actin branching regulation.* The Arp2/3 complex preferentially assembles at barbed ends of existing/mother filaments. Arp2 and Arp3 proteins structurally resemble actin monomers and can nucleate a branching filament in a complex with two nucleation promoting factors (NPFs). NPFs are localized to membranes via interactions with phosphoinositides and binding to adaptors, usually through N-terminal domains. The release of the NPF verprolin, central, acidic (VCA) domain to recruit profilin-bound actin monomers is regulated by the binding of GTPases to the GTPases binding domain, phosphorylation, and ubiquitination. Once nucleation is achieved, polymerization continues at the barbed end until filament capping via capping proteins occurs. Polymerized actin can be disassembled by actin-binding proteins that either sever filaments (e.g. cofilin) or debranch branching points of filaments (e.g. GMF $\gamma$ ).

The other major class of actin nucleation proteins, which includes spire, APC, cordon-bleu (Cobl), leiomodin (Lmod), and JMY, all nucleate actin by binding 3 or more actin subunits to make the formation of a critical nucleus of the subunits more favorable [152]. Spire was shown to be a nucleation factor in 2005 by Dyche Mullins' group [158]. Spire contains four

tandem 5 kDa WASP homology 2 (WH2) domains, which can each bind actin monomers, as well as an additional actin binding domain unique to Spire proteins [159]. Spire-mediated nucleation collaborates with the formin Cappuccino in the formation of cytoskeletal networks [160], a cooperation similarly observed between APC and mDia1 [161]. A fascinating feature of these nucleation factors is the multiple roles that they can play in actin polymerization kinetics beyond nucleation, despite their simple architecture [162]. Cobl, which was discovered in 2007 by Britta Qualmann's group, can nucleate, cap, and sever actin filaments as well as sequester actin monomers [163]. This has led the Marie-France Carlier's group to describe Cobl as a "dynamizer" of the actin cytoskeleton [164].

#### **1.6.4 Nucleation promoting factors**

Upon binding to existing actin filaments, the Arp2/3 complex alone is not a potent nucleator of actin, as the addition of an actin monomer to the Arp2-Arp3 dimer remains energetically unfavorable. Nucleation becomes highly favorable upon the binding of actin nucleation promoting factors (NPFs) of the Wiskott-Aldrich Syndrome protein (WASp) family. These proteins use a conserved verprolin homology/central/acidic region (VCA) domain to interact with the Arp2/3 complex and to recruit a single actin monomer [165]. The WASp family of proteins includes WASp and N-WASp, SCAR/WAVE, WASH and WHAMM, which are grouped according to the domains (N-terminal to the VCA domain) critical for their interactions with binding partners that regulate their localization and activity [166, 167]. Although all NPFs use the same essential mechanism for actin polymerization, it is the localization of their action that specifies their unique functions in cellular processes such as endocytosis (WASp), membrane ruffling (WAVE), and endocytic (WASH) or ER to Golgi (WHAMM) trafficking.

The activation of WASp, WAVE, WASH and WHAMM all involve exposing the VCA domain to the Arp2/3 complex, however, the signaling events that lead to this event are distinct [166]. WASp was the first identified NPF and the actin polymerization activity of its more ubiquitously expressed homologue N-WASp was shown to be stimulated by the binding of GTP-bound (activated) Cdc42 GTPase [168]. This finding, made in 1996 by Alan Hall's group, was the first direct molecular connection between the activation of GTPases and the cytoskeleton [169]. The binding of Cdc42 to the GTPase binding domain (GBD) of N-WASp was subsequently shown by Marc Kirshner's group to release N-WASp from an autoinhibited state in which the VCA domain folded within the NPF and interacted near the GBD [170, 171]. The activation of WASp is regulated spatially via an interaction between the polybasic region found near the GBD and PI(4,5)<sub>2</sub>, as well as by its recruitment to a number of receptors and co-receptors through SH3 domain-containing adaptor proteins that bind proline rich domains [172]. In this way, WASp can be rapidly recruited and stabilized at the PM in multivalent complexes where adaptor proteins (e.g. Nck) that contain multiple SH3 and SH2 (phospho-tyrosine binding) domains bridge the NPFs to phosphorylated receptors (e.g. nephrin) [173]. These multi-molecular complexes that are formed in response to receptor signaling increase the polymerization reaction of Cdc42-bound WASp [173].

The WAVE1, 2, and 3 NPFs exist constitutively within a hetero-pentameric WAVE regulatory complex (WRC) [174] and are also activated by a Rho family GTPase, in this case Rac [174]. Binding to phosphoinositides, in this case PI(3,4,5)P<sub>3</sub> and to a lesser extent PI(4,5)<sub>2</sub> [175], as well as phosphorylation, is required for their activation [176]. Although WAVE lacks a GTPase binding domain, its VCA domain is inhibited via multiple interactions within the complex and can be released upon the binding of active Rac to the complex [174, 177]. The four

proteins that associate with WAVE in the WRC are Sra1/Cyfp1, Nap1/Hem-2, Abi and HSPC300. These act collectively to regulate the NPF activity of WAVE by either competitively binding the VCA domain, mediating the localization of the complex, or recruiting kinases that phosphorylate WAVE. For example, Abi (Ableson interacting protein) binds to Ableson kinase which phosphorylates a single tyrosine residue Y151 to destabilize an interaction between WAVE and Sra1 important for sequestration of the VCA domain within the complex [172, 177]. The phosphorylation of a number of other tyrosine residues within WAVE also regulate its activity.

The WASH (WASp and SCAR Homologue) NPF, discovered in 2007 by Barbara Trask's group to localize at endosomes [178], has subsequently been shown to constitutively exist in a large macromolecular complex structurally similar to WAVE by work done in Daniel Billadeau's group [179]. The WASH regulatory complex (SHRC) is comprised of the NPF with relatively uncharacterized proteins FAM21, Strumpellin, coiled-coil domain containing protein 53 (CCDC53) and KIAA1033 (now called SWIP for Strumpellin and WASH interacting protein) [179]. While work on the SHRC is in the very early days, some fascinating discoveries about its regulation are already being made. It is now been shown that FAM21 specifically localizes the complex to endosomes via binding to the VPS35 retromer [180, 181]. On endosomes, the VCA domain of WASH is sequestered within the SHRC preventing interaction with Arp2/3 until the NPF is ubiquitinated on the lysine residue K220 by the Trim27 E3 ubiquitin ligase [182]. The precise mechanism activating Trim27 activity is not known, however, the JNK signaling pathway has been implicated. Finally, the most recently discovered NPF, WHAMM (for WASP Homologue associated with Actin, Membranes, and Microtubules) also functions in trafficking [183]. Matthew Welch's showed in 2008 that WHAMM associated with the Golgi apparatus and

along tubular membranes. While the past 5 years have not brought much light on the mechanism of activating WHAMM, Rho GTPases (specifically RhoD) have been shown to bind and activate the NPF [184] and the original work of Welch speculated a regulation by GTPases with known roles in ER to Golgi transport like the Sar, Rab, and Arf families of GTPases [183].

### **1.6.5 Reconstitution of actin-based motility**

Dynamic reorganization of actin networks at membranes is essential for the movement of vesicles and provides structure for membrane deformation that drives protrusion or endocytosis. In order to infect host cells and move within their dense cytoplasm, many pathogens hijack this actin polymerization machinery [185]. For example, the *Listeria* effector ActA mimicks N-WASp, *Shigella* and EHEC effectors IcsA and EspFu recruit and activate N-WASp in a Cdc42-like fashion, and many *Salmonella* effectors (SopE, SopE2, SopB, SigD) lead to the activation of Rho family GTPases [185]. In a *Nature* paper published in 1999, Marie-France Carlier exploited this behavior of the pathogens *E. coli* and *Shigella* to determine the essential components of the actin polymerization reaction that mediate productive movement of the bacteria [186]. When the Gram-positive bacteria *Listeria* (self-coated in ActA) or *E.coli* coated in IcsA are added to purified actin, ATP, and Arp2/3, they nucleate and form dense arrays of highly branched F-actin from their outer membrane, but do not move as they do in cells or in cell extracts. This seminal work demonstrated that the addition of purified ADF/cofilin and capping protein was sufficient to break the symmetry of the dense F-actin arrays to generate comet tails of F-actin and productive movement of the bacterium (2-4  $\mu\text{m}/\text{min}$ ) similar to those observed in whole cell extracts [186]. While profilin and VASP could accelerate the movement of the bacteria, the minimal essential components for actin based motility is now understood to be ATP, actin, Arp2/3, an NPF, cofilin, and a capping protein [147].

The mechanism by which cofilin and capping proteins work in concert to propel the bacteria forward in media was originally postulated to be as follows: 1) cofilin increases the turnover of filaments via severing them to release G-actin from the pointed end, 2) capping protein binds the barbed ends of self-assembled filaments in the solution as well as filaments in the comet tail no longer binding the nucleation machinery to limit non-productive polymerization [186]. These mechanisms both act to increase the G-actin concentration at the membrane of the bacterium for new polymers and cofilin turns over old polymers leading to a treadmilling effect of the network (note this is a different type of treadmilling described for a self-assembled actin filament in solution without actin binding proteins) [147]. As should be true for engines of network treadmilling, both cofilin and capping protein concentrations exhibit a biphasic relationship with the motility of the bacteria in which high concentrations resulted in either too much severing or too much capping to lead to productive motility. Although not essential for actin-based motility, profilin accelerates the rate at which the bacteria move in solution. Profilin may bind ATP-G-actin monomers, catalyze the exchange of ADP to ATP on actin monomers or prevent their incorporation at pointed ends by binding the barbed face of the monomer. Once the actin monomer is incorporated at the barbed end, profilin rapidly dissociates from actin. The addition of profilin in these experiments, therefore, increased the incorporation of ATP-G-actin specifically at the barbed end such that the hydrolysis rate of ATP-actin to ADP-actin (2 seconds) will set a timer on the filament. Cofilin then preferentially binds to ADP-actin and begins to decorate the filament. As more cofilin binds to the filament, it will eventually lead to a structural twist of the filament, breaking the filament near the interface of the ADP- and ATP-loaded actin [187].

I have discussed the machinery and regulation of nucleation extensively and will now detail the action and regulation of the severing protein cofilin in fueling F-actin dynamics.

### **1.6.6. Cofilin**

The cofilin family of proteins (ADF, cofilin 1, and cofilin 2) are small (19 kDa) F-actin severing proteins. The severing action of cofilin is non-enzymatic. Cofilin preferentially binds ADP-actin and leads to the destabilization of non-covalent bonds between actin subunits, which increases the flexibility of the filament and can propagate torsional forces to the interface of cofilin-bound (flexible) F-actin and non-cofilin-bound (rigid) F-actin [187]. The rigidity of the non-cofilin-bound end of the filament may be enhanced by scaffolding the filament to other rigid filaments via F-actin bundling proteins such as fascin, as demonstrated by Jan Faix and colleagues [188]. Rigidity could also increase if the filament is bound to immobile protein complexes like those on the surface of beads or bacteria used in the aforementioned actin-based motility assay, or are immobilized with antibodies as used in new TIRF based techniques. Other actin proteins can enhance cofilin-mediated filament severing by defining the boundary between cofilin-bound and non-cofilin bound actin within a filament. Bruce Goode's group described coronin as one such F-actin binding protein that binds to newly incorporated ATP-actin and further decreases cofilin binding to these regions of the filament [189].

Recently, cofilin binding to actin filaments has also been shown to cause “bursts” of actin disassembly and debranching [190]. The bursts of actin disassembly were observed using fluorescent actin filaments in TIRF-based experiments with the addition of Aip1 (a cofilin and F-actin binding protein) and coronin. Remarkably, filament stretches up to 800 nm were lost in what appeared to be single frames of 16 ms [190]. It is important to note that in these

experiments, the actin cross-linking protein filamin was used to adhere the filaments to the coverslip and bursts of actin disassembly were observed under perfusion, leading to the possibility that cofilin-decorated flexible regions of the filament were rapidly released from the coverslip. In any case, the coordination of filament disassembly by cofilin and coronin remains of great interest. The debranching of actin filaments originating at sites on the mother filament that are bound by Arp2/3 is another new function of cofilin, suggesting that cofilin may disassemble filament meshworks in addition to severing actin filaments and recycling G-actin [191]. Because the cytoplasmic concentration of the Arp2/3 complex is 2-4  $\mu\text{M}$  while the concentration of actin is 65  $\mu\text{M}$ , roughly a 1:20 ratio [192], this may preclude the requirement for Arp2/3 recycling. The debranching of filaments would be a rapid mechanism for the release of filaments to be severed and the remodeling of dense actin meshworks. Once released from branch points, cofilin may act more effectively on the unbound filament pointed end by exerting a greater torsional force. Debranching is achieved through a number of mechanisms. First, the ATP hydrolysis of the Arp2 subunit of the Arp2/3 complex can directly result in debranching [193]. Second, the cofilin homologue GMF can bind to either Arp2 or Arp3 and destabilize the interaction within the critical nucleus between actin and the actin related proteins, as modeled by Bruce Goode's group [194]. Third, Thomas Pollard's group has recently shown that the force propagated within a filament by cofilin can directly reduce the affinity of Arp2/3 for the filament and this can result in the entire complex dissociating from the mother filament [191]. This study also showed that cofilin could compete for Arp2/3 complex binding sites on actin filaments [191]. Collectively, the net activities of cofilin on filament meshworks situate this F-actin binding protein as a "dynamizer" of the actin cytoskeleton. Cofilin can promote actin nucleation by 1) creating barbed ends, the preferred sites of Arp2/3 complex binding, 2) blocking sites of

Arp2/3 complex binding to ADP-actin regions of filaments, and importantly 3) increasing free G-actin. Cofilin can also promote network turnover by 1) destabilizing and breaking down old filaments and 2) debranching daughter filaments and 3) releasing the Arp2/3 complex from branching points. Undoubtedly, cofilin activity results in greater F-actin turnover (polymerization and depolymerization) in many cell types [195-197].

Cofilin acts by binding to actin filaments. It is therefore not unexpected that the control of its localization and ability to bind actin filaments is tightly regulated. The two key mechanisms by which cofilin activity is inhibited are phosphorylation and the binding to PI(4,5)P<sub>2</sub> [187]. The phosphorylation of cofilin on a single serine residue (Ser3) prevents its binding to actin [198] while the binding to PIP<sub>2</sub> sequesters cofilin at the PM, away from actin filaments [199]. Cortactin, which has a critical role in stabilizing Arp2/3 nucleation points in branched actin, further reduces actin disassembly by binding to cofilin and preventing it from binding to F-actin [200]. In 1998, Kensaku Mizuno and colleagues showed that cofilin was kept inactivated via its phosphorylation by LIM kinase (LIMK) [201]. LIMK was originally thought to be activated by Rac GTPases. However, subsequent studies have demonstrated the main mechanism of LIMK phosphorylation and activation is through the Rho kinase ROCK [198].

It is useful to describe the regulation of cofilin in the context of a migrating cell where cofilin is only active at the leading edge. In the presence of numerous chemoattractants, Rho GTPases are active and elevate LIMK and cofilin phosphorylation (i.e. global inhibition). At the leading edge of migrating cells, a number of mechanisms can lead to cofilin activation (i.e. local excitation). First, the cleavage of PIP<sub>2</sub> by phospholipase C into DAG and IP<sub>3</sub> may release cofilin from the PM [199]. Second, the local activity of the Na<sup>+</sup> H<sup>+</sup> exchange channel (NHE1) may increase the local pH to disrupt the bridge between a protonated Histidine residue (His133) and

an Asparagine residue (Asp122), which mediates the interaction between cofilin and PIP<sub>2</sub> [202]. Cortactin can be phosphorylated by the Src and Arg kinases in response to chemoattractants (i.e. EGF), which allows it to bind and activate NHE1 [203]. Third, most chemoattractants lead to the activation of PI3K, which can increase the local concentration of PI(3,4,5)P<sub>3</sub> by phosphorylating PIP<sub>2</sub> [204]. This could decrease the local concentration of PIP<sub>2</sub> at the leading edge, but also lead to the activation of Rac GTPases, which inhibit the activation of Rho [205]. Indeed, PI3K activity is required for actin dynamics at the leading edge of migrating cells [204]. Given that pH gradients within cells are shallow [206], and blocking NHE1 activity does not inhibit leading edge dynamics (SAF, MRG, CDR unpublished observations), this mechanism appears more attractive than the preceding ones. Finally, the activation of the cofilin phosphatases Slingshot 1 and 2 and chronophin (CIN) at the leading edge may locally lead to enhanced binding of cofilin to actin filaments [198]. Slingshot is activated by the release from 14-3-3 proteins such that it can bind F-actin. The release of Slingshot from 14-3-3 is mediated by coronin 1B, calcineurin, Rac, and PI3K [198].

Clearly there are multiple mechanisms leading to the local activation of cofilin, highlighting its activity as a point of convergence that governs actin dynamics during cell motility. John Condeelis' group designed an elegant experiment to demonstrate this point [207]. They first engineered a cofilin in which the critical serine 3 residue is mutated to a cysteine residue (which renders the cofilin active if membrane sequestration is not a factor). They then covalently modified the cysteine residue with the addition of bromo-(2-nitrophenyl) acetic acid (BNPA), a modification that blocks F-actin binding but can be reversed by irradiation with 300 nm light. When they microinjected this modified cofilin S3C into cells and then irradiated small regions of interest, they were able to define the location of the leading edge and direct cells to the

orientation of the light. This experiment argues that cofilin activation alone can coordinate the actin dynamics of the leading edge. In completely different experiments carried out by Chris Bakal in Norbert Perrimon's lab using a *Drosophila* cell line, cofilin and cofilin regulators (including Slingshot and the Rap GTPases, see Chapter 3) emerged in a screen for proteins at the top of a hierarchy that mediates changes in cell shape [208]. The remodeling of F-actin at the cell cortex by cofilin allows deformation of the PM and the formation of cellular protrusions that mediate cell spreading and membrane ruffling. This is central to many cellular processes, including cell motility, B cell spreading across the surface of APCs, and IS formation. Hence this is a central focus of this dissertation.

## **1.7 Rap GTPases: regulators of actin dynamics and adhesion**

### **1.7.1 Control of Rap GTPase Activation**

The Rap family of GTPases, which are closely related to the Ras GTPases, consists of 5 proteins encoded by different genes: Rap1a, Rap1b, Rap2a, Rap2b, and Rap2c. All Rap isoforms are 21kDa; Rap1a and Rap1b are 184 amino acids and share 95% amino acid identity, Rap2a, Rap2b, and Rap2c are 183 amino acids and share ~65% amino acid identity with Rap1 (<http://blast.ncbi.nlm.nih.gov>). As do all GTPases, Rap functions like a molecular switch, cycling between inactive GDP-bound and active GTP-bound conformational states. The cycling between these states is mediated by the action of GTPase activating proteins (GAPs) and guanine nucleotide exchange factors (GEFs) (Figure 7). The intrinsic hydrolysis of GTP bound to the Ras GTPase, for example, occurs with a half-life of 20 min [209]. GAPs accelerate this hydrolysis rate by greater than 20,000 fold such that the half-life is 50 ms [209]. GEFs cause the

release of GDP from the guanine nucleotide-binding pocket such that the more abundant GTP readily enters the site. Both GAPs and GEFs function via the insertion of their catalytic domains into the nucleotide binding pocket of the GTPase and the specificity for GTPases is governed by these interactions [210]. In the case of Rap, GEFs use an  $\alpha$ -helix in their Cdc25 homology domain and GAPs use an asparagine side chain [210]. A number of Rap GEFs can also act as effectors, binding Rap once it is active via Ras/Rap association (RA) domains [210]. This may feed back on Rap activity, keeping the GTPase active as long as the effector remains bound.

**Figure 7**

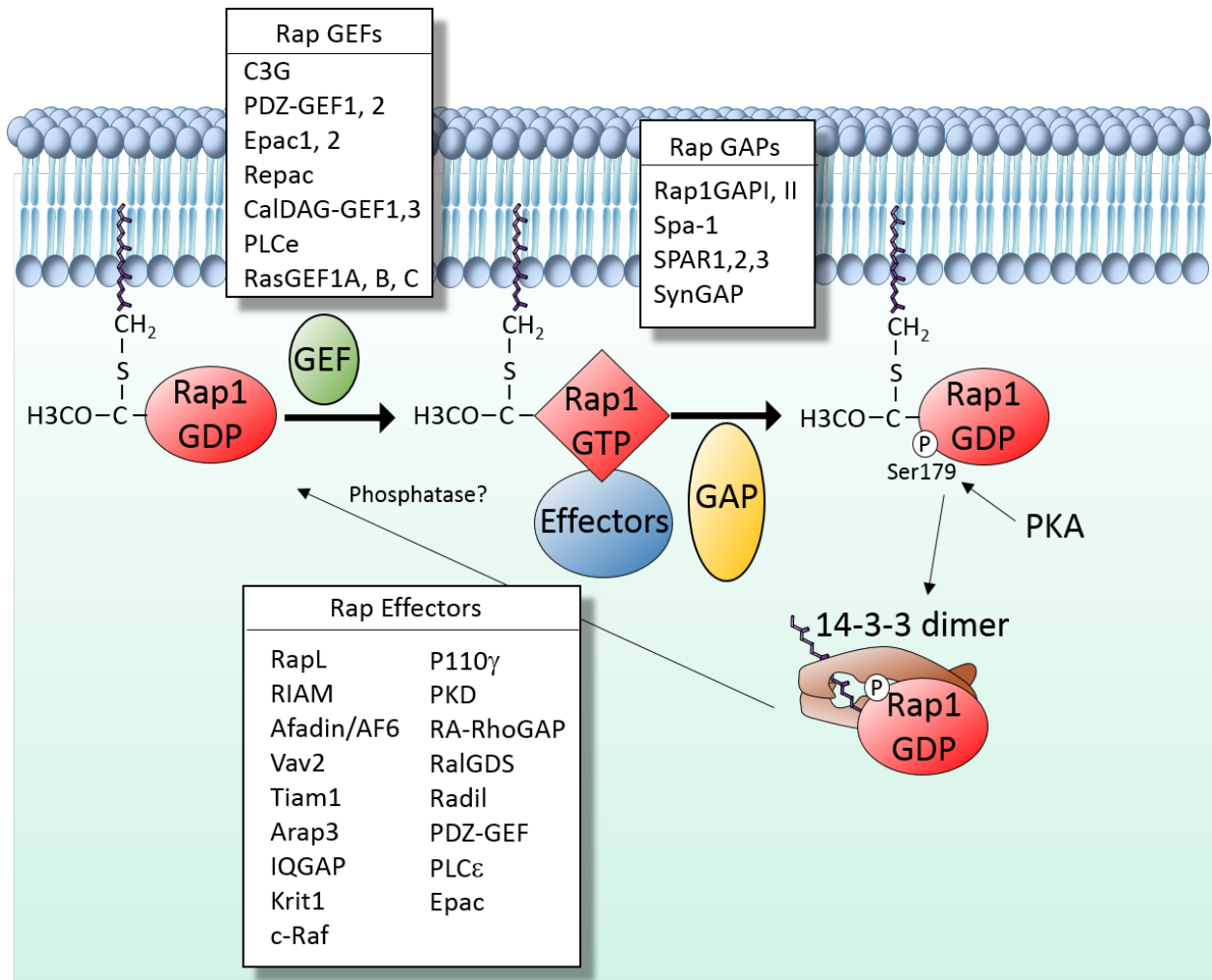


**Figure 1.7. Rap activation at cell membranes.** Rap1 is post-translationally modified by geranylgeranylation. Rap GEFs and GAPs can cycle the Rap1 GTPase between active (GTP-bound) and inactive (GDP-bound) states. Many GEFs and GAPs are localized to cell membranes. Activation of GEFs by second messengers (cAMP, DAG, etc.) leads to the activation of Rap GTPases. Rap1-GTP can recruit and stabilize effectors to the membrane. When phosphorylated by PKA, Rap1 can be solubilized by 14-3-3 dimers.

Another major mechanism regulating GTPase activity is localization to membranes via lipid based post-translational modification (PTM). For Ras family GTPases, this is mediated by polyisoprenylation on the C-terminal CAAX box (where C is a cysteine and is the prenylated residue, A can be any aliphatic amino acid, and X determines the type of prenylation) [211] and the palmitoylation of cysteine residues just N-terminal of the CAAX box in the hypervariable region (HVR) [212]. There are two types of prenyl modifications: farnesylation (15 carbon isoprenoid) and geranylgeranylation (20 carbon isoprenoid) [213]. An X residue in the CAAX box of either leucine or phenylalanine leads to geranylgeranylation while methionine, serine, or glutamine leads to farnesylation. In the Rap family of GTPases, there is considerable divergence of the CAAX box. Rap1a, for example, has a CAAX box with the sequence CLLL and is geranylgeranylated by GGTases whereas Rap2a has a CAAX box with the sequence CNIQ and is farnesylated by FTases. Rap1 and Rap2 have both overlapping and unique functions. It is not known whether the difference in post-translational modification of the CAAX box specifies distinct functions or targets these different isoforms to different cellular membranes or membrane domains. Within just the Rap2 GTPases, Rap2b has a CAAX box of CVIL and Rap2c of CVLS, suggesting concerted evolutionary pressure on the C-terminus of Rap with the expansion of isoforms. While the Ras GTPases H-Ras and N-Ras are frequently palmitoylated, the Rap family of GTPases shows relatively weak palmitoylation despite containing cysteine residues within the HVR.

In addition to cycling of GTPases from GDP and GTP-bound states, the cycling of membrane localization as mediated by lipid based PTMs is an important regulatory mechanism. In the case of Rho and Rab GTPases, this is mediated by dissociation inhibitors (GDIs), which can solubilize the GTPases at membranes by sequestering the prenyl group [214]. The

solubilization can occur independently of the nucleotide bound state of the GTPase, however, there is preference for solubilization of GDP-bound GTPases and depending on the localization/concentration of GEFs or GAPs at the membrane versus the cytosol, GDIs can largely impact the activities of Rho and Rab GTPases [215]. Rho GDI-like proteins for the Ras family of GTPases have been challenging to uncover. Two recent studies, described in the following paragraphs, illustrate why this has been a difficult task, and in so doing, have determined the exquisite control of the localization of Ras GTPases via lipid PTMs.

The GDI-like solubilizing factor (GSF) PDE $\delta$  was predicted to have a GDI-like function given its structural similarity to RhoGDI [216]. PDE $\delta$  does not, however, have the N-terminal region of Rho-GDI, which interacts with the switch-like region of GTPases, conferring the ability to preferentially bind GDP-bound GTPases. This led to a recent study by Bastiaens and colleagues that determined PDE $\delta$  indeed acts like a GDI but does not discriminate specificity based on the nucleotide binding of Ras GTPases [215]. Instead, it can only solubilize de-palmitoylated, farnesylated Ras [215]. H-Ras and N-Ras are palmitoylated at the Golgi and trafficked to the PM. PDE $\delta$  can therefore regulate the spatial organization of these Ras family members by solubilizing Ras at endomembranes to be returned to the Golgi for re-palmitoylation [215]. Additionally, PDE $\delta$  can solubilize the non-palmitoylated K-Ras indiscriminately, to increase its turnover at all membranes [215]. This allows for the polybasic region of K-Ras to preferentially localize the GTPase to the inner leaflet of the PM in cellular homeostasis which contains phosphatidylserine (PS), phosphatidic acid (PA), and phosphoinositols giving it an overall negative charge [217]. Remarkably, a subsequent study demonstrated that disrupting the interaction between PDE $\delta$  and Kras using small molecules alone could impair oncogenic K-Ras signaling propagated at the PM and tumor cell proliferation [218]. Because Rap isoforms are

only weakly palmitoylated, the mechanism of PDE $\delta$  recycling Ras family GTPases from endomembranes is expected to have a negligible role on its cycling and activity [215].

The second study revealed a novel regulatory mechanism of lipid PTM-mediated membrane binding of the Rnd and Rap GTPases by 14-3-3 protein dimers. In 2013, Anne Ridley and colleagues found that 14-3-3 dimers formed a hydrophobic groove with high affinity that could accommodate the prenyl group on the CAAX box of Rnd1, Rnd2, Rnd3, and Rap1a. Binding by 14-3-3 solubilized Rnd GTPases when they were serine phosphorylated by the Rho kinase ROCK1 or protein kinase C (PKC) [219]. Three serine residues contributed to 14-3-3 binding, the most important of which, Ser240, localized just next to the CAAX box and is phosphorylated by ROCK1 [219]. While the study focused on Rnd GTPases, particularly Rnd3, they also showed that the C-terminus of Rap1a (KKKSCLLL) when geranylgeranylated bound with very high affinity to 14-3-3 $\zeta$  [201]. This region of Rnd3 when geranylgeranylated had a dissociation constant ( $K_D$ ) of 23 nM with a 14-3-3 peptide and Rap1a had a  $K_D$  of 24 nM. Conversely, when not lipid-modified, Rnd3 and Rap1a C-termini showed  $K_D$  values greater than 1  $\mu$ M [219]. Although it is known that Rap1 can be serine phosphorylated by PKA at serine 179/180 next to its CAAX box and this regulates its localization to the PM [220], whether or not this is important for 14-3-3 binding was not determined [219].

### **1.7.2 Rap Activation in Cell Polarity**

The localization of active Rap is regulated by the GEFs and GAPs which control the nucleotide binding pocket, prenylation, phosphorylation, and also ubiquitination by Nedd4-1 and Rab40/Cullin5 ubiquitin ligases [221, 222]. Hence, the localization of the GEFs, GAPs, kinases, and ubiquitin ligases are themselves spatially controlled via a number of protein-protein

interactions, PTMs, and second messengers such as cAMP and DAG [223]. The ultimate output of this regulation is the temporal and spatial activation of Rap. Rap can localize to most membranes in cells including the PM, Golgi, endoplasmic reticulum (ER), endocytic vesicles, secretory vesicles, and the nuclear envelop [223]. An asymmetric distribution of activated Rap is essential for cell migration in response to chemokine gradients and the formation of synapses in neurons and immune cells (i.e. an asymmetric, extrinsic cue), migration on 2D matrices (i.e. a symmetric extrinsic cue), and positioning of bud sites in yeast (i.e. an asymmetric, intrinsic cue), which has led to an investigation of the spatial control of Rap activation and the role of Rap-GTP in cellular polarity.

Cell polarity, whether mediated by extrinsic or intrinsic cues, follows a common plan: a spatial cue is sensed, the cue is marked/interpreted, the marked cue is reinforced, and the cue is propagated [224]. A number of polarity cues activate Rap locally, including those induced by the binding of extracellular ligands to adhesion receptors, Ag receptors, and chemokine receptors. In the case of budding yeast, polarized growth/budding occurs with a distinct pattern in the cortex where haploid yeast bud proximal to the bud scar in the mother cell (axial growth) [225]. Given these predicted cell division axes, mutants can be readily identified [226, 227]. From genetic screens of budding mutants, the Rap ortholog (Rsr/Bud1), a Rap GEF (Bud5), and Rap GAP (Bud2) were identified as being essential for correct axial bud site positioning [226, 227]. Subsequent studies showed that mutating the cysteine residue in the CAAX box region to a serine of Bud1 (C269S) or expression of a constitutively-active form of Bud1 (G12V) also resulted in random budding similar to that observed in Bud1  $\Delta$  mutants [225]. The Bud1, Bud5, Bud2 module is essential for the positioning of the Rho GTPase, Cdc42, and is the primary marker of polarity. Constitutively-active forms of Cdc42 (G12V or Q61L), for example, can

still polarize in the presence of endogenous Cdc42, placing Bud1/Rap cycling as the most upstream signaling event in determining cell polarity in this model [225].

The polarization of axial budding requires pre-existing bud sites (i.e. spatial landmarks) marked by a second group of proteins: septins, Bud3, Bud4, Ax11, and Ax12. Less is known about this landmark group of proteins, however, Ax12 is a transmembrane glycoprotein unique to yeast that has been compared to integrins [225]. It is not known if Ax12 has an extracellular ligand (e.g. a component of the cell wall), although the entire landmarking group of proteins localizes to the septin ring of the bud scar and all are important for the localization of the Bud1 module. The localization of the Bud1 module and the landmark module is not constitutive, but rather, is regulated in part by kinases and cyclins controlled by the cell cycle [228, 229]. During yeast mating, which is mediated by cell-cell contact and the secretion of pheromones sensed by G-protein coupled receptors STE2 and STE3, the single yeast cell requires overriding imprinted patterning of division axes. Dynamic components of the axis patterning (i.e. the Bud module, and to some extent, septins) do not require specific regulation in the pheromone response, however, the landmark proteins Ax12 and Bud4 are indeed targets of pheromone signaling and are downregulated [225]. This demonstrates what is likely a fundamental principle in common systems of polarity: in order to adapt to changing spatial cues, transmembrane proteins that mark the spatial cue must be either disengaged from their ligand or downregulated, while proteins that reinforce or propagate the cue must remain dynamic in order to relocalize to new cues at the PM. Clearly, the dynamic regulation of Bud1 activity and membrane localization is required for polarity responses and for changes in polarity complex assembly because: 1) the requirement for Bud1, 2) the requirement for Bud1 GEFs and GAPs (Bud1 cycling) and 3) the requirement for dynamic interaction with inner leaflet lipids. Of note, “symmetry breaking” in a  $\Delta$ Bud1

background can still occur and result in polarized localization of Cdc42 and subsequent budding, however, this has not been determined using a non-cycling Bud1G12V mutant.

Very generally, cellular polarity can be explained using the “local excitation, global inhibition” (LEGI) theory [230]. During axial budding in yeast, the localization of Rap/Bud1 cycling that mediates the activation of Cdc42 and subsequent actin dynamics (discussed in the next section) provides the local excitation. However, it is not known if there is a global inhibitor of actin dynamics. It is interesting to speculate that maintaining cofilin in an inactive state at all sites other than where Bud1/Rap is active could limit actin turnover as it does in mammalian cells [197]. Yeast express one form of cofilin, Cof-1, the deletion of which is lethal. However, studies by David Drubin that employed temperature-sensitive mutants showed that cofilin is required for the polarization and dynamics of cortical actin patches [231].

In Figure 8, I have combined a theoretical framework for polarity establishment described by David Drubin and James Nelson [224] together with a model of LEGI theory [230] to introduce the activation of Rap GTPases and cofilin as *response regulators*. In the case of adhesion as a spatial cue, the presence of Rap-GTP at adhesion sites can act as both a regulator of the spatial cue (e.g. integrin activation) and a reinforcer of that cue (e.g. actin dynamics at adhesions). I will now use these combined theoretical frameworks to discuss the role of Rap activation in integrin-mediated adhesion and actin dynamics in the context of cell migration (an anterior-posterior polarity event) and cell spreading (an apicobasal polarity event).

## Figure 8

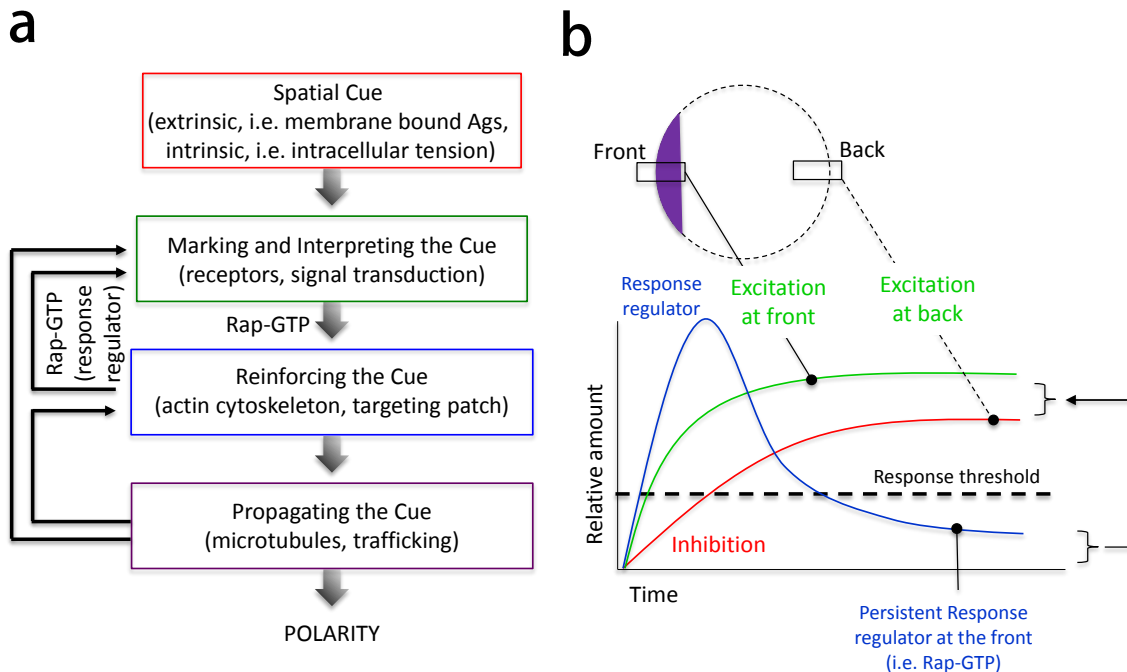


**Figure 1.8. Establishing cell polarity.** A) In order for cells to achieve polarity, a spatial cue must first be determined by receptor engagement or an intracellular landmark (e.g. bud scar in yeast) and marked by creating asymmetry of receptors and/or their signal transduction (e.g. asymmetry of kinase and phosphatase activity, Rap activation). Reinforcement and propagation of the spatial cue are achieved via multiple cytoskeletal mechanisms. B) Local excitation global inhibition (LEGI) is achieved once activation of a response regulator passes a threshold on one side of the cell. Once this threshold is achieved to give front and back polarity, the persistence of the response regulator at the front can be much lower than this initial burst of activity given the feedback on the spatial cue. For example, if one side of a cell has higher adhesion and integrin activation, this could initially increase Rap-GTP levels above a threshold. Rap could then act on a number of effectors that increase actin dynamics as well as the adhesive cue itself by increasing integrin activation. This could sustain a polarized morphology provided that integrin signaling maintained asymmetry of Rap-GTP.

### 1.7.3 Rap activation in cell migration

Cellular systems can achieve polarity of an excitable network (a system where stimuli can elicit responses greater than the initial perturbation) even with a uniform stimulus. This polarization is usually not sustained and results in a rapid flux of actin dynamics in a region of the PM without persistence beyond a few minutes [230]. However, the expression of the constitutively active Rap1V12 mutant in T cells, for example, results in spontaneous polarization of the cytoskeleton [232]. Interestingly, this is not observed when expressing constitutively active forms of Cdc42 or Rac. The active form of Rap is also sufficient to cluster integrins and chemokine receptors at the front or leading ledge of the cell without stimulus, suggesting the organization of receptors in the membrane is a mechanism underlying Rap-mediated cell polarization [232].

In the presence of shallow chemokine gradients, a rapid initial response establishes polarity such that the leading edge of the cell is the site of highest receptor occupancy (Figure 8). This response generates a large intracellular gradient of actin dynamics provided that the spatial cue also activates intracellular signaling systems that have positive feedback loops to overcome a threshold [230]. The receptors are quickly desensitized, however, such that the front/back polarity must be sustained by persistent response regulators that continue to orchestrate the self-assembly of F-actin networks at the leading edge. By this theoretical framework, response regulators and the actin dynamics that they control can sustain polarity and drive cell migration [230].

Rap is activated by chemokines and by integrins, both of which are spatial cues in cellular migration. Chemokine receptors activate Rap via a PLC $\gamma$ /DAG signaling pathway that

stimulates the activity of the Rap GEF, CalDAG-GEF1 (RasGRP2), which contains a DAG-binding domain [233-235]. Integrins can activate Rap by recruiting complexes containing the Crk adaptor protein and the Rap GEF C3G to bind to the integrin-associated scaffolding protein p130Cas [236, 237]. Cytoskeletal tension applied through p130Cas reveals a cryptic tyrosine residue, exposing it to Src family kinases (SFK) [236]. SFK-mediated phosphorylation of this tyrosine residue creates a binding site for the SH2 domain of Crk [236]. The SH3 domain of Crk binds constitutively to C3G, which functions as a GEF after being phosphorylated by the Abl kinase [238].

Once activated, Rap binds a number of effector proteins that coordinate cytoskeleton dynamics and integrin activation to reinforce the polarity cue marked by Rap-GTP (Figure 8). Rap-GTP binds to the RIAM adaptor, which recruits the ENA/VASP/profilin complex. ENA/VASP proteins can antagonize filament capping of barbed ends, while profilin primes actin-GTP monomers [239]. The net result of these activities is to promote actin polymerization and filament extension. Active Rap also promotes the activation of the small Rho GTPases Cdc42 and Rac. Rap-GTP can bind the Rac GEFs Vav2 and Tiam1 and thereby recruit them to the leading edge of the cell. As well, the Rap-GTP-dependent recruitment of the Par polarity complex (Par3/Par6/PKC $\zeta$ ), which requires the activation of Cdc42 downstream of Rap-GTP, results in the full activation of Tiam1 by PKC $\zeta$ -mediated phosphorylation [232]. Once Cdc42 and Rac are activated, they stimulate Arp2/3-mediated actin nucleation by WASp and the WAVE complex respectively. Active Rap also binds to the Rho GAP, Arap3 [240], presumably decreasing the amount of Rho-GTP at the leading edge. Reducing the amount of linear actin polymerization induced by the Rho-GTP/formin pathway shifts actin networks to a more

branched organization as this allows WASp/WAVE/Arp2/3 nucleation complexes to instead initiate branched actin polymerization at barbed ends.

Cell migration often requires coordinating actin dynamics at the front of the cell/leading edge with integrin-mediated adhesion to either the ECM or cell membrane ligands such as ICAM or VCAM-1. Integrins are heterodimeric non-enzymatic adhesion receptors containing an  $\alpha$  and  $\beta$  subunit. They bind extracellular ligands when in an extended conformation via a headpiece in the dimer. The affinity of integrins for their ligand is increased when the cytoskeleton applies tension to the  $\beta$  chain cytoplasmic tail and those forces are then transduced through the  $\beta$  subunit to cause changes in the structure of the ectodomain [241]. Conversely, force applied to integrin ectodomains are transduced across the membrane to the actin cytoskeleton, which is connected to the  $\beta$  subunit tail via scaffolding proteins. An opposing force on the ligand-bound integrin may be mediated by fluid shear experienced by cells in the vasculature [242]. In order for integrins to reach an extended conformation, an initial step in integrin activation, it is thought that interactions between the  $\alpha$  and  $\beta$  subunits must be disrupted [243]. This disruption can be the result of proteins binding to either the cytoplasmic tail of the  $\alpha$  by RapL [244] or the  $\beta$  subunit by kindlins or talin [245]). Rap-GTP directly recruits RapL (regulator of adhesion and cell polarity enriched in lymphoid tissues) to the PM such that it can bind to a GFFKR motif in the cytoplasmic tail of the  $\alpha_L$  subunit of LFA-1 [244]. Rap-GTP also recruits the scaffold protein RIAM to the PM. RIAM contains an RA domain as well as a talin-binding domain and can therefore bridge Rap-GTP to talin at. The recruitment of RIAM-talin complexes to the  $\beta$  integrin cytoplasmic tail can disrupt interactions with the  $\alpha$  subunit cytoplasmic tail [246]. It was

recently shown by Mark Ginsberg's group that fusing the C-terminus of Rap, which contain its CAAX box, to RIAM was sufficient to activate integrins in the absence of active Rap [247].

The importance of Rap-GTP and the Rap effectors RapL and RIAM in initiating integrin-mediated adhesion is apparent from a number of gain- and loss-of-function experiments. Expression of Rap1V12 increases activation of the  $\alpha_M\beta_2$  integrin (the CR3 complement receptor) and CR3-mediated phagocytosis of opsonized targets by macrophages [248]. Rap1V12 expression also increases the activation of the LFA-1 and VLA-4 integrins in T cells, resulting in increased adhesion to the cellular ligands, ICAM-1 and VCAM-1 respectively [249, 250]. Conversely, the expression of a dominant negative form of Rap1, Rap1N17, or Rap1GAP in these systems ablated integrin activation [249, 250]. Similarly, Rap1a<sup>-/-</sup> mice show decreased adhesion of macrophages to fibronectin, vitronectin, and ICAM-1 [251]. Rap1b<sup>-/-</sup> mice have a bleeding defect due to abrogated activation of the platelet integrin,  $\alpha_{IIb}\beta_3$ , required for platelet aggregation and clotting [252]. A similar phenotype is observed in mice lacking the Rap1 GEF, RasGRP2 [253]. RapL<sup>-/-</sup> mice show decreased adhesion to ICAM-1, do not polarize or cluster integrins in response to chemokines, and show defective migration of T and B cell *in vitro* and *in vivo* [244, 254]. Collectively, these data have centered Rap activation as the master GTPase regulating integrin-mediated adhesion.

Based on numerous studies from yeast to murine models, Rap-GTP is posited as an immediate interpreter of spatial cues, and importantly, is a key response regulator in the maintenance of cellular polarity (Figure 8). In order to surmount a threshold for initial polarization, response regulators must situate in positive feedback loops. Chemokine receptors have been shown to activate Rap, and Rap activation alone has been shown to cluster and

polarize chemokine receptors. Integrin engagement has been shown to activate Rap, and Rap activation leads to structural changes that initiate further integrin activation and also increase actin dynamics so as to cluster and stabilize integrin adhesion complexes. Because Rap is also directly activated by signals that are transduced mechanically at adhesions via p130Cas/Crk/C3G, this confers the potential for Rap to act as a tension sensor that amplifies spatial cues of tension. Mechanical activation of Rap could be a potential mechanism for self-perpetuating migration in the absence of extracellular gradients. Initial stochastic symmetry breaking of tension could rapidly lead to an asymmetry of Rap-GTP, which could be reinforced through these feedback loops (Figure 8). This type of migration is observed in many cell types including keratinocytes and tumor cells on simple 2D ECM or plastic, where directional migration is observed for long (i.e. hours) periods of time.

#### **1.7.4 Rap activation in cell spreading and adhesion on membranes**

The formation of integrin-based adhesions requires their clustering in the PM. Native and remodeled ECMs present multiple, repetitive integrin binding sites that can induce integrin clustering, whereas membrane-bound integrin ligands (e.g. ICAM-1) require the initiation of integrin signaling in order to induce integrin clustering. The binding and clustering of membrane-integrin ligands is particularly important for lymphocyte extravasation from the vasculature where vascular endothelial cells express high levels of VCAM-1 on their surface and upon encounter of membrane-bound Ags on Ag presenting cells (APCs) that express high levels of ICAM-1. The clustering of cellular integrin ligands is important for the spreading and close contact of lymphocytes in the *de novo* junctions they formed in the vasculature or on APCs. Spreading and migrating across the surface of other cells is important for lymphocyte extravasation and for lowering the threshold for lymphocyte activation.

The spreading of T and B cells on the PM of APCs results in the formation of an IS [92, 100], which is first initiated by the formation of small clusters of Ag receptors-Ag and integrin-ICAM-1, as previously discussed [98]. TCR or BCR signaling leads to the activation of PLC $\gamma$ , Rap, Vav2, Rac, and cofilin, which remodel in the cortical/submembrane actin cytoskeleton [54, 60, 62, 95, 195]. The remodeling of actin is required for cell spreading, but also the enhanced mobility of unengaged receptors [54]. In mechanisms previously outlined, Rap-GTP leads to integrin activation in a feedback loop, providing traction for the spreading response. These actions of accelerating actin dynamics and engaging integrin result in increased chances for Ag receptors to bind ligands because 1) receptors are more mobile and 2) there is increased contact with the APC membrane. Given that Rap is required for the actin dynamics and integrin activation in response to TCR/BCR signaling, it is not surprising that Rap activation is required for IS formation [95]. Although it has been shown that the spatial cue (i.e. quality and quantity of Ag, as well as integrin activation) can set the threshold by which the cellular spreading response occurs on the APC PM [84, 255, 256], whether or not Rap activation tunes these thresholds has yet to be determined.

The IS shows no polarity in 2D and is characterized as having a “bull’s eye” shape, where integrins are localized to the periphery and Ag receptors are localized to the center [100, 257]. This symmetrical pattern can be broken, in T cells at least, where a symmetric IS switches to become a kinapse (asymmetrical pattern) and T cells begin to move on APCs [258]. This seems to occur for a few minutes before the T cell switches back again to the characteristic pattern. Very little is known about how a “front” and “back” is established to override the apicobasal polarization. However, it seems to involve a connection between the Par complex and the actomyosin cytoskeleton regulators WASp and myosin [258]. Interestingly, T cells

encountering weak stimuli (in the form of pMHC that is not perfectly complementary for the TCR) only integrate signals via kinapses and cannot arrest to a stable IS. Sustained polarization on APCs by T cells or in secondary T cell-T cell synaptic interactions may be essential for asymmetric division and/or differentiation to give rise to effector and memory populations. Indeed, mice lacking ICAM-1, in which sustained immune synapses are not observed, as well as mice lacking LFA-1 in their T cell compartment do not have strong memory responses to Ags [99, 259]. In secondary homotypic T cell-T cell interactions, IFN $\gamma$  is made, secreted, and shared by T cells at sites of close contact during a period where CD8 $^+$  memory is generated [259]. Cellular polarity mediated by the integration of actin and integrin based adhesion is therefore critical in the migration, adhesion, and also differentiation of immune cells during immune responses.

## **1.8 Tumor cell metastasis**

### **1.8.1 Overview**

Tumor cell metastasis accounts for more than 90% of cancer related deaths. It is a multistep process sometimes referred to as a cascade wherein primary tumor cells become invasive, move through the stroma to intravasate local vasculature, enter circulation, and traffic to distant sites [260]. To establish secondary tumors at these sites, malignant cells must arrest within and exit from the microvasculature, invade the stroma of the new organ, and proliferate. Given the numbers of steps limiting tumor cell dissemination, particular attention has been paid to the steps in the metastatic cascade that are potentially targetable and, concurrently, which are efficient [261, 262].

Although the majority of studies on metastasis have focused on how cells invade the local stroma of primary tumors, growing evidence suggests that once a tumor has been detected, almost certainly there will be thousands or even millions of tumor cells already in circulation (termed circulating tumor cells or CTCs) [263, 264]. Despite CTCs being the eventual source of distant metastatic lesions, relatively little is known about their composition and how this compares to cells at the primary tumor, largely because CTCs have been so difficult to isolate from a sea of normal blood cells [263, 265]. Indeed, studies using sophisticated microfluidic chambers to capture CTCs have found a range from 5 to >1000 CTCs/mL of blood or between 0.005-0.1% of mononuclear cells in pancreatic, breast, and prostate cancers [264]. Other studies have yielded even fewer CTCs/mL, again making characterization of these cells difficult [266]. Additionally, some of these CTCs may be clinically irrelevant, as patients with benign disease (i.e. Crohn's or benign polyps) can present with harmless circulating epithelial cells [267]. Despite the challenge in isolating and characterizing bona fide CTCs, it remains an important area of pursuit given that their presence correlates with disease progression and survival [268, 269], primary tumor responses to treatment [264], and metastasis [266, 270].

The shedding of CTCs into the blood is a continuous process given 1) the close relationship between CTCs and tumor volume in short courses of treatment [264] and that 2) CTCs are generally much larger than capillary beds of the lung for example, resulting in lodging in this closed vasculature (i.e. quickly taking them out of circulation) [261, 263, 271]. This requires the continuous removal of CTCs from the blood via filtration, apoptosis, or their active exit from the vasculature [261]. Collectively, studies on CTCs suggest that tumor cell arrest and extravasion at distant sites are not rate limiting steps in the metastatic cascade [261]. In fact, careful analysis of CTCs that were injected directly into circulation in mice has shown that tumor

cell arrest and extravasation at distant sites occurs at remarkably high efficiencies [272]. For example, 98% of B16F10 cells injected by tail vein can arrest in the lung (target organ) while 83% of B16F1 cells injected into the mesenteric vein arrest, extravasate, and survive in the liver (target organ) [272]. Even non-transformed fibroblasts [272], weakly metastatic melanoma lines (B16F0, SF, MG, CR unpublished observations), and weakly metastatic breast cancer lines (HMT-3522-T4-2) [273] show high efficiencies of arrest and extravasation. Consistently, at least in melanoma and breast carcinomas, very few of these cells (<2%) form micrometastases at secondary sites and many fold fewer (0.02%) go on to form tumors, suggesting that overcoming tumor cell dormancy (i.e. the inability to proliferate in new niches) is a critical and inefficient step in the metastatic cascade once tumor cells enter the vasculature [261, 272, 273].

Although intrinsic genetic and epigenetic changes in tumor cells can influence all steps of the metastatic cascade [262, 274], including the transition from dormancy to secondary lesion establishment, there is a growing appreciation for how the tissue microenvironment at primary and secondary sites can impact disease progression [275-277]. In line with this, tissue stiffness, ECM remodeling, immune response evasion, and co-opting cells of the immune system in pro-tumorigenic ways have been incorporated into models for cancer “hallmarks” [277, 278]. These extrinsic factors at secondary sites make up the metastatic niche that can be pre-established (i.e. ‘primed’), established by newly arrived tumor cells, or occur in late relapse stages of the disease.

### **1.8.2 Inflammation and metastasis**

Perhaps the most striking results to implicate immune response evasion in the establishment of new lesions arise from studies that have investigated the tumor-initiating potential of single or small numbers of tumor cells [279, 280]. These studies were motivated by

longstanding observations that introducing thousands or millions of tumor cells into circulation yields only tens or perhaps hundreds of metastases, as well as more recent observations that this efficiency increased by first sorting cells for stem cell-like traits (i.e. the tumor stem cell hypothesis) [281-283]. By injecting serial dilutions of melanoma cells from patients into NOD/SCID mice, Sean Morrison's group demonstrated that, on average, only 1 in  $10^6$  cells had tumor-initiating potential. If they further crippled the immune system by deleting the IL-2 receptor gamma chain, eliminating the function of natural-killer cells for example, now 27% of single melanoma cells initiated tumors in a sub-cutaneous injection [280]. In the same NSG mouse model (NOD/SCID/gamma), injecting just 100 breast cancer cells gave rise to tumors 100% of the time [279]. These data nicely summarize what has become an entire field of investigation demonstrating that the immune system does a remarkable job at eliminating or preventing the establishment of cancers [277].

Although tumor cells must evade the immune response in order to avoid destruction, cancers can be initiated and growth can be augmented by inflammation [284]. Up to 20% of cancers are caused by chronic inflammation or infectious agents [285]. High levels of  $\text{TNF}\alpha$  and IL-6 produced locally by *H. pylori* infection can cause gastric cancer and MALT lymphoma (5.5% of all cancers) [285]. Viruses like HPV (5%), HepB and C (5%), Epstein-Barr (1%), and HIV together with human herpes virus 8 (1%) are causative in a substantial number of cancers [285].

In the early progression of primary tumors, immune infiltrates, which are present in virtually all adult solid tumors, directly release or stimulate stromal cells (e.g. tumor associated fibroblasts) to release pro-growth/pro-invasion mediators such as EGF,  $\text{TGF}\beta$ ,  $\text{TNF}\alpha$ , FGFs,

VEGF, Wnt, various cytokines, chemokines, histamine, heparins, and proteolytic enzymes [277]. Many of these factors are produced by tumor-associated macrophages (TAMs). More than 80% of studies have shown a correlation between macrophage density and poor patient prognosis. This is particularly true for lung cancers and melanomas. At sites of metastasis, resident macrophages have been postulated to promote tumor cell extravasation and growth [276]. Indeed, the critical role of macrophages in tumor progression is illustrated by the fact that tumor cells are selected for high levels of VCAM-1 on their surface in order to initiate and maintain close associations with macrophages that provide growth factors [286]. Similarly, TAMs can be recruited by CSF1 and CXCL12 that is produced by the tumor cells. In LOF models, depletion of TAMs reduces the metastasis of mouse mammary cancer [287]. Similarly, depletion of CD4+ [288] or all T cells in different metastatic models also abrogates metastasis, presumably by blocking macrophage activation [289].

Priming of the metastatic niche can occur via macrophage activation, which is controlled by T cell-derived cytokines, by ECM deposition by tumor cells, or by inflammation. For example, versican secretion by Lewis lung carcinomas (LLC) can potently activate macrophages via TLR2 and TLR6 [290]. Activated macrophages then secrete TNF $\alpha$ , which is required for LLC metastasis [290]. Versican can bind hyaluronic acid (HA), another ECM component that has been implicated in metastasis [291, 292]. Recently, it was shown that the intrinsic ability of tumor cells to produce the ECM component tenascin C abrogates tumor cell and promotes lung colonization [293]. Similarly, during angiogenesis, the ECM components SPARC and osteonectin are released by endothelial tip cells to bring breast cancer cells out of dormancy [273]. Collectively, the intrinsic ability of tumors cell to produce ECM or interact with resident macrophages, as well as the extrinsic presence of inflammation, which also induces ECM

remodeling and secretion of ECM components, appears to be largely pro-tumorigenic at the metastatic niche.

### **1.8.3 The tensional phenotype, Rap activation, and metastasis**

A major factor in tumorigenesis is the loss of tissue homeostasis (tissue dysplasia) and disrupted tissue architecture can be described as the tensional or “mechanical” phenotype [294, 295]. Tissue stiffness, as measured by an elastic modulus, is a poor prognostic indicator in different cancers, and drives invasion and growth [296]. The tensional phenotype has a reciprocal relationship between tumor cells/stromal cells, neighbouring cells, and the surrounding ECM where forces exerted by cells pull and remodel matrices while the ECM and tissue has an opposing elastic resistance [296, 297]. The net result of this relationship governs mechanotransduction at the PM, a process in which mechanical signals are converted to intracellular biochemical signals that impact transcription and growth [294, 298, 299]. The tensional phenotype also influences the maturation of focal adhesions and migratory capacity of cells [295], cell division axis orientation [300, 301], the action of a number of mechanosensitive channels [302], and more direct connections with the nucleus via the linker of nucleoskeleton and cytoskeleton (LINC) complex [298]. In mechanotransduction initiated at the plasma membrane, forces exerted by extracellular and intracellular matrices or by physical stimuli (e.g. sound) result in conformational changes of proteins that can affect their function and/or reveal cryptic binding sites within the protein [303-306] [302]. In a similar vein, LINC and other connections to the nucleus, when under force, can lead to nuclear matrix distortion, opening of nuclear pores, and DNA melting [298, 307].

I have previously described Rap GTPases as mechano-responsive proteins that transduce such inputs to integrins and the actin cytoskeleton. Whether Rap, which is chronically activated in many cancers (see Table 2), dysregulates the reciprocal relationship between tumor cells and their extracellular adhesive cues, and in this way contributes to dysplasia is not known. In an Appendix of this dissertation, I show that Rap GTPases are activated in tumor cells in response to extracellular tension and that Rap activation is then required for the turnover of adhesions, which in turn promotes invasion and tumor cell growth.

**Table 1.2**

**Rap GTPase Activity in Cancer**

Cancer Type	Study	Role of Rap	Reference
brain	Used neuroblastoma cell lines SK-N-SH and SH-SY5Y and knocked down Rap1 or overexpressed <b>Rap1GAP</b> after finding the anaplastic lymphoma kinase (Alk) activates Rap via the phosphorylation of the Rap GEF, <b>C3G</b> .	Both knocking down Rap1 as well as overexpressing Rap1GAP reduced the growth of the neuroblastoma cell lines.	Schonherr <i>et al.</i> ( <i>Oncogene</i> , 2010)
breast	Identified <b>Radil</b> , a Rap effector, binds to KIF14. KIF14 expression and Rap activity concurrently are upregulated in many cancers. Used a knockdown of KIF14 in breast cancer cell lines to infer the role of Rap using this model.	Binding of Rap to Radil brought RapGTP to microtubules. This may be important for the turnover of RapGTP at the plasma membrane, as the KIF14 knockdown resulted in increased cell spreading but decreased cell migration and invasion.	Ahmed <i>et al.</i> ( <i>JCB</i> , 2012)
	The loss of the Rap effector <b>AF6</b> occurs in 15% of breast cancers and associates with poor prognosis, increased metastasis. AF6 can localize Rap-GTP to nectin-based cell-cell junctions. Knocked down AF6 in 3 breast cancer lines (MCF7, SK-BR-3, and MDA-MB-231), assessed expression in 16 cell lines.	Found AF6 more frequently was not expressed in invasive cell lines. Found that reducing AF6 levels increased cell motility of single cells and cells that maintained junctions (collective migration) and increase metastasis <i>in vivo</i> . Implicates Rap-GTP localization from junction adhesion complexes to ECM contacts increases cell motility of breast cancer cells.	Fournier <i>et al.</i> ( <i>Oncogene</i> , 2011)
	Identified activation of Rap downstream of junctional adhesion molecule-A (JAM-A) in MCF-7 breast cancer cells. Knocked down JAM-A and used a Rap1 pharmacological inhibitor, GGTI-298.	Decreased expression of JAM-A or blocking Rap activation led to decreased adhesion and migration on FN matrices. Reduced levels of JAM-A and Rap1 expression in 3 patient tumor lines as compared to non-tumor lines.	McSherry <i>et al.</i> ( <i>Breast Cancer Res.</i> , 2011)
	Used an immunohistochemical quantification to measure protein expression levels of Rap1 in 90 samples of breast tissue (17 normal, 16 benign, 15 carcinoma in situ, and 42 invasive carcinomas).	Found that women with invasive cancers were four times more likely to have elevated levels of Rap1 than those with non-invasive lesions.	Furstenau <i>et al.</i> ( <i>Breast Cancer Res Treat.</i> , 2011)
	Used breast epithelial cell lines, a malignant HMT-3522 T4-2 and the non-malignant S1 counterparts, to analyze Rap activation in epithelial morphogenesis in 3D culture. Expressed a dominant negative form of Rap1 (Rap1N17) or a dominant active form (Rap1V12) to determine how these events are affected.	Expression of Rap1N17 led to a normalization of the T4-2 cells morphologically and reduced tumor incidence. Rap1V12, conversely, opposed conversion of the T4-2 cells by inhibitors of EGFR and MAPK.	Itoh <i>et al.</i> ( <i>Cancer Res.</i> , 2007)
	Analyzed a loci in the murine genome that substantially influences metastatic efficiency in mammary tumors (Mtes1). Identifies Sipa1 gene, which encodes the Rap GAP, <b>SPA-1</b> , as a candidate underlying Mtes1. Carried out metastasis assays with overexpression or knockdown of SPA-1 in cell lines.	Found that SPA-1 can be sequestered from hydrolyzing Rap-GTP by AQP2, an interaction which requires the PDZ domain of SPA-1. In mice with Mtes1, the Sipa1 gene is mutated, leading to an amino acid substitution in the PDZ domain which prevents this interaction and decreases Rap-GTP levels. Overexpressing SPA-1 in Mvt1 mammary carcinoma cells enhanced metastasis.	Park <i>et al.</i> ( <i>Nat Genet.</i> , 2005)

Rap GAP or GEF    Rap effector    miRNA

**Table 1.2**

<b>colon</b>	Used a knock-down of <b>Rap1GAP</b> to elevate RapGTP levels.	The increased Rap activation lead to increased invasion. Rap GTP opposed Rho/ROCK activity in these cells, and cells were more elongated/mesenchymal, less contractile.	Tsygankora <i>et al.</i> ( <i>JBC</i> , 2013)
	Found that <b>miR-139</b> is downregulated in colorectal carcinoma and downregulation correlated with more advanced CRC and lower patient survival. miR-139 targets Rap1B. Used an overexpression of miR-139 as well as a knockdown of Rap1b to show that both result in antiproliferative effects in CRC cells.	Increased Rap1 expression correlated with CRC progression.	Guo <i>et al.</i> ( <i>Int J Biochem Cell Biol</i> , 2012)
	Used an overexpression system of <b>Rap1GAP</b> in human colon cancer cells.	Found that Rap1GAP more strongly impairs adhesions with the ECM than cell-cell adhesions mediated by beta-catenin and E-cadherin.	Vuchak <i>et al.</i> ( <i>Cell Adh Migr.</i> , 2011)
	Used a knockdown of <b>Rap1GAP</b> or Rap1 in human colon carcinoma cell lines.	Determined that cells depleted of Rap1GAP show increased adhesion and spreading on collagen but also a disruption of cell-cell contacts and in Rap1GAP depleted cells, silencing Rap can normalize their morphology.	Tsygankova <i>et al.</i> ( <i>Mol Cell Biol.</i> , 2010)
<b>esophageal</b>	Identified <b>miR-518b</b> as targeting Rap1b in esophageal squamous cell carcinoma (ESCC). miR-518b is down-regulated in ESCC. The authors overexpress miR-518b or anti-miR-518 in different ESCC lines.	Overexpression of miR-518b suppressed proliferation and decreased invasion in ESCC cells, suggesting higher levels of Rap1b enhances proliferation and invasion of ESCC.	Zhang <i>et al.</i> ( <i>FEBS Letters</i> , 2012)
	Identified <b>miR-196a</b> as targeting Rap1a in esophageal squamous cell carcinoma (ESCC). Mutations in the miR-196a binding site of the RAP1A 3'UTR was associated with ESCC risk. Overexpressed or knocked-down Rap1 in the ESCC EC109 cell line.	Found a correlation between Rap1A expression as controlled by miR-196a binding and risk in patients with ESCC. Rap1A expression was shown to be required for invasion and migration of the EC109 cell line.	Wang <i>et al.</i> ( <i>Carcinogenesis</i> , 2012)
<b>head and neck</b>	Analyzed Rap 1A expression by RT-PCR in 256 samples from patients with oral cavity squamous cell carcinoma (OCSCC). Overexpressed Rap1A or knocked down Rap1A in OCSCC cell lines.	Expression of Rap1A negatively correlated with 5 year survival rate of patients. Increasing Rap1A levels promoted migration and invasion of cells in culture while the loss of Rap1A decreased cell motility	Chen <i>et al.</i> ( <i>Am J Pathol.</i> , 2013)
	Determined that Enhancer of Zeste Homolog 2 (EZH2), a histone methyltransferase, methylates the promotor of <b>Rap1GAP</b> to downregulate its expression and that EZH2 itself is regulated by miR-101 in multiple	Found that EZH2 promotes proliferation of HNSCC and knocking down EZH2 increases Rap1GAP expression, decreases Rap activation, and decreases cell proliferation in culture.	Banerjee <i>et al.</i> ( <i>Oncogene</i> , 2011)
	Overexpression of <b>Rap1GAP</b> in oropharyngeal squamous cell carcinoma	Blocking Rap activation decreased ERK activation and proliferation and led to smaller tumors in nude mice compared to controls.	Zhang <i>et al.</i> ( <i>Am J Pathol.</i> , 2006)

**Table 1.2**

<b>kidney</b>	Used renal cell carcinoma (RCC) cell lines to investigate promoter methylation of <b>Rap1GAP</b> . Determined the promoter of Rap1GAP shows hypermethylation in more invasive RCC cell lines. Rescued expression by expressing Rap1GAP under a different promoter.	Found rescued expression of Rap1GAP decreases invasion of the RCC cell line SN12C on collagen, fibronectin, and MatriGel.	Kim <i>et al.</i> ( <i>Cancer Letters</i> , 2012)
<b>leukemia</b>	Investigated chemokine mediated transendothelial migration which requires autocrine VEGF production for the clustering of integrins in chronic lymphocytic leukemia (CLL).	Found that in CLLs, Rap is not activated in response to chemokine receptor engagement and this prevents the activation of integrins. VEGF, which permits CLL TEM, activates Rap to clusters and activate integrins.	Till <i>et al.</i> ( <i>Cancer Res.</i> , 2008)
	Investigated the onset and progression of chronic myelogenous leukemia (CML) in <b>SPA1</b> <sup>-/-</sup> mice. Complemented this work by overexpression of either constitutively active Rap1 (Rap1E63) or SPA1 in normal progenitors.	SPA1 <sup>-/-</sup> mice develop CML after a phase of selective expansion of marrow pluripotential hematopoietic progenitors characterized by increased Rap1-GTP. Overexpression of Rap1E63 caused progenitor expansion, SPA-1 opposed it.	Ishida <i>et al.</i> ( <i>Cancer Cell</i> , 2003)
<b>lung</b>	Analyzed a region of recurrent amplification on chromosome 22q11.21 in a subset of primary lung adenocarcinoma and non-small cell lung cancer (NSCLC) cells finding that it contains CRKL. CRKL activates Rap via recruitment of the effector <b>C3G</b> . Used an overexpression and knockdown approach of CRKL in NSCLC.	Overexpression of CRKL promoted anchorage independent growth and resistance to drugs against EGFR while knocking down expression of CRKL induced cell death. These data demonstrate a potential role for Rap activation in the anchorage independent growth of NSCLC.	Cheung <i>et al.</i> ( <i>Cancer Discov.</i> 2011)
	Differentially expressed genes in lung squamous cell carcinomas across 28 samples were analyzed. 10 normal bronchial tissues were used as controls. 220 upregulated genes were identified.	Rap2B was found to be upregulated in 18/28 (64.3%) of the SCCs.	Liu <i>et al.</i> ( <i>Lung Cancer</i> , 2007)
<b>lymphoma</b>	RAPL <sup>-/-</sup> mice developed lymphomas. <b>RapL</b> is a Rap effector involved in adhesion and microtubule based trafficking of vesicles.	RapL was found to regulate the localization of p27(kip1) a cyclin-dependent kinase inhibitor.	Katagiri <i>et al.</i> ( <i>Immunity</i> , 2011)
	Overexpression of <b>Rap1GAPII</b> in the A20 lymphoma cell line.	Rap activation was shown to be important for the adhesion, transendothelial migration, and invasion of lymphoma cells into distant sites once in circulation including the liver.	Lin <i>et al.</i> ( <i>Oncogene</i> , 2010)
<b>melanoma</b>	Investigated the role of the Rap1 and the Rap effector <b>RIAM</b> in the BLM melanoma cell line by overexpressing an active Rap1 form (Rap1V12), silencing Rap1A expression, or silencing RIAM.	Decreased Rap1A or RIAM expression led to decreased invasion while expressing Rap1V12 increased invasion through MatriGel towards CXCL12. RIAM is required for persistent directional migration of the cells, ERK and Akt activation in response to CXCL12, adhesion to fibronectin or type I collagen, anchorage independent growth, and metastasis <i>in vivo</i> .	Hernandez-Varas <i>et al.</i> ( <i>JBC</i> , 2011)

**Table 1.2**

	Overexpression of <b>Rap1GAPII</b> and a constitutively active form of Rap1 (Rap1V12) in murine and human melanoma cell lines.	Both the cycling and activation of Rap were shown to be important for migration on 2D matrices and through endothelial junctions as well as the colonization of the lungs once the cells were put into circulation. Invasion of the melanoma cells into 3D matrices also required Rap activation but was unaltered or enhanced with Rap1V12 expression.	Freeman <i>et al.</i> ( <i>Cancer Res.</i> , 2010)
	Investigated <b>Rap1GAP</b> expression and Rap activation in human melanoma tumors and melanoma cell lines.	Found that Rap1GAP expression is lost in human melanomas via promotor hypermethylation, that re-expressing Rap1GAP decreases melanoma proliferation, focal adhesion formation, and migration.	Zheng <i>et al.</i> ( <i>Cancer Res.</i> , 2009)
<b>pancreatic</b>	Identified an <b>EPAC</b> inhibitor, ESI-09, and added it to pancreatic cancer cell lines. EPAC is a Rap GEF.	ESI-09 inhibition of EPAC mediated Rap activation decreases the migration and invasion of AsPC-1 and PANC-1 pancreatic cancer cell lines.	Almahariq <i>et al.</i> ( <i>Mol Pharmacol.</i> , 2013)
<b>prostate</b>	Found a positive correlation of <b>SPA-1</b> , a Rap specific GAP, with progression and metastasis of tumor specimens from prostate cancer patients. Used an overexpression of SPA-1, a knockdown of SPA-1, and an overexpression of Rap1V12 in the PC3 cell line.	Determined a negative correlation between Rap activation and metastasis of prostate cancer.	Shimizu <i>et al.</i> ( <i>Cancer Sci.</i> , 2011)
	Investigated Rap activation in a number of prostate cancer cell lines (PC3-M, PC3, DU-145, LNCaP, and LNCaP-c81). Overexpressed <b>Rap1GAP</b> and knocked down Rap1A or overexpressed a constitutively active form of Rap1 (Rap163E).	Found that Rap activation was higher in more invasive prostate lines, that blocking Rap activation with Rap1GAP or Rap1A siRNA decreased migration, invasion, and integrin activation, and that Rap163E resulted in higher metastasis <i>in vivo</i> when cells were injected intracardially.	Bailey <i>et al.</i> ( <i>Cancer Res.</i> , 2009)
<b>sarcoma</b>	Investigated homozygous genomic deletions in the mouse <i>NF2<sup>+/-</sup> TP53<sup>+/-</sup></i> model which reproducibly gives rise to fibrosarcomas and osteosarcomas. Identified deletion of <b>DOCK4</b> , a Rap GEF, which is also frequently mutated in human prostate and ovarian cancer cell lines. Used wildtype and mutant DOCK4 forms in osteosarcoma cells.	DOCK4 activated Rap at adherens junctions, important for their formation. Overexpression of DOCK4 but not mutant DOCK4 in osteosarcoma lines suppressed growth in soft agar and invasion <i>in vivo</i> . Suggests Rap activation at adherens junctions limits the growth of sarcomas.	Yajnik <i>et al.</i> ( <i>Cell</i> , 2003)
<b>thyroid</b>	Analyzed 197 thyroid tumor samples for <b>Rap1GAP</b> expression, promotor methylation. Overexpressed Rap1GAP in TPC1 and Hth83 thyroid cancer cell lines.	Found the decreased expression of Rap1GAP via hypermethylation of the promotor region to occur in all malignant tumors and that expressing Rap1GAP into TPC1 and Hth83 cell lines reduced invasion and growth <i>in vitro</i> .	Zuo <i>et al.</i> ( <i>Cancer Res.</i> , 2010)
	RET/papillary thyroid carcinoma oncoproteins formed from an in-frame fusion of the RET receptor tyrosine kinase with protein dimerization motifs were shown to activate Rap1. A dominant negative form of Rap1 (Rap1N17) was expressed in these cells.	RET/PTC1 recruits Gab1, CrkII, and <b>C3G</b> to activate Rap which was involved in stimulation of the BRAF kinase and the p42/p44 mitogen-activated protein kinases. Rap1N17 opposes this signaling pathway and blocks proliferation.	De Falco <i>et al.</i> ( <i>Cancer Res.</i> , 2007)

## **1.9 Thesis aims**

**Aim 1:** To investigate signaling pathways that control BCR diffusion and signaling via the submembrane actin cytoskeleton

**Aim 2:** To investigate the role of Rap activation in BCR microcluster formation

**Aim 3:** To determine whether Rap activation and cycling are required for circulating tumor cells to metastasize to distant organ sites

## **2. TLR ligands increase the sensitivity of BCR signalling by increasing cytoskeletal dynamics and reducing BCR spatial confinement<sup>1</sup>**

### **2.1 Introduction**

Integrating signals from multiple receptors allows cells to interpret the physiological context in which a signal is received. We describe a mechanism for receptor crosstalk in which regulating the dynamics of the actin cytoskeleton lowers the threshold for signalling by other receptors. We show that Toll-like receptors (TLRs) that recognize microbial components enhance signalling by the B cell antigen receptor (BCR) by activating the actin-severing protein cofilin and thereby increasing actin dynamics. Single-particle tracking showed that this reduces the spatial confinement of the BCR within the plasma membrane and increases BCR mobility, allowing more frequent collisions between BCRs and greater signalling in response to low densities of membrane-bound antigen. These findings implicate actin dynamics as a target for tuning receptor signalling and as a key mechanism by which B cells are primed to discriminate between inert antigens and those that are accompanied by indicators of microbial infection.

Immune cells routinely integrate signals from multiple receptors. Signals from one receptor can alter the threshold for cellular responses by modulating the cell surface expression or signalling output of another receptor, or alter the nature of the cellular response by selectively modulating downstream signalling pathways. Although the spatial organization of receptors and their mobility within the plasma membrane significantly impact receptor signaling [308], it is not

---

<sup>1</sup> A version of this chapter has been submitted for publication in Jan 2014. Spencer A. Freeman Valentin Jaumouillé, Raibatak Das, Brian E. Hsu Kate Choi, Marcia L. Graves, Daniel Coombs, Calvin D. Roskelley, Sergio Grinstein, and Michael R. Gold. TLR ligands increase the sensitivity of BCR signalling by increasing cytoskeletal dynamics and reducing BCR spatial confinement.

clear whether receptor crosstalk can be mediated by such biophysical changes. Because B cell receptor (BCR) mobility within the plasma membrane is a critical determinant of BCR signalling output [60, 309], we hypothesized that other receptors that impact B cell activation modulate BCR mobility.

The differentiation of B-lymphocytes into antibody-producing cells is initiated by the antigen (Ag)-specific BCR. However, the magnitude of the antibody response and the amount of Ag required to stimulate such a response, is determined by Toll-like receptors (TLRs) and other receptors that recognize danger signals [310, 311]. TLR ligands include microbial structures such as lipopolysaccharide (LPS), peptidoglycan, and DNA containing unmethylated CpG motifs [312-314]. Ags that are associated with TLR ligands are effective immunogens whereas non-infectious, inert Ags generally elicit weak responses unless co-injected with adjuvants that contain TLR ligands.

The physical nature of the Ag determines whether B-cell intrinsic TLR signalling is required for antibody responses. For soluble Ags, TLR ligands enhance antibody responses by acting on dendritic cells [315, 316]. However, antibody responses to virus-like particles require B-cell intrinsic TLR signalling via the MyD88 adaptor protein [315, 316]. B cells can also be activated by Ag-presenting cells (APCs) such as follicular dendritic cells and subcapsular sinus macrophages, which capture Ags via Fc receptors, complement receptors, and cell surface lectins, and then display intact Ags on their surface [71, 72, 80]. Such two-dimensional arrays of membrane-bound Ags can cluster BCRs and initiate BCR signaling [71, 84]. It is not known whether TLR ligands enhance the ability of B cells to respond to membrane-associated Ags, as they do for particulate Ags.

The activation of B cells by Ags that are mobile within a two-dimensional membrane requires dynamic spatial reorganization of the BCR. Upon contact with membrane-bound Ags, BCRs coalesce into microclusters that interact with CD19 and recruit signalling enzymes such as phosphoinositide 3-kinase (PI3K), Vav, and phospholipase C- $\gamma$  [317-320]. Forming these microsignalosomes [320] increases the efficiency of BCR signalling and reduces the amount of Ag required for B cell activation [97, 318, 321]. B cell responses to membrane-associated Ags require CD19 and CD81, a tetraspanin that immobilizes CD19 in the membrane, whereas CD19 and CD81 are dispensable for responses to soluble Ags [63, 318]. Thus the spatial organization of the BCR in the membrane, and its ability to interact with other membrane proteins, are unique determinants of B cell responsiveness to membrane-associated Ags.

BCR clustering is controlled by the submembrane actin cytoskeleton [62, 309, 322]. In resting cells the BCR is kept relatively immobile by an F-actin 'picket fence' that is linked to the plasma membrane via scaffolding proteins such as ezrin [60, 62]. This limits Ag-independent BCR clustering, allowing only low-level tonic signaling [60], which is required for B cell survival [323]. Removing F-actin barriers to BCR diffusion is sufficient to induce robust BCR signaling [60, 62, 63]. Consistent with this, optimal BCR signalling in response to membrane-associated Ags requires two pathways that alter the submembrane actin cytoskeleton in a manner that allows increased BCR mobility and microcluster formation. First, BCR-induced inactivation of ezrin causes local release of the submembrane actin cytoskeleton from the membrane [62]. At the same time, activation of the Rap GTPase by the BCR promotes dephosphorylation and activation of the actin-severing protein cofilin [195]. Cofilin-mediated actin severing increases actin turnover dynamics, which promotes the formation of BCR microclusters [195, 324].

The critical role of the actin cytoskeleton in controlling BCR mobility and signalling suggests that other receptors on B cells could tune the threshold for B cell activation by regulating actin dynamics. We show here that TLR signalling primes B cells for activation by low amounts of membrane-bound Ag and that this is dependent on TLR-induced increases in actin dynamics and BCR mobility, both of which require cofilin-mediated severing of F-actin.

## 2.2 Results

### 2.2.1 TLR ligands prime B cells to respond to low densities of membrane-bound antigen

To test whether TLR ligands increase the sensitivity of B cells to membrane-associated Ags, B cells were added to APCs with different cell surface densities of a transmembrane anti-Igk light chain antibody that can bind the BCR (**Fig. 2.1a**). Within 3 min, clustering of this surrogate Ag, as well as phosphotyrosine (pTyr)-based signalling at BCR microclusters, was observed at the B cell:APC contact site (**Fig. 2.1b**), as shown previously [195]. At low densities of surrogate Ag on the APC surface, B cells that had been cultured overnight with LPS or CpG DNA exhibited significantly greater pTyr signaling at the B cell:APC contact site than resting B cells, i.e. naïve *ex vivo* B cells or B cells that had been cultured with the survival cytokine B-cell activating factor (BAFF) (**Fig. 2.1b,c**). In contrast, at high surrogate Ag density, similar levels of pTyr signalling were observed in resting and TLR-activated B cells (**Fig. 2.1c**). Thus TLR priming enhances B cell responses to membrane-bound Ags that are present at low density on an APC surface but is not necessary at high Ag density.

The ability of B cells to gather membrane-bound Ags and initiate microcluster-based BCR signalling depends on both the BCR and the Ag being mobile within the cell membranes. Indeed, fixing APCs with paraformaldehyde prior to adding the B cells attenuated BCR

signalling (**Fig. 2.1c**). Immobilizing the surrogate Ag in this manner also ablated the enhancing effect of TLR priming (**Fig. 2.1c**), suggesting that TLR ligands increase the sensitivity of BCR signalling by regulating BCR mobility within the membrane.

### **2.2.2 TLR signalling reduces BCR confinement and increases BCR diffusion**

Single-particle tracking (SPT) was used to assess the mobility of the BCR within the plasma membrane prior to Ag encounter, as done by Treanor *et al.* [60] and Tolar *et al.* [58]. To visualize individual BCRs, B cells were labeled on ice with a limiting amount (1 ng/ml) of monovalent biotin-conjugated anti-IgM Fab fragments, followed by streptavidin-655 nm Quantum dots (Qdots). Excess biotin was added to prevent BCR crosslinking. The cells were then adhered to non-stimulatory anti-MHCII-coated coverslips [60, 63] and warmed to 37°C before imaging the ventral surface of the cells in real time. The cells did not mount a response to the anti-MHCII antibodies (**Fig. 2.9a**) and we confirmed that this protocol labeled single BCRs and that the labeled mIgM remained on the cell surface during imaging (**Fig. 2.9b,c**). Data from video recordings were analyzed using particle-tracking algorithms [325] to reconstruct the trajectories of individual membrane IgM (mIgM) molecules.

Culturing B cells with LPS or CpG DNA enhanced the mobility of mIgM-containing BCRs, as compared to *ex vivo* B cells or B cells cultured with BAFF. Plotting the ‘instantaneous velocity’ (i.e. single-state analysis) for individual BCRs by determining the diffusion coefficients (D) for the first 5 frames of trajectory recordings (~ 150 ms) showed that BAFF-cultured B cells had both slow-moving ( $D < 10^{-2} \mu\text{m}^2/\text{s}$ ) and fast-moving ( $D > 10^{-2} \mu\text{m}^2/\text{s}$ ) BCR populations (**Fig. 2.2a**). LPS treatment increased the ratio of fast- to slow-moving BCRs. We then analyzed trajectories using an algorithm that employs a two-state hidden Markov model to divide

individual trajectories into slow- and fast-moving segments [326]. This showed that LPS treatment increased the diffusion coefficients for both the slow and fast segments of individual BCR tracks, increased the frequency of transitions from the slow to the fast state by more than 2-fold, and slightly decreased the frequency of fast-to-slow transitions (**Fig. 2.2b,c**).

The ability of BCRs to encounter Ags on the surface of an APC is limited by the area that individual BCRs can scan (i.e. mean square displacement [MSD]). Although the MSD is dependent on the receptor's diffusion coefficient, it is strongly impacted by whether the movement of the receptor is free, confined, or directed [327]. Therefore we used particle-tracking algorithms that employ moment scaling spectrum (MSS) analyses [328, 329] to determine both the MSD and the spatial confinement properties of BCR trajectories. This allowed us to classify individual BCR trajectories as free or confined (<5% exhibited directed motion), after which diffusion coefficients and confinement region diameters could be calculated, as described by Jaqaman *et al.* [330].

More than 75% of the BCRs on *ex vivo* and BAFF-cultured B cells exhibited confined trajectories (**Fig. 2.3a,b** and **Supplementary Video 1**) with median confinement diameters of 120-160 nm (**Fig. 2.3c, Fig. 2.10a**, and **Supplementary Table 1**) and diffusion coefficients that were much lower than for those freely-diffusing BCRs on the same cells (**Fig. 2.3d**). Thus confined BCRs are restricted to spatially limited zones and also move more slowly within those zones than free receptors. Culturing B cells overnight with TLR ligands enhanced BCR mobility in three distinct ways: it increased the fraction of freely diffusing BCRs by ~2-fold (**Fig. 2.3a,b,e,f,g** and **Supplementary Videos 1-3**), it caused a 2-fold increase in the median diameter of the confinement area for BCRs exhibiting confined motion (**Fig. 2.3c,h, Fig. 2.10a**, and **Supplementary Table 2.1**), and it increased the diffusion coefficients for both the confined and

free receptors (**Fig. 2.3d**). The combined result of these changes was that BCRs on TLR-activated cells had much greater mobility than those on resting B cells, as reflected by increased MSD (**Fig. 2.3a,f** and **Supplementary Videos 1-3**). This increase in BCR mobility required at least a 3- 6-hour exposure to TLR ligands (**Fig. 2.3f-h**). Culturing B cells with LPS for 10-30 min had no effect on BCR mobility (data not shown).

### **2.2.3 BCR confinement and diffusion are controlled by the actin cytoskeleton**

The actin cytoskeleton limits BCR mobility, as determined by measuring diffusion coefficients [60]. Our MSS analyses provided additional information, showing that partially disrupting the actin cytoskeleton by treating resting B cells with latrunculin B for 3 min caused a ~2-fold increase in the fraction of BCRs exhibiting free diffusion, such that it was similar to that in LPS-treated cells, and caused a 2-fold increase in the confinement diameter for BCRs that remained confined (**Fig. 2.4a,b**, **Supplementary Video 4**, and **Supplementary Table 1**). Latrunculin treatment also increased the median diffusion coefficients for both confined and free BCRs (**Fig. 2.4c**), indicating that the actin cytoskeleton limits BCR mobility not only by creating relatively stable barriers that confine receptors but also by controlling local diffusion rates, even in regions of the membrane in which receptors are not confined, as defined by the MSS algorithm [330]. This was true even in LPS-activated cells, where latrunculin caused further increases in the diffusion coefficients (**Fig. 2.4c** and **Supplementary Video 5**).

### **2.2.4 TLR signalling increases actin cytoskeleton dynamics and activates cofilin**

Because TLR signalling had similar effects as latrunculin in terms of reducing BCR confinement and increasing diffusion coefficients for both confined and free BCRs (**Figs. 2.3** and

**2.4**), we investigated the effects of TLR signaling on cytoskeleton dynamics. Increased turnover dynamics of the submembrane actin cytoskeleton could reduce the lifetime and local density of actin-dependent barriers that limit the diffusion of proteins within the membrane, mimicking the effects of latrunculin. We found that culturing B cells with LPS or CpG DNA caused marked reorganization of the actin cytoskeleton characterized by the formation of F-actin-rich membrane ruffles (**Fig. 2.5a**). Although TLR signalling did not alter the ratio of F-actin to G-actin monomers (**Fig. 2.5b**), TLR-activated B cells had greater actin-polymerizing activity than resting B cells. This was shown by disassembling pre-existing F-actin polymers in cell extracts by sonication and then measuring the *de novo in vitro* polymerization of actin into insoluble filaments (**Fig. 2.5c**). Similarly, when fluorescent actin monomers were added to semi-permeabilized cells, more actin was incorporated into filaments in TLR-activated B cells than in resting B cells (**Fig. 2.5d**). TLR-activated B cells also had increased F-actin severing activity compared to resting B cells, as assessed by the ability of cell extracts to cleave fluorescent F-actin filaments *in vitro* (**Fig. 2.5e,f**). The LPS- and CpG DNA-induced increase in actin-severing activity was dependent on TLR signalling because it did not occur in B cells from mice lacking the MyD88 adaptor protein (**Fig. 2.5f**), which links TLRs to downstream signalling pathways [331]. Thus TLR signalling increases both actin-polymerizing and actin-severing activities in B cells, suggesting that the F-actin networks in TLR-primed B cells are more dynamic, and hence more transient.

TLR signalling activates a number of enzymes that regulate the actin cytoskeleton. These include the Rap1, Rac, and RhoA GTPases, as well as the Syk tyrosine kinase and PI3K, both of which contribute to the activation of these GTPases. We found that Syk activity was essential for BCR mobility as the Syk inhibitor, piceatannol, greatly decreased BCR diffusion in both resting

and TLR activated B cells (**Fig. 2.10b**, **Fig. 2.11a**, **Supplementary Video 6**, and **Supplementary Table 2.1**). As well, PI3K activity was important for TLR signalling to enhance BCR mobility. Treating LPS-activated B cells with the pan-PI3K inhibitor LY294002 significantly reduced the percent of freely diffusing BCRs as well as the median confinement diameter for confined BCRs (**Fig. 2.11b** and **Supplementary Table 2.1**). The level of active GTP-bound Rac, which promotes actin polymerization and reorganization via WAVE proteins [332], was slightly elevated in LPS-treated cells compared to BAFF-cultured cells (data not shown). Conversely, RhoA activation, which stabilizes actin filaments, promotes formin-dependent actin polymerization, and actomyosin-based contractility [332] was slightly decreased (data not shown). In contrast to these modest effects on Rac and RhoA, culturing B cells with LPS or CpG DNA dramatically increased the levels of activated Rap1 (**Fig. 2.5g**). We have previously shown that activated Rap1 controls actin dynamics and reorganization in B cells [95, 195], in part by regulating the activity of cofilin [195], which is the major actin-severing protein in LPS-activated B cells [195].

Actin-severing proteins such as cofilin and Cordon-Bleu can ‘dynamize’ the cytoskeleton by linking actin severing to actin polymerization, thereby increasing the net turnover of actin networks [164]. Cofilin increases actin dynamics by severing existing filaments, increasing the pool of free G-actin available for actin polymerization, and generating new barbed ends where the Arp2/3 complex can nucleate the formation of branched actin filaments [333]. Because TLR ligands increased both actin-severing activity and actin polymerization in B cells (**Fig. 2.5a-f**), and activated Rap1 (**Fig. 2.5g**), we asked if cofilin activity was increased by TLR signalling. The ability of cofilin to bind actin filaments and initiate severing is dependent on dephosphorylation of serine 3 (S3) [334]. Culturing B cells with LPS or CpG DNA resulted in substantial

dephosphorylation of cofilin on S3, which was dependent on MyD88 (**Fig. 2.5h**). The TLR-induced increase in active (i.e. dephosphorylated) cofilin correlated with the increased F-actin severing and polymerization (**Fig. 2.5c-f**). TLR-induced cofilin dephosphorylation required at least a 2-3 h exposure to LPS or CpG DNA and was not evident at earlier time points (data not shown). This parallels the kinetics of the TLR-induced increase in BCR mobility (**Fig. 2.3f-h**). Together, these data suggest that TLR-induced activation of cofilin dynamizes the B-cell cytoskeleton, which may underlie TLR effects on BCR mobility.

### **2.2.5 TLR enhancement of BCR mobility is dependent on actin severing**

To test whether TLR-induced increases in BCR mobility are dependent on F-actin severing, we used a combination of two cell-permeable peptides (M, W), each consisting of one of the two F-actin-binding regions of cofilin that was coupled to penetratin. These peptides block the binding of cofilin to F-actin in T cells [335] and we found that they blocked the *in vitro* severing of F-actin filaments by extracts of LPS-stimulated B cells (**Fig. 2.12**). Moreover, treating LPS-activated B cells with the M/W peptides resulted in the elimination of membrane ruffles and a more homogeneous cortical F-actin density (**Fig. 2.6a**), suggesting that they decreased actin dynamics. The control Q peptide in which key residues required for actin binding were mutated [335] had no effect on the morphology or actin organization of LPS-activated B cells (**Fig. 2.6a**). Treating LPS-activated B cells with the M/W cofilin-blocking peptides reduced the percent of freely diffusing BCRs, decreased the median diffusion coefficients for both confined and free BCRs, and decreased BCR confinement diameters to approximately the levels seen in BAFF-cultured cells (**Fig. 2.6b-d**, **Fig. 2.10c**, **Supplementary Table 2.1**, and **Supplementary Video 7**). This suggests that increasing F-actin severing is a primary mechanism

by which TLR signalling reduces BCR confinement and enhances BCR mobility. In contrast, the cofilin-blocking peptides had very little effect on BCR mobility in BAFF-cultured B cells (**Fig. 2.6b-d**), perhaps because the submembrane actin cytoskeleton is already very stable in these cells.

If TLR signalling enhances BCR mobility by promoting F-actin severing and decreasing the density of the submembrane actin cytoskeleton, then inhibiting cofilin and increasing the density of cortical F-actin should oppose TLR effects on BCR mobility. To test this, we treated TLR-activated B cells with a cell-permeable peptide that activates RhoA [336, 337]. Activated RhoA binds to and increases the catalytic activity of LIM domain kinase, which phosphorylates and inactivates cofilin [338]. Indeed, treating TLR-activated B cells with the RhoA activator mimicked the effects the cofilin-blocking peptides, suppressing membrane ruffling, increasing the density of cortical F-actin, and decreasing actin polymerization at new barbed ends (**Fig. 2.6e-g**). Importantly, the RhoA activator increased the confinement of the BCR (**Fig. 2.6h**, **Fig. 1.10b**, **Supplementary Table 2.1**, and **Supplementary Video 8**), similar to what was observed when the cofilin-blocking peptides were used to prevent F-actin severing. Taken together, our findings indicate that the ability of TLR signalling to reduce BCR confinement and increase BCR mobility is dependent on actin severing that is controlled by cofilin.

### **2.2.6 TLR engagement increases BCR-BCR collisions and tonic BCR signalling**

Tonic Ag-independent BCR signalling, which is required for B cell survival *in vivo* [323, 339], may be due to random BCR-BCR collisions and the interaction of BCR nanoclusters with CD19 [63, 340]. Such physical interactions are limited by the actin cytoskeleton [63, 340]. The rapid increase in actin turnover that occurs in response to Ag binding [61] may be a ‘tipping

point' that increases the frequency of such collisions, leading to greatly amplified BCR signalling that promotes B cell activation [340, 341]. Similarly, the enhanced actin dynamics and BCR mobility in TLR-activated B cells could increase BCR-BCR collisions and Ag-independent BCR signalling. To test this, we analyzed SPT data using merge-split detection algorithms [330] in order to quantify BCR-BCR collisions, which were defined as pairs of BCR trajectories that coalesced and then separated again. We found that the probability of BCR collisions increased ~3-fold when B cells were cultured overnight with LPS instead of BAFF (**Fig. 2.7a,b**). This is likely due, at least in part, to the TLR-induced increase in freely diffusing BCRs (**Fig. 2.4b**), which had a greater probability of undergoing merge-split events than confined BCRs (**Fig. 2.7c**).

The increased frequency of BCR collisions in TLR-activated B cells correlated with increased Ag-independent BCR signalling, as illustrated by the increased levels of phospho-ERK and phospho-Akt compared to resting B cells (**Fig. 2.7d** and **Fig. 2.13**; compare DMSO samples). The TLR-induced increase in tonic BCR signalling could be recapitulated by treating BAFF-cultured cells with latrunculin A (**Fig. 2.7d** and **Fig. 2.13**), indicating that F-actin barriers that limit BCR diffusion also limit tonic BCR signalling. As was the case for BCR mobility (**Fig. 2.4d**), latrunculin caused a further increase in the Ag-independent BCR signalling in TLR-activated cells (**Fig. 2.13**), likely because TLR signalling does not completely disrupt the cytoskeleton. Nevertheless, these findings indicate that the increased actin dynamics and BCR mobility caused by TLR ligands results in increased Ag-independent BCR signalling.

### **2.2.7 TLR enhancement of antigen-induced BCR signalling depends on actin dynamics**

In addition to increasing tonic BCR signalling (**Fig. 2.7d**), TLR ligands increased BCR signalling in response to low densities of APC-associated Ag (**Fig. 2.1c**). This enhanced response to membrane-bound Ags was also dependent on actin severing. Treating TLR-activated B cells with the cofilin-blocking peptides, to prevent F-actin severing, or with the RhoA activator, to increase the cortical F-actin density, significantly reduced microcluster-associated pTyr signalling (**Fig. 2.8a,b**). This suggests that the removal of cytoskeletal barriers, and the resulting increase in BCR mobility, is critical for TLR signalling to prime B cells to respond to membrane-bound Ags.

Because BCR signalling also promotes cofilin dephosphorylation and actin turnover [195], this raised the possibility of synergy between TLR-mediated priming of B cells by microbial danger signals and acute Ag-induced BCR signalling. Indeed, immunoblotting for phospho-cofilin showed that TLR ligands increased the basal level of active, dephosphorylated cofilin and also increased the ability of BCR signalling to cause further cofilin dephosphorylation (**Fig. 2.8c**).

### **2.2.8 Naturally primed B cell populations have an elevated level of active cofilin**

To assess whether modulation of cofilin activity is a general mechanism for tuning B cell responses to Ag, we separated murine splenic B cells into follicular (FO) and marginal zone (MZ) B cells. MZ B cells express high levels of TLRs and mount rapid antibody responses to microbial Ags when activated via the combination of BCR and TLR signaling [342, 343]. MZ B cells resemble TLR-activated FO B cells in that they have greater Ag presentation abilities than FO B cells, as well as higher expression of activation T-cell co-stimulatory molecules [342, 343].

When plated on immobilized anti-Ig antibodies, MZ B cells spread to a greater extent than FO B cells, suggesting that they have a more dynamic cytoskeleton (data not shown). Consistent with this, when MZ B cells were added to APCs expressing the surrogate Ag, they gathered more Ag into microclusters than FO B cells (**Fig. 2.8d**). This correlated with lower levels of phosphocofilin in MZ B cells (**Fig. 2.8e**). This increased cofilin activation in MZ B cells, compared to FO B cells, likely results in greater actin dynamics and this may account for the increased ability of MZ B cells to gather Ag into microclusters.

### **2.3 Discussion**

The response to membrane-bound or particulate Ags by B cells requires the release of BCRs and CD19 from confinement zones that are structured by submembrane F-actin networks and tetraspanins [60, 62, 63]. We report here that TLR signaling lowers the threshold for this response by dynamizing the actin cytoskeleton via cofilin activation such that BCR confinement is reduced and the diffusion of both free and confined receptors is increased. Free BCRs were more likely to encounter each other in the plasma membrane, and the TLR-induced increase in the fraction of free BCRs correlated with increased tonic BCR signaling. The TLR-induced changes in BCR mobility represents a paradigm for receptor crosstalk in which microbial danger signals detected by germline-encoded PRRs provide contextual information that lowers the threshold for signaling by clonally restricted Ag receptors (Figure 8A).

Although we classified BCR trajectories as being either confined or free, membrane protein diffusion is the product of numerous dynamic interactions between the receptor and its membrane environment [118]. For example, in the resting state, transmembrane ‘pickets’ can bind and unbind actin filaments that act as ‘fences’ and limit receptor diffusion [326, 344]. Like

other membrane proteins, the BCR may switch between confined and free states, where the dynamic of actin filaments (i.e. the opening and closing of corrals) may contribute to the rates at which switching occurs. Indeed, in resting B cells where F-actin was less dynamic, BCRs exhibited more frequent switching to a slow-moving state and less frequent switching to a fast-moving state; the reverse was true in TLR-activated cells in which the F-actin network was more dynamic (Figure 8b,c). Increasing the density of the submembrane F-actin network by treating cells with the RhoA activator made the state-switching behavior in LPS-activated cells resemble those of resting B cells, supporting the idea that TLR signaling enhances BCR mobility by dynamizing the actin cytoskeleton. The dynamics of transmembrane protein diffusion is certainly more complex than what can be described by this two-state model, as evidenced by the differences in the diffusion of free BCRs and free CD45 within the same membrane. Nevertheless, our data support the idea that the F-actin network is the major regulator of membrane protein diffusion [118].

The inter-relationship between F-actin dynamics, BCR mobility, and tonic BCR signaling may allow B cells to respond to their environment by increasing the level of tonic BCR signaling such that the cell achieves a “primed” state in which less Ag is required for its activation than for resting B cells. Such a primed state may be recapitulated *in vivo* in MZ B cells, which are specialized for making rapid responses to blood-borne microbial Ags. The positive feedback loop in which tonic BCR signaling enhances actin dynamics and leads to increased BCR diffusion, which promotes BCR-BCR collisions and further tonic BCR signaling, is illustrated by the observation that, deleting downstream effectors of BCR signaling such as PLC $\gamma$ 2 or Vav1/2 reduces the diffusion coefficient of the BCR in resting B cells [60]. Similarly, we found that the Syk inhibitor, piceatannol, caused significant alteration in F-actin in both resting and LPS-

activated B cells (data not shown), and that this resulted in greatly decreased BCR diffusion in both the resting and activated cells (Supplementary Fig. S3c and Fig. S8; Supplementary Video S8). At the same time, we show in this report that signaling by receptors that dynamize the actin cytoskeleton increases both BCR mobility and tonic BCR signaling, which in turn may further increase BCR mobility. This increased BCR mobility and tonic BCR signaling may have two important effects. First, when B cells attach to Ag-bearing APCs, greater BCR mobility may increase the probability of BCRs encountering Ag at the B cell:APC interface. This may be especially important when the membrane-bound Ag is present at low density. Increased actin dynamics and the resulting removal of barriers to BCR diffusion also favors the formation of BCR microclusters and their interaction with CD19 to initiate signaling. At the same time, the increased levels of tonic BCR signaling may reduce the amount of Ag-induced BCR signaling required for B cells to exceed the threshold for activation. In this way, a variety of receptors that target the cytoskeleton may tune the threshold for B cell activation. It will be interesting to determine whether cytokines and chemokines that regulate B cell function modulate B cell activation thresholds via the cytoskeleton, as is the case for TLRs. A related question is whether the ability of TLR ligands to stimulate Ag-independent BCR signaling is required for their action as polyclonal B cell activators. TLR ligands have been shown to activate both Lyn and Syk in B cells [345] but it is not known whether this is dependent on the BCR. More generally, it will be important to assess whether receptor crosstalk via the cytoskeleton is a general process that occurs in many cell types. As well, given the positive feedback loop between actin dynamics and BCR signaling, it will be interesting to identify proteins that normally limit this process such that it does not result in spontaneous B cells activation.

Several lines of evidence suggest that dysregulation of the submembrane cytoskeleton and/or TLR signaling, which we showed dynamizes the B cell cytoskeleton, may be key factors in autoimmune diseases or the development of B-cell lymphomas. Patients with loss-of-function mutations in the actin nucleation-promoting factor WASp frequently develop autoimmunity and autoantibodies early in life [346, 347], as do mice in which only the B cell compartment lacks WASp [348]. Moreover, in a number of mouse models with autoimmune disease, genetic ablation of TLRs or proximal TLR signaling components such as MyD88 significantly blunt the production of autoantibodies [113]. Finally, activating mutations in MyD88, which cause it to constitutively associate with TLRs and initiate TLR signaling, are frequently observed in a subset of diffuse large B cell lymphomas with chronic BCR signaling [349, 350]. The potential role of cytoskeletal dynamics in these disease processes suggests that cytoskeletal regulators could be therapeutic targets.

Although membrane associated F-actin can limit receptor diffusion by an order of magnitude or more [351], how the architecture of the submembrane cytoskeleton is regulated is not fully understood. In this report we show that both cofilin and RhoA act as central regulators of this network of F-actin and receptor diffusion. Rather than simply altering the amount of G- or F-actin in cells, we propose that signaling by receptors such as TLRs can increase cytoskeletal dynamics by activating actin-severing proteins, leading to the opening of actin corrals (i.e. fences) which limit receptor diffusion. Such actin severing causes the concomitant actin nucleation, leading to branched actin networks. The interaction of these highly branched F-actin networks with transmembrane proteins that form pickets or with proteins such as ezrin, which couple transmembrane proteins to the actin cytoskeleton, may be quite different than that exhibited by more linear/contractile submembrane F-actin networks present in resting cells. We

found that TLR signaling increased the mobility of confined populations of CD45, which are presumably tethered to actin filaments in resting cells. The increased mobility of this ‘picket’ may be due to disruption of its interactions with actin via the spectrin and ankyrin scaffolding proteins. It will be interesting to assess whether increasing the mobility of a highly abundant picket contributes to the increased mobility of other membrane proteins. Regardless, we found that the increase in free CD45 correlated with greater kinetic segregation of CD45 from BCR signaling microclusters when B cells bound to APCs, suggesting that reduced confinement of transmembrane proteins may allow for more rapid reorganization of surface proteins. This kinetic segregation of transmembrane proteins with large extracellular domains such as CD45 and CD148 [92, 352, 353] may be particularly important for B cells to make close contacts with APCs in order to scan for Ags on the APC surface.

The interplay of cytoskeletal dynamics, receptor mobility, and signaling thresholds likely plays an important role in many biological processes. In particular, the dynamics of the submembrane actin cytoskeleton may be an important mechanism by which cells integrate signals from many diverse receptors that sense the extracellular environment. Such mechanisms can regulate both the signaling output from individual receptors and determine the amount of ligand-induced signaling required for cell activation. A variety of pathological situations could arise from alterations that allow tonic signaling by unliganded receptors to exceed the threshold for cell activation, resulting in inappropriate cell activation or proliferation including lymphoma and autoimmunity.

## 2.4 Figures

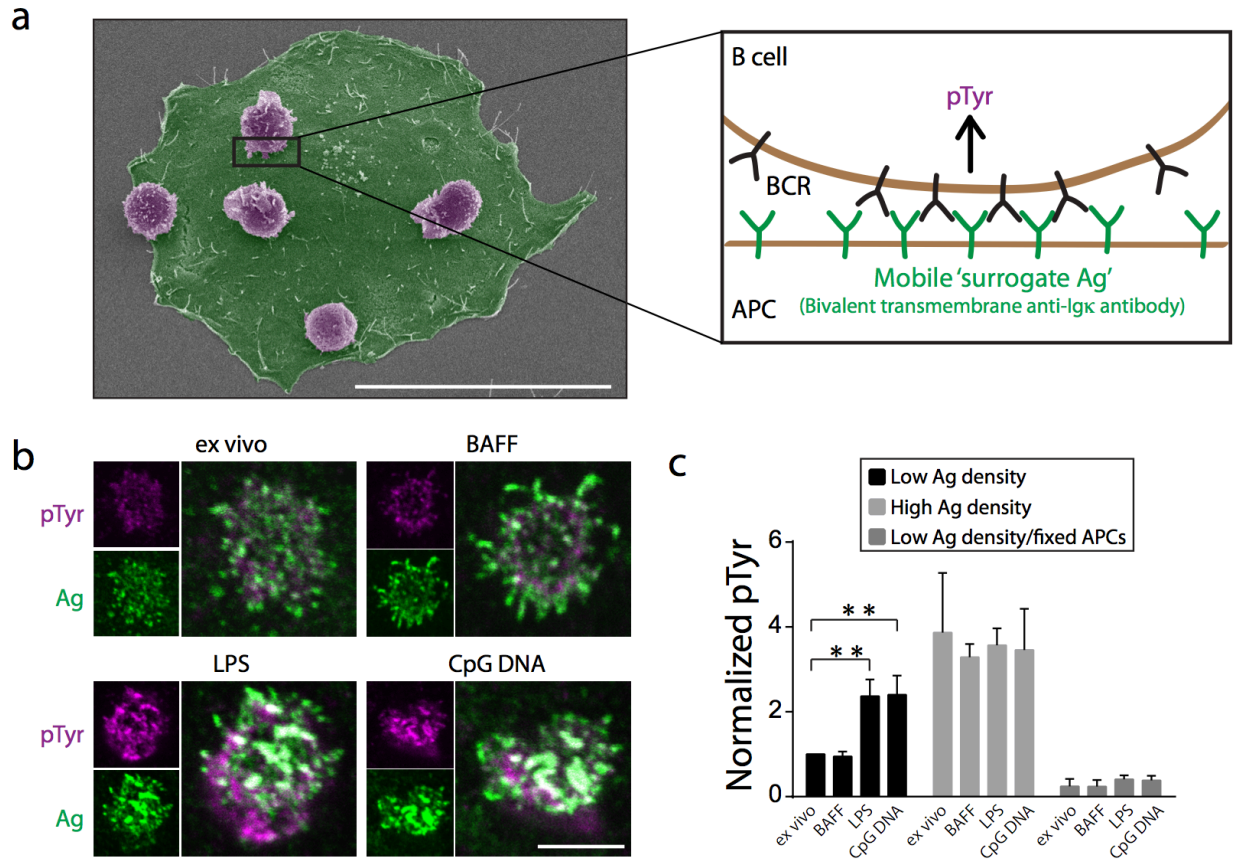


**Figure 2.1** TLR priming increases the sensitivity of B cells to membrane-bound Ags. **(a)** Model for B cell:APC interactions. The APCs are adherent cells expressing a transmembrane form of a rat anti-mouse Igk light chain antibody. This ‘surrogate Ag’ is mobile with the plasma membrane of the APC and can bind to the BCR on the B cells. The pseudocolored scanning EM image shows murine B cells (purple) that were allowed to attach to an APC (green) for 3 min. Scale bar, 50 μm. **(b)** Confocal images of the contact site between B cells and APCs expressing low amounts of surrogate Ag on their surface. *Ex vivo* B cells, as well as B cells that had been cultured for 16 h with 5 ng/ml BAFF, BAFF + 5 μg/ml LPS, or BAFF + 0.5 μg/ml CpG DNA were allowed to adhere to the APCs for 3 min and then stained for pTyr and for the surrogate Ag,

which was visualized with an anti-rat Ig Ab. At the settings used, only clustered surrogate Ag can be detected. Scale bar, 5  $\mu\text{m}$ . (c) Total pTyr intensity at the B cell:APC contact site was quantified from images similar to those in **b** after B cells were allowed to adhere to live or paraformaldehyde-fixed APCs for 3 min. The density of the surrogate Ag on individual APCs was classified as high or low by quantifying the Alexa488 anti-rat Ig fluorescence on areas of the APC that were not in contact with B cells; this required increasing the gain for that channel. Mean  $\pm$  s.e.m. for 3 experiments (n > 30 B cells per point in each experiment). pTyr signals were normalized to those in *ex vivo* B cells that had bound to live APCs expressing a low density of surrogate Ag.  $^{***}P < 0.01$ . Note that culturing B cells with LPS or CpG DNA for 16-24 h did not increase the levels of the BCR or CD19 on the cell surface (data not shown).

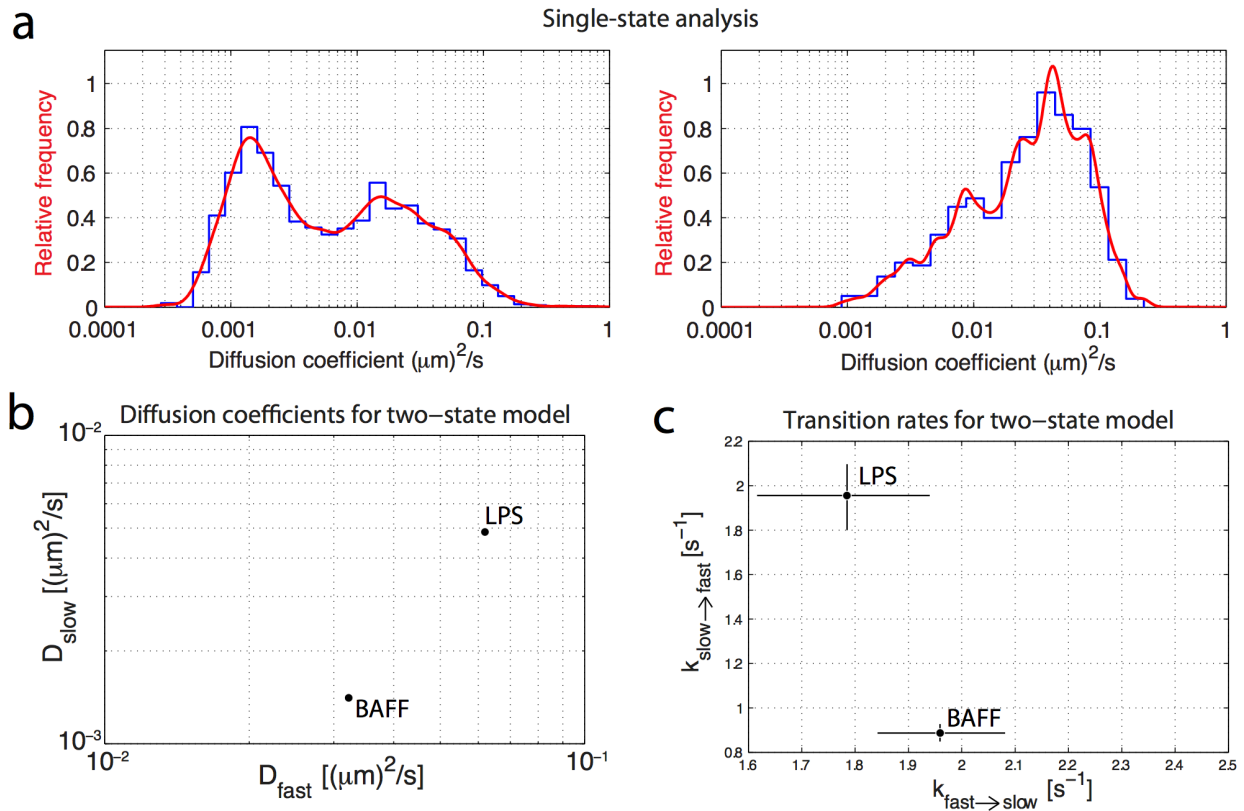


**Figure 2.2.** Single-state and two-state analysis of BCR mobility. B cells that were cultured overnight with 5 ng/ml BAFF or BAFF + 5  $\mu\text{g}/\text{ml}$  LPS were labeled with biotinylated anti-IgM Fab fragments plus streptavidin-655 nm Qdots. Trajectories of individual mIgM-containing BCRs were generated from live-imaging videos taken at 33 frames/s for 20 s (see **Supplementary Videos 1 and 2**). SPT analysis for individual mIgM-containing BCRs was performed. **(a)** For each BCR track, the diffusion coefficient ( $D$ ) was calculated for the first 5 frames of the trajectory. The distribution of diffusion coefficients from  $>15$  videos from one experiment is shown. **(b,c)** Individual BCR trajectories were divided into slow and fast segments using an algorithm that employs a two-state hidden Markov model[326]. The mean diffusion coefficients for the slow and fast states **(b)**, as well as the frequency of slow-to-fast transitions

and fast-to-slow transitions (mean + s.d.) (c), are plotted for B cells that were cultured overnight with either BAFF or BAFF + LPS. For each condition, >500 BCR trajectories were analyzed.

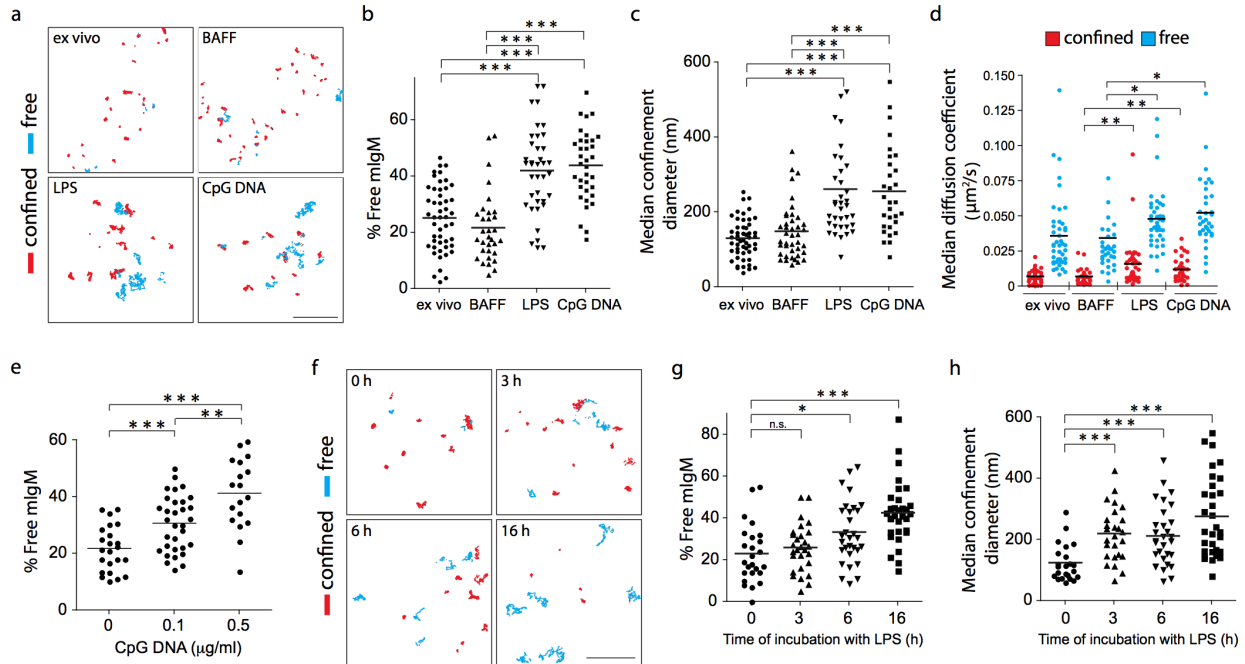


**Figure 2.3.** TLR ligands decrease BCR confinement and increase BCR mobility. (a-d) *Ex vivo* B cells or B cells that were cultured overnight with 5 ng/ml BAFF, BAFF + 5  $\mu\text{g/ml}$  LPS, or BAFF + 0.5  $\mu\text{g/ml}$  CpG DNA were labeled with biotinylated anti-IgM Fab fragments plus streptavidin-655 nm Qdots. Trajectories of individual mIgM-containing BCRs (a) were generated from live-imaging videos taken at 33 frames/s for 20 s (see **Supplementary Videos 1-3**). Scale bar, 5  $\mu\text{m}$ . Red, confined trajectories; cyan, free/unconfined trajectories, as determined by MSS analyses. Linear and undetermined trajectories (< 5% of total) are not shown. The percent of mIgM molecules that exhibited free diffusion, as opposed to confined diffusion is shown (b), along with median confinement diameters for the confined mIgM BCRs (c), and median diffusion coefficients for both confined and free mIgM BCRs (d). Each dot represents

the percent of freely diffusing BCRs (**b**) or the median values for all of the trajectories (**c,d**) in a single video. The horizontal bars represent the mean values for > 30 videos per condition; >1500 trajectories per condition were analyzed. Similar results were obtained when BCRs were directly labelled with Cy3-conjugated anti-IgM Fab fragments and imaged by total internal reflection microscopy (TIRF) (see **Supplementary Fig. 1.7**), confirming that only BCRs on the cell surface were tracked and that the observed diffusion properties were not dependent on the labelling method. (**e**) Percent of mIgM molecules that exhibited free diffusion in B cells that were cultured for 16 h with BAFF plus the indicated concentration of CpG DNA. (**f-h**) B cells were cultured overnight in BAFF, with 5  $\mu\text{g/ml}$  LPS added for the indicated lengths of time. Trajectories were generated from videos taken at 33 frames/s for 10 s. Scale bar, 3  $\mu\text{m}$ . Each dot is from one video;  $n > 20$  videos per condition; >500 trajectories per condition were analyzed. The percent of freely diffusing mIgM molecules (**g**) and the median confinement diameter for confined mIgM BCRs (**h**) are shown. \*\*\* $P < 0.001$ ; \*\* $P < 0.01$ ; \* $P < 0.05$ ; n.s., not significant.

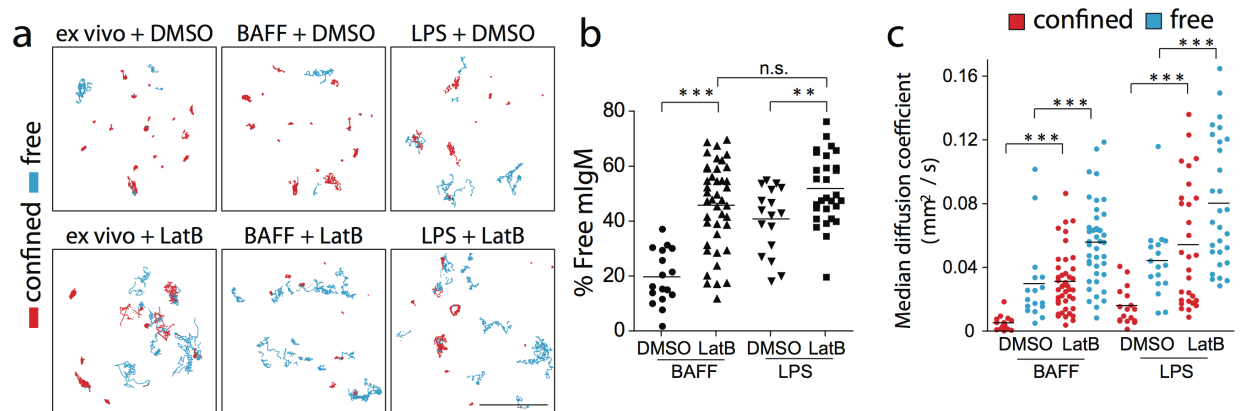


**Figure 2.4.** BCR confinement and diffusion are controlled by the actin cytoskeleton. *Ex vivo* B cells, as well as B cells that had been cultured overnight with either BAFF or BAFF + 5  $\mu\text{g/ml}$

LPS, were treated with DMSO or 1  $\mu$ M latrunculin B (LatB) for 3 min before performing SPT as in **Fig. 1.3**. **(a)** BCR trajectories were generated from videos taken at 33 frames/s for 10 s (see **Supplementary Videos 4-5**). Scale bar, 5  $\mu$ m. Red, confined trajectories; cyan, free/unconfined trajectories. **(b,c)** The percent of mIgM molecules that exhibited ‘free’ diffusion, as opposed to ‘confined’ diffusion is shown **(b)**, along with the median diffusion coefficients for both confined and free mIgM-containing BCRs **(c)**. Horizontal bars represent the mean values for > 15 videos per condition; >300 trajectories per condition were analyzed. \*\*\* $P < 0.001$ , n.s., not significant.

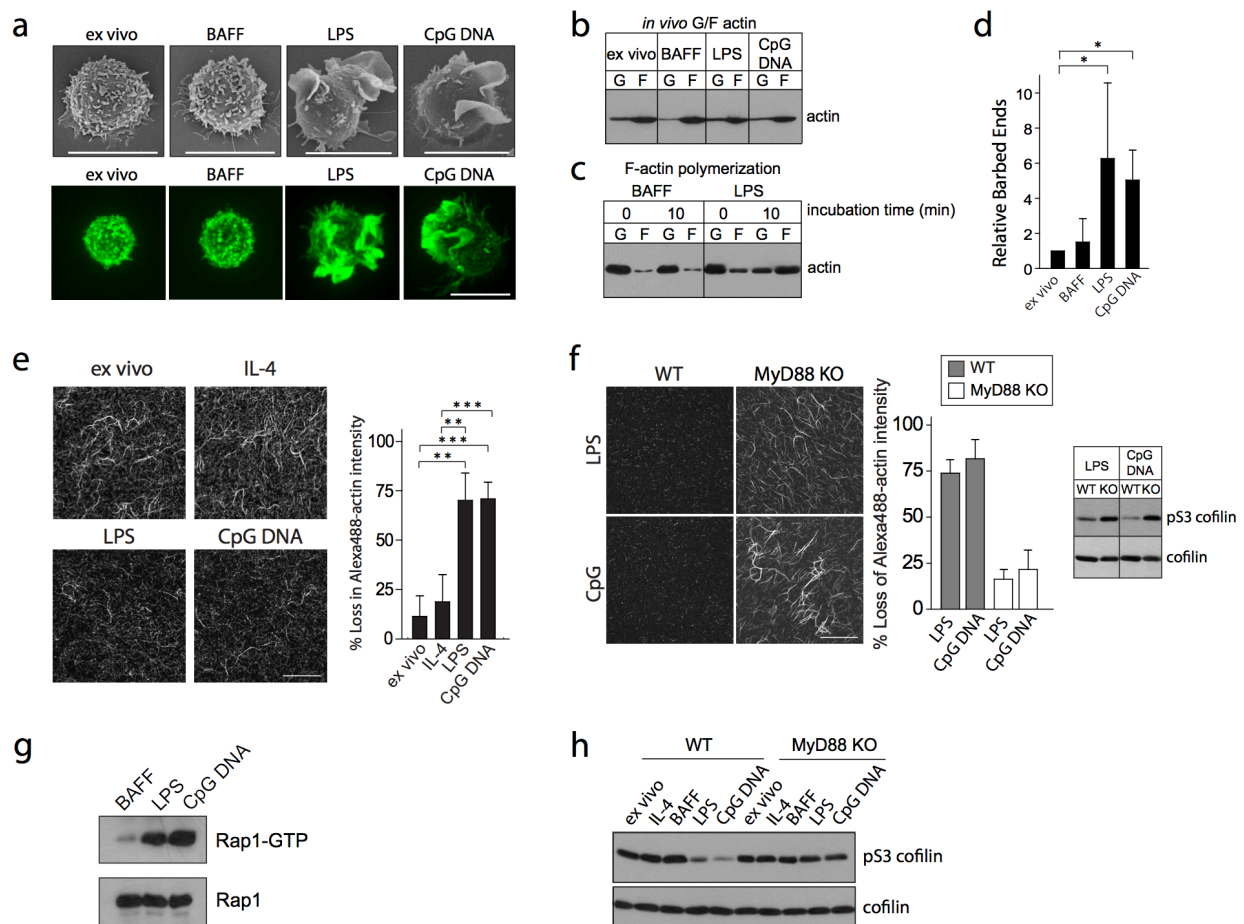


**Figure 2.5.** TLR signalling enhances actin dynamics and activates cofilin. B cells were analyzed *ex vivo* or after being cultured overnight with survival cytokines (BAFF or IL-4) alone or with

survival cytokines plus 5  $\mu\text{g/ml}$  LPS or 0.5  $\mu\text{g/ml}$  CpG DNA. **(a)** Cells were imaged by scanning EM (top; scale bar = 10  $\mu\text{m}$ ) or stained with Alexa488-phalloidin and imaged by confocal microscopy (bottom; scale bar = 5  $\mu\text{m}$ ). Z-projections of confocal images are shown. **(b)** Cells were solubilized and then separated into soluble and insoluble fractions containing G- and F-actin, respectively, before blotting for actin. **(c)** Cell extracts were sonicated to destroy pre-existing actin filaments and, where indicated, incubated for 10 min to allow *de novo in vitro* actin polymerization. Soluble and insoluble fractions containing G- and F-actin, respectively, were probed for actin. For **b** and **c**, representative blots from 3 experiments are shown. **(d)** Cells were rendered semi-permeable in the presence of Alexa488-actin for 10 s in order to measure actin polymerization at barbed ends of existing filaments. After staining for total F-actin, the Alexa488-actin/F-actin ratio was determined for >30 cells per condition and normalized to *ex vivo* cells. Mean  $\pm$  s.e.m for 3 experiments is shown.  $*P < 0.05$ . **(e,f)** Actin filaments containing Alexa488-actin and biotinylated actin monomers were adhered to slides coated with anti-biotin antibodies and then incubated with cell lysates for 5 min. F-actin severing was quantified by imaging before and after adding the cell lysates and determining the average loss of Alexa488-actin fluorescence for multiple fields (mean  $\pm$  s.e.m. for 4 experiments).  $***P < 0.001$ ;  $**P < 0.01$ . The blot in **f** shows the levels of inactive cofilin that is phosphorylated on S3 (pS3 cofilin) as well as total cofilin in the cell lysates. **(g,h)** Blots show the levels of activated GTP-bound Rap1 and total Rap1 (**g**) or pS3 cofilin and total cofilin (**h**) in cell lysates. Similar results were obtained in 5 experiments.

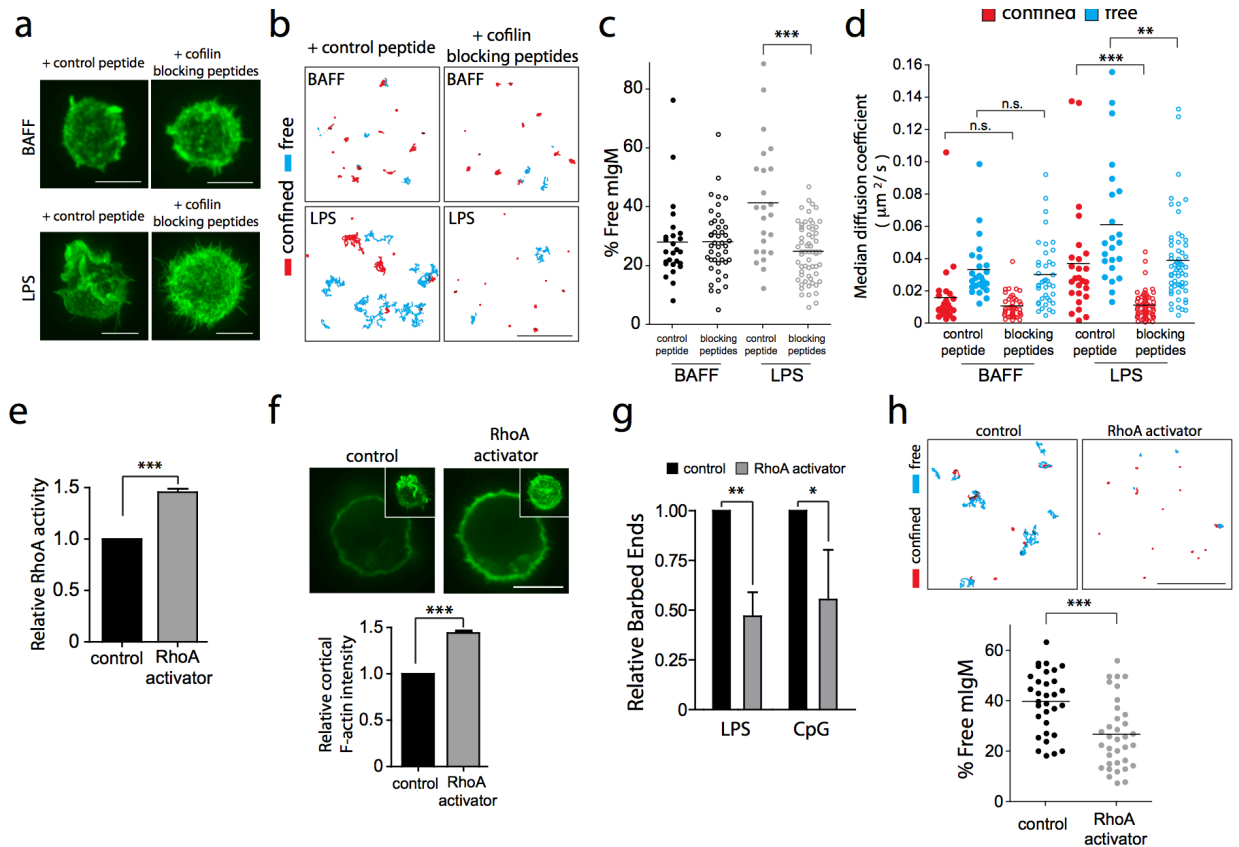


**Figure 2.6.** TLR enhancement of BCR mobility is dependent on actin severing. **(a)** Z-projections of F-actin staining in B cells that had been cultured overnight with either BAFF or BAFF + 5  $\mu\text{g/ml}$  LPS and then treated with 5  $\mu\text{M}$  of the M/W cofilin-blocking peptides or the control Q peptide for 5 min at 37°C. Scale bar, 3  $\mu\text{m}$ . **(b-d)** B cells were cultured with BAFF or BAFF + LPS and then treated with the cofilin-blocking peptides or the control peptide as in **a**. SPT and MSS analyses were performed as in Fig. 3. Trajectories were generated from videos taken at 33 frames/s for 10 s (see **Supplementary Video 7**). Scale bar, 5  $\mu\text{m}$ . Red, confined trajectories; cyan, free/unconfined trajectories. The percent of mIgM molecules that exhibited ‘free’ diffusion, as opposed to ‘confined’ diffusion is shown **(c)**, along with the median diffusion coefficients for both confined and free mIgM-containing BCRs **(d)**. Horizontal bars represent the mean values for > 20 videos per condition; >600 trajectories per condition were analyzed.

(e-h) B cells that were cultured overnight with BAFF + 5  $\mu\text{g/ml}$  LPS were incubated with or without the RhoA-activating peptide for 2-3 h. In e, a RhoA-specific G-LISA was used to quantify RhoA activity, which was normalized to that in untreated cells. Mean  $\pm$  s.e.m. for 3 experiments. In f, the cells were fixed and stained with Alexa488-phalloidin. Cortical F-actin intensity was measured at regions in xy planes that excluded membrane ruffling and fluorescence intensities per unit area were normalized to those in control cells. Mean  $\pm$  s.e.m. for 3 experiments. The insets show Z-projections of the cells. In g, the cells were rendered semi-permeable and incubated with Alexa488-actin for 10 s before being fixed and stained for F-actin. Ratios of Alexa-488 actin/F-actin were calculated and normalized to control cells. Mean  $\pm$  s.e.m. for 3 experiments is shown. In h, SPT of mIgM-containing BCRs was performed as in b (see **Supplementary Video 8**).  $***P < 0.001$ ;  $**P < 0.01$ ;  $*P < 0.05$ ; n.s., not significant.

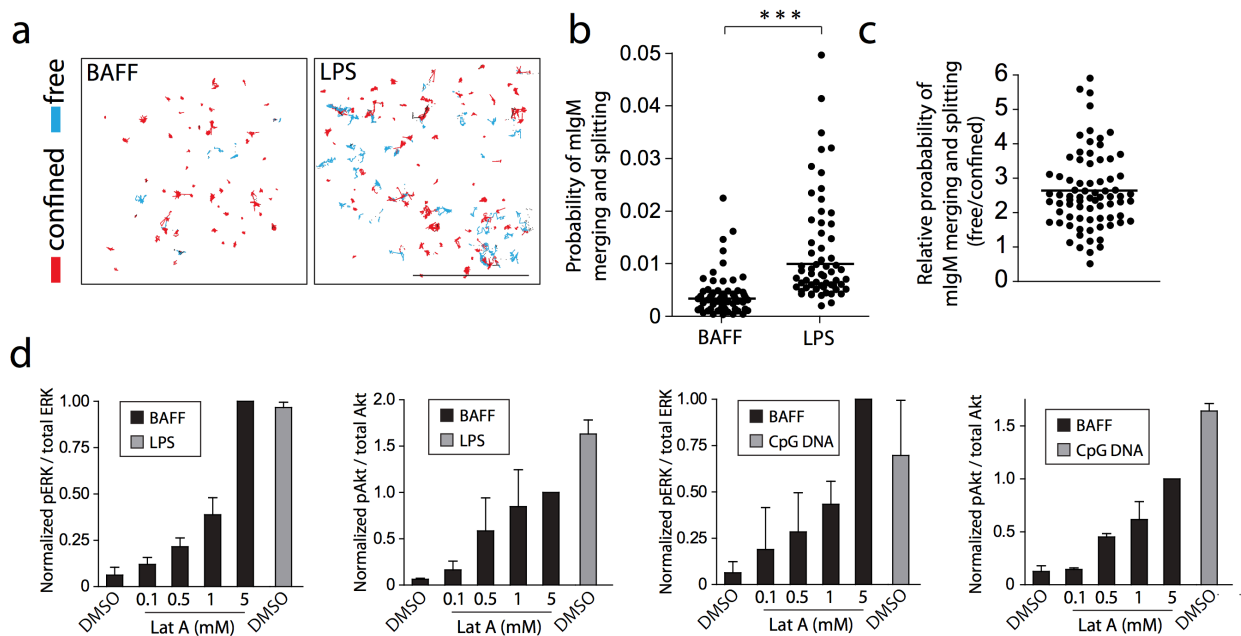


**Figure 2.7.** TLR ligands increase BCR-BCR collisions and tonic BCR signalling. (a-c) SPT of mIgM-containing BCRs on B cells that had been cultured overnight with BAFF or BAFF + LPS.

Trajectories were generated from videos taken at 10 frames/s for 5 s (**a**). Scale bar, 3  $\mu\text{m}$ . Red, confined trajectories; cyan, free/unconfined trajectories. The probability of a single BCR undergoing a collision with another BCR in a 5 s video was determined by applying merge-split algorithms to the trajectories (**b**). Each dot represents the probability for all of the BCRs in an individual video ( $n > 50$  videos).  $***P < 0.001$ . The relative probability of free versus confined BCRs undergoing merge-split events in LPS-stimulated cells is shown in **c**. (**d**) B cells were cultured overnight with BAFF, BAFF + LPS, or BAFF + CpG DNA and then treated with DMSO or 1  $\mu\text{M}$  latrunculin A for 5 min. Cell extracts were analyzed by immunoblotting with anti-phospho-ERK (pERK) or anti-phospho-Akt (pAkt) as well as total ERK or Akt. Graphs show the ratios of p-ERK/ERK signals or pAkt/Akt signals from at least 2 experiments (average  $\pm$  range or mean  $\pm$  s.e.m.). Representative blots are shown in **Fig. 2.13**.

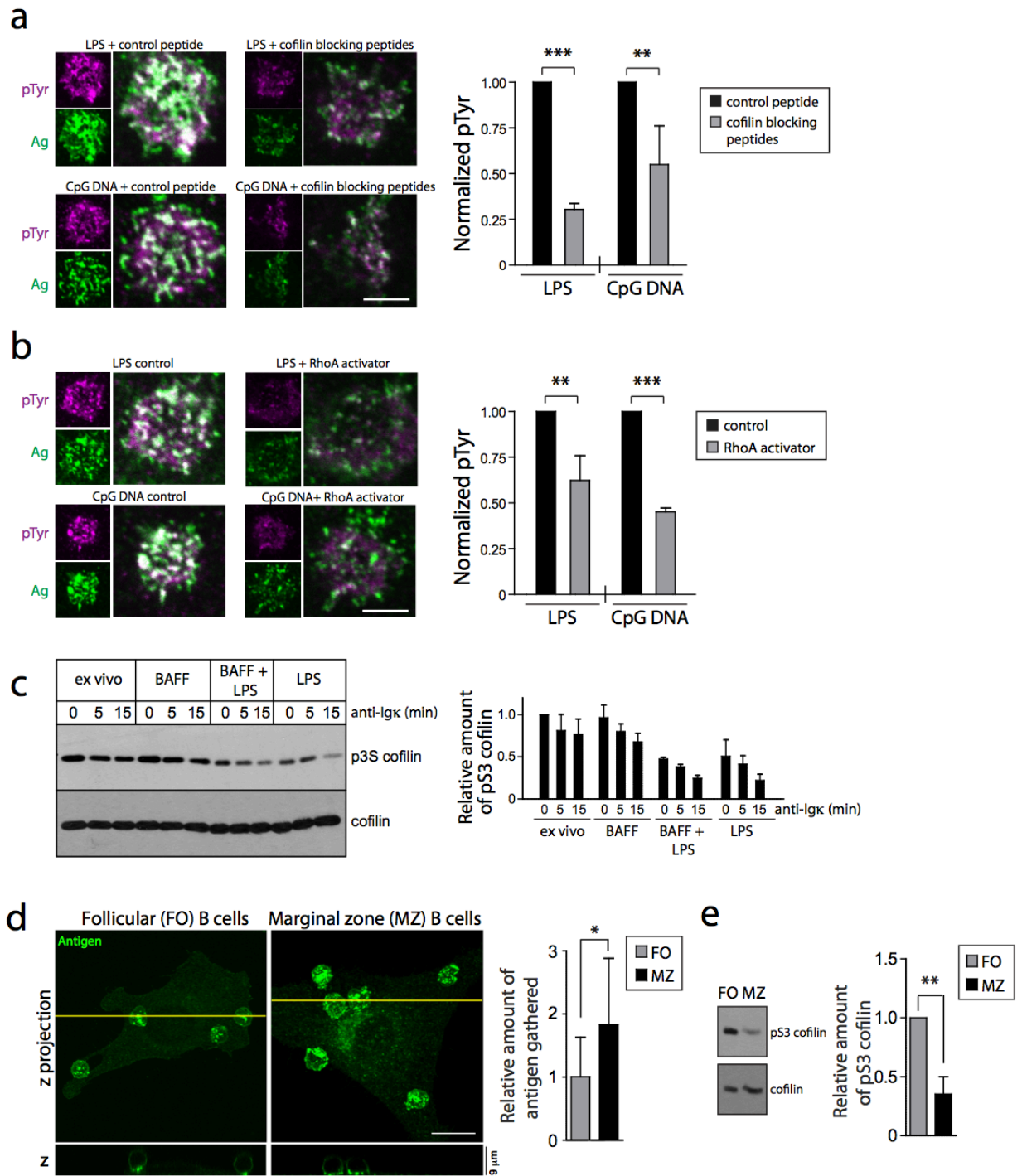


**Figure 2.8.** B cell responses to APC-bound Ags are dependent on actin dynamics that correlate with cofilin activation. **(a,b)** B cells were cultured overnight with LPS or CpG DNA and then treated with either cofilin-blocking peptides **(a)** or the RhoA activator **(b)** before being added to APCs expressing low densities of surrogate Ag for 3 min. The cells were then stained for pTyrosine

and for the surrogate Ag. Representative images of the B cell:APC contact site are shown. Scale bar, 5  $\mu$ m. The total pTyr signal at the contact site was quantified for >20 cells from 3 experiments for each condition and the mean  $\pm$  s.e.m. is expressed relative to that in cells that were not treated with the cofilin peptides or the RhoA activator. **(c)** TLR signalling decreases basal cofilin phosphorylation and enhances BCR-induced cofilin dephosphorylation. *Ex vivo* B cells, as well as B cells that were cultured overnight in BAFF, BAFF + LPS, or LPS alone were left unstimulated (0) or stimulated with soluble anti-Ig $\kappa$  antibodies for 5 or 15 min. Blots show inactive cofilin that is phosphorylated on S3 (pS3 cofilin) as well as total cofilin. Graphs show the relative amounts of pS3 cofilin from 3 experiments (mean  $\pm$  s.e.m.). **(d)** FACS-sorted MZ and FO B cells were added to APCs expressing low densities of the surrogate Ag for 3 min before staining for the surrogate Ag. The amount of Ag that was gathered into microclusters was quantified as in [195]. The data represent the mean  $\pm$  s.e.m. for >30 cells in 2 experiments. **(e)** Extracts of FO and MZ B cells were probed for pS3 cofilin and total cofilin. The ratio of pS3 cofilin/total cofilin is expressed relative to that in FO B cells and plotted as the mean  $\pm$  s.e.m. for 3 experiments. \*\*\* $P < 0.001$ ; \*\* $P < 0.01$ ; \* $P < 0.05$ .

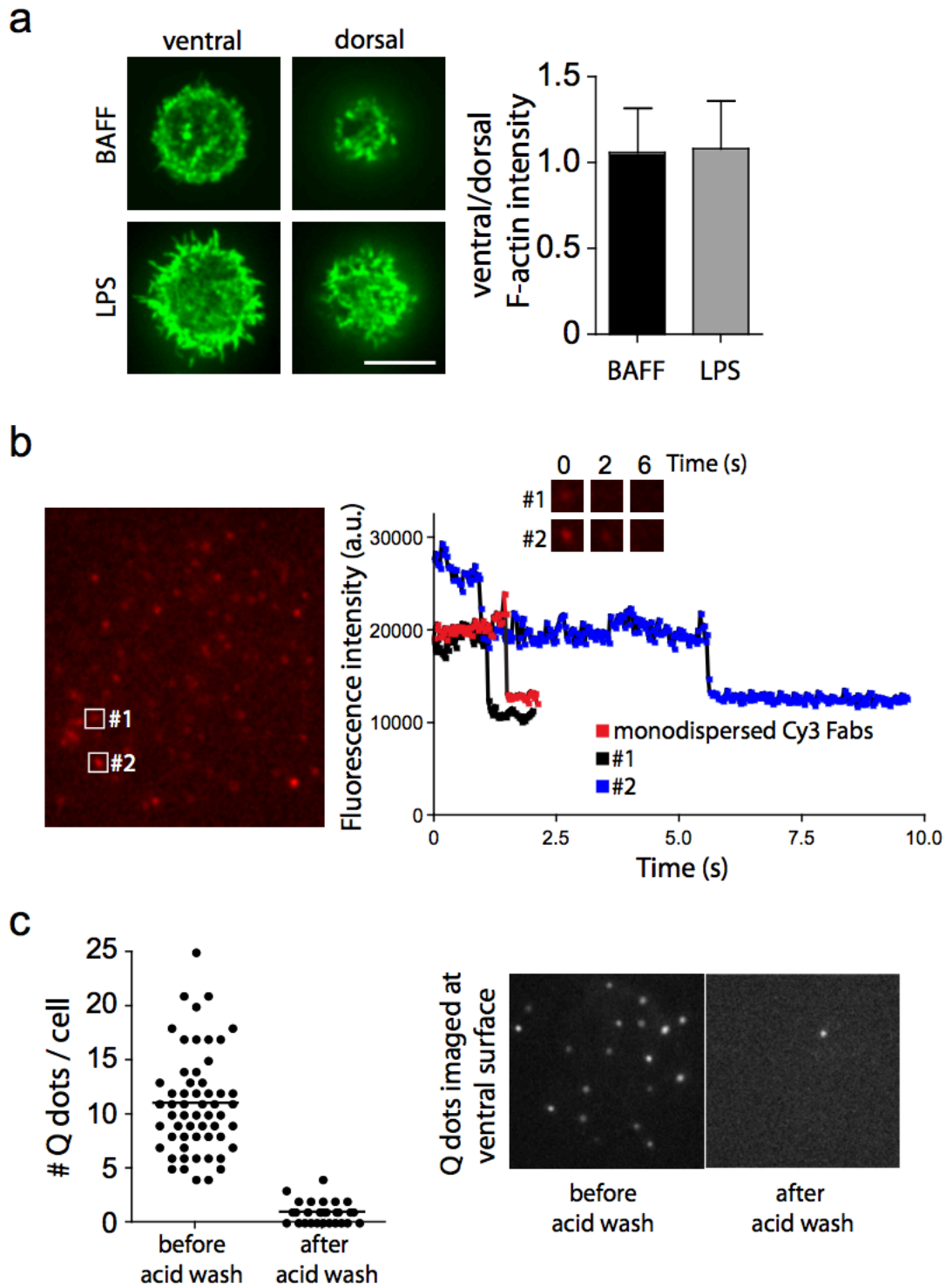
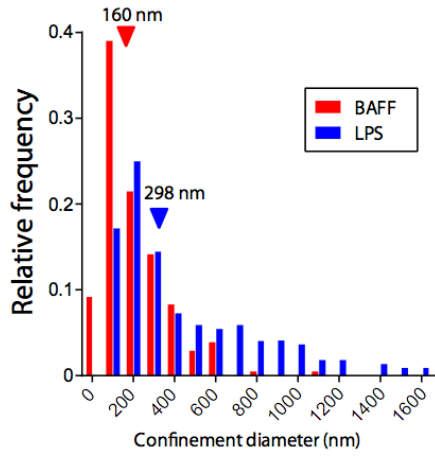


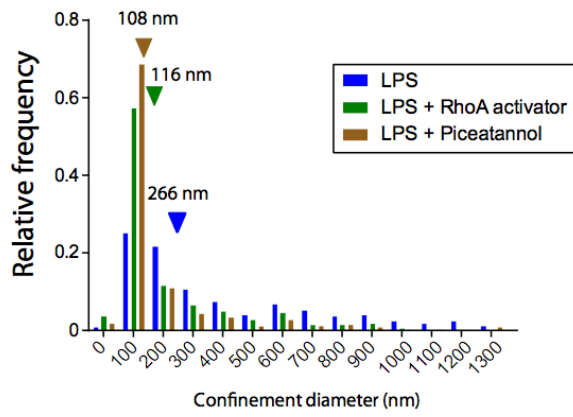
**Figure 2.9.** Single particle labeling of the BCR on B cells adhered to anti-MHCII-coated coverslips. (a) B cells that had been cultured overnight with BAFF or with BAFF + 5  $\mu\text{g/ml}$  LPS were adhered to anti-MHCII-coated coverslips and stained with Alexa488-phalloidin. F-actin at

the ventral and dorsal surfaces of the cell was visualized by confocal microscopy. The ratio of F-actin fluorescence intensity per unit area at the ventral and dorsal surfaces was determined for >10 cells in each experiment and the mean  $\pm$  s.e.m. for 3 experiments is shown. Scale bar, 10  $\mu$ m. The F-actin density remained similar on the dorsal and ventral sides of the cells, indicating that the cells did not mount a response to the anti-MHCII antibodies **(b)** *Ex vivo* B cells ( $1 \times 10^7$ ) were labeled on ice with 5 ng/ml Cy3-labeled anti-IgM Fab fragments, before adhering the cells to anti-MHCII-coated coverslips. The cells were imaged by TIRF at 33 frames/s for 10 s with laser settings that allowed photobleaching to be observed. The fluorescence intensity within regions of interest is graphed as a function of time and is compared to that for monodispersed soluble Cy3-labeled anti-IgM Fab fragments that were imaged using the same settings. Single particle labeling is indicated by a spot within a region of interest exhibiting a single quantized fluorescence decrease that is identical in magnitude (e.g. region #1, black trace) to that for monodispersed Cy3-anti-IgM (red trace). This analysis revealed that only a small fraction of spots contained more than one Cy3-labelled Fab (e.g. region #2, blue trace, contained two Cy3-labeled Fabs). Note that the concentration of Cy3-labeled fragments used in this experiment is 5 times the concentration of biotinylated anti-IgM Fab fragments used for experiments involving Qdot detection, and that it resulted in almost 5 times the number of identified particles. The nearly linear relationship between the concentration of Fab fragments used and the number of particles detected is consistent with the labeling of mostly single BCRs. **(c)** B cells were labeled with 1 ng/ml biotin-anti-IgM Fab plus streptavidin 655 nm-Qdots before imaging the ventral surface by confocal microscopy. The number of Qdots at the ventral surface was determined before and after washing cells with stripping buffer (200 mM acetic acid, 150 mM NaCl, pH 2.8) for 3 min at 37°C as in[330]. Acid-dissociable Qdots are assumed to be on the cell surface.

a



b



c

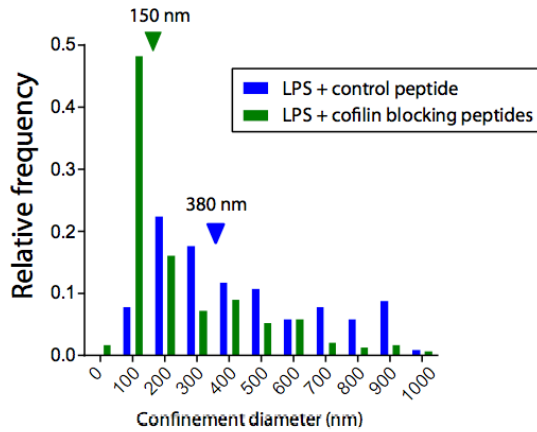


**Figure 2.10.** Representative distributions of BCR confinement diameters. SPT of mIgM-containing BCRs was performed as in Fig. 3. The trajectories of individual mIgM-containing BCRs were generated from videos taken at 33 frames/s for 20 s and the confinement diameters for mIgM BCRs exhibiting confined motion were determined. Confinement diameter values for individual BCRs were sorted into bins centered around multiples of 100 nm, e.g.  $100 \pm 50$  nm. The graphs display the relative frequency of BCR confinement diameters in all of the videos in which cells in a specific treatment group were analyzed within a single experiment. The total number of BCR trajectories per condition was  $>600$  and the median confinement diameter values are indicated by the triangles. Confinement diameter distributions are shown for mIgM-containing BCRs on (a) B cells that had been cultured overnight with either 5 ng/ml BAFF or BAFF + 5  $\mu$ g/ml LPS (see **Supplementary Videos 1 and 2**, respectively), (b) B cells that had been cultured overnight with BAFF + 5  $\mu$ g/ml LPS and then treated with either 10  $\mu$ M of the Syk inhibitor, piceatannol, for 5 min (see **Supplementary Video 6**) or 1  $\mu$ g/ml of the RhoA activator for 2-3 h (see **Supplementary Video 8**), or (c) B cells that had been cultured overnight with BAFF + 5  $\mu$ g/ml LPS and then treated with cofilin-blocking peptides or a control peptide for 5 min (see **Supplementary Video 7**).

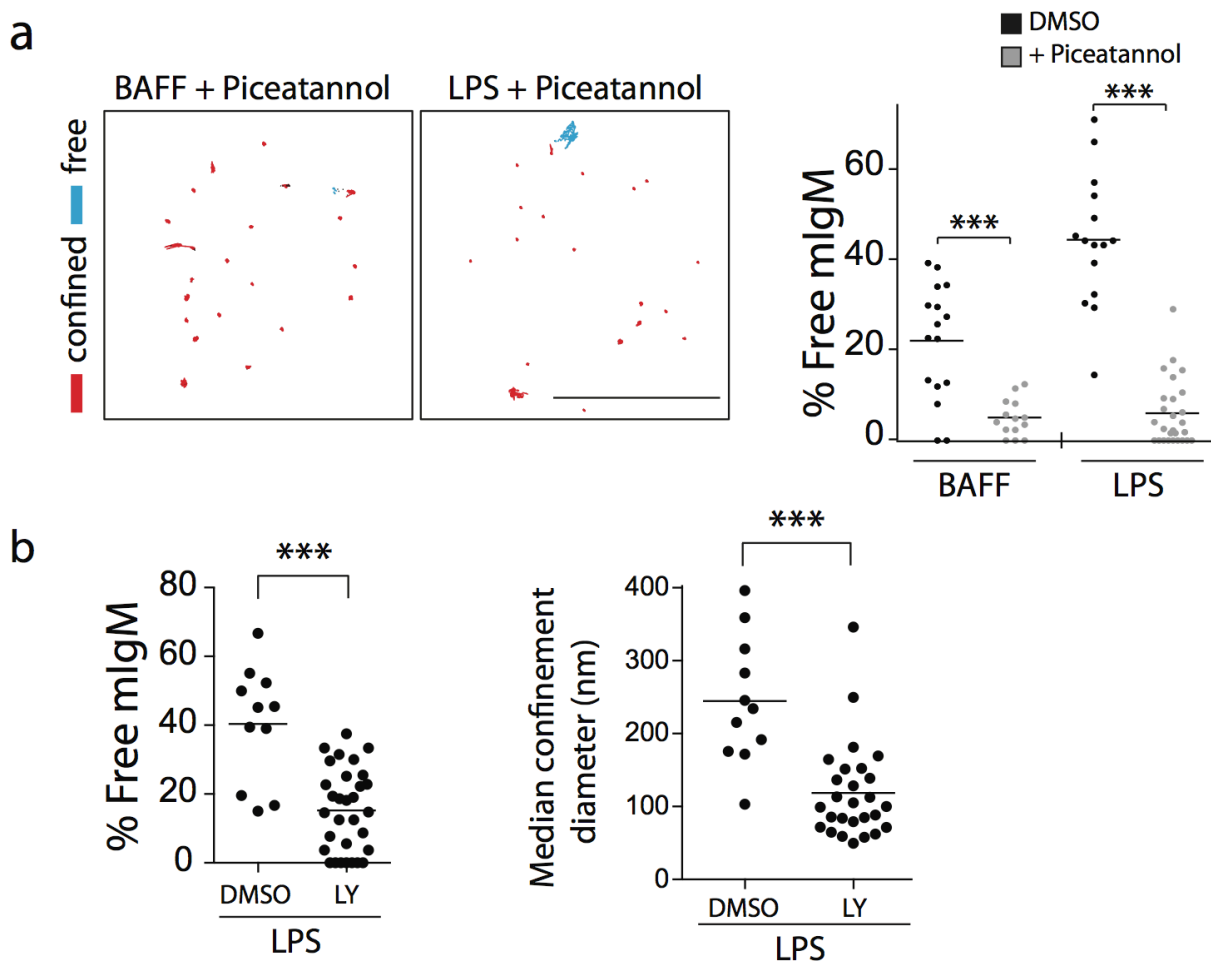


**Figure 2.11.** Syk and PI3K regulate BCR mobility. **(a)** B cells were cultured overnight with 5 ng/ml BAFF or BAFF + 5  $\mu$ g/ml LPS and then treated with 10  $\mu$ M piceatannol or an equal volume of DMSO for 5-10 min. Trajectories of individual mIgM-containing BCRs were generated from live-imaging videos taken at 33 frames/s for 20 s (see **Supplementary Video 6**). SPT and MSS analyses were performed as in Fig. 3. Scale bar, 3  $\mu$ m. Red, confined trajectories; cyan, free/unconfined trajectories. The percent of mIgM molecules that exhibited free diffusion is shown. **(b)** LPS-activated B cells were treated with 10  $\mu$ M Ly294002 or an equal volume of DMSO for 10 min. Trajectories were analyzed as in **a**. The percent of BCRs that exhibited free diffusion, as well as confinement diameter for BCRs exhibiting confined diffusion, is shown.

Horizontal bars represent the mean values for > 15 videos per condition; >500 trajectories per condition were analyzed. \*\*\* $P < 0.001$ .

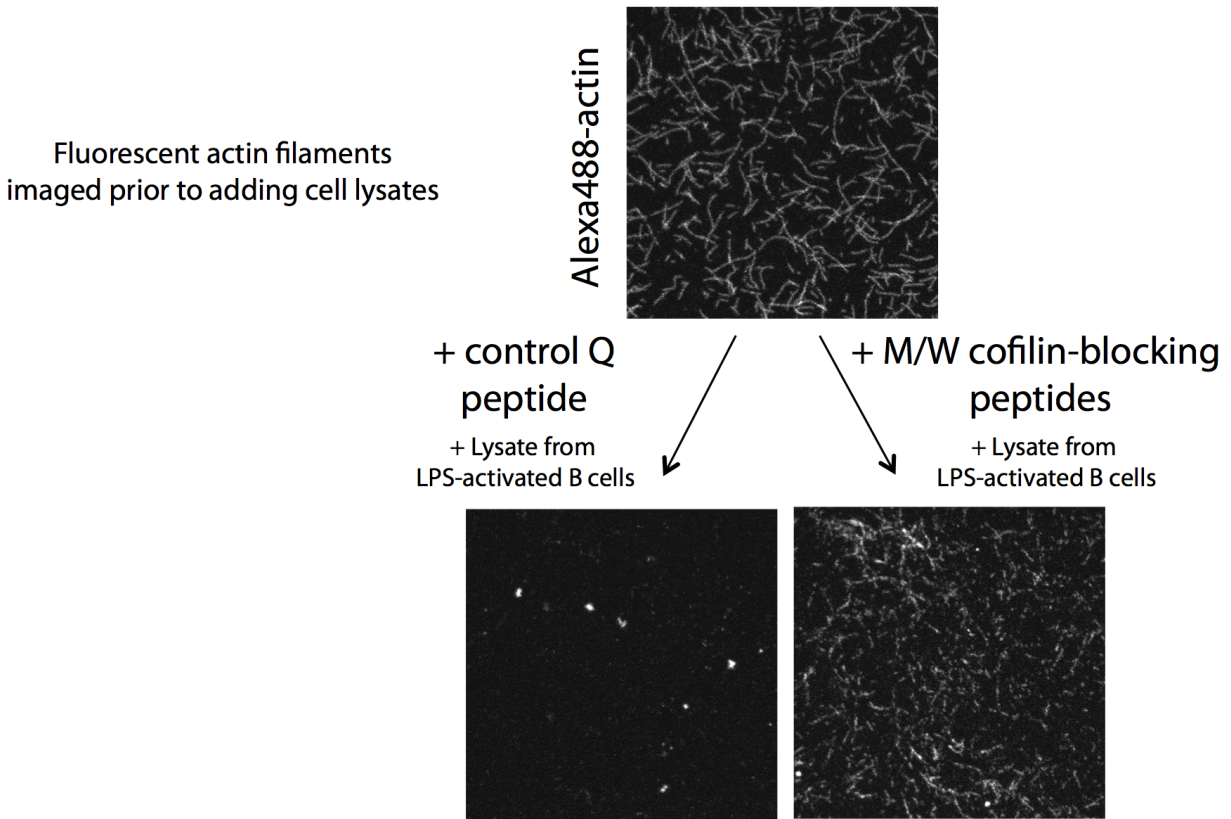


**Figure 2.12.** Cofilin-blocking peptides inhibit the *in vitro* severing of actin filaments by cell extracts. Actin filaments containing Alexa488-actin and biotinylated actin monomers were adhered to slides coated with anti-biotin antibodies and then imaged. Either the control Q peptide or the M/W cofilin-blocking peptides were then allowed to bind to the immobilized actin filaments before washing the slides, and adding lysates from LPS-activated B cells. Substantial actin severing, as indicated by the decrease in fluorescent filaments that remained attached to the slide, occurred in the presence of the control Q peptide whereas the M/W cofilin-blocking peptides greatly reduced F-actin severing.

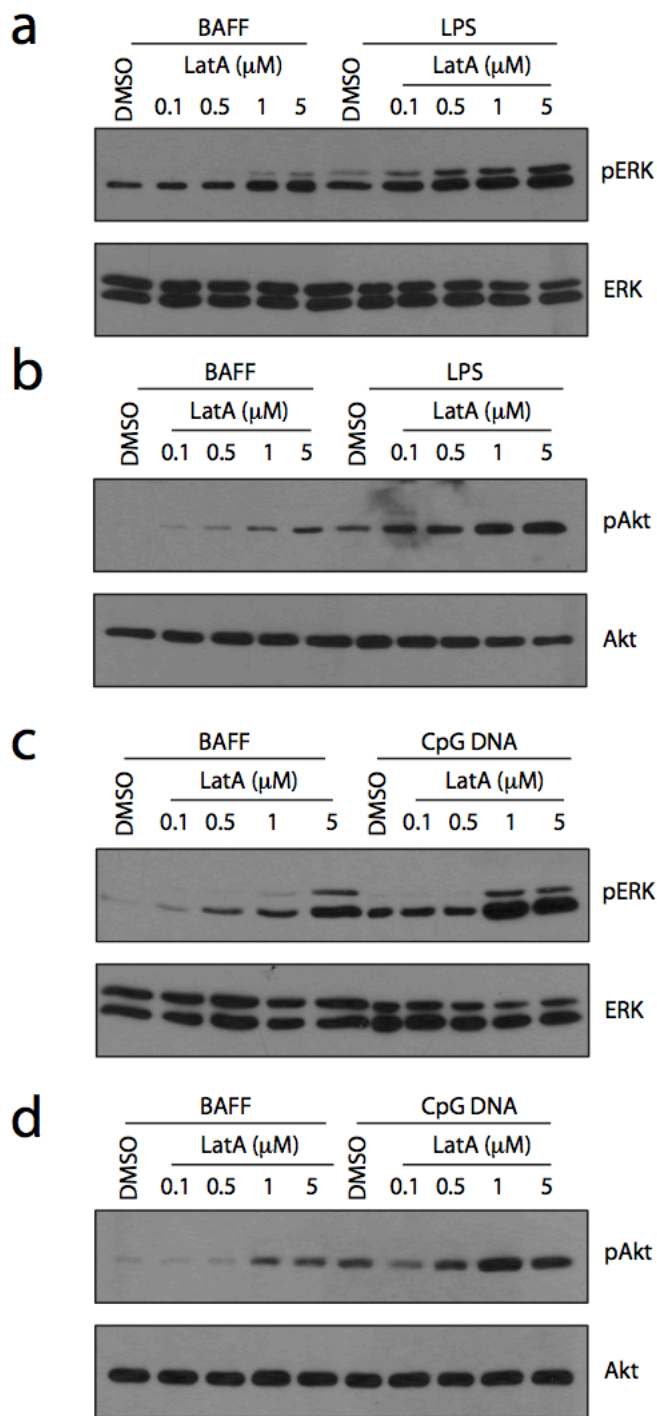


**Figure 2.13.** Disrupting the actin cytoskeleton increases Ag-independent BCR signalling in both resting and TLR-activated B cells. B cells were cultured overnight with BAFF, BAFF + 5  $\mu$ g/ml LPS, or BAFF + 0.5  $\mu$ g/ml CpG DNA and then treated with DMSO or the indicated

concentrations of latrunculin A for 5 min. Cell extracts were analyzed by immunoblotting with anti-phospho-ERK (pERK) and then anti-ERK or with anti-phospho-Akt (pAkt) and then anti-Akt. Comparing the DMSO samples for BAFF-cultured B cells versus TLR-activated B cells shows that overnight exposure to TLR ligands increased tonic Ag-independent BCR signalling.

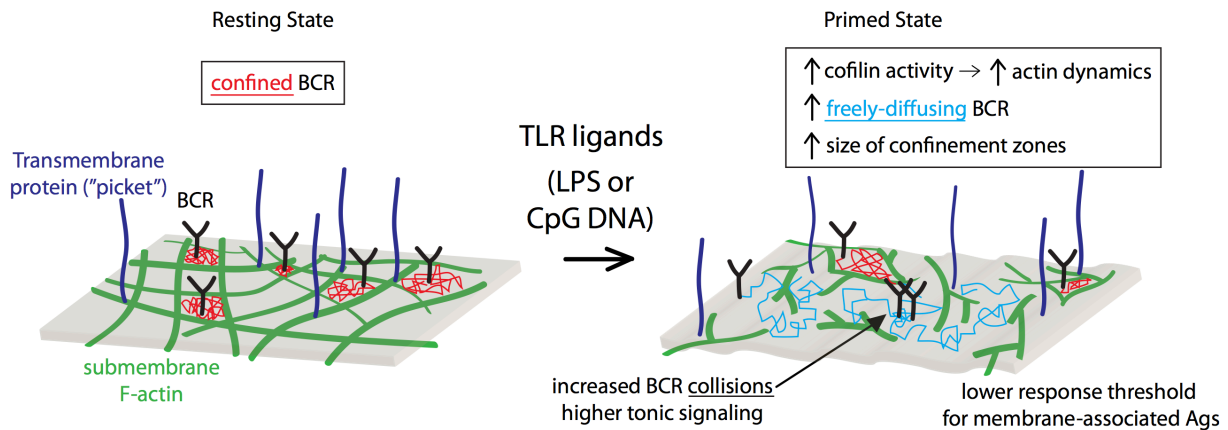


**Figure 2.14.** Model for TLR-induced transition of B cells from a resting state to an activated state. The TLR-activated state is characterized by increased cofilin activity, which increases the turnover dynamics of the actin cytoskeleton. This reduces actin-based barriers to BCR diffusion resulting in an increase in BCRs exhibiting free diffusion rather than confined diffusion, an increase in the size of remaining confinement zones, and increased diffusion coefficients for both free and confined BCRs. This increased BCR mobility allows a greater frequency of BCR-BCR collisions, which leads to increased Ag-independent tonic BCR signalling. This activated state characterized by increased BCR mobility allows for greater BCR microcluster formation when APC-bound Ags are present at lower densities, resulting in greater Ag-induced BCR signalling. In this way TLR priming of B cells increases their sensitivity to low densities of membrane-bound Ags. See the discussion for additional details.

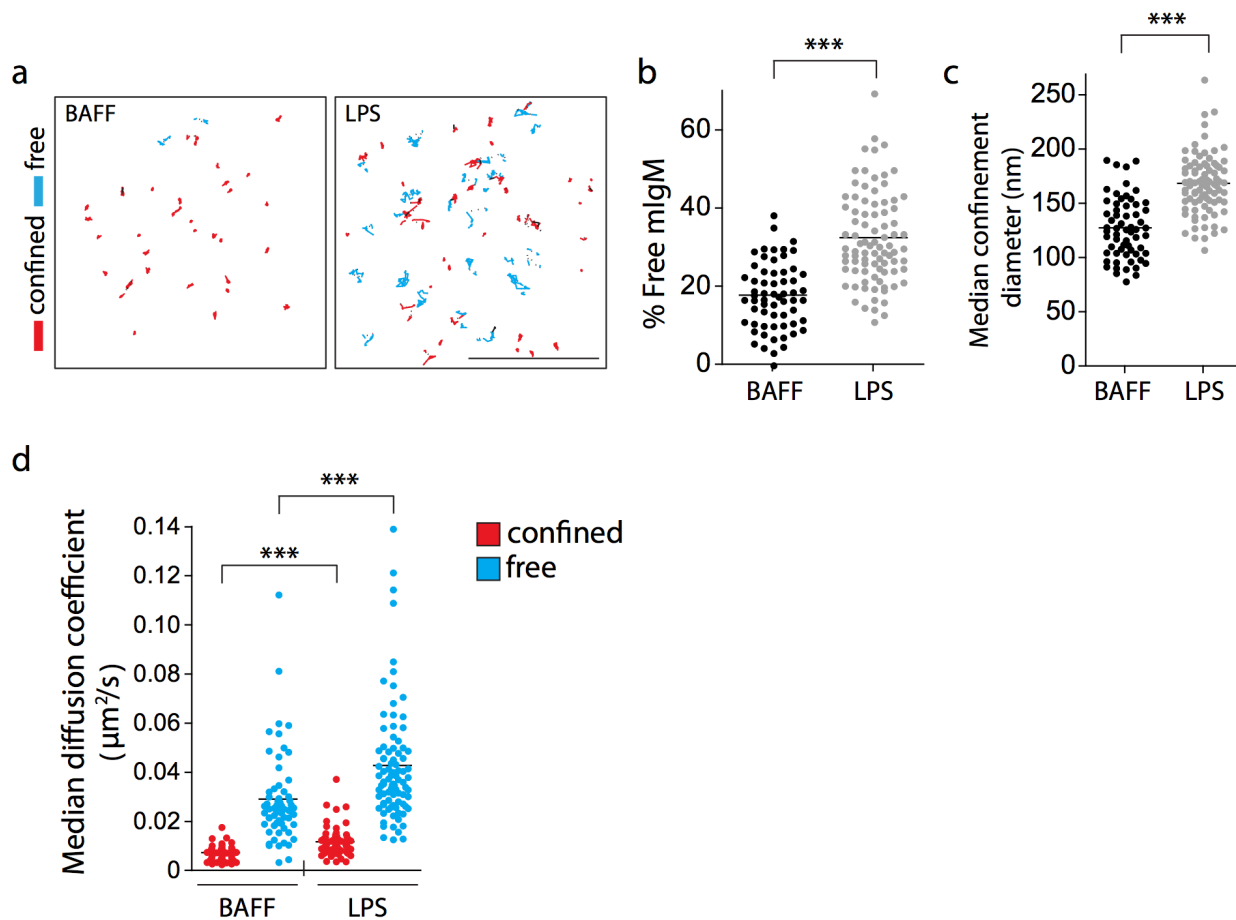


**Figure 2.15.** TIRF imaging of mIgM yields similar particle motion behavior as confocal microscopy. B cells that were cultured overnight with 5 ng/ml BAFF or BAFF + 5  $\mu\text{g}/\text{ml}$  LPS were labeled with 1-5 ng/ml Cy3-labeled anti-IgM Fab fragments and imaged by TIRF. Trajectories of individual mIgM-containing BCRs were generated from live-imaging videos taken at 10 frames/s for 10 s (**a**). Scale bar, 5  $\mu\text{m}$ . Red, confined trajectories; cyan, free/unconfined trajectories; linear and undetermined trajectories ( $< 5\%$  of total) are not shown. The percent of mIgM BCRs that exhibited free diffusion, as opposed to confined diffusion is shown (**b**), along with median confinement diameters for the confined mIgM BCRs (**c**), and median diffusion coefficients for both confined and free mIgM BCRs (**d**). Each dot represents

the trajectories from a single video. Horizontal lines are mean values for > 50 videos per condition; >3000 trajectories per condition were analyzed. \*\*\* $P < 0.001$ .

**Supplementary Table 2.1**

<b>Condition</b>	<b>Confinement diameter (nm) + s.e.m.</b>
<i>Fig. 3a-d</i>	
<i>Ex vivo</i>	129.8 + 7.3
BAFF	148.7 + 11.3
LPS	261.4 + 23.8
CpG DNA	255.2 + 21.2
<i>Fig. 3f-h</i>	
Control	124.0 + 12.4
LPS, 3 h	219.6 + 17.1
LPS, 6 h	211.6 + 17.8
LPS, 16 h	276.0 + 23.6
<i>Fig. 4</i>	
BAFF + DMSO	128.4 + 16.7
BAFF + LatB	276.6 + 33.9
LPS + DMSO	316.7 + 14.3
LPS + LatB	387.1 + 23.4
<i>Supplementary Fig. 3a</i>	
BAFF + piceatannol	71.6 + 9.1
LPS + piceatannol	87.7 + 10.5
<i>Fig. 6b-d</i>	
BAFF + control peptide	178.7 + 17.2

BAFF + cofilin-blocking peptide	179.8 + 12.4
LPS + control peptide	226.8 + 27.0
LPS + cofilin-blocking peptide	140.5 + 8.5
<b>Fig. 6h</b>	
LPS + DMSO	228.3 + 14.2
LPS + RhoA activator	142.6 + 10.8
LPS + 4% paraformaldehyde	33.2 + 3.7

**Table 2.1.** Summary of changes in BCR confinement diameters in response to experimental treatments. The confinement diameters for those BCRs exhibiting confined diffusion, as determined by the MSS algorithm, was quantified using SPT and MSS analyses, as described in Figure 3 and in the Methods section. Cells were cultured overnight with BAFF or with TLR ligands plus BAFF, except in Figure 3f-h in which LPS was added for different lengths of time before imaging the cells. After being cultured with BAFF alone or with BAFF plus TLR ligands, the cells were treated briefly with latrunculin B (LatB), the Syk inhibitor piceatannol, cofilin-blocking peptides or a control peptide, the RhoA activator, or 4% paraformaldehyde before being imaged. Details of these treatments are provided in the relevant figures, which are indicated. The median confinement diameter for all of the confined BCRs analyzed in an individual video was determined as in Figure 3 and the values in this table are the mean + s.e.m. for these median confinement diameters from > 10 videos per condition; >500 trajectories were analyzed per condition. For each treatment, representative experiments showing the confinement diameter, as well as other mobility parameters, are shown in the indicated figures. When the B cells were fixed with 4% paraformaldehyde, BCRs were rendered immobile. The median confinement diameter calculated for these fixed cells reflects the size of the Qdot (15-20 nm) as well as

vibrational movement of the Qdot. This value provides an estimate of the accuracy of the confinement diameter measurements. For almost all conditions shown in this table, this confinement diameter value for immobile BCRs on fixed cells was <25% of the measured confinement diameter value. Changes in the confinement diameter values caused by various treatments were sufficiently large that this value for immobile BCRs does not affect the conclusions that are drawn from the data.

## 2.5 Experimental procedures

### B-cell isolation and culture

Primary B cells were obtained from the spleens of C57BL/6 mice, MyD88 knockout mice (Jackson Laboratory), or CD-1 mice using a B-cell isolation kit from Stemcell Technologies to deplete non-B cells. B cells were cultured in RPMI-1640 supplemented with 10% FCS, 2 mM glutamine, 1 mM pyruvate, 50  $\mu$ M 2-mercaptoethanol, 15 U/ml penicillin, and 50  $\mu$ g/ml streptomycin (complete medium) with 5 ng/ml BAFF or 5 ng/ml IL-4 (both from R&D Systems) in the presence or absence of LPS (Sigma-Aldrich) or CpG DNA (ODN1826; InvivoGen). Fluorescence-activated cell sorting was used to obtain highly enriched populations of CD21<sup>int</sup>CD23<sup>hi</sup> follicular B cells and CD21<sup>hi</sup>CD23<sup>lo</sup> marginal zone B cells, as described previously [354]. All animal protocols were approved by the University of British Columbia Animal Care Committee or by the Hospital for Sick Children Animal Care Committee. Similar results were obtained with B cells from C57BL/6 and CD-1 mice.

### Analysis of BCR microcluster formation and signalling on antigen-presenting cells (APCs)

Experiments were carried out as described in Freeman *et al.* [195]. Lipofectamine 2000 (Invitrogen) was used to transiently transfect B16F1 cells (American Type Culture Collection) with a plasmid encoding the surrogate antigen (Ag), which is a fusion protein consisting of a single-chain Fv generated from the 187.1 rat anti-Ig $\kappa$  monoclonal antibody, the hinge and membrane-proximal domains of rat IgG1, and the transmembrane and cytoplasmic domains of the H-2K<sup>b</sup> allele of MHCI[355]. After 24 h, the cells were detached using cell dissociation buffer (0.5 mM EDTA, 100 mM, NaCl, 1 mM glucose, pH 7.4), plated on chamber slides that had been coated with 10  $\mu$ g/ml fibronectin, and then cultured for 2 h. B cells were added to these APCs

and allowed to attach for 3 min at 37 °C. Where indicated, the APCs were fixed with 4% paraformaldehyde and washed extensively with PBS before adding the B cells. B cell:APC conjugates were fixed with 4% paraformaldehyde and the cells were permeabilized with 0.5% Triton X-100 in PBS for 3 min and then blocked with 2% BSA in PBS for 20 min. The cells were stained with rabbit anti-pTyr (BD Biosciences) and then with Alexa568 goat anti-rabbit IgG (Molecular Probes-Invitrogen) to visualize pTyr, and with Alexa488 goat anti-rat IgG (Molecular Probes-Invitrogen) to visualize the single-chain anti-Ig $\kappa$  antibody (i.e. the surrogate Ag). Confocal imaging and the quantification of fluorescence signals were performed as described[195]. Images were captured using an Olympus FV1000 confocal microscope with a 100X objective or with a spinning disk confocal system consisting of an Axiovert 200M microscope (Carl Zeiss Inc.) with a 100X NA 1.45 oil objective, a 1.5X-magnifying lens, and a Hamamatsu C9100-13 camera (Hamamatsu Photonics) for image acquisition. ImagePro version 6.2 software (Media Cybernetics) or Volocity version 4.1.1 software (PerkinElmer) was used to analyze confocal images and to quantify fluorescence.

### **F-actin staining and confocal microscopy**

After being fixed and permeabilized as described above, cells were stained with rhodamine-phalloidin (Molecular Probes-Invitrogen) in order to visualize F-actin. Images were captured using an Olympus FV1000 confocal microscope. FluoView v1.6 and ImagePro software were used to analyze confocal images, generate Z-projections, and quantify fluorescence.

### **Single-particle tracking (SPT) and merge-split analysis**

*Immunolabeling:* To label single molecules of mIgM, B cells were resuspended to  $10^7$  cells/ml, blocked with 5% rat serum for 10 min, and then incubated in Hanks Balanced Salt Solution (HBSS) for 5 min with 1 ng/ml Cy3- or biotin-labeled anti-IgM Fab fragments (Jackson ImmunoResearch Laboratories). When biotinylated Fab fragments were used, the cells were subsequently incubated with streptavidin-655 nm Quantum dots (Qdots) (Invitrogen; 1:1000 dilution) for 5 min and then washed twice with HEPES-buffered RPMI-1640 as a source of free biotin to prevent streptavidin-mediated clustering of the BCR. For merge-split analysis, Cy3 anti-IgM Fab fragments were used at 5 ng/ml. All labeling steps were carried out at 4°C in order to minimize lateral mobility and clustering of the BCR. After labeling, the cells were washed and warmed to 37°C before imaging.

*Image acquisition for single particle tracking:* As described by Treanor *et al.*[60], B cells were immobilized for imaging by allowing them to attach for 5 min to coverslips that had been coated with 1 µg/ml of the M5/114 anti-MHCII monoclonal antibody (eBioscience). Live-cell imaging of Qdot-labeled IgM on the ventral surface of B cells was performed using a Zeiss Axiovert 200 epifluorescence microscope equipped with a 100× oil-immersion objective (NA 1.45), a custom-made 2.4× lens, a 32012 excitation/40 nm-emission filter cube specific for 655 nm-emitting Qdots (Chroma Technology, Bellows Falls, VT), and an Exfo X-Cite 120 light source. A Hamamatsu 9100-13 deep-cooled EM-CCD camera was used for recording and Volocity software was used for image acquisition. Images were acquired continuously at 33 frames per second for 10–20 s. Imaging of Cy3-labeled mIgM was performed using an Olympus IX81 TIRF microscope equipped with a 150× oil-immersion objective (NA 1.45) and a Hamamatsu C9100-

13 camera. Images were acquired at 10 frames per second for 10 s. Comparable results were obtained using Cy3 labeling and Qdots.

*Validation of single particle tracking of proteins on the cell surface:* To validate that the labeling techniques we used were detecting single molecules, the fluorescence intensity of regions on the cell surface was measured over time and compared to the fluorescence of soluble monodispersed Cy3-labeled anti-IgM Fabs imaged using the same microscope settings. The quantized decreases in cell fluorescence due to photobleaching were of identical magnitude for the cell-bound and soluble Cy3-labeled anti-IgM Fabs (**Supplementary Fig. 1a**), indicating that the cell-associated fluorescent signals corresponded to single Cy3-labeled Fab fragments. To confirm that only cell surface mIgM was being imaged, and that these BCRs were not being endocytosed, the cells were washed in low pH stripping buffer (200 mM acetic acid, 150 mM NaCl, pH 2.8) for 3 min at 37°C, as described Jaqaman et al. [330], before transferring the cells to complete medium with 10 mM HEPES. Only cell surface-associated Qdots exposed to the medium should be removed by the low pH treatment and we found that nearly all of the Qdot fluorescence was removed by this treatment (**Supplementary Fig. 1c**).

*Particle Tracking:* Single-particle tracking (SPT) was performed as described previously [325]. Briefly, Gaussian kernels were fit to local maxima intensities that were detected by imaging in order to determine particle positions. Particles were tracked using a two-step algorithm to generate complete trajectories by closing gaps and capturing merging and splitting events. First, the algorithm was used to link particle positions between consecutive frames using optimized spatial assignments that were applied identically for all videos generated using either Qdots or

Cy3-labeled particles. Generated tracks ended as a result of particle disappearance or the merging of particles. Therefore the algorithm generated complete particle trajectories by linking track segments from (a) end-to-start in order to close gaps resulting from temporary particle disappearance due to Qdot “blinking”, (b) from end-to-middle, to capture merging events, and (c) from middle-to-start to capture splitting events. The cost functions employed to weigh competing particle and track segment assignments were based on distance and intensity, as well as on motion models that aided tracking by allowing particle position propagation by employing the Kalman filter algorithm. Tracks lasting at least five frames were retained for trajectory analysis.

*Single-state analysis of BCR mobility:* For individual BCR trajectories, the mean square displacement (MSD), which represents the spatial extent of the area that the particle ‘explores’ was used to determine the diffusion coefficient,  $D$ , in  $\mu\text{m}^2/\text{s}$ , for the first 5 frames of trajectory recordings ( $\sim 150$  ms).

*Two-state analysis of BCR mobility:* An algorithm developed by Das *et al.* [326], which employs a two-state hidden Markov model to divide individual trajectories into slow and fast segments, was applied to individual BCR trajectories. The mean diffusion coefficients for the slow and fast states were determined as were the frequency of transitions between the two states.

*Trajectory Analysis:* Two measures were used to identify and characterize trajectory types: The first classified trajectory shape based on the degree of anisotropy of the scatter of particle positions along a trajectory [325, 356]. The second extracted diffusion types using moment

scaling spectrum (MSS) analysis of particle displacements [328, 329]. The MSS analysis was applied to full two-dimensional displacements and to one-dimensional displacements in the case of linear trajectories. Particle diffusion coefficients were calculated from the MSS analysis. The confinement dimension for confined and linear trajectories was derived via eigenvalue decomposition of the variance-covariance matrix of particle positions along each trajectory as done by Jaqaman *et al.* [330].

### **Scanning electron microscopy**

B cell:APC conjugates, or B cells that were immobilized on coverslips coated with anti-MHCII antibodies, were fixed with glutaraldehyde and then processed for scanning EM as described previously [95]. After fixation with 2.5% glutaraldehyde in 0.1 M cacodylate buffer pH 7.37, the samples were microwaved at 100W under vacuum at 37°C for four 2 min cycles, each separated by 2 min, using a Pelco Biowave microwave processing system (Ted Pella, Redding, CA). The samples were then rinsed with 0.1 M cacodylate buffer pH 7.2 and microwaved at 22°C without vacuum for 40 s at 300W, before being treated with 1% osmium tetroxide at 22°C under vacuum and then again microwaved at 100W for four 2 min cycles, each separated by 2 min. After rinsing with water and microwaving at 110W for 40 s, the samples were dehydrated by sequential treatments with 50%, 70%, and 95% ethanol, followed by three treatments with 100% ethanol, microwaving the samples under vacuum for 40 s at 110W after each treatment. Coverslips were dried using a CPD 020 critical point dryer (Bal-Tec, Balzers, Lichtenstein) and covered with a ~25 nm layer of gold/palladium using a SEMPrep II sputter coater (Nanotech, Manchester, UK). Images were obtained using the Hitachi S-4700 field emission scanning electron microscope in the University of British Columbia Bioimaging Facility.

### **Determination of G-actin/F-actin ratio**

Using a G-actin/F-actin *in vivo* assay kit (Cytoskeleton Inc.), cells were lysed and F-actin filaments stabilized according to the manufacturer's instructions. Cell extracts were separated into soluble and insoluble fractions by ultracentrifugation (100,000 x g, 1 h, 37°C), and these fractions were analyzed by immunoblotting with a mouse  $\beta$ -actin antibody (Sigma-Aldrich) to detect insoluble F-actin and soluble G-actin, as described previously [195].

### ***In vitro* actin-polymerization activity in cell extracts**

As described previously [195], cells were lysed in RIPA buffer containing 1 mM ATP and then sonicated for 1 min to destroy pre-existing F-actin. The sonicated cell extracts were then incubated at 37°C for 10 min to allow *in vitro* actin polymerization. After adding F-actin stabilization buffer (Cytoskeleton Inc.) for 10 min at 37°C, the cell extracts were separated into soluble and insoluble fractions as described above. The insoluble F-actin generated during the 10-minute *in vitro* incubation was assessed by immunoblotting with a  $\beta$ -actin antibody.

### ***In vitro* F-actin severing activity**

As described previously [195], chamber slides (ibidi) were incubated with 20  $\mu$ g/ml anti-biotin antibodies in ISAP buffer (20 mM Tris-HCl, pH 7.5, 5 mM EGTA, 2 mM MgCl<sub>2</sub>, 50 mM KCl, 1 mM ATP, 1 mM DTT) for 1 h at room temperature, washed with ISAP buffer, and then blocked with ISAP buffer containing 0.5 mg/ml BSA for 5 min. Biotinylated fluorescent F-actin filaments were generated by incubating 0.2  $\mu$ M Alexa488-actin, 0.2  $\mu$ M biotinylated actin, and 0.4  $\mu$ M unlabeled actin (all from Cytoskeleton Inc.) in ISAP buffer for 1 h at 20°C. This mixture was then diluted 1:5 with ISAP buffer containing 5 mg/ml BSA and 100 mM DTT and added to

the anti-biotin-coated chamber slide for 5 min. The chambers were washed with ISAP buffer containing 5 mg/ml BSA and imaged using an Olympus FV1000 confocal microscope to determine the pre-assay fluorescence intensity of adhered F-actin filaments. Cells were lysed in 0.5 ml ice-cold lysis buffer (20 mM Tris-HCl, pH 8, 5 mM EDTA, 0.5 mM MgCl<sub>2</sub>, 0.5% Triton X-100, 0.5 mM ATP, 5 mg/ml BSA, 6 mg/ml glucose, 100 mM DTT, 1 mM PMSF, 10 µg/ml leupeptin, 1 µg/ml aprotinin, 1 µg/ml pepstatin, 1 mM Na<sub>3</sub>VO<sub>4</sub>, 25 mM β-glycerophosphate) for 20 min on ice. Insoluble material was removed by centrifugation, after which the cell lysates were added to the chamber slides for 5 min. The chambers were then washed and imaged to determine the fluorescence intensity of remaining F-actin filaments. Fluorescence intensities were quantified using ImagePro 3D software (Media Cybernetics).

#### **Actin polymerization at barbed ends of actin filaments in permeabilized cells**

The incorporation of Alexa488-actin at the barbed ends of actin filaments was performed as described [195]. Cells were rendered semi-permeable by a 10-second incubation with warm permeabilization buffer (20 mM HEPES, pH 7.5, 138 mM KCl, 4 mM MgCl<sub>2</sub>, 3 mM EGTA, 0.4 mg/ml saponin, 1% BSA) containing 1 mM ATP and 0.4 µM Alexa488-actin (Cytoskeleton Inc.). Cells were then fixed with 4% paraformaldehyde in PBS for 20 min at 20°C, stained with rhodamine-phalloidin for 20 min, and imaged by confocal microscopy. Fluorescence intensities were quantified using ImagePro software and the ratio of Alexa-488 actin/F-actin fluorescence was calculated for individual cells.

### **Cell stimulation, preparation of cell extracts, and immunoblotting**

B cells ( $5 \times 10^6$ ) in 0.4 ml modified HEPES-buffered saline (25 mM sodium HEPES, pH 7.2, 125 mM NaCl, 5 mM KCl, 1 mM  $\text{CaCl}_2$ , 1 mM  $\text{Na}_2\text{HPO}_4$ , 0.5 mM  $\text{MgSO}_4$ , 1 mg/ml glucose, 2 mM glutamine, 1 mM sodium pyruvate, 50  $\mu\text{M}$  2-mercaptoethanol) were stimulated in suspension with anti-Igk light chain antibodies (SouthernBiotech) or with latrunculin A (Enzo Life Sciences). Cells were lysed in RIPA buffer containing protease and phosphatase inhibitors (30 mM Tris-HCl, pH 7.4, 150 mM NaCl, 1% Igepal [Sigma-Aldrich], 0.5% sodium deoxycholate, 0.1% SDS, 2 mM EDTA, 1 mM PMSF, 10  $\mu\text{g/ml}$  leupeptin, 1  $\mu\text{g/ml}$  aprotinin, 1 mM  $\text{Na}_3\text{VO}_4$ , 25 mM  $\beta$ -glycerophosphate, 1  $\mu\text{g/ml}$  microcystin-LR). Proteins were separated by SDS-PAGE and transferred to nitrocellulose. Filters were blocked with TBS (10 mM Tris-HCl, pH 8, 150 mM NaCl) containing 1% (w/v) BSA or 5% (w/v) milk powder, and washed with TBS plus 0.1% Tween 20. Primary antibodies were added for 1-2 h at room temperature or overnight in the cold. After washing, the filters were incubated with HRP-conjugated secondary antibodies for 1 h at room temperature. Bands were visualized using ECL (GE Life Sciences). Antibodies against cofilin, cofilin that is phosphorylated on S3, ERK, phospho-ERK, Akt, and phospho-Akt were all obtained from Cell Signaling Technologies.

### **Cofilin peptides, RhoA-activating peptide, and Syk inhibitor**

Cell-permeable peptides that inhibit the cofilin-mediated severing of F-actin[335] were synthesized by Biopeptide Inc. (San Diego, CA). The M (CDYKDDDDKMASGVAVSDGVK) and W (CDYKDDDDKWAPESAPLKS KM) peptides that correspond to actin-binding regions from cofilin, as well as the Q peptide (CDYKDDDDKWAPESAPLQSQM) in which key lysine residues in the W peptide are changed to glutamates so as to ablate F-actin binding [357], were

coupled to penetratin (KKWKMRRNQFWIKIQR-3-nitro-2-pyridinesulfenyl). Penetratin-peptide conjugates were purified by HPLC, and peptide masses were confirmed by mass spectrometry. B cells were resuspended in cold PBS and incubated with 5  $\mu$ M each of the M and W peptides or with 5  $\mu$ M of the Q peptide for 10 min on ice before placing the cells at 37°C for 5 min and then adhering them to anti-MHCII-coated coverslips or adding them to APCs. The RhoA activator II peptide CN03 [336, 337] was purchased from Cytoskeleton Inc. B cells were incubated with 1  $\mu$ g/ml of this peptide in complete medium for 2-3 h at 37°C in order to activate RhoA. The cells were then resuspended in HBSS, warmed to 37°C, and allowed to attach to anti-MHCII-coated coverslips or APCs. The Syk inhibitor piceatannol was purchased from Calbiochem. Cells were adhered to anti-MHCII-coated coverslips and then treated with 5  $\mu$ M piceatannol in HBSS for 5 min at 37°C before being imaged.

### **RhoA activation assay**

The relative amounts of active RhoA in extracts from  $5 \times 10^6$  B cells were determined using the RhoA G-LISA kit from Cytoskeleton Inc. according to the manufacturer's instructions.

### **Statistical analysis**

Student's two-tailed unpaired *t* test was used to compare sets of matched samples.

### **3. Cofilin-mediated F-actin severing is regulated by the Rap GTPase and controls the cytoskeletal dynamics that drive lymphocyte spreading and BCR microcluster formation<sup>2</sup>**

#### **3.1 Introduction**

When lymphocytes encounter antigen-presenting cells (APCs) bearing cognate antigen, they spread across the surface of the APC to scan for additional antigens. This is followed by membrane contraction and the formation of antigen receptor microclusters that initiate the signaling reactions that lead to lymphocyte activation. Breakdown of the submembrane cytoskeleton is likely to be required for the cytoskeleton reorganization that drives cell spreading and for removing physical barriers that limit antigen receptor mobility. In this report we show that antigen receptor signaling via the Rap1 GTPase promotes the dephosphorylation and activation of the actin-severing protein cofilin and that this results in increased severing of cellular actin filaments. Moreover, we show that this cofilin-mediated actin severing is critical for the changes in actin dynamics that drive B and T cell spreading, for the formation of BCR microclusters, and for the increased mobility of BCR microclusters within the plasma membrane after BCR engagement. Finally, using a model APC, we show that activation of this Rap-cofilin signaling module controls the amount of antigen that is gathered into BCR microclusters and that this is directly related to the magnitude of the resulting BCR signaling that is initiated during B

---

<sup>2</sup> A version of this chapter is published. Spencer A. Freeman, Victor Lei, May Dang-Lawson, Calvin D. Roskelley, and Michael R. Gold. (2011) Cofilin-Mediated F-actin Severing is Regulated by the Rap GTPase and Controls the Cytoskeletal Dynamics that Drive Lymphocyte Spreading and BCR Microcluster Formation. *The Journal of Immunology*.

cell-APC interactions. Thus Rap-dependent activation of cofilin is critical for the early cytoskeletal changes and BCR reorganization that are involved in APC-dependent lymphocyte activation.

Lymphocytes are highly motile within lymphoid organs and make frequent contacts with potential antigen-presenting cells (APCs) cells. T cells are activated by peptide:MHC complexes on APCs whereas B cells can be activated by antigens (Ags) or immune complexes that are captured by APCs [71]. Signaling via the BCR or TCR induces rapid spreading of the lymphocyte across the surface of the APC [84, 358], allowing additional Ag receptors (AgRs) to encounter Ags and form microclusters [317, 359]. Within 5-10 minutes, cell spreading is replaced by membrane contraction, ultimately leading to formation of an immune synapse (IS) in which Ag-bound TCRs or BCRs are concentrated into a central supramolecular activation cluster (cSMAC) [84, 358]. In contrast to the cSMAC, which may be primarily a site for AgR internalization [91, 360], AgR microclusters nucleate signalosome assembly and are thought to be the main site of AgR signaling [317, 359, 361]. The extent to which lymphocytes spread on the surface of APCs, encounter Ag, and form AgR microclusters determines the magnitude of AgR signaling and whether or not lymphocyte activation ensues. Thus, elucidating the mechanisms that control cytoskeleton and microcluster dynamics is critical for understanding APC-induced lymphocyte activation.

The changes in cell morphology and AgR organization that occur during APC-mediated lymphocyte activation are driven by dynamic rearrangement of the submembrane cytoskeleton [362]. In particular, cell spreading requires the formation of branched F-actin networks that exert outward force on the plasma membrane. The Rap1 and Rac2 GTPases have been implicated in AgR-induced actin polymerization and are important for B cell spreading and IS formation [95,

363]. The active GTP-bound form of Rap1 binds multiple proteins that promote actin polymerization, including Vav2 and TIAM, upstream activators of the Rac and Cdc42 GTPases, respectively [364]. Activated Rac and Cdc42 act via WAVE and WASP to activate the Arp2/3 complex, which initiates the formation of branched actin filaments. Rap1-GTP also binds RIAM and AF-6 [364], scaffolding proteins that recruit profilin, a protein that primes actin monomers for addition to the barbed ends of actin filaments.

In addition to actin polymerization, the severing of existing cortical F-actin filaments is likely to be a prerequisite for the cytoskeletal reorganization that underlies changes in lymphocyte morphology. Indeed, F-actin severing or depolymerization occurs within 15 seconds of BCR engagement [61]. F-actin severing releases actin monomers that can be assembled into new filaments but also generates new barbed ends, which are preferred sites for the formation of branched actin filaments by the Arp2/3 complex [333]. Thus breakdown of the cortical cytoskeleton is coupled to the subsequent assembly of branched actin networks that drive cell spreading.

F-actin severing is also likely to be important for the formation of AgR microclusters. In resting cells, the lateral diffusion of AgRs is limited to small membrane domains created by the submembrane actin cytoskeleton (“actin corrals”, “picket fences”), which is tethered to the membrane by ezrin-radixin-moesin (ERM) family proteins [340]. Constraining AgRs within these actin corrals allows Ag-independent formation of small microclusters that provide tonic survival signals but prevents large-scale microcluster formation that would initiate lymphocyte activation [60]. AgR signaling causes the breakdown of submembrane F-actin structures, as well as dephosphorylation and inactivation of ezrin [60, 365]. Ezrin inactivation, which causes localized release of the plasma membrane from the submembrane cytoskeleton [366], enhances

AgR mobility and microcluster formation [62]. However, localized breakdown of the submembrane cytoskeleton may also be critical for these initial events in APC-mediated lymphocyte activation [362]. The AgR signaling pathways that initiate cytoskeletal breakdown are not well understood but they are likely to target F-actin severing proteins such as gelsolin and cofilin. Indeed, cell-permeable peptides that block the binding of cofilin to F-actin prevent IS formation in T cells [335].

Based on our previous findings that activation of the Rap GTPases is required for lymphocyte spreading and IS formation [95], we tested the hypothesis that AgR-induced Rap activation leads to increased F-actin severing, and that this is required for the initial changes in cytoskeleton, membrane, and AgR dynamics that occur after Ag binding. We now show that the F-actin severing protein cofilin is a downstream target of the Rap GTPases and that AgR-induced activation of this Rap-cofilin module is essential for the changes in cytoskeletal dynamics that underlie B and T cell spreading as well as BCR microcluster formation, mobility, and signaling.

## **3.2 Results**

### **3.2.1 AgR-induced cell spreading is associated with increased actin dynamics**

Plating lymphocytes on AgR ligands that are immobilized on rigid substrates allows one to study lymphocyte spreading while limiting subsequent membrane contraction. Rapid and sustained cell spreading occurred when B cells contacted anti-IgM-coated surfaces and when T cells contacted anti-CD3/CD28-coated surfaces (**Fig. 3.14; Supplemental Videos 1 and 2**). This was associated with increased actin dynamics, as shown by transfecting primary B or T cells with actin-GFP and then monitoring fluorescence recovery after photobleaching (FRAP) in

membrane-proximal regions of interest (ROIs) containing F-actin structures (**Fig. 3.1B; Supplemental Videos 3 and 4**). We found that plating cells on anti-IgM or anti-CD3/CD28 increased the maximal recovery of actin-GFP fluorescence in photobleached ROIs. This indicates that AgR signaling increased the incorporation of actin-GFP monomers into peripheral F-actin structures, relative to their release by depolymerization of actin filaments. Consistent with this, AgR signaling increased the amount of actin polymerizing activity present in B and T cell extracts (**Fig. 3.1C**). To show this, cell extracts were sonicated to destroy pre-existing actin filaments and then incubated *in vitro* under conditions in which actin polymerization could occur, as indicated by the generation of insoluble F-actin that could be pelleted by centrifugation. Extracts from activated lymphocytes generated more F-actin than extracts from unstimulated cells. Similarly, when B cells were rendered semi-permeable and then briefly incubated in the presence of Alexa488-labeled actin monomers, cells plated on immobilized anti-IgM incorporated more Alexa488-actin into F-actin than unstimulated cells (**Fig. 3.1D**). Much of this BCR-induced *de novo* actin polymerization occurred at the peripheral lamellipodia that are associated with cell spreading (**Fig. 3.1D**).

Despite the increased incorporation of actin monomers into actin filaments, AgR engagement did not cause a significant increase in the total amount of F-actin within the cells (**Fig. 3.1, D middle graph and E**). This suggests that AgR signaling causes reorganization of the actin cytoskeleton in which new actin polymerization is coupled to the severing of existing actin filaments. This is consistent with the idea that actin polymerization in cells occurs mainly by addition of actin monomers to the uncapped barbed ends of actin filaments [367], which are generated by actin severing [368]. Therefore we investigated the role of actin severing in lymphocyte spreading.

### 3.2.2 AgR signaling stimulates cofilin-mediated F-actin severing

Jasplakinolide, a drug that stabilizes polymerized actin filaments, inhibited B and T cell spreading (**Fig. 3.2A**), indicating that F-actin severing is essential for lymphocyte spreading. To test whether AgR signaling increases cellular actin-severing activity, we used an assay [368] in which a mixture of biotinylated, Alexa488-conjugated, and unlabelled actin monomers is assembled into filaments *in vitro* and then attached to slides coated with a low concentration of Abs to biotin. Severing of the actin filaments results in release of actin polymers or monomers that are not directly bound to the anti-biotin Abs. We found that extracts from anti-IgM-stimulated B cells caused much greater release of Alexa488-labeled actin filaments from the slides than extracts of unstimulated B cells (**Fig. 3.2B**), indicating that BCR engagement increased cellular F-actin severing activity. F-actin-severing proteins include cofilin and gelsolin. However, adding an Ab against cofilin to the cell extracts completely abrogated F-actin severing activity (**Fig. 3.2B**). Thus the BCR-induced increase in actin-severing activity was mediated by cofilin.

Dephosphorylation of serine 3 (S3) activates cofilin, allowing it to bind actin filaments and initiate severing [334]. As assessed using a phosphosite-specific Ab, stimulating murine splenic B cells with soluble, bead-bound, or plate-bound anti-IgM resulted in dephosphorylation of cofilin on S3 (**Fig. 3.2C**). Dephosphorylation of cofilin on S3 also occurred when murine splenic T cells or Jurkat T cells were stimulated with soluble or plate-bound anti-CD3/CD28 (**Fig. 3.2, D and E**). Thus AgR signaling induces cofilin dephosphorylation, which correlates with increased F-actin severing activity within the cells.

### 3.2.3 The Rap GTPases control peripheral actin dynamics, F-actin severing, and cofilin activation

Because BCR-induced activation of the Rap GTPases is required for B cell spreading and IS formation [95] we assessed whether Rap activation was required for the increased actin dynamics and cofilin-mediated F-actin severing that accompanied lymphocyte spreading. To assess the effects of blocking Rap activation, we used A20 cells, an IgG<sup>+</sup> B cell line, that had been stably transfected with RapGAPII [95], a Rap-specific GTPase-activating protein that enzymatically converts active GTP-bound Rap to the inactive GDP-bound state. We also interfered with Rap activation and function by transiently expressing Rap1N17, a dominant-negative (DN) form of Rap1.

Actin-GFP-expressing A20 cells underwent rapid spreading when plated on immobilized anti-IgG and this was accompanied by the incorporation of actin-GFP into peripheral F-actin structures (**Fig. 3.3A**). In contrast, when Rap activation was blocked by expression of RapGAPII, the cells did not spread and incorporated less actin-GFP into peripheral F-actin structures (**Fig. 3.3A**). Similarly, expressing Rap1N17 in Jurkat cells blocked anti-CD3/CD28-induced spreading (see Fig. 5C). Real-time confocal imaging of the cell-substrate contact region revealed dynamic incorporation of actin-GFP into peripheral actin structures when murine splenic B cells, A20 cells, and Jurkat cells contacted surfaces coated with anti-Ig or anti-CD3/CD28 Abs (**Fig. 3.12**). In contrast, GFP-labeled F-actin structures in RapGAPII-expressing A20 cells and Rap1N17-expressing Jurkat cells were more static (**Fig. 3.13, B and C**). FRAP analysis also showed that peripheral F-actin structures were more dynamic in A20/vector cells than in A20/RapGAPII cells (**Fig. 3.3B**). In A20/vector cells, 70-80% of the actin-GFP fluorescence in peripheral ROIs was recovered by 60 s after photobleaching, compared to ~30% in A20/RapGAPII cells. Thus Rap

activation is required for lymphocyte spreading and for the underlying peripheral actin dynamics.

Rap activation was also required for BCR engagement to stimulate both actin severing and actin polymerization at barbed ends. To assess actin severing in live cells we developed an assay for visualizing the release of fluorescent actin monomers from F-actin filaments in real time. Cells were co-transfected with a photo-convertible form of actin-GFP that assumes a fluorescent conformation when subjected to UV illumination, and with the actin-binding domain (ABD) of utrophin fused to red fluorescent protein (RFP), which can be used to visualize actin filaments in live cells [369]. Real-time imaging of a membrane-proximal ROI allowed us to visualize dissociation of the actin-GFP from F-actin structures, as indicated by loss of the GFP signal from the ROI. This showed that BCR-induced dissociation of actin-GFP from actin filaments occurred to a greater extent in A20/vector cells than in A20/RapGAPII cells (**Fig. 3.3C**). Rap activation was required not only for BCR-induced F-actin severing but also for actin polymerization at the barbed ends of actin filaments, as judged by the *de novo* incorporation of Alexa488-actin into F-actin structures in semi-permeabilized cells (**Fig. 3.3D**).

Consistent with the finding that Rap activation was important for BCR-induced F-actin severing, AgR-induced dephosphorylation and activation of cofilin also required Rap activation. Blocking Rap activation by expressing RapGAPII in A20 cells prevented the dephosphorylation of cofilin induced by soluble, bead-bound, and plate-bound anti-Ig (**Fig. 3.4, A-C**). Similarly, expressing the DN Rap1N17 protein in Jurkat cells blocked anti-CD3/CD28-induced cofilin dephosphorylation (**Fig. 3.4D**). Importantly, the increase in cofilin-mediated F-actin severing activity caused by BCR engagement was completely abrogated when Rap activation was blocked (**Fig. 3.4E**). Thus, Rap activation is required for AgR-induced cofilin activation, F-actin severing, and subsequent actin polymerization at barbed ends.

### 3.2.4 Cofilin activation is required for lymphocyte spreading and actin dynamics

To test whether the activation of cofilin by its dephosphorylation on S3 is required for lymphocyte spreading, we expressed in A20 cells a catalytically inactive form of Slingshot (SSH), the major phosphatase that acts on cofilin [370]. Cells expressing this mutant SSH with a C→S replacement in its active site (SSH-C/S) had increased levels of phosphorylated cofilin, and when plated on immobilized anti-Ig spread to a lesser degree than neighboring untransfected cells or cells transfected with the empty vector (**Fig. 3.5A**). We also implicated cofilin activation in AgR-induced spreading by expressing a mutant form of cofilin that assumes an inactive conformation because of an S→D phospho-mimetic substitution at position 3. A20 cells expressing this cofilin S3D mutant as a mCherry fusion protein (**Fig. 3.13**) did not spread on immobilized anti-Ig (**Fig. 3.5B**) and exhibited impaired actin dynamics, i.e. reduced recovery of actin-GFP fluorescence after photobleaching (**Fig. 3.5D, left panel**). Thus cofilin dephosphorylation and activation are required for BCR-induced cell spreading and the underlying actin dynamics.

To test if Rap-GTP promotes cell spreading and actin dynamics primarily by controlling cofilin activation, we asked whether expressing a non-phosphorylatable “active” mutant form of cofilin (S→A mutation at position 3) could overcome the effects of blocking Rap activation. Indeed, expressing a cofilin S3A-mCherry fusion protein (**Fig. 3.13**) restored the ability of A20/RapGAPII cells to spread on immobilized anti-Ig (**Fig. 3.5B**) and the ability of Rap1N17-expressing Jurkat cells to spread on anti-CD3/CD28 (**Fig. 3.5C**). Cofilin S3A expression also restored peripheral actin dynamics in both A20/RapGAPII cells and Rap1N17-expressing Jurkat cells, as shown by the increased recovery of actin-GFP fluorescence after photobleaching

compared to A20/RapGAPII cells (**Fig. 3.5D, right panel**) or Jurkat cells expressing only Rap1N17 (**Fig. 3.5E**). The inability of WT cofilin to bypass the block in Rap activation in A20/RapGAPII cells (**Fig. 3.5B and Fig. 3.5D, right panel**) indicates that cell spreading and actin dynamics require increased cofilin activity and not just increased levels of cofilin.

### **3.2.5 The Rap-cofilin pathway is required for B cells to spread across APCs and gather Ag into microclusters**

The spreading of lymphocytes on APCs bearing cognate Ag allows additional AgRs to encounter Ag and promotes the formation of AgR microclusters that initiate signaling. To model these events, we generated surrogate APCs by transfecting B16F1 cells with a dimeric transmembrane form of a single chain rat anti-mouse Ig $\kappa$  Ab [355], which can cluster  $\kappa$  chain-containing BCRs (**Fig. 3.6A**). After allowing B cells to bind these APCs, we used Alexa488-anti-rat IgG to detect the single chain anti-Ig $\kappa$  Ab and anti-phosphotyrosine (p-Tyr) staining to visualize BCR signaling. LPS/IL-4-activated splenic B cells that bound to these APCs gathered the single chain anti-Ig $\kappa$  surrogate Ag into microclusters that corresponded to sites of p-Tyr signaling (**Fig. 3.6, B and C**). Very similar responses were observed when we imaged the interaction of IgM<sup>+</sup> WEHI-231 B-lymphoma cells (**see Figure 3.14B**) and IgG<sup>+</sup> A20 B-lymphoma cells (**see Figure 3.7A**) with B16F1 cells expressing the single chain anti-Ig $\kappa$  Ab. Analysis of splenic B cells that had adhered to B16F1 expressing different levels of the single chain anti-Ig $\kappa$  surrogate Ag revealed a roughly linear relationship between the amount of Ag gathered by a B cell and the amount of p-Tyr signaling (**Fig. 3.6D**). We were also able to express the single chain anti-Ig $\kappa$  at a low frequency in bone marrow-derived dendritic cells (DCs) and showed that splenic B cells formed an IS when they adhered to these transfected DCs (**Fig.**

**3.14A).**

We then used the B16F1 surrogate APC system to assess how the Rap-cofilin pathway affects Ag gathering, BCR microcluster formation, and BCR signaling in the context of B cell-APC interactions. Imaging the B cell-APC interface showed that A20/vector cells that were allowed to attach to the surrogate APCs for 5 min extended F-actin-rich membrane processes along the surface of the APC and formed small p-Tyr-rich microclusters that co-localized with the surrogate Ag (**Fig. 3.7A**). By 10 min, the size and number of these microclusters increased as the A20 cells began to contract (**Fig. 3.7A**). In contrast, A20/RapGAPII did not spread to the same extent on the surface of the APC, as indicated by lower amounts of F-actin at the contact site. Importantly, this correlated with a significant reduction in the amount of Ag gathered, the number and size of BCR microclusters, and the amount of p-Tyr signaling (**Fig. 3.7A**). Similar results were obtained when we compared vector control and RapGAPII-expressing WEHI-231 B cells (**Fig. 3.14B**). As well, both BCR microcluster formation and p-Tyr signaling were greatly decreased when the DN Rap1N17 protein was expressed in primary B cells (**Fig. 3.7B**). Thus BCR-induced Rap activation is required for B cells to spread on the surface of APCs, gather Ag, and form BCR microclusters that initiate p-Tyr signaling.

To assess whether Rap-GTP promotes Ag gathering and BCR microcluster formation via its ability to initiate cofilin-dependent F-actin severing, we modulated cofilin activity in A20 cells. Preventing cofilin activation by expressing SSH-C/S, as well as by expressing the cofilin S3D phospho-mimetic mutant, significantly reduced the gathering of Ag into microclusters and the p-Tyr signaling at B cell-APC contact sites (**Fig. 3.8**). Conversely, expressing the activated cofilin S3A mutant protein in A20/RapGAPII cells overcame the defect in Ag gathering and microcluster-based p-Tyr signaling caused by blocking Rap activation (**Fig. 3.8**). For all cell

types analyzed, there was a roughly linear relationship between the amount of Ag gathered by the B cell at the contact site and the amount of microcluster-based p-Tyr signaling (**Fig. 3.15**). Thus the Rap-cofilin module controls the ability of B cells to gather Ag and this is directly related to the amount of BCR signaling that ensues.

ERM protein inactivation, which uncouples the plasma membrane from the cytoskeleton and decreases membrane rigidity [366, 371], is important for lymphocyte spreading and microcluster formation [62]. However, we found that abrogating ERM-mediated coupling of the plasma membrane to the cytoskeleton did not bypass the requirement for cofilin-mediated actin severing. Overexpressing a truncated, DN form of ezrin that cannot bind actin, and which presumably prevents endogenous ERM proteins from linking the plasma membrane to the cytoskeleton, did not restore normal levels of Ag gathering in A20 cells in which cofilin-mediated actin severing was blocked by expressing either SSH-C/S or RapGAPII (**Fig. 3.9 and Fig. 14C**). Thus F-actin severing is important for BCR microcluster formation and its role in this process is not redundant with that of ERM protein inactivation.

### **3.2.6 The Rap-cofilin pathway controls the mobility of BCR microclusters**

The submembrane cytoskeleton acts as a barrier to BCR diffusion, thereby preventing spontaneous BCR signaling [362]. Treating B cells with actin-depolymerizing drugs results in increased BCR mobility, Ag-independent microcluster formation, and Ag-independent BCR signaling [60, 61]. We found that disrupting the actin cytoskeleton with latrunculin A induced Ag-independent ERK phosphorylation to the same extent in A20/vector and A20/RapGAPII cells (**Fig. 3.10A**). This finding suggests that the main function of Rap activation in the initiation of BCR signaling is to promote cytoskeletal disassembly and allow the formation of signaling-

active BCR microclusters.

To test whether the Rap-cofilin pathway regulates the mobility of nascent BCR microclusters, we used A20 cells that express two different BCRs, one containing the endogenous murine IgG (mIgG) and the other containing human IgM (hIgM). This allowed us to initiate signaling by the hIgM-containing BCRs using anti-hIgM immobilized on a coverslip while inducing the formation of small, mobile mIgG-containing microclusters using a low concentration of Cy3-labeled anti-mIgG F(ab')<sub>2</sub> plus a 10-fold excess of unlabeled anti-mIgG Fab fragments. By using cells transfected with actin-GFP we could employ real-time total internal reflection fluorescence microscopy (TIRFM) to image the mobility of nascent mIgG-containing BCR microclusters at the contact site, relative to the F-actin cytoskeleton. Although BCR microclusters exhibited a wide-range of diffusion coefficients, Rap1N17- and SSH-C/S-expressing cells had fewer fast-diffusing microclusters than control cells (Fig. 10, *B* and *C*; and Supplemental Videos 6-9). The mean diffusion coefficient of mIgG microclusters in cells expressing Rap1N17 or SSH-C/S (0.026 and 0.034  $\mu\text{m}^2\text{s}^{-1}$ , respectively) was about half that in A20 cells transfected with the empty vector (0.069  $\mu\text{m}^2\text{s}^{-1}$ ) (**Fig. 3.10B**) and was similar to the mean diffusion coefficient of BCR microclusters in unstimulated A20 B cells [60]. This suggests that BCR signaling increases BCR microcluster mobility by activating the Rap-cofilin pathway and promoting F-actin severing. Consistent with this idea, the density of submembrane F-actin, as assessed by TIRFM, was greater in Rap1N17- and SSH-C/S-expressing cells than in control cells (**Fig. 3.10D**; and **Supplemental Videos 7-9**). Taken together, these data indicate that activation of the Rap-cofilin pathway by the BCR removes cytoskeletal barriers that limit the formation of BCR microclusters as well as their mobility within the plasma membrane.

### 3.3 Discussion

Severing of the cortical membrane cytoskeleton is a rate limiting step in cell shape change [208] as well as an initiating event in which Arp2/3-mediated actin polymerization at newly created barbed ends leads to a dynamic branched F-actin network that exerts outward force on the plasma membrane. We show for the first time that cofilin activation and cofilin-mediated F-actin severing are regulated by the Rap GTPases. Previous work had shown that activated Rap promotes actin polymerization via effector proteins such as Vav2, TIAM1, and RIAM [364]. Thus, Rap acts as a master regulator of cell morphology and cytoskeletal organization via its ability to promote both cofilin-mediated F-actin severing and subsequent branched actin polymerization.

B cell activation *in vivo* may often involve the interaction of B cells with APCs bearing captured Ags. The ability of B cells to spread across the surface of an APC increases potential encounters with membrane-bound Ags, thereby enhancing the formation of BCR microclusters that initiate signaling. Thus the cytoskeletal reorganization that promotes B cell spreading is a critical determinant of whether BCR signaling exceeds the threshold for B cell activation. Our data provide new insights into how these cytoskeletal changes are initiated (summarized in Fig. 11). We show that Rap-dependent activation of cofilin is required for BCR signaling to stimulate F-actin severing and to initiate the accelerated actin dynamics that drive cell spreading. Moreover, by using surrogate APCs we show that activation of the Rap-cofilin signaling module promotes the formation of BCR microclusters and is a key determinant of the extent of Ag gathering by BCR microclusters and the magnitude of resulting BCR signaling. BCR-induced activation of the Rap-cofilin module also leads to increased mobility of nascent BCR microclusters, presumably by breaking down cytoskeletal barriers that limit BCR diffusion. This

can facilitate the formation of larger, more mature microclusters with enhanced signaling capabilities. Thus activation of the Rap-cofilin signaling module couples cell spreading with increased BCR mobility, thereby optimizing Ag encounter, microcluster formation, and BCR signaling.

Although *ex vivo* murine splenic B cells transiently extend membrane processes across Ag-bearing surfaces (3), LPS/IL-4-activated primary B cells exhibit much more dramatic spreading on Ag-bearing APCs than do resting B cells (Freeman and Gold, unpublished observations). This is consistent with previous work by Severinson and colleagues showing that LPS/IL-4-activated primary B cells undergo a sustained spreading response when plated on immobilized Abs against membrane Ig, CD44, LFA-1, and other cell surface proteins, whereas resting B cells do not [372]. By altering cytoskeletal regulation, danger signals such as TLR ligands may prime B cells for enhanced actin dynamics and BCR microcluster mobility upon APC encounter. This could increase the probability of the APC-B cell interaction leading to B cell proliferation and Ab production, especially when Ag densities are low. This may be a novel mechanism by which danger signals lower the threshold for B cell activation when antigens are presented in the context of microbial infections or adjuvants. It is intriguing to speculate that memory B cells are also primed for enhanced actin dynamics and undergo robust spreading in the absence of TLR stimulation, as is the case for the B cell lines we examined. Although the nature of this TLR-induced change in B cell cytoskeletal regulation is not known, our preliminary results indicate that the extent of BCR-induced cofilin dephosphorylation is significantly greater in LPS- or CpG DNA-activated primary B cells than in *ex vivo* cells, even though the basal levels of phosphorylated cofilin is similar in resting and activated B cells (Freeman and Gold, unpublished observations). We are now testing whether B cell activation

increases the expression or activity of Slingshot, or other phosphatases that can dephosphorylate cofilin, and whether this is the key regulatory switch that enhances actin dynamics and cell spreading in activated B cells.

To study the relationship between Ag gathering and BCR signaling, we developed a novel surrogate APC system that can be used with any B cell expressing mouse  $\kappa$  light chain. Using this system we validated observations made using lipid bilayers, demonstrating a relationship between the extent of lymphocyte spreading, the amount of Ag gathered into BCR microclusters, and the magnitude of resulting BCR signaling. Such surrogate APCs can facilitate detailed studies of the mechanisms that underlie the dynamic cytoskeletal and membrane reorganization that occur when B cells encounter Ag-bearing APCs. In this report we show that both Rap activation and cofilin dephosphorylation are important for cell spreading, Ag gathering, microcluster formation, and BCR signaling induced by APC-associated Ags. Our observation that expressing the non-phosphorylatable S3A 'active' form of cofilin overcame the impaired cell spreading and Ag gathering caused by blocking Rap activation indicates that promoting cofilin activation is one of the main functions of Rap during APC-induced B cell activation. Activated Rap also promotes integrin activation in B cells (21), which enhances B cell spreading in lipid bilayer models of B cell-APC interactions [321]. However, expressing the cofilin S3A mutant protein did not restore the ability of A20/RapGAPII cells to adhere to and spread on immobilized integrin ligands (data not shown). This indicated that the active cofilin S3A protein restored BCR-induced spreading in A20/RapGAPII cells via its effects on actin dynamics, as opposed to restoring integrin activation.

Dephosphorylation of cofilin on S3 exposes a globular region that can bind to actin filaments and induce a structural twist that leads to severing of the filament [373]. The

mechanism by which BCR-induced Rap activation promotes cofilin dephosphorylation remains to be determined. Cofilin is phosphorylated on S3 by LIM domain kinase (LIMK) but BCR signaling did not reduce the amount of phosphorylated, active LIMK in B cells (data not shown). Instead, Rap-GTP could act through various effector proteins to increase the enzymatic activity of SSH or promote the release of SSH from 14-3-3 proteins that sequester it away from cofilin. Rap may also control cofilin dephosphorylation by regulating local cytoskeletal dynamics. Consistent with this idea, disrupting the actin cytoskeleton with latrunculin A increased cofilin phosphorylation in A20 cells whereas stabilizing the actin cytoskeleton with jasplakinolide caused complete dephosphorylation of cofilin, even when Rap activation was blocked (data not shown).

Another question that remains to be addressed is which Rap proteins regulate cofilin dephosphorylation in B and T cells. There are five Rap proteins, Rap1A, Rap1B, Rap2A, Rap2B, and Rap2C, each of which is encoded by a separate gene. We have shown that the BCR activates both Rap1 and Rap2 proteins and that RapGAPII expression, as we have done here, blocks the activation of both Rap1 and Rap2 by the BCR (21). Further studies using cells in which individual Rap genes are disrupted or silenced would be required to assess the relative roles of the different Rap proteins in regulating cofilin.

The submembrane skeleton of cortical actin filaments is linked to the plasma membrane by ERM family proteins, creating cytoskeletal barriers that limit the diffusion of membrane proteins. These actin corrals or picket fences maintain lymphocytes in a resting state by limiting spontaneous AgR aggregation and signaling [60]. The removal of these barriers allows AgR microclusters to form and assemble signalosomes. These initial events in AgR signaling appear to involve both the inactivation of ERM proteins [362] and F-actin severing. We showed that

BCR-induced activation of the Rap-cofilin signaling module is important for BCR microcluster formation and that it acts independently of ERM protein inactivation. The activation of both Rap and cofilin was required for BCR-induced cell spreading and microcluster formation even when ERM protein-mediated coupling of the membrane to the cytoskeleton was abrogated by expressing a DN form of ezrin.

In summary, our demonstration that F-actin severing initiated by the Rap-cofilin pathway is important for AgR microcluster formation and microcluster-based signaling provides new insights into these critical early events in AgR signaling.

### 3.4 Figures

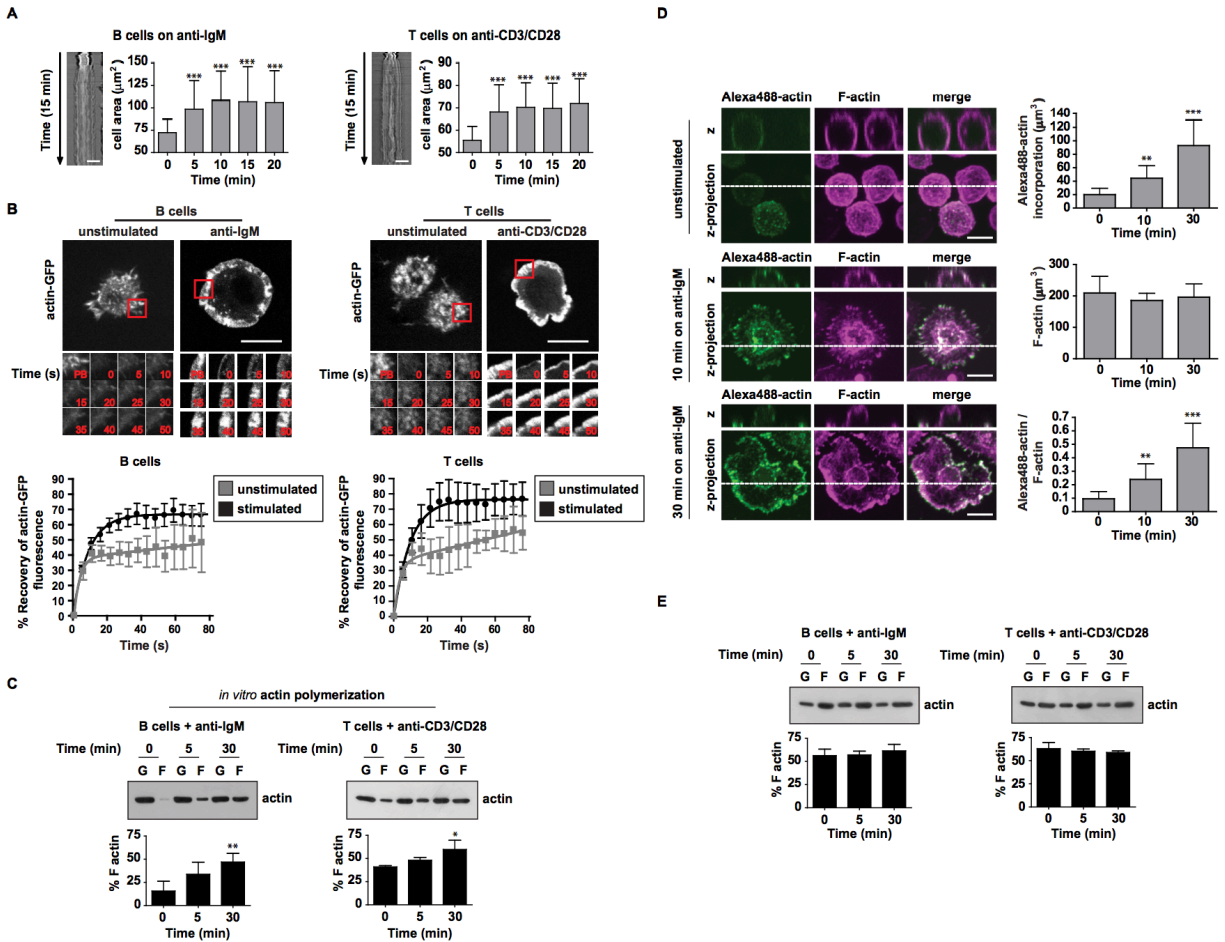
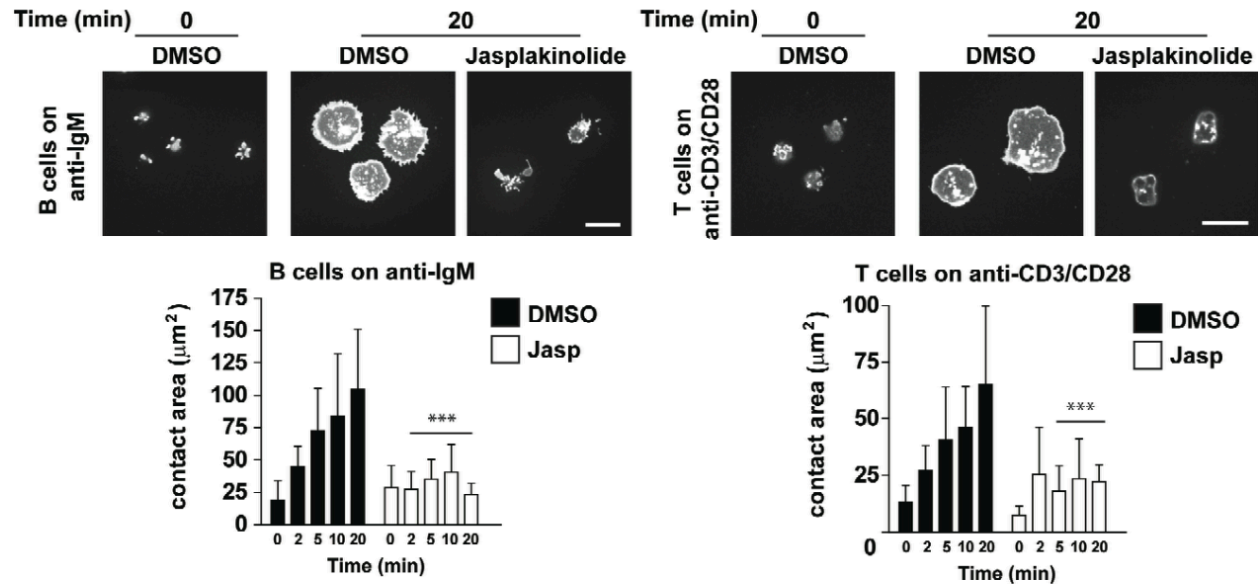


**Figure 3.1.** *B* and *T* cell spreading is associated with increased actin dynamics and actin reorganization. *A*, Kymographs showing the spreading of representative LPS/IL-4-activated murine *B* cells or IL-2-activated murine *T* cells were generated from DIC images of the cell-substrate contact that were collected in real time (see Supplemental Videos 1 and 2). The cell area (mean  $\pm$  SD for  $>60$  cells from 3 experiments) was determined at the indicated times after the cell first contacted the substrate. \*\*\* $p < 0.001$  relative to time 0. *B*, FRAP analysis of membrane-proximal ROIs in LPS/IL-4-activated *B* cells or IL-2-activated *T* cells that had been transfected with actin-GFP and then plated on fibronectin (unstimulated) or fibronectin plus immobilized anti-IgM or anti-CD3/CD28 (stimulated) for 1 h. After recording the pre-bleach

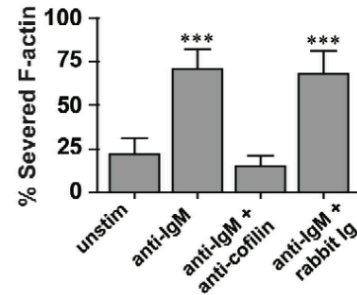
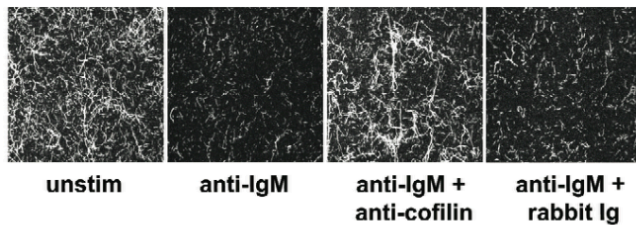
(PB) fluorescence intensity in a membrane-proximal region of interest (ROI) indicated by the red box, the ROI was photobleached and fluorescence recovery was measured at 5 s intervals over 1 min (see Supplemental Videos 3 and 4). Representative fluorescence images for single cells are shown in the *left panels*. Scale bars, 10  $\mu\text{m}$ . The recovery of actin-GFP fluorescence after photobleaching (mean  $\pm$  SD for 30 cells from 3 experiments) is graphed in the *right panels*. *C*, Primary B cells were stimulated in suspension with 10  $\mu\text{g/ml}$  anti-IgM. Primary T cells were stimulated in suspension with anti-CD3 plus goat anti-hamster IgG to cluster the TCR, along with anti-CD28. After the indicated stimulation times, the cells were solubilized. The cell extracts were sonicated to destroy pre-existing actin filaments and then incubated at 37°C for 10 min before being separated into soluble and insoluble fractions containing G- and F-actin, respectively. A representative blot is shown and the amount of F-actin generated *in vitro*, expressed as a percent of the total F- plus G-actin (mean  $\pm$  SEM from 3 experiments), is graphed. \* $p < 0.05$ , \*\* $p < 0.01$  relative to time 0 (unstimulated cells). *D*, *De novo* actin polymerization was assessed in splenic B cells that were left in suspension (unstimulated) or plated on anti-IgM. Cells were permeabilized and incubated with Alexa488-actin for 30 s. Total F-actin was visualized with rhodamine-phalloidin. Representative images of Z-axis projections and single Z-slices along the dotted lines are shown. The graphs show newly incorporated Alexa488-actin (top), total F-actin (middle), and Alexa488-actin incorporation relative to total F-actin (bottom), which were calculated from 3D images of 20 cells from 3 experiments (mean  $\pm$  SD). Scale bars, 10  $\mu\text{m}$ . \*\* $p < 0.01$ , \*\*\* $p < 0.001$  relative to time 0. *E*, Murine B or T cells were stimulated in suspension for the indicated times, as in *C*. Soluble and insoluble fractions containing G- and F-actin, respectively, were analyzed by immunoblotting with a  $\beta$ -actin Ab. A representative blot is shown and data from 3 experiments are graphed as the percent of total actin present as F-actin

(mean  $\pm$  SEM).

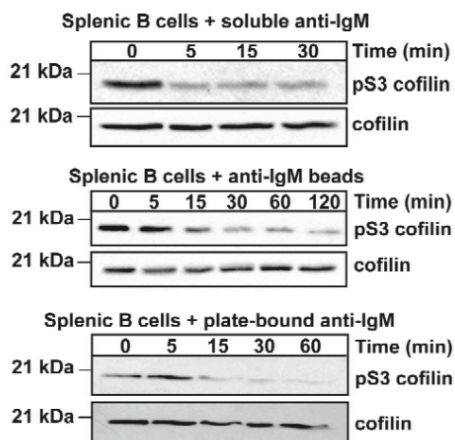
**A**



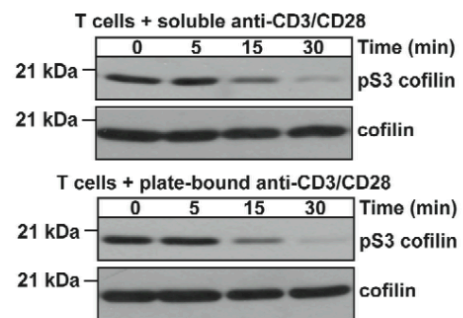
**B**



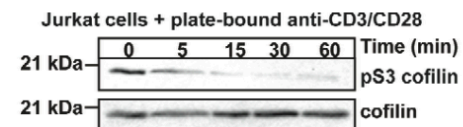
**C**



**D**

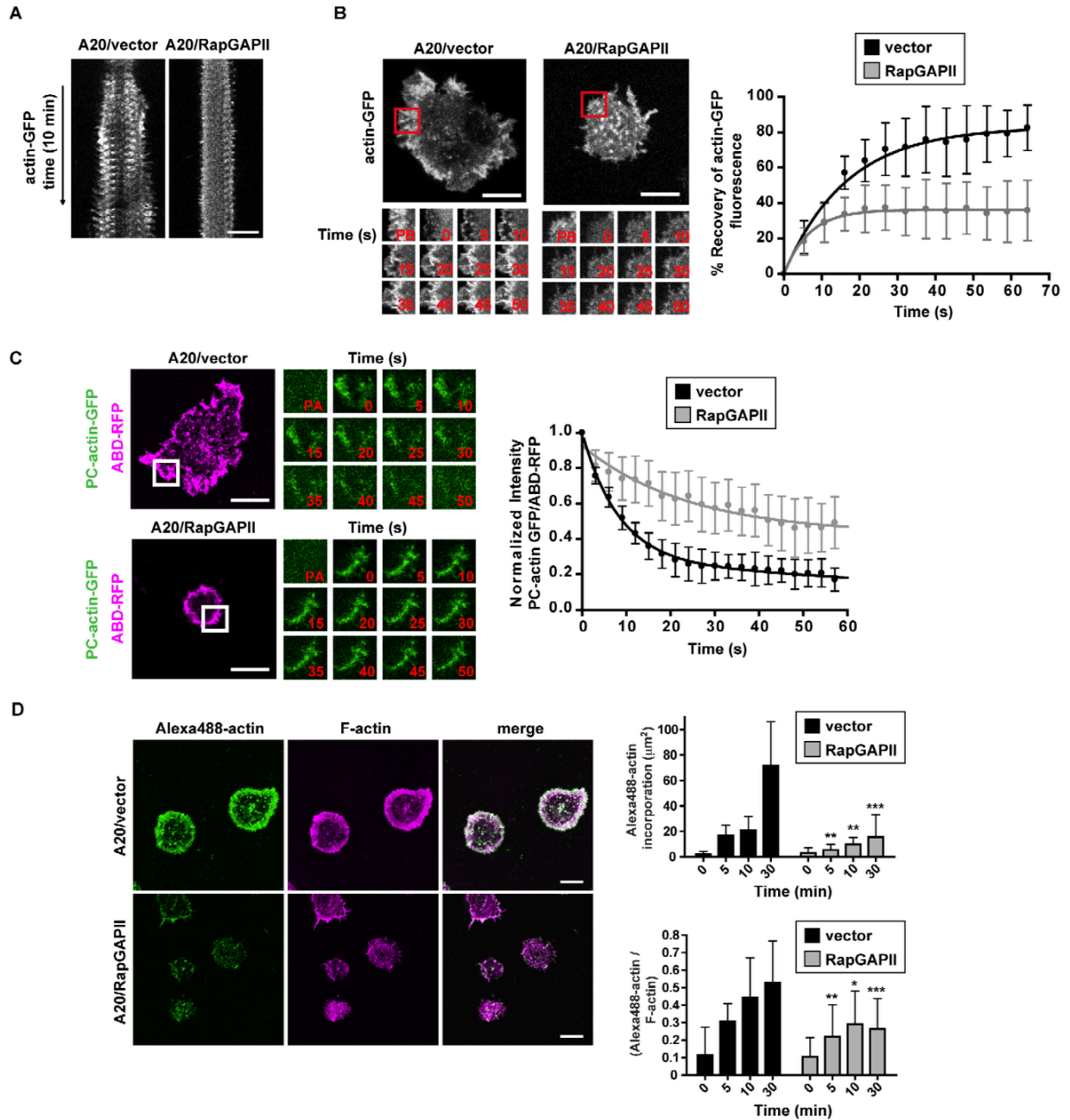


**E**



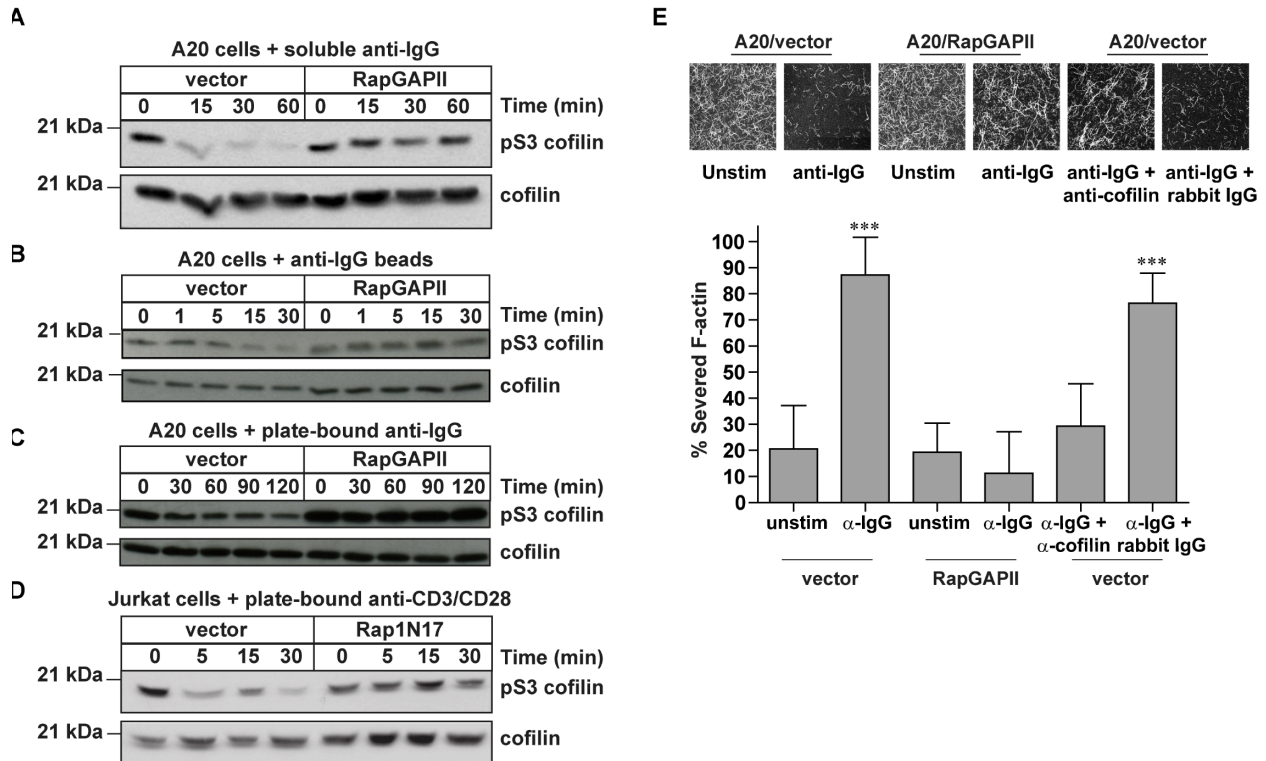
**Figure 3.2.** *AgR* signaling induces cofilin-mediated F-actin severing and cofilin dephosphorylation. *A*, LPS/IL-4-activated murine splenic B cells or IL-2-activated murine T

cells were incubated with CellMask Orange to label their plasma membranes. The cells were then treated for 1 min with DMSO or with 2  $\mu$ M jasplakinolide (Jasp) to stabilize F-actin filaments before being added to chamber slides coated with anti-IgM or anti-CD3/CD28. Fluorescence images of the cell-substrate interface were collected in real time using confocal microscopy. The *upper panels* show representative still images taken when the cells first contacted the substrate (0 min) or after 20 min of contact with the substrate. Scale bars, 10  $\mu$ m. Cell-substrate contact areas were calculated from these images and are graphed (mean  $\pm$  SD for >100 cells from 3 experiments) in the *lower panels*. \*\*\*p <0.001 compared to DMSO-treated cells at the same time point. *B*, Actin filaments containing Alexa488-labeled and biotinylated actin monomers were immobilized on slides using anti-biotin Abs and imaged before and after adding extracts from unstimulated or anti-IgM-stimulated (for 10 min) murine splenic B cells for 5 min. Representative images are shown. Where indicated, a cofilin Ab or rabbit IgG was added to the stimulated cell extract. The percent of F-actin released was calculated according to the equation:  $[1 - (\text{fluorescence after incubation with cell extract}) / (\text{fluorescence before adding cell extract})] \times 100\%$ . For each condition, the mean  $\pm$  SEM for 3 random fields from each of 3 experiments is graphed. \*\*\*p <0.001 compared to unstimulated cells. Cell lysis buffer alone did not cause detectable F-actin severing (data not shown). *C-E*, Phosphorylation of cofilin on serine 3 (pS3 cofilin) in LPS/IL-4-activated murine splenic B cells, murine T cells, or Jurkat cells was assessed by immunoblotting. For each panel, similar results were obtained in 2-4 experiments.

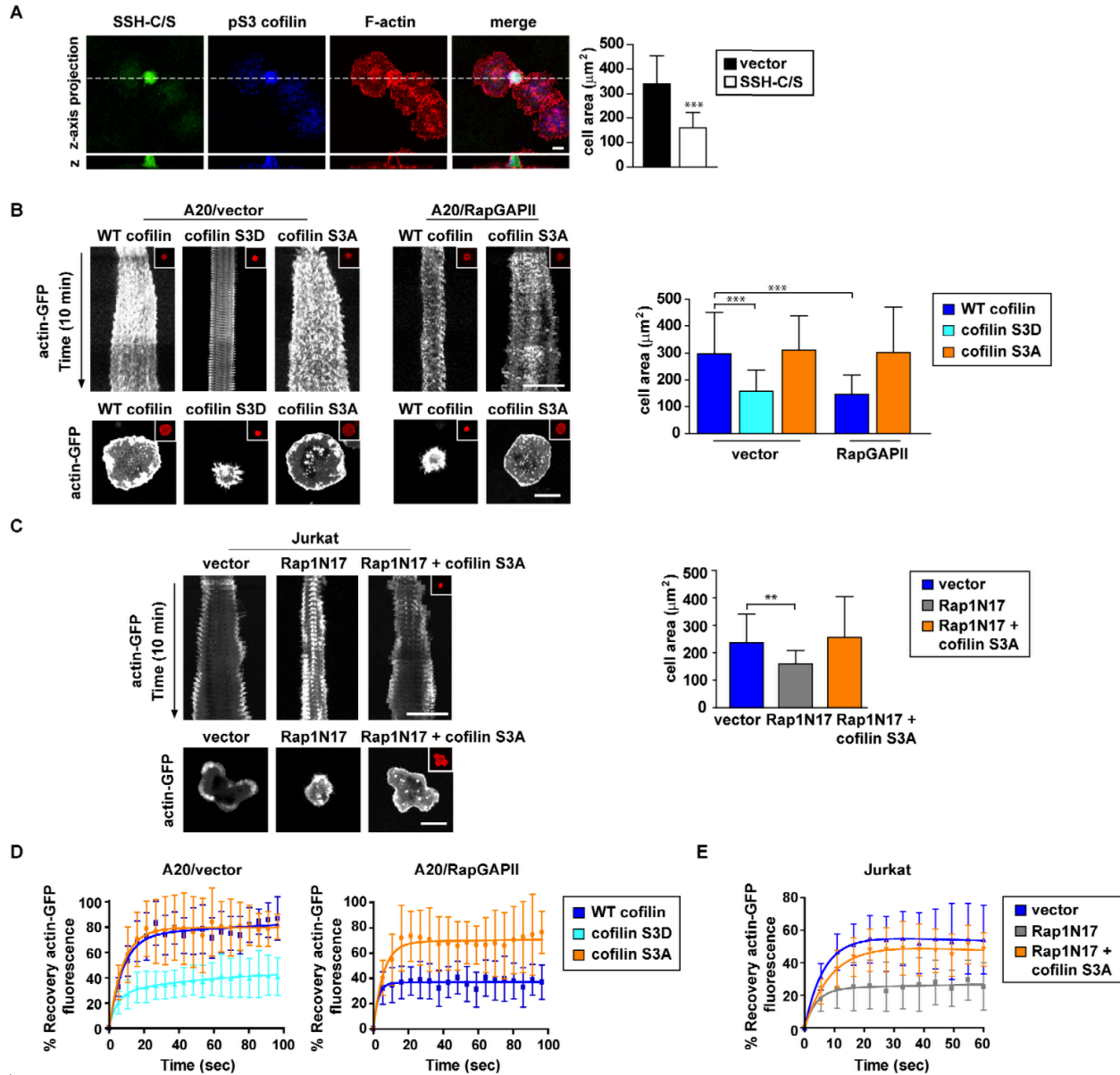


**Figure 3.3.** Rap activation is required for peripheral actin dynamics, F-actin severing, and actin incorporation at barbed ends. *A*, Cells were transiently transfected with actin-GFP, plated on anti-IgG-coated slides, and imaged in real time by confocal microscopy for 10 min. Videos recordings of the GFP and DIC channels (see Supplemental Video 5) were combined to generate kymographs from representative cells. Scale bars, 10  $\mu\text{m}$ . *B*, FRAP analysis of actin dynamics in

membrane-proximal ROIs of cells that were transiently transfected with actin-GFP and plated on anti-IgG for 1 h. Representative images show FRAP in single cells (*left panels*). Scale bars, 10  $\mu$ m. Fluorescence recovery over time (mean  $\pm$  SEM for 30 cells from 3 experiments) is graphed (*right panel*). *C*, Cells expressing utrophin actin binding domain-RFP (ABD-RFP) and photoconvertible (PC) actin-GFP were plated on anti-IgG. After initiating actin-GFP fluorescence in a membrane-proximal ROI (white box) by brief UV illumination, GFP and RFP signals were monitored in real time by confocal microscopy. Representative images show the loss of GFP fluorescence from the ROI. Scale bars, 10  $\mu$ m. The graph shows the ratios of the actin-GFP signal to the ABD-RFP signal (a measure of total F-actin) in the ROI, relative to the time 0 value. Each point is the mean  $\pm$  SEM for 30 cells from 3 experiments. *D*, Cells were plated on anti-IgG for 1 h and then permeabilized for 30 s in the presence of Alexa488-actin. F-actin was visualized with rhodamine-phalloidin. Scale bars, 10  $\mu$ m. The graphs show Alexa488-actin incorporation and the ratio of this value to the total F-actin in the cell (mean  $\pm$  SEM for 20 cells from 3 experiments). \* $p < 0.05$ , \*\* $p < 0.01$ , \*\*\* $p < 0.001$  compared to A20/vector cells at the same time point.

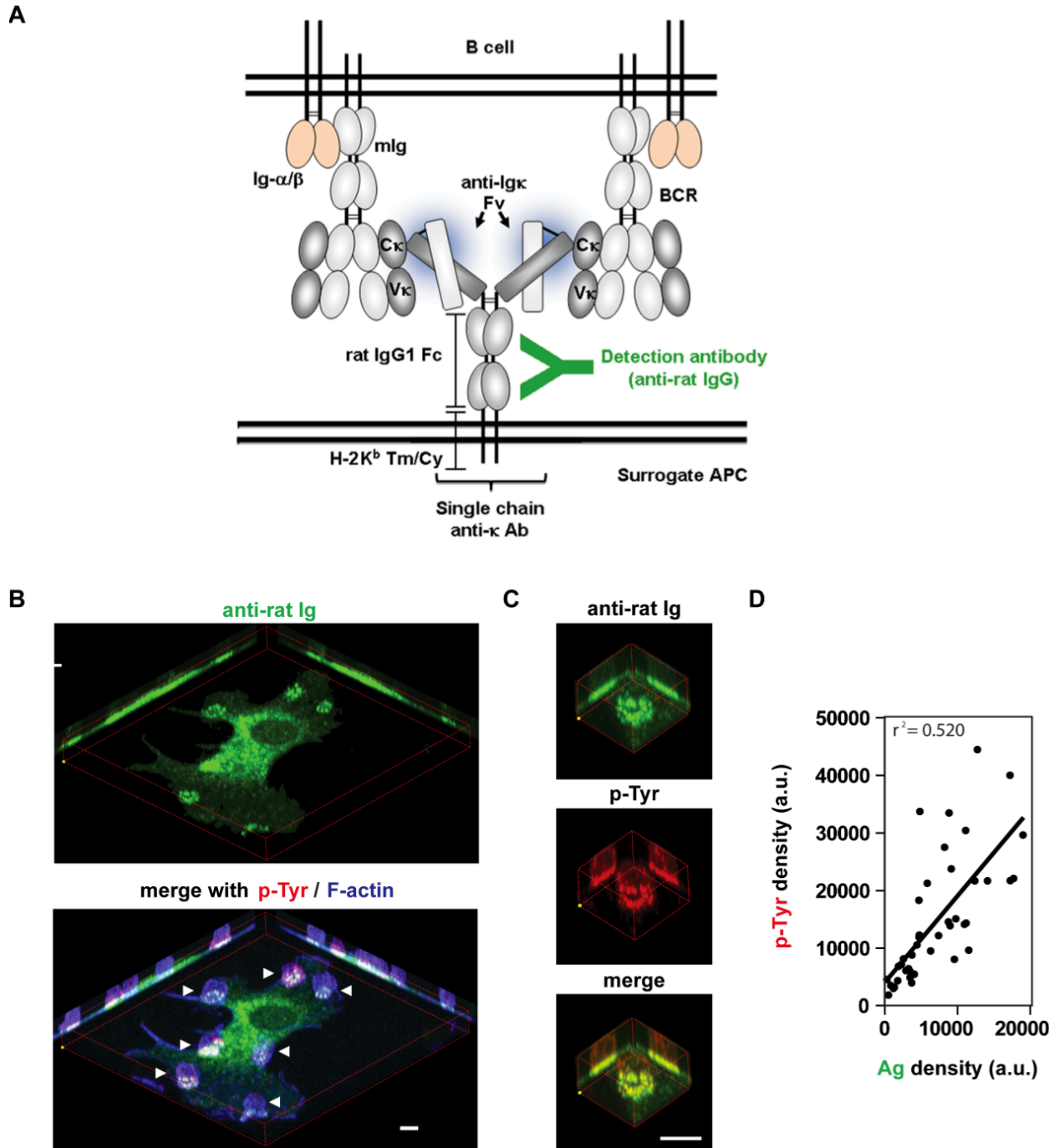


**Figure 3.4.** *AgR*-induced cofilin dephosphorylation depends on *Rap* activation. *A-D*, Cells were stimulated for the indicated times. Cofilin phosphorylation was assessed by immunoblotting. *E*, Extracts from unstimulated or anti-IgG-stimulated (10 min) cells were assayed for actin-severing assay as in Figure 2*B*. Where indicated, a cofilin Ab or rabbit IgG was added to the cell extracts. \*\*\* $p < 0.001$  compared to unstimulated (unstim) A20/vector cells. For each panel, similar results were obtained in 2-4 experiments.



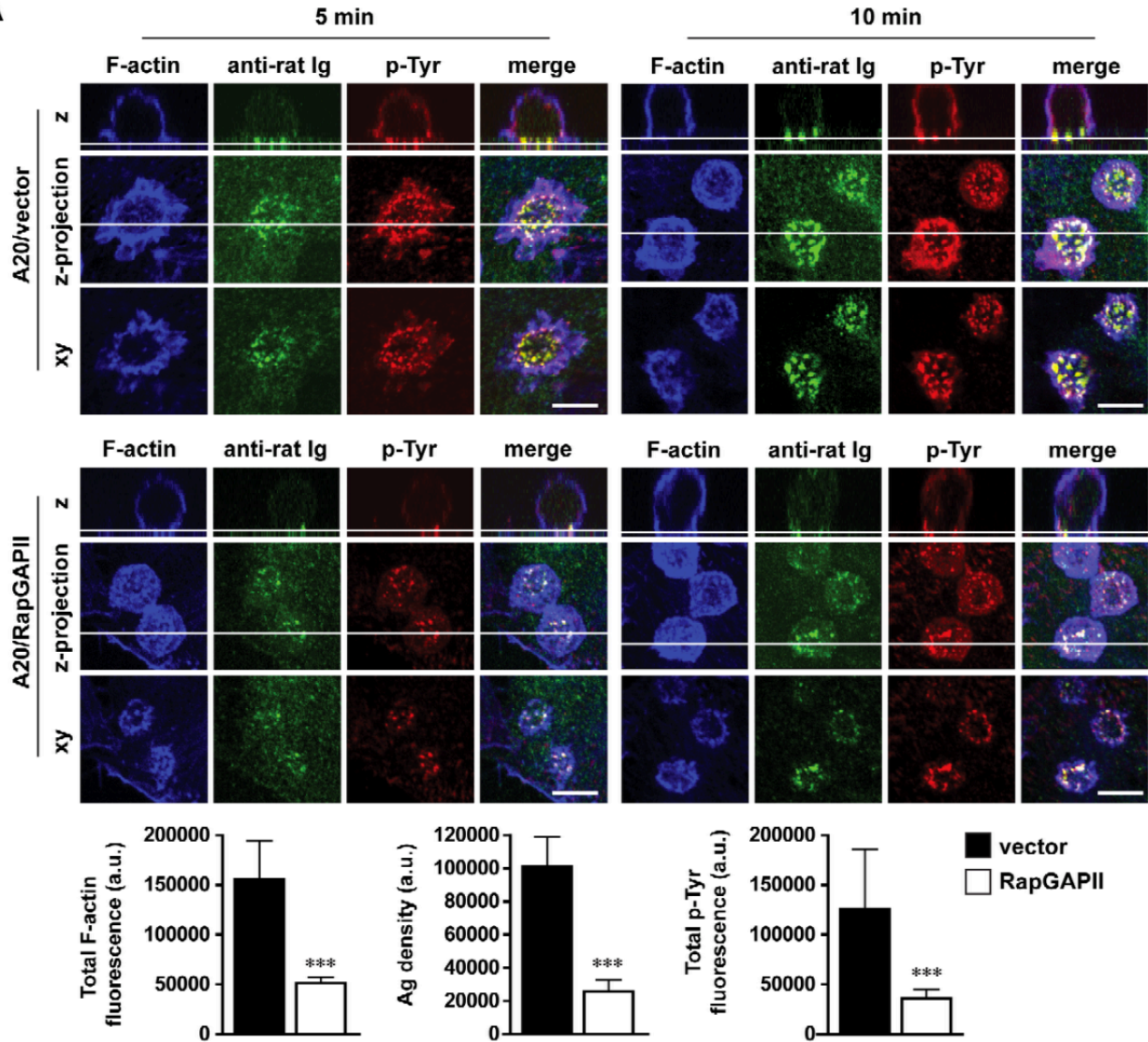
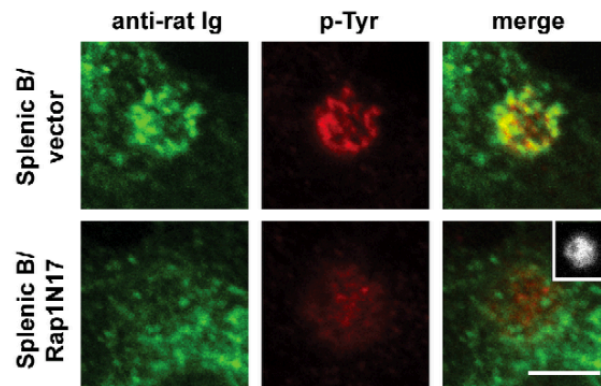
**Figure 3.5.** *Rap-dependent cofilin dephosphorylation is required for cell spreading and actin dynamics.* *A*, A20 cells were transiently transfected with Myc-tagged SSH-C/S, plated on immobilized anti-IgG for 1 h, and then stained for Myc (green), phospho-cofilin (blue), and F-actin (*left panel*). Representative images of Z-axis projections and a single Z-slice along the dotted line are shown. Scale bars, 10  $\mu\text{m}$ . In the *right panel*, A20 cells were transiently transfected with either Myc-tagged SSH-C/S or the empty vector, plated on immobilized anti-IgG for 1 h, and then stained for Myc (green) and F-actin. The cell area for cells expressing Myc-

tagged SSH-C/S or transfected with the empty vector (mean  $\pm$  SEM for 30 cells from 3 experiments) is graphed. \*\*\*p <0.001 *B* and *C*, A20/vector and A20/RapGAPII cells (*B*) were transiently transfected with actin-GFP as well as WT or mutant forms of cofilin fused to mCherry. Jurkat cells (*C*) were transiently transfected with actin-GFP and the indicated constructs. Cells were plated on anti-Ig or anti-CD3/CD28 and mCherry-expressing cells (inset: red) were imaged in real time as in Figure 3*A*. Kymographs (*upper panels*) show superimposed DIC and actin-GFP images for representative cells. Images of cell-substrate contacts for representative mCherry-expressing cells (*lower panels*) are shown, along with cell area (mean  $\pm$  SEM) for 30 cells from 3 experiments (*right panels*). Scale bars, 10  $\mu$ m. \*\*p <0.01, \*\*\*p <0.001. *D* and *E*, FRAP was performed as in Figure 1*B*. Recovery of actin-GFP fluorescence within photobleached ROIs (mean  $\pm$  SD for 30 cells from 3 experiments) is graphed.

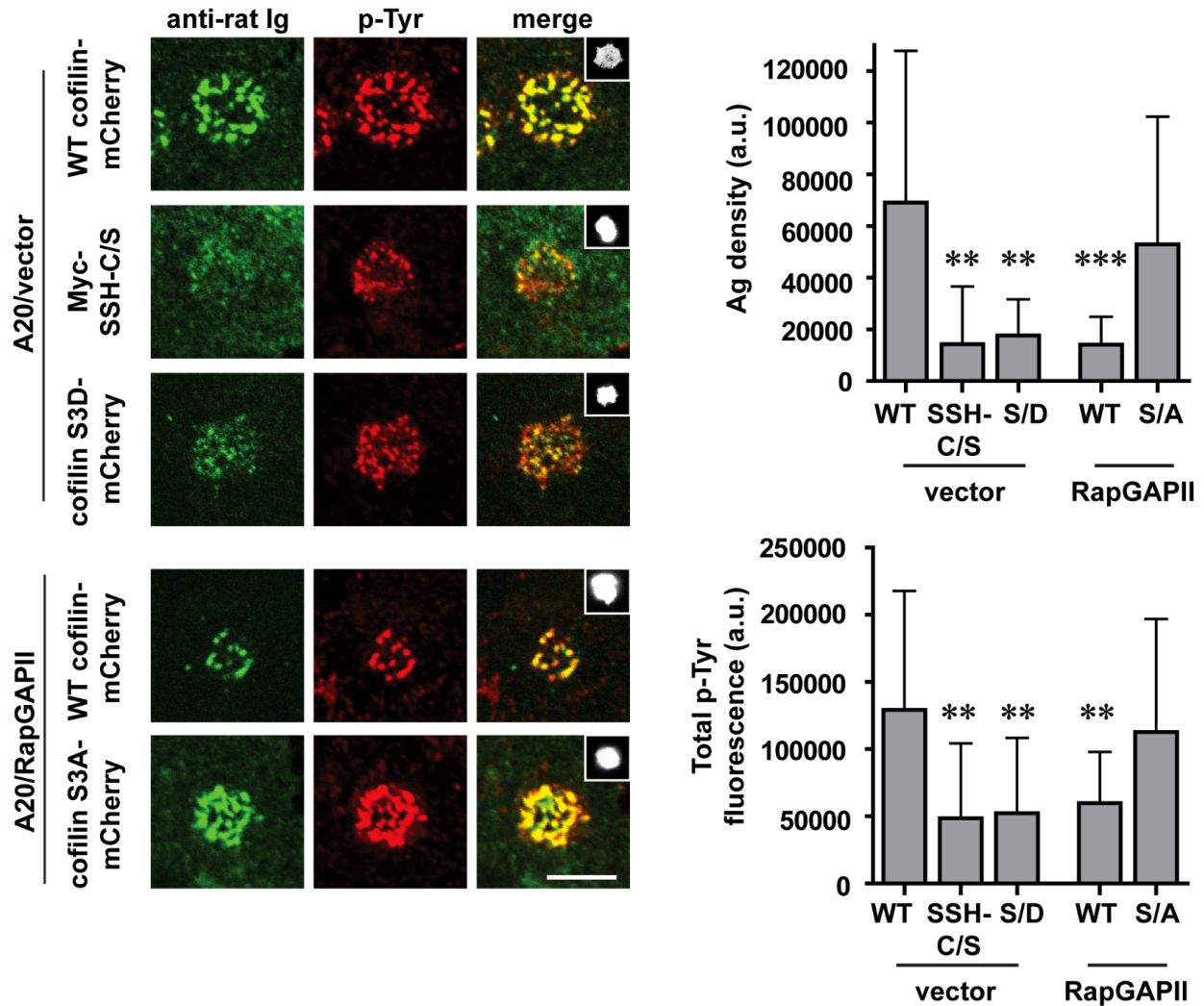


**Figure 3.6.** Surrogate APCs expressing a single chain anti-Ig $\kappa$  Ab induce B cell spreading, BCR microcluster formation, and BCR signaling. *A*, Schematic of BCR engagement by B16F1 cells expressing a transmembrane form of a single chain anti-Ig $\kappa$  Ab. *B-D*, LPS/IL-4-activated splenic B cells were plated on these APCs for 10 min and conjugates were stained for the anti-Ig $\kappa$

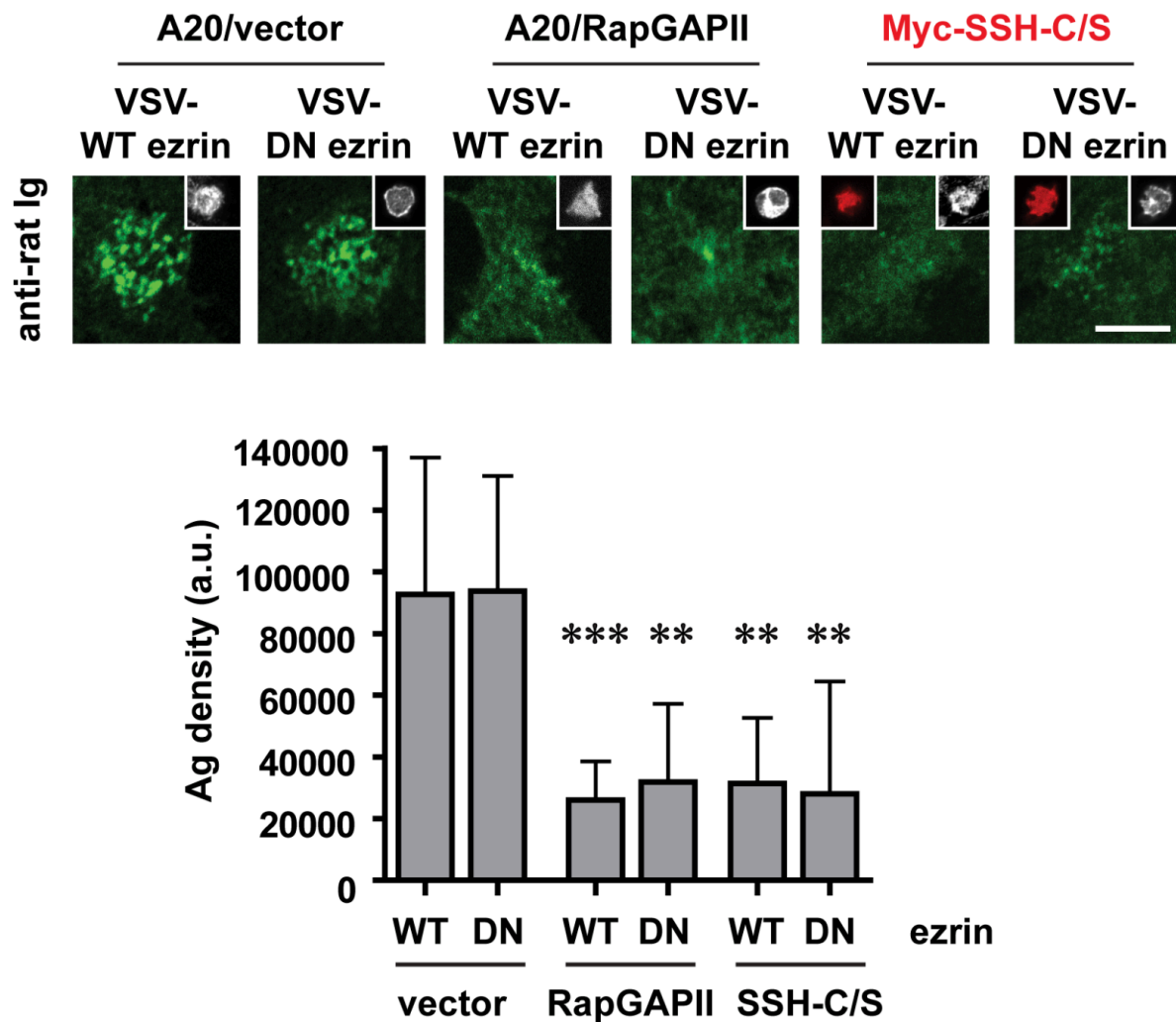
surrogate Ag (green), p-Tyr (red), and F-actin (blue). Representative 3D images show multiple B cells (arrowheads) bound to a single APC (*B*). Enlarged images of a single B cell show co-localization of the surrogate Ag and p-Tyr signaling (*C*). The relationship between the fluorescence signals representing the amount of Ag gathered and the amount of p-Tyr signaling, expressed as arbitrary units (a.u.) is plotted (*D*). Each dot is an individual B cell. Scale bars, 10  $\mu\text{m}$ .

**A****B**

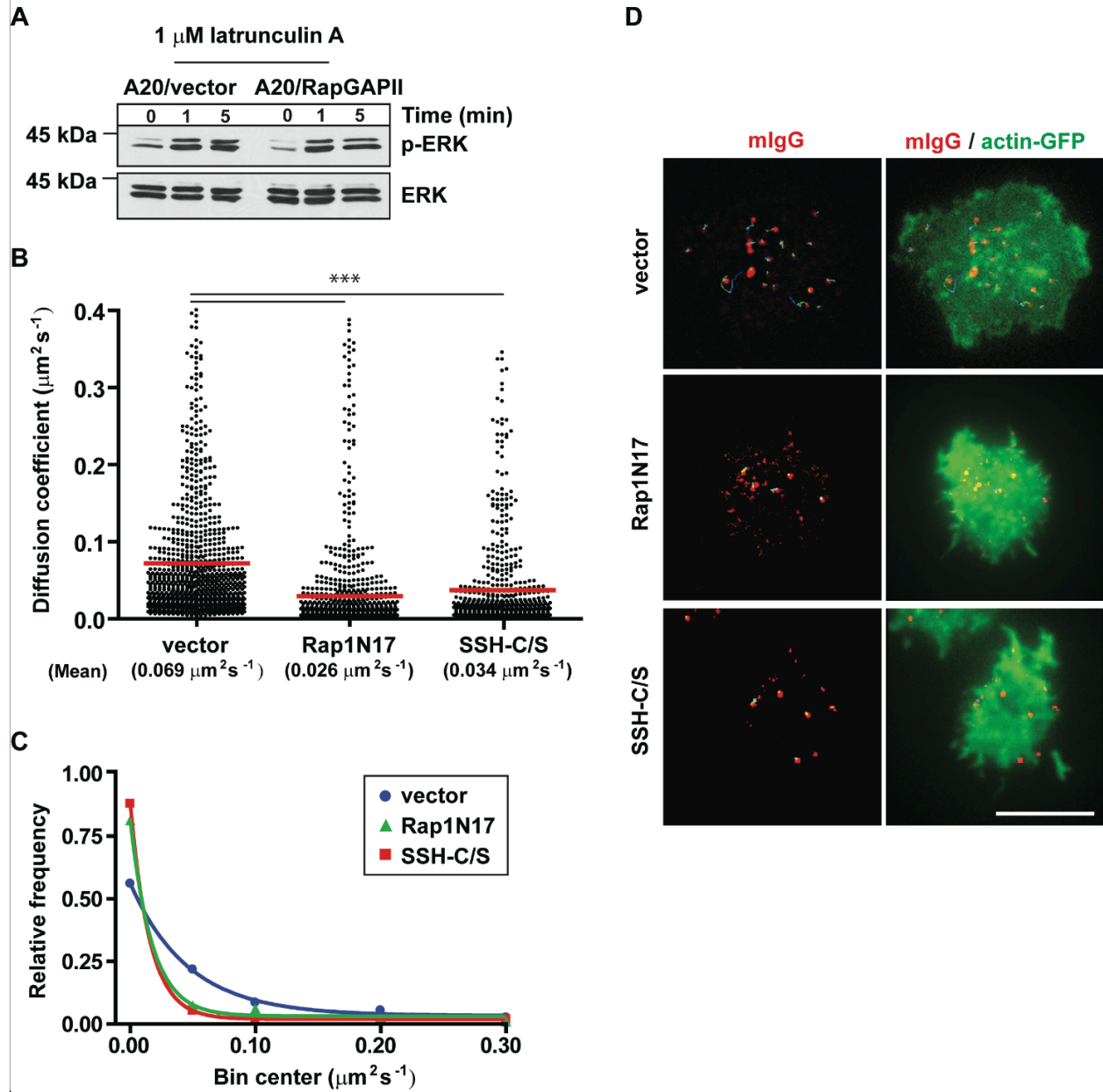
**Figure 3.7.** *Rap* activation is important for B cell spreading, Ag gathering, and BCR signaling during B cell-APC interactions. *A*, A20/vector cells (upper panels) and A20/RapGAPII cells (lower panels) were allowed to adhere to B16F1 cells expressing the single chain anti-Ig $\kappa$  Ab for 5 or 10 min and then stained as in Figure 6. Images of a single Z-slice along the dotted line (top rows), the Z-projection (middle rows), and the XY plane at the B cell-APC contact site (bottom rows) are shown for representative cells. Graphs show quantification in arbitrary units (a.u.) of F-actin in the A20 cells, the amount of Ag gathered, and the p-Tyr signal in the A20 cells at the plane of contact with the APC (mean  $\pm$  SD for >60 APC-associated A20 cells from 3 experiments). Scale bars, 10  $\mu$ m. \*\*\**p* <0.001. *B*, LPS/IL-4-activated splenic B cells were transiently transfected with a 1:3 ratio of a plasmid encoding GFP and either pCDNA3.1 or pCDNA3.1-Rap1N17. The cells were allowed to adhere to B16F1 cells expressing the single chain anti-Ig $\kappa$  Ab for 10 min and then stained with rabbit anti-p-Tyr and with Alexa568-anti-rat IgG to image the single chain anti-Ig $\kappa$ . Representative images of GFP-positive cells (inset: white) are shown. Scale bars, 10  $\mu$ m.



**Figure 3.8.** Cofilin dephosphorylation is important for B cell spreading, Ag gathering, and BCR signaling during B cell-APC interactions. A20/vector or A20/RapGAPII cells were transfected with either mCherry-tagged WT cofilin, cofilin S3A (S/A), cofilin S3D (S/D), or Myc-tagged SSH-C/S (inset: white). The cells were allowed to adhere to B16F1 cells expressing the single chain anti-Igk Ab for 10 min before imaging the plane of contact. Representative images are shown. Scale bars, 10  $\mu$ m. Ag gathering and p-Tyr signaling at the B cell-APC contact site were quantified as in Figure 7A. \*\*p < 0.01, \*\*\*p < 0.001.



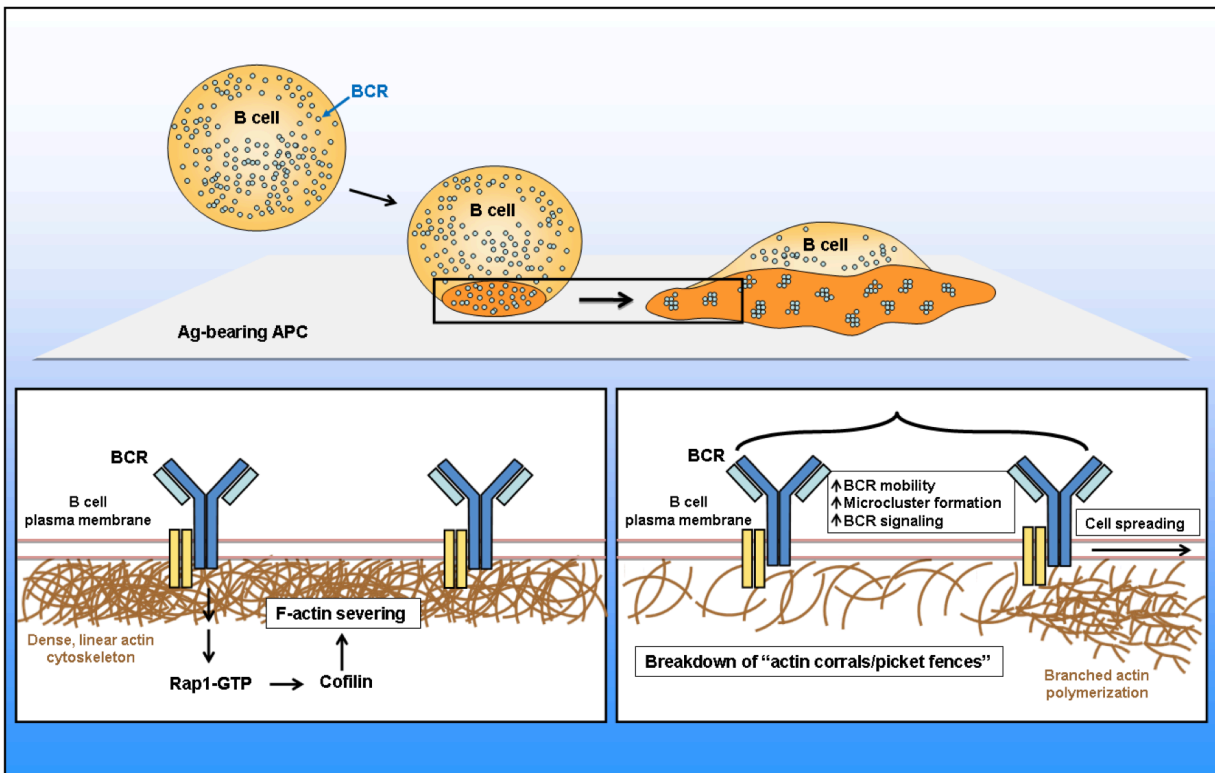
**Figure 3.9.** *The Rap-cofilin module acts independently of ezrin.* A20/vector and A20/RapGAPII cells, as well as A20 cells transiently transfected with Myc-SSH-C/S (inset: red), were transfected with VSV-G-tagged WT or DN ezrin (inset: white). The A20 cells were allowed to adhere to B16F1 cells expressing the single chain anti-Igk Ab for 10 min before imaging the plane of contact with surrogate APCs. Representative images are shown. Scale bars, 10  $\mu$ m. Additional images are shown in Supplemental Fig. 3C. Ag gathering at the contact site was quantified as in Figure 7A. \*\*p < 0.01, \*\*\*p < 0.001.



**Figure 3.10.** The Rap-cofilin pathway controls BCR microcluster mobility.

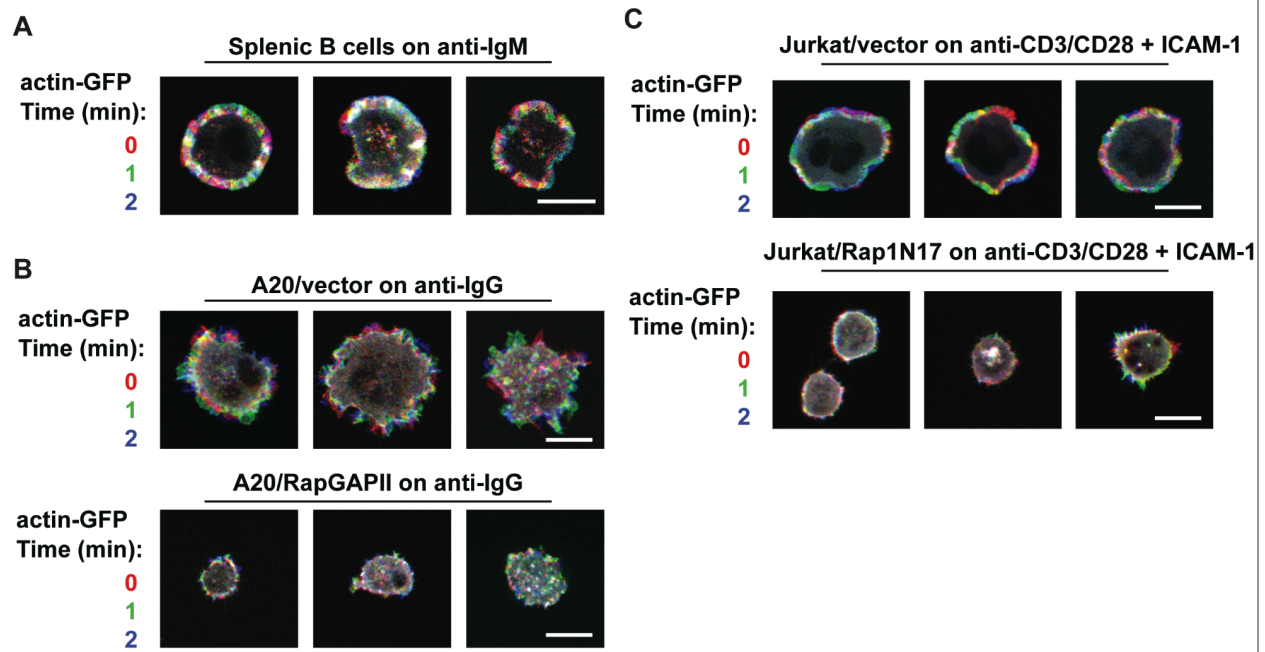
*A*, Cells were treated with latrunculin A for the indicated times. Cell extracts were probed for phospho-ERK (p-ERK) and total ERK. *B-D*, A20 cells that express both hIgM and mIgG were transfected with actin-GFP plus Rap1N17, SSH-C/S, or the empty pcDNA3.1 vector. The cells were mixed with 100 ng/ml Cy3-labeled anti-mIgG F(ab')<sub>2</sub> plus 1  $\mu\text{g}/\text{ml}$  anti-mIgG Fab, plated on anti-hIgM for 2 min, and then imaged by TIRFM. *B* shows the diffusion coefficients for BCR

microclusters (>500 tracks from >25 cells in 5 experiments; \*\*\*p <0.001 compared to cells transfected with the empty vector). *C* shows the relative frequencies of mIgG microclusters with diffusion coefficients in the indicated ranges. In *D* shows representative images of BCR microclusters (red) and their tracks (blue lines) alone (*left panels*) or merged with the actin-GFP signal (*right panels*). Scale bars, 10  $\mu$ m. BCR microcluster movement is shown in Supplemental Videos 6-9.



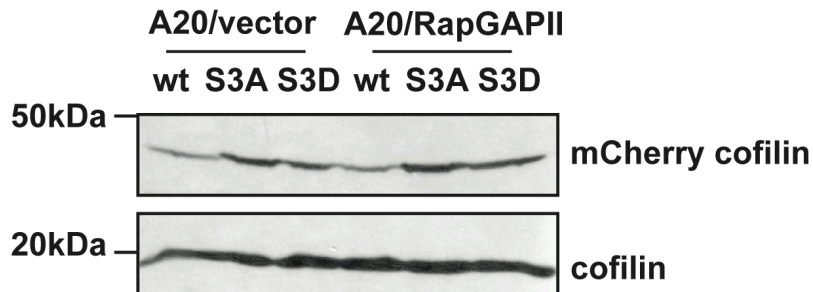
**Figure 3.11.** *The Rap-cofilin pathway promotes B cell spreading and BCR microcluster formation.* BCR signaling via the Rap1 GTPase activates cofilin by inducing its dephosphorylation. Activated cofilin initiates F-actin severing. The resulting breakdown of “actin corrals” enhances BCR mobility, leading to increased formation of BCR microclusters that can assemble signalosomes and initiate BCR signaling pathways. At the same time, free barbed ends of actin filaments that are generated by F-actin severing serve as sites where the

Arp2/3 complex can initiate branched actin polymerization. Such dendritic actin networks can exert outward force on the plasma membrane that promotes cell spreading.

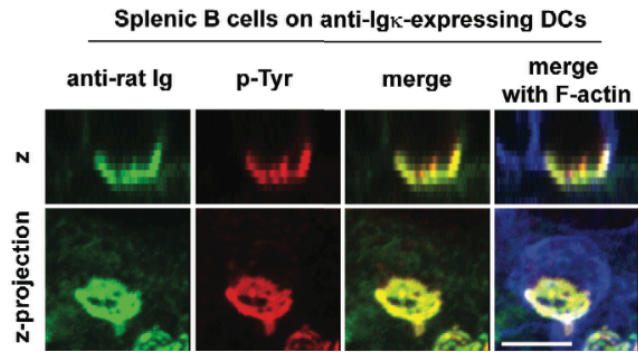
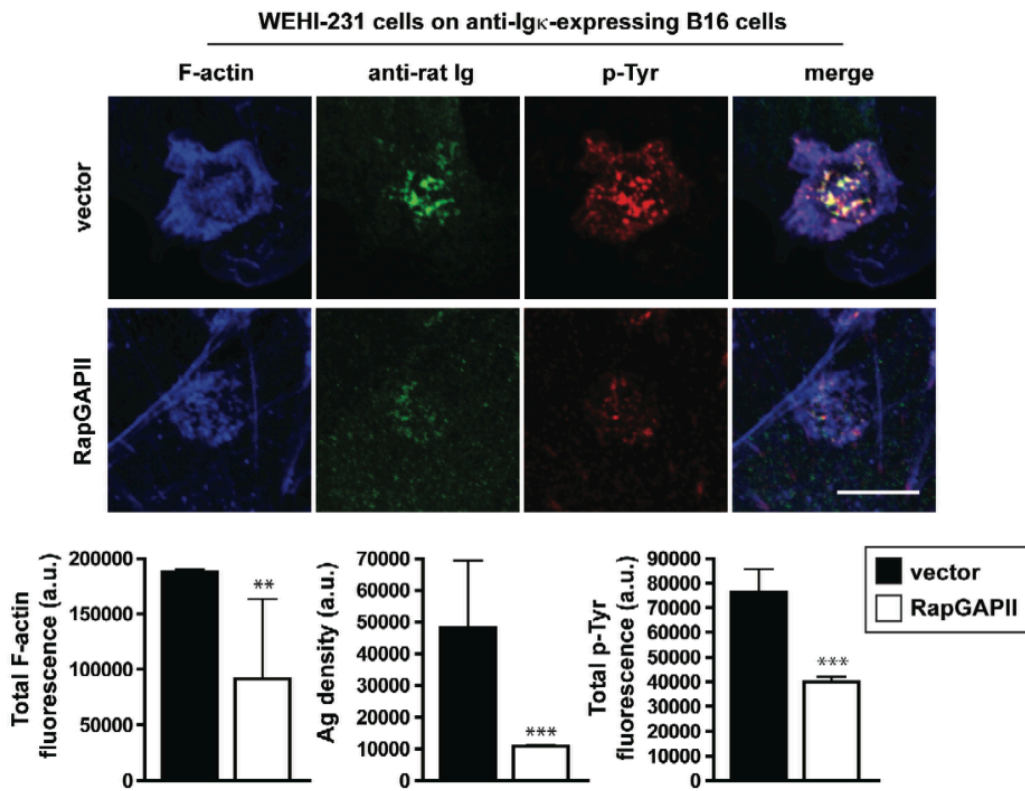
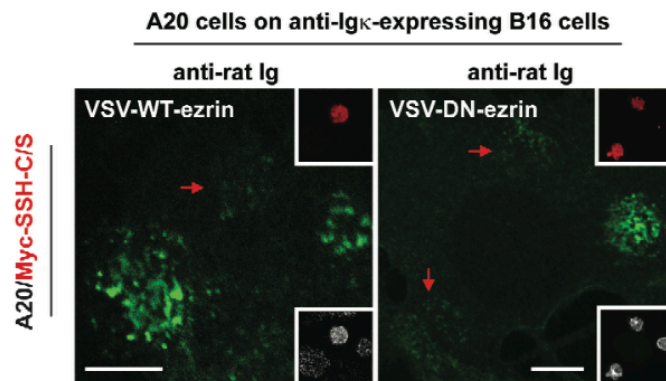


**Figure 3.12.** *Rap* activation is required for Ag receptor-induced increases in cytoskeletal dynamics. LPS/IL-4-activated murine splenic B cells were transiently transfected with a plasmid encoding actin-GFP and plated on immobilized anti-IgM (A). A20/vector and A20/ RapGAPII cells were transiently transfected with a plasmid encoding actin-GFP and plated on immobilized anti-IgG for 1 h (B). Jurkat cells were transiently co-transfected with actin-GFP plus either the empty pcDNA3.1 vector or pcDNA3.1 encoding Rap1N17, a dominant-negative form of Rap. The cells were then plated on slides coated with anti-CD3/anti-CD28 plus ICAM-1 for 1 h (C). Cells were imaged by confocal microscopy and actin-GFP fluorescence was imaged in real time for 2 min. For representative cells, the actin-GFP signals in still images taken at 0, 1, and 2 min were pseudo-colored and overlaid. Merged signals that appear white indicate static F- actin

structures, in contrast to the dynamic assembly and disassembly of F-actin structures indicated by individual colors. Cells expressing either RapGAPII or Rap1N17 had more static F-actin structures and did not spread to the same degree as control cells. Scale bars, 10  $\mu$ m.



**Figure 3.13.** *Expression of cofilin-mCherry fusion proteins.* A20/vector and A20/RapGAPII cells were transiently transfected with fusion proteins consisting of mCherry fused to either wild type (WT) cofilin, a non-phosphorylatable “active” mutant form of cofilin (S3A), or a mutant form of cofilin with a phosphomimetic aspartic acid residue (S3D). After 24 h, expression of these cofilin-mCherry fusion proteins, as well as the endogenous cofilin, was assessed by immunoblotting with a cofilin Ab. Fluorescence microscopy showed that ~20-30% of the cells were transfected (data not shown).

**A****B****C**

**Figure 3.14.** *The Rap-cofilin pathway regulates B cell spreading, Ag gathering, and BCR signaling during B cell-APC interactions, acting independently of ezrin.*

A, LPS/IL-4-activated splenic B cells were allowed to adhere for 10 min to primary DCs expressing the anti-Ig| surrogate Ag. The cells were then stained with Alexa488-anti-rat IgG to image the surrogate Ag, rabbit anti-p-Tyr to visualize BCR signaling, and rhodamine-phalloidin to visualize F-actin. Representative Z-projections as well as Z-axis sections are shown. Scale bars, 10  $\mu$ m. B, Vector control and RapGAPII-expressing WEHI-231 B-cells were allowed to adhere to B16F1 cells expressing the single chain anti-Ig| Ab for 10 min. The cells were then stained as in A. Representative images are shown. Graphs show quantification in arbitrary units (a.u.) of F- actin in the WEHI-231 cells, the amount of Ag gathered, and the p-Tyr signal in the WEHI-231 cells at the plane of contact with the APC (mean + SD for >60 APC-associated WEHI-231 cells from 3 experiments). \*\*p <0.01, \*\*\*p <0.001. C, A20 cells were transiently transfected with plasmids encoding Myc-tagged SSH-C/S (upper inset: Myc staining in red) plus either WT- or DN-ezrin (lower inset: VSV-G staining in white). The cells were allowed to adhere to B16F1 cells expressing the single chain anti-Ig| Ab for 10 min. Arrows indicate cells expressing both SSH-C/S and either WT-ezrin or DN-ezrin. Expressing either WT-ezrin or DN-ezrin did not restore Ag gathering to the level exhibited by untransfected A20 cells (cells without red arrows).

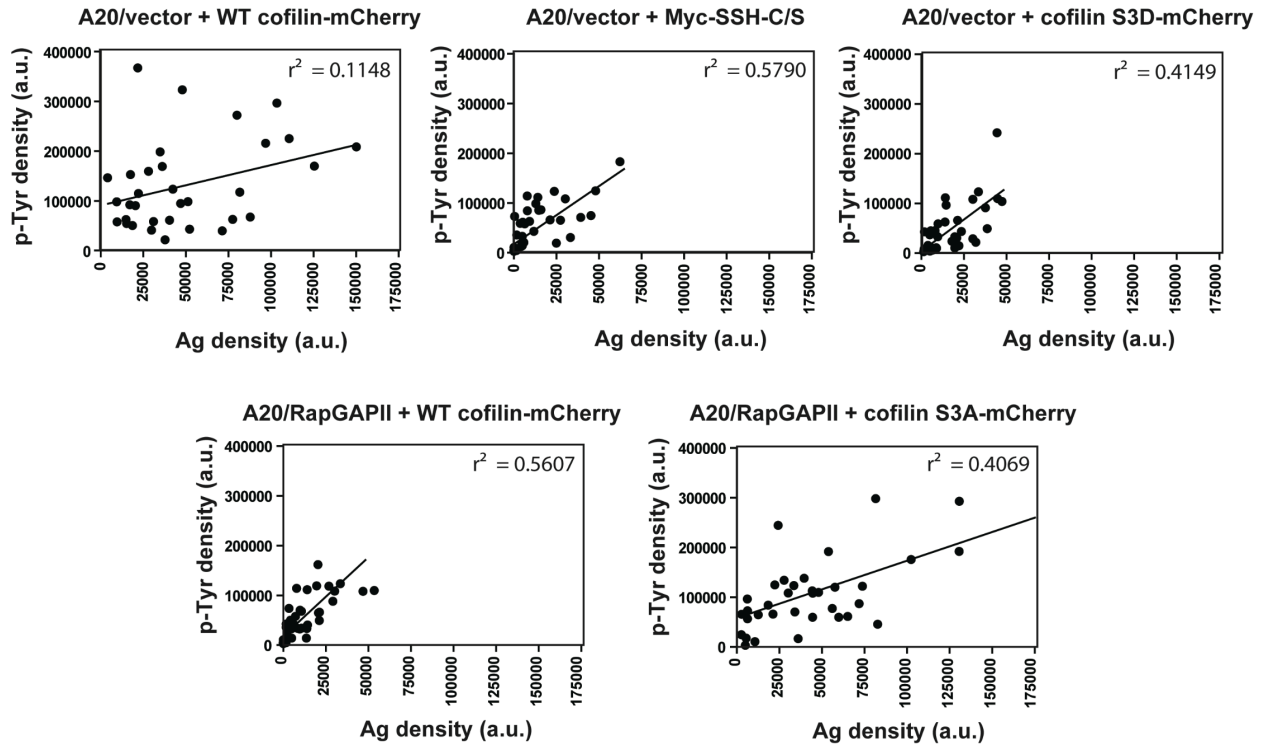


**Figure 3.15.** The magnitude of *p*-Tyr signaling is related to the amount of Ag gathered into microclusters at the B cell-APC contact. A20/vector or A20/RapGAPII cells were transiently transfected with the indicated cofilin-mCherry fusion protein or with Myc-tagged SSH-C/S (which was detected by staining for Myc). These cells were allowed to adhere to B16F1 cells expressing the single chain anti-Ig| Ab for 10 min. The fluorescence signals representing the amount of Ag gathered and the amount of *p*-Tyr signaling at the B cell-APC contact site were quantified as in Figure 6 and are expressed as arbitrary units (a.u.). Each point represents one B cell:APC conjugate. Note that expressing proteins that prevent activation of the Rap-cofilin signaling module (RapGAPII, cofilin-S3D-mCherry, Myc-SSH-C/S) limited the magnitude of Ag gathering and *p*-Tyr signaling, as indicated by the relative absence of cells with high values on both axes. Expressing the “active” cofilin S3A mutant protein bypassed the block in Rap

activation and allowed increased Ag gathering and p-Tyr signaling in A20 cells expressing RapGAPII.

### **3.5 Supplemental Videos**

Supplemental videos 1-9 can be found at the following website:

<http://www.jimmunol.org/content/187/11/5887/suppl/DC1>

### **3.6 Experimental Procedures**

#### **3.4.1 Cell preparation and culture**

Primary cells from C57BL/6 mice were isolated according to protocols approved by the University of British Columbia Animal Care Committee. Splenic B cells, as well as T cells from the spleen and lymph nodes, were isolated by depletion of non-B cells or non-T cells using kits from Stemcell Technologies. B cells were activated for 24-48 h with 5 µg/ml LPS plus 5 ng/ml IL-4 (R&D Systems) and T cells were activated for 24-48 h with 2.5 ng/ml IL-2 (R&D Systems) prior to being used for experiments. Dendritic cells (DCs) were obtained by culturing bone marrow cells in medium with 20 ng/ml GM-CSF for 8 days. A20 and WEHI-231 B-lymphoma cells, as well as Jurkat clone E6-1 cells, were obtained from the ATCC. A20 and WEHI-231 cells stably transfected with the pMSCVpuro vector (BD Biosciences) or with the pMSCV-FLAG-RapGAPII vector have been described previously [95, 374]. A20 cells expressing a transfected human IgM [375] were a gift from D. Lankar (Institut Curie, Paris, France). Cells were cultured in RPMI-1640 supplemented with 10% FCS, 2 mM glutamine, and 1 mM

pyruvate, with the addition of 50  $\mu$ M 2-ME for B cells.

### **3.4.2 Plasmids and transient transfections**

$\beta$ -actin-GFP was a gift from Dr. Robert Nabi (University of British Columbia). The pcDNA3.1 and pcDNA3.1-Rap1N17 plasmids have been described previously [95]. RFP fused to the F-actin-binding domain of utrophin (amino acids 1-261) [369] was a gift from Dr. William Bement (University of Wisconsin). Photo-convertible  $\beta$ -actin-GFP was a gift from Dr. Shernaz Bamji (University of British Columbia). Myc-tagged catalytically-inactive Slingshot (SSH-CS) in the pcDNA3.1 vector was a gift from Dr. Kensaku Mizuno (Tohoku University, Sendai, Japan). Cofilin cDNA was subcloned into the pmCherry-C1 vector (Clontech). The S3A and S3D mutations were made using the PCR QuikChange Lightning Site-Directed Mutagenesis kit (Stratagene). VSV-G-tagged DN ezrin (C-terminal truncation lacking amino acid residues 310-586) [376] was a gift from Dr. Monique Arpin (Institut Curie, Paris, France). Lymphocytes were transfected by nucleofection (Amaxa Biosystems). Amaxa mouse B cell or T cell transfection kits were used for LPS/IL-4-activated primary B cells and IL-2-activated primary T cells, respectively. Amaxa transfection kit V was used for A20 cells, WEHI-231 cells, Jurkat cells, and DCs. Cells were used for experiments 24 h after transfection.

### **3.4.3 Antibodies**

Goat anti-mouse IgM, goat anti-mouse IgG, goat anti-hamster IgG, goat anti-mouse IgG Fab fragment, and Cy3-labeled goat anti-mouse IgG F(ab')<sub>2</sub> fragment were obtained from Jackson ImmunoResearch Labs. The OKT3 anti-human CD3 mAb, the 145-2C11 anti-mouse CD3 mAb, and the 37.51 anti-mouse CD28 mAb were obtained from eBioscience. The 9.3 anti-human

CD28 mAb is described in [377]. Rabbit Abs against cofilin and cofilin that is phosphorylated on serine 3 (S3) were purchased from Cell Signaling Technologies. Mouse  $\beta$ -actin Ab was from Sigma-Aldrich. The biotinylated anti-Myc monoclonal Ab (9E10) was from BD Bioscience. The rabbit anti-VSV-G Ab was from Abcam. Alexa488- and Alexa647-labeled goat anti-rabbit IgG or goat anti-rat IgG, as well as streptavidin-FITC, were obtained from Molecular Probes-Invitrogen. Rabbit anti-p-Tyr was from BD Biosciences.

#### **3.4.4 Cell Spreading**

Tissue culture chambers (ibidi) were coated as in [95] with goat anti-mouse IgM or IgG (Jackson Immunoresearch) or with 10  $\mu$ g/ml human fibronectin (Sigma-Aldrich) plus anti-mouse CD3/CD28 (2C11 and 37.51 mAbs) or anti-human CD3/CD28 (OKT3 and 9.3 mAbs). Cells ( $5 \times 10^5$ ) in 0.3 ml modified HEPES-buffered saline (mHBS; 25 mM sodium HEPES, pH 7.2, 125 mM NaCl, 5 mM KCl, 1 mM CaCl<sub>2</sub>, 1 mM Na<sub>2</sub>HPO<sub>4</sub>, 0.5 mM MgSO<sub>4</sub>, 1 mg/ml glucose, 2 mM glutamine, 1 mM sodium pyruvate, 50  $\mu$ M 2-ME) were added to the chambers and imaged in real time at 37°C using a UPlan Apochromat 60 $\times$ /1.35 numerical aperture (NA) objective on an Olympus FV1000 confocal microscope. In some experiments the plasma membranes of the cells were labeled with CellMask Orange (Molecular Probes-Invitrogen) prior to imaging the cells. Videos were generated from time-lapse video recordings using FluoView 1.6 software (Olympus). ImagePro software (Media Cybernetics) was used to quantify cell area and generate kymographs.

#### **3.4.5 Cell stimulation and immunoblotting**

B cells ( $5 \times 10^6$  in 0.4 ml mHBS) were stimulated in suspension with 10  $\mu$ g/ml anti-IgM (splenic

B cells), 10 µg/ml anti-IgG (A20 cells), or 10<sup>7</sup> anti-Ig-coated beads prepared as in [95]. T cells were stimulated in suspension with 5 µg/ml anti-CD3, 10 µg/ml anti-CD28, and 10 µg/ml goat anti-hamster IgG. To stimulate cells with plate-bound Abs, tissue culture plates were coated with 10 µg/ml anti-Ig or with 10 µg/ml anti-CD3 plus 20 µg/ml anti-CD28, as in [95]. For immunoblot analysis, cells were lysed in RIPA buffer (30 mM Tris-HCl, pH 7.4, 150 mM NaCl, 1% Igepal (Sigma-Aldrich), 0.5% sodium deoxycholate, 0.1% SDS, 2 mM EDTA, 1 mM PMSF, 10 µg/ml leupeptin, 1 µg/ml aprotinin, 1 mM Na<sub>3</sub>VO<sub>4</sub>, 25 mM β-glycerophosphate, 1 µg/ml microcystin-LR). Cell extracts were then separated by SDS-PAGE and transferred to nitrocellulose filters. Filters were blocked with TBS (10 mM Tris-HCl, pH 8, 150 mM NaCl) containing 1% (w/v) BSA or 5% (w/v) milk powder, and washed with TBS plus 0.1% Tween-20. Primary Abs were added for 1-2 h at room temperature or overnight in the cold. After washing, the filters were incubated with horseradish peroxidase-conjugated secondary Abs for 1 h at room temperature. Bands were visualized using ECL (GE Life Sciences).

#### **3.4.6 Assays for G-actin/F-actin and *in vitro* actin-polymerizing activity**

Using a G-actin/F-actin *in vivo* assay kit (Cytoskeleton Inc.), cells were lysed and F-actin filaments stabilized according the manufacturer's instructions. Cell extracts were separated into soluble and insoluble fractions by ultracentrifugation and these fractions were analyzed by immunoblotting with a mouse β-actin Ab. To assay actin-polymerizing activity in cell extracts, cells were lysed in RIPA buffer containing 1 mM ATP and then sonicated for 1 min to destroy pre-existing F-actin. The sonicated cell extracts were incubated at 37°C for 10 min to allow *in vitro* actin polymerization. F-actin stabilization buffer (Cytoskeleton Inc.) was then added for 10 min before separating the extracts into soluble and insoluble fractions, which were analyzed by

immunoblotting with a  $\beta$ -actin Ab.

### **3.4.7 Fluorescence recovery after photobleaching (FRAP)**

Cells were incubated at 37°C on eight-well ibiTreat  $\mu$ -slides (ibidi) that had been coated with either 10  $\mu$ g/ml fibronectin, 10  $\mu$ g/ml anti-Ig, or 10  $\mu$ g/ml anti-CD3 plus 20  $\mu$ g/ml anti-CD28. FRAP was performed as described previously [378] using an Olympus FV1000 confocal microscope to image regions of interest (ROIs). After measuring the pre-bleach fluorescence signal, the ROI was photobleached using a 405 nm laser (100% intensity, 0.1 s). Fluorescence recovery within the ROI was then imaged over 1 min. FluoView v1.6 software was used to quantify the fluorescence signal within the ROI, which was normalized to the pre-bleach intensity. Curves representing the single exponential fit of the data were generated using Prism 4 software (GraphPad).

### **3.4.8 Labeling of actin filament barbed ends**

The incorporation of Alexa488-actin at barbed ends of actin filaments was performed as described [379]. Cells were stimulated as for spreading assays and then rendered semi-permeable by a brief incubation with warm permeabilization buffer (20 mM HEPES, pH 7.5, 138 mM KCl, 4 mM MgCl<sub>2</sub>, 3 mM EGTA, 0.4 mg/ml saponin, 1% BSA). Barbed ends were labeled by adding permeabilization buffer containing 1 mM ATP and 0.4  $\mu$ M Alexa488-actin. After 30 s at 37°C, cells were fixed by adding an equal volume of 8% paraformaldehyde in PBS. After 20 min at 20°C, the cells were stained with rhodamine-phalloidin for 20 min and imaged by confocal microscopy.

### **3.4.9 Immunofluorescence**

Immunofluorescence was performed as described previously [378]. After being fixed with 4% paraformaldehyde, cells were permeabilized with PBS containing 0.5% Triton X-100 for 3 min and then blocked with 2% BSA in PBS for 20 min. Primary Abs were added for 1 h and visualized with Alexa488- or Alexa647-labeled goat anti-rabbit IgG or goat anti-rat IgG, or with streptavidin-FITC. F-actin was visualized with rhodamine-phalloidin. Chambers or coverslips were treated with ProLong Gold anti-fade reagent containing DAPI (Molecular Probes). Images were captured using an Olympus FV1000 confocal microscope. FluoView v1.6 and ImagePro software were used to analyze confocal images and quantify fluorescence.

### **3.4.10 *In vitro* F-actin severing**

Cells were stimulated in suspension and lysed in 0.5 ml ice-cold lysis buffer (20 mM Tris-HCl, pH 8, 5 mM EDTA, 0.5 mM MgCl<sub>2</sub>, 0.5% Triton X-100, 0.5 mM ATP, 5 mg/ml BSA, 6 mg/ml glucose, 100 mM DTT, 1 mM PMSF, 10 µg/ml leupeptin, 1 µg/ml aprotinin, 1 µg/ml pepstatin, 1 mM Na<sub>3</sub>VO<sub>4</sub>, 25 mM β-glycerophosphate) for 20 min on ice. Insoluble material was removed by centrifugation. Severing assays were performed as described [368]. Chamber slides (ibidi) were incubated with 20 µg/ml anti-biotin Abs in ISAP buffer (20 mM Tris-HCl, pH 7.5, 5 mM EGTA, 2 mM MgCl<sub>2</sub>, 50 mM KCl, 1 mM ATP, 1 mM DTT) for 1 h at room temperature, washed with ISAP buffer, and then blocked with ISAP buffer containing 0.5 mg/ml BSA for 5 min. Biotinylated fluorescent F-actin filaments were generated by incubating 0.2 µM Alexa488-actin, 0.2 µM biotinylated actin, and 0.4 µM unlabeled actin (all from Cytoskeleton Inc.) in ISAP buffer for 1 h at 20°C. This mixture was then diluted 1:5 with ISAP buffer containing 5 mg/ml BSA and 100 mM DTT and added to the anti-biotin-coated chamber slide for 5 min. The

chambers were washed with ISAP buffer containing 5 mg/ml BSA and imaged using an Olympus FV1000 confocal microscope to determine the pre-assay fluorescence intensity of adhered F-actin filaments. Cell extracts were then added for 5 min, after which the chambers were washed and imaged to determine the fluorescence intensity of remaining F-actin filaments. Fluorescence intensities were quantified using ImagePro 3D software.

#### **3.4.11 *In vivo* F-actin severing**

Cells were transiently co-transfected to express the F-actin-binding domain (ABD) of utrophin fused to RFP (ABD-RFP) [369] as well as photo-convertible GFP [380] fused to  $\beta$ -actin. Peripheral ROIs containing F-actin structures were identified by ABD-RFP fluorescence and the actin-GFP in the ROI was converted to a fluorescent conformation by illumination with a 405 nm laser with a SIM scanner (1-5% intensity, 0.1 s). GFP and RFP fluorescence within the ROI were then monitored in real time at 37°C. Single exponential fit curves of the GFP/RFP ratio were generated using Prism 4 software.

#### **3.4.12 BCR microcluster formation on surrogate APCs**

B16F1 melanoma cells (ATCC) were grown in RPMI-1640 plus 8% FCS. Lipofectamine 2000 (Invitrogen) was used to transiently transfect these cells with a plasmid encoding a fusion protein consisting of a single chain Fv generated from the 187.1 rat anti-Ig $\kappa$  mAb, the hinge and membrane proximal domains of rat IgG1, and the transmembrane and cytoplasmic domains of H-2K<sup>b</sup> (Ait-Azzouzene et al., 2005). After 24 h, the B16F1 cells were detached in cell dissociation buffer (0.5 mM EDTA, 100 mM NaCl, 1 mM glucose, pH 7.4) and plated on chamber slides coated with 10  $\mu$ g/ml fibronectin for 4 h to promote flattening and spreading. B

cells ( $10^5$  cells in 100  $\mu$ l tissue culture medium) were added and allowed to attach to the B16 cells for 5-10 min at 37°C. After fixation and permeabilization, the cells were stained with rabbit anti-p-Tyr and then with Alexa568-goat anti-rabbit IgG to visualize p-Tyr, Alexa488-goat anti-rat IgG to visualize the single chain anti-Ig $\kappa$ , and rhodamine-phalloidin to visualize F-actin, before being imaged by confocal microscopy. FluoView v1.6 and ImagePro software were used to analyze confocal images and quantify fluorescence signals.

#### **3.4.13 BCR microcluster mobility**

Cells were incubated on ice with 100 ng/ml Cy3-labeled goat anti-mouse IgG F(ab')<sub>2</sub> plus 1  $\mu$ g/ml unlabeled goat anti-mouse IgG Fab for 10 min before being pelleted and resuspended in 30°C mHBS. The cells were then plated on chamber slides coated with goat anti-human IgM for 2 min and imaged at 30°C in order to limit endocytosis. Live imaging of the cell-substrate interface by TIRFM was performed using an inverted Zeiss Axiovert 200 microscope with a 100 $\times$ /1.45 NA TIRFM objective. For diffusion coefficient measurements, one-channel recordings from a 561 nm laser were acquired at 20 frames/s. Tracks that were followed for >1s were analyzed with Slidebook 5.0 software (Intelligent Imaging Innovations).

#### **3.4.14 Statistical analysis**

Student's two-tailed t test was used to compare sets of matched samples. GraphPad Prism software was used to generate non-linear regression curves.

## **4. Preventing the activation or cycling of the Rap1 GTPase alters adhesion and cytoskeletal dynamics and blocks the extravasation of metastatic melanoma cells into the lungs<sup>3</sup>**

### **4.1 Introduction**

In the preceding chapters, I described Rap as a GTPase that controls cytoskeletal responses in B cells that govern morphological changes and receptor diffusion. Rap GTPase are also master regulators of cell adhesion, polarity, and migration. In this chapter, we show that both blocking Rap1 activation and expressing a constitutively active form of Rap1 reduced the ability of B16F1 melanoma cells to extravasate from the microvasculature and form metastatic lesions in the lungs. This correlated with a decreased ability of the tumor cells to undergo transendothelial migration (TEM) *in vitro* and form dynamic, F-actin-rich pseudopodia that penetrate capillary endothelial walls *in vivo*. Using multiple tumor cell lines, we show that the inability to form these membrane protrusions, which likely promote TEM and extravasation, can be explained by altered adhesion dynamics and impaired cell polarization that result when Rap1 activation or cycling is perturbed. Thus, targeting Rap1 could be a useful approach for reducing the metastatic dissemination of tumor cells that undergo active TEM.

Solid tumor metastasis is a multi-step process wherein primary tumor cells become invasive, move through the stroma, penetrate blood or lymphatic vessels, enter the circulation, and traffic to distant sites. To establish secondary tumors at these sites, malignant cells must arrest within and exit from the microvasculature, invade the stroma of the new organ, and

---

<sup>3</sup> A version of this chapter is published. Spencer A. Freeman, Sarah J. McLeod, Janet Dukowski, Pamela Austin, Crystal C.Y. Lee, Brandie Millen-Martin, Paul Kubes, Donna-Marie McCafferty, Michael R. Gold, and Calvin D. Roskelley (2010). Preventing the Activation or Cycling of the Rap1 GTPase Alters Adhesion and Cytoskeletal Dynamics and Blocks the Extravasation of Metastatic Melanoma Cells into the Lungs. *Cancer Research*.

proliferate [381-385]. Individual steps in this metastatic cascade can proceed by different mechanisms. For example, tumor cell invasion can occur via a 'mesenchymal' mode or an 'amoeboid' mode [383], distinct types of cell motility that are driven by mutually antagonistic signaling pathways [386]. Thus, the design of anti-metastatic therapies targeting a particular signaling pathway must take into account both tumor cell- and phenotype-specific contexts.

This is especially relevant for the Rap1 GTPase, a central regulator of cell adhesion and motility [387]. Extracellular matrix (ECM) ligand binding by integrins leads to increased levels of the active GTP-bound form of Rap1 which, in turn, increases the affinity of integrins for their ligands and promotes the assembly of focal adhesion complexes [387, 388]. Additionally, an initial asymmetric distribution of activated Rap1 promotes cell polarity and migration by remodeling the actin cytoskeleton at the cell's leading edge [232, 389-392]. Thus, Rap1 likely regulates multiple steps in the metastatic cascade. Indeed, altered expression of Rap1, the exchange factors that activate Rap1, or the GTPase-activating proteins (GAPs) that convert Rap1 to the inactive-GDP bound state, has been observed in several tumor types, including melanoma [393-398]. However, how altered Rap1 activation affects specific aspects of the metastatic cascade is cell type-dependent. For example, activated Rap1 promotes the metastatic invasion of breast, pancreatic, and prostate carcinoma cells but inhibits invasion by osteosarcoma and squamous cell carcinoma cells [393-396, 399, 400].

We now show that Rap1 may be a potential target for impeding the metastatic progression of tumors that exit the vasculature via transendothelial migration (TEM). Modeling the interactions between tumor cells and vascular endothelial cells *in vitro* showed that both blocking Rap1 activation and enforcing constitutive Rap1 activation altered tumor cell adhesion dynamics and decreased their ability to migrate across endothelial cell monolayers. Importantly,

the ability of metastatic B16F1 murine melanoma cells [401, 402] to exit the lung microvasculature and form secondary lesions *in vivo* was greatly reduced when Rap1 activation was modulated in these ways.

## 4.2 Results

### 4.2.1 Modulating Rap1 activation alters focal adhesion formation by tumor cells

Tumor cell motility on 2-dimensional (2D) substrates requires the activation of ECM-binding integrins and the subsequent formation and turnover of integrin-containing focal adhesion complexes. The Rap1 GTPase is a central regulator of integrin activation and when murine B16F1 melanoma cells were plated on 2D fibronectin or laminin, the level of active GTP-bound Rap1 increased (**Fig. 4.1A**). This led us to hypothesize that Rap1 activation may regulate focal adhesion formation in tumor cells.

To test this, we modulated Rap1 activation in B16F1 cells and other tumor cell lines by expressing either the constitutively-active Rap1V12 mutant protein, or Rap1GAPII, a Rap-specific GAP that blocks Rap1 activation (**Fig. 4.7**). Imaging the cell-ECM interface such that only adhesive clusters of immunostained proteins were detected showed that Rap1-GTP levels correlated with focal adhesion formation. In both B16F1 (**Fig. 4.1B**) and K1735M1 (**Fig. 4.1C**) murine melanoma cells, the total area per cell occupied by clustered  $\beta 1$  integrins was increased by Rap1V12 expression and decreased by Rap1GAPII expression. Similarly, using the HUTS4 antibody [403] to detect the active conformation of human  $\beta 1$  integrins in A375 human melanoma cells and MDA-MB-231 human breast carcinoma cells showed that Rap1-GTP levels correlated with the amount of active  $\beta 1$  integrin clustered at the cell-ECM interface (**Fig. 4.1C and Fig. 4.8**). The same was true for paxillin and talin, cytosolic proteins that are recruited to

focal adhesion complexes, and for the phosphorylated form of FAK, an indicator of focal adhesion signaling (**Fig. 4.1B**). Consistent with these effects on focal adhesion formation, Rap1V12 expression increased, and Rap1GAPII expression decreased, the adhesiveness of B16F1 cells to rigid substrata (**Fig. 4.9**). Although Rap1V12 expression and Rap1GAPII expression had opposite effects on the number of focal adhesions formed, both disrupted cell polarization and focal adhesion dynamics (see below).

#### **4.2.2 Modulating Rap1 activation impairs adhesion dynamics, cytoskeletal dynamics, cell polarization, and cell motility**

Cell motility requires the dynamic turnover of focal adhesions and the establishment of a polarized morphology where integrin signaling drives dynamic reorganization of the actin cytoskeleton at the cell's leading edge. Real-time imaging of paxillin-GFP clustering indicated that vector control B16F1 cells plated on a rigid fibronectin ECM formed new adhesions at their anterior ends and disassembled existing adhesions at their posterior ends (**Fig. 4.2A**). In contrast, Rap1V12-expressing cells formed stable adhesions that were localized radially along the cell periphery in a non-polarized fashion. Rap1GAPII-expressing B16F1 cells formed few focal adhesions, but those that did form were also very stable, with little evidence of a polarized arrangement. Thus, focal adhesion turnover required both Rap1 activation and Rap1 cycling between the active GTP-bound and inactive GDP-bound states.

Modulating Rap1 activation or cycling also prevented B16F1 cells from establishing a polarized morphology with a dynamic actin cytoskeleton. Vector control cells generated a polarized distribution of F-actin (**Fig. 4.10A**) and real-time imaging of actin-GFP indicated a highly dynamic turnover of actin-GFP filaments at the leading edge (**Fig. 2B**). In contrast,

Rap1V12-expressing cells spread radially and generated non-polarized parallel arrays of stable actin filaments (**Fig. 4.2B, Fig. 4.10A and B**). Rap1GAPII-expressing B16F1 cells formed thin peripheral actin filaments that were also stable and not polarized (**Fig. 4.2B, Fig. 4.10A and B**). These effects on actin correlated with a failure to establish a polarized distribution of PIP<sub>3</sub> (**Fig. 4.10B**), a lipid that recruits cytoskeletal regulatory proteins. The establishment of cytoskeletal polarity required both Rap1 activation and cycling not only in B16F1 cells but also in K1735M1, A375, and MDA-MB-231 cells (**Fig. 4.10C**).

The loss of anterior-posterior polarity caused by modulating Rap1 activation, as well as the decreased adhesion and cytoskeletal dynamics, resulted in a significant decrease in cell motility. As assessed using a bead-clearing assay, the movement of B16F1 cells on rigid 2D fibronectin substrata was greatly reduced when Rap1V12 was expressed and when Rap1 activation was blocked by expressing either Rap1GAPII or the dominant-negative Rap1N17 protein (**Fig. 4.2C**).

### **4.2.3 Modulating Rap1 activity inhibits the metastatic extravasation of B16F1 cells from the lung microvasculature**

Because altering Rap1 activation had dramatic effects on the *in vitro* adhesion, polarity, and migration of B16F1 cells, we asked if it interfered with tumorigenesis and metastasis *in vivo*. Modulating Rap1 activation did not prevent B16F1 cells from forming subcutaneous primary tumors in mice, although Rap1GAPII expression did decrease tumor growth in this context (**Fig. 4.3A**). In contrast, both Rap1GAPII expression and Rap1V12 expression dramatically reduced the ability of B16F1 cells to form metastatic pulmonary lesions after tail vein injection (**Fig. 3B**).

To identify specific aspects of the metastatic cascade that require Rap1 activation and

cycling, vector control B16F1 cells were co-injected into the tail vein with differentially labeled Rap1V12- or Rap1GAPII-expressing B16F1 cells. After 15 minutes, similar numbers of each co-injected cell population were present in the lungs (**Fig. 4.4A**). However, after 2 hours vector control cells vastly outnumbered the Rap1V12- and the Rap1GAPII-expressing cells that remained in the lungs (**Fig. 4.4A**). Although Rap1GAPII-expressing cells exhibited impaired  $\beta 1$  integrin-mediated adhesion to endothelial cells under flow conditions *in vitro* (**Fig. 4.4B**), a decrease in adhesion to the vascular wall cannot fully account for the dramatic decrease in post-arrest retention in the lungs as Rap1V12-expressing cells in fact adhered very efficiently to endothelial cells *in vitro* (**Fig. 4.4B**). This suggested that active extravasation might be essential for sustained retention of B16F1 cells in the lung.

To assay extravasation, we injected fluorescently-labeled B16F1 cells intravenously and determined their localization in the lungs relative to the capillary microvasculature. Four hours after injection, 45% of the vector control cells in the lung tissue had extravasated and no longer co-localized with the red dextran that was co-injected to mark the microvasculature (**Fig. 4.4C**). In contrast, far fewer Rap1V12- and Rap1GAPII-expressing cells moved out of the microvasculature and into the surrounding lung tissue (**Fig. 4.4C**). Rap1GAPII-expressing B16F1 cells also exhibited a decreased ability to invade pliable 3D collagen gels *in vitro* (**Fig. 4.4D**), as noted previously [398]. However, Rap1V12-expressing B16F1 cells did invade collagen gels as well as control cells (**Fig. 4.4D**), indicating that movement across the endothelial wall is more dependent on Rap1 cycling than the subsequent invasion of the stromal ECM.

#### **4.2.4 Modulating Rap1 activation inhibits transendothelial migration (TEM) by tumor cells**

In closed capillary beds such as those of the lungs, tumor cells actively extend membrane

processes across the endothelial wall as they extravasate [404, 405]. To assess the effect of modulating Rap1 activation on this form of TEM, we used confocal microscopy to monitor process formation and the subsequent movement of B16F1 tumor cells across microvascular endothelial cell monolayers *in vitro*. After being in contact with endothelial cells for 1 h, vector control B16F1 cells spread on the top of the endothelial cells and extended F-actin-containing processes along them (**Fig. 4.5A, left panel**). After 16 hours, the majority of the vector cells had undergone TEM by migrating across the endothelial monolayer and reaching its bottom side (**Fig. 4.5A and B**). In contrast, Rap1V12-expressing cells spread radially atop the endothelial cell monolayers, did not extend membrane processes, and exhibited a greatly reduced frequency of TEM compared to control cells (**Fig. 5A and B**). Rap1GAPII-expressing B16F1 spread poorly on the endothelial monolayers, did not extend processes, and also exhibited a significant reduction in TEM (**Fig. 4.5A and B**). This effect was not limited to B16F1 cells as altering Rap1 activation and cycling significantly reduced TEM in K1735M1, A375, and MDA-MB-231 cells (**Fig. 4.5B**).

#### **4.2.5 Modulating Rap1 activation alters adhesion dynamics in tumor cells interacting with endothelial cells**

TEM by tumor cells requires the dynamic assembly and disassembly of adhesive contacts with the endothelial cells [385]. Because modulating Rap1 activation altered the adhesion dynamics of tumor cells on rigid 2D substrata, we determined if this was also the case when tumor cells interact with endothelial cell monolayers. To visualize activated  $\beta 1$  integrins only in the tumor cells, we seeded A375 and MDA-MB-231 human tumor cells on murine endothelial monolayers and stained them with the HUTS4 antibody that recognizes active human, but not

murine,  $\beta 1$  integrins.

In vector control cells, clusters of active  $\beta 1$  integrins at the tumor cell-endothelial cell interface were localized in a polarized fashion, predominantly on one side of the cell (**Fig. 4.5C**). Rap1GAPII expression significantly decreased the ability of the A375 and MDA-MB-231 human tumor cells to form such adhesive clusters. Moreover, FRAP analyses indicated that the mobility of  $\beta 1$  integrin-GFP molecules within the adhesions that did form in the Rap1GAPII-expressing cells was increased (**Fig. 4.5D and Fig. 4.11**), likely reflecting a reduction in integrin activation and ligand engagement when Rap1 activation is blocked.

Although Rap1V12-expressing tumor cells formed as many active  $\beta 1$  integrin-containing adhesions as vector control cells, these adhesions were, for the most part, organized radially, in a non-polarized pattern (**Fig. 4.5C**). Additionally, FRAP analyses indicated that the mobility of  $\beta 1$  integrin-GFP molecules within the adhesions of Rap1V12-expressing cells was significantly decreased (**Fig. 4.5D; Fig. 4.12**). This decreased rate of integrin exchange may indicate maturation of the adhesions into stable cytoskeleton-associated complexes. Indeed, disrupting the actin cytoskeleton with latrunculin A greatly increased  $\beta 1$  integrin mobility within the adhesions of the Rap1V12-expressing tumor cells (**Fig. 4.11**). Thus the reduced ability of Rap1V12-expressing tumor cells to move along, and migrate through, the endothelial monolayer may be due in part to the increased maturity and stability of their adhesive complexes, compared to control cells.

#### **4.2.6 Modulating Rap1 activation inhibits the formation of polarized protrusions by tumor cells lodged within capillaries *in vivo***

To better understand how Rap1 modulation inhibits TEM and extravasation *in vivo*, we

directly imaged the dynamic behavior of B16F1 tumor cells within capillary beds. Because we could not image live cells within the lungs, we injected fluorescently-labeled B16F1 cells into the femoral artery and used intravital microscopy to image them within the superficial capillaries of the cremaster muscle, which were marked with fluorescently-labeled PECAM-1 antibodies.

We found that the initial arrest of B16F1 cells within the cremaster capillaries appeared to be independent of active cell adhesion. Trypsinizing vector control cells prior to injection to remove cell surface molecules did not prevent their arrest in the capillaries (Fig. 6A, right panel). Moreover, Rap1GAPII-expressing B16F1 cells, which adhered poorly to endothelial cells *in vitro* (Fig. 4.4B), arrested in the capillaries just as efficiently as non-trypsinized vector controls and the highly-adherent Rap1V12-expressing cells (Fig. 4.6A).

Although it was not technically feasible to image cremaster capillaries long enough to detect completed tumor cell extravasation, real-time imaging of fluorescently-labeled or actin-GFP-expressing cells showed that the majority of vector control B16F1 cells that arrested within capillaries formed dynamic, actin-rich pseudopodial protrusions that crossed the endothelial cell wall and entered the interstitium (Fig. 4.6A-C). The formation of these protrusive pseudopods was significantly reduced in Rap1V12-expressing B16F1 cells and in Rap1GAPII-expressing B16F1 cells (Fig. 4.6C). Thus both Rap1 activation and cycling contribute to the formation of dynamic membrane protrusions, which likely facilitate tumor cell TEM and extravasation during metastasis (Fig. 4.6D).

### 4.3 Discussion

Our results show that modulating Rap1 activation and cycling has distinct effects on different steps in the metastatic cascade. Blocking Rap1 activation in B16F1 mouse melanoma

cells resulted in decreased adhesion and migration, as observed previously in human melanoma and human thyroid carcinoma cells [398, 406]. This correlated with impaired invasion into 3D collagen gels *in vitro*, decreased subcutaneous tumor growth, and greatly reduced pulmonary metastasis. Conversely, expressing the constitutively active Rap1V12 protein in B16F1 cells increased adhesion but, surprisingly, also blocked metastatic colonization of the lungs.

The reduced ability of both Rap1GAPII- and Rap1V12-expressing B16F1 cells to form lung metastases appears to be mediated, at least in part, by an impaired ability to exit the lung microvasculature. Previous studies showed that B16F1 cells extend protrusions through the capillary wall and into the subendothelial matrix prior to extravasation [405]. We found that modulating Rap1 activation prevented B16F1 cells from forming such protrusions *in vivo*. Moreover, as summarized in Figure 6D, our *in vitro* analyses showed that Rap1 activation and cycling were both important for tumor cells that had attached to endothelial cells to form dynamic adhesions and generate actin-rich protrusions that may promote TEM.

Blocking Rap1 activation and expressing constitutively activating Rap1 altered tumor cell-endothelial cell interactions in distinct ways. In Rap1GAPII-expressing tumor cells, decreased TEM was associated with a reduced ability of the cells to form adhesion complexes and spread on the apical surface of the endothelial cells. In contrast, Rap1V12-expressing cells formed robust, stable adhesions but did not extend polarized protrusions towards the junctions between the endothelial cells and underwent TEM very inefficiently. Although Rap1V12 expression also altered adhesion stability and reduced tumor cell migration on rigid 2D ECM substrata, as recently noted [388], this is the first report that this occurs when tumor cells interact with vascular endothelial cells. The highly stable focal adhesions that form in Rap1V12-expressing cells may limit the ability to generate protrusive leading edges that drive tumor cell

migration, both on endothelial cells and rigid substrata.

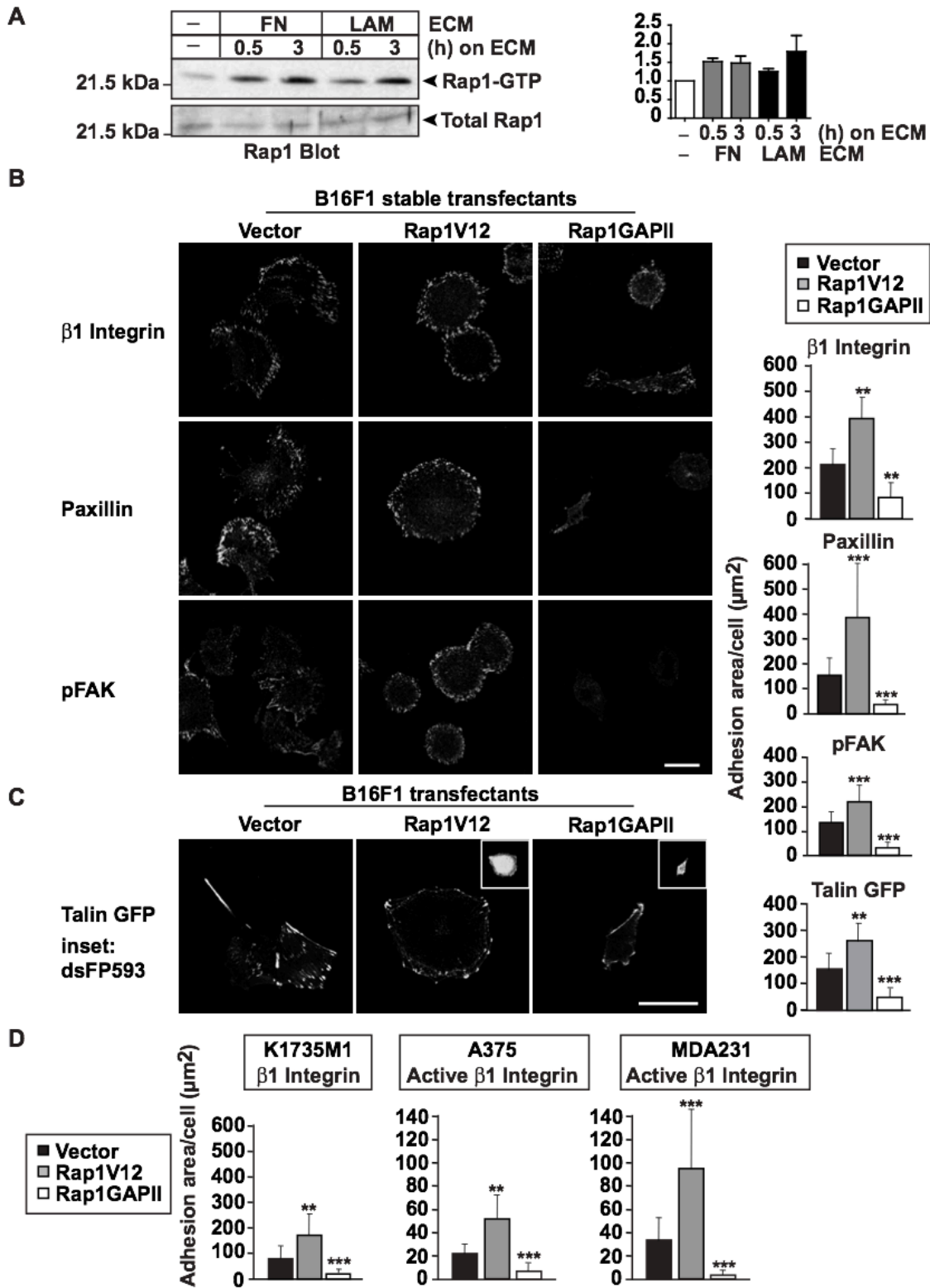
In contrast to our findings with melanoma cells, expressing constitutively active Rap1 increases the metastasis of prostate carcinoma cells to bone [399]. This may reflect differences in the microvasculature of the two target organs. Unlike the closed capillaries of the lungs, the bone marrow sinusoids are mostly open. Thus, prostate carcinoma cells could reach the osteoblastic stroma without actively migrating along, or sending protrusions through, endothelial walls. The increased metastasis of Rap1V12-expressing prostate carcinoma cells may therefore reflect increased invasiveness into the tissue, as opposed to increased TEM. Consistent with this, we found that Rap1V12-expressing B16F1 cells efficiently invaded compliant 3D collagen gels, even though they exhibited reduced migration on rigid 2D substrata and reduced TEM across endothelial cell monolayers.

The ability of Rap1V12 expression to inhibit 2D motility but support 3D invasion may relate to the biophysical properties of the substrata [407]. Cell attachment to rigid 2D substrata or to the surface of firmly attached endothelial cells may increase cytoskeletal tension within the tumor cell to the point where it augments the ability of Rap1-GTP to stabilize adhesions and impede cell movement; more compliant 3D matrices may not do so. This could be tested directly by altering the stiffness of the collagen matrix, as has done with breast carcinoma cells [295].

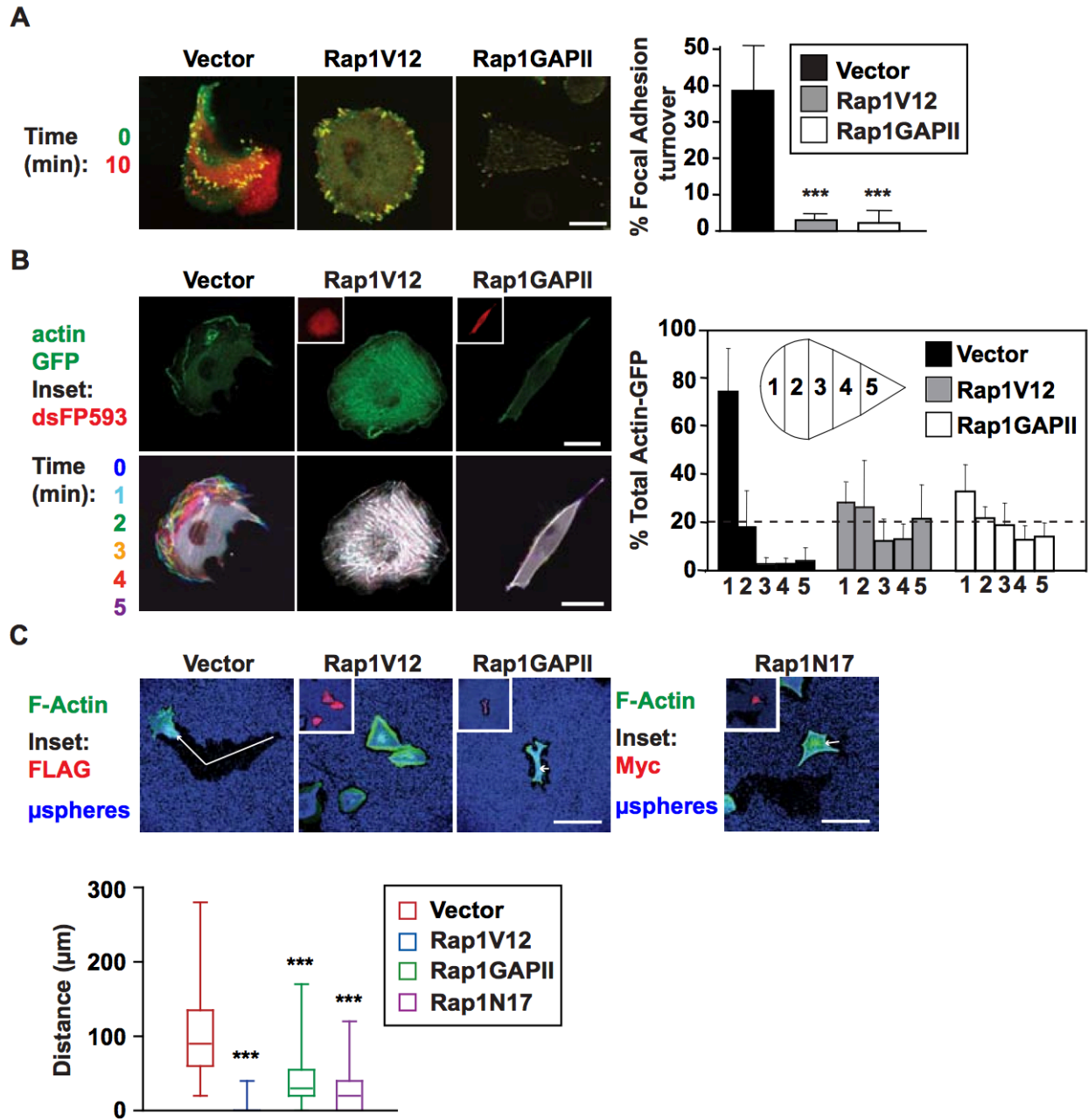
Although several studies concluded that extravasation is not a rate-limiting step in metastatic progression [408-410], our findings suggest that the Rap1-dependent formation of membrane protrusions that promote active extravasation may be a functionally important aspect of the process. Previous attempts to prevent extravasation by targeting matrix metalloproteinases [411, 412], integrins [410], or tetraspanins [385] have been unsuccessful. Our findings suggest

that Rap1 could be a novel target for limiting the dissemination of metastatic cells that exit the vasculature via active TEM.

## 4.4 Figures

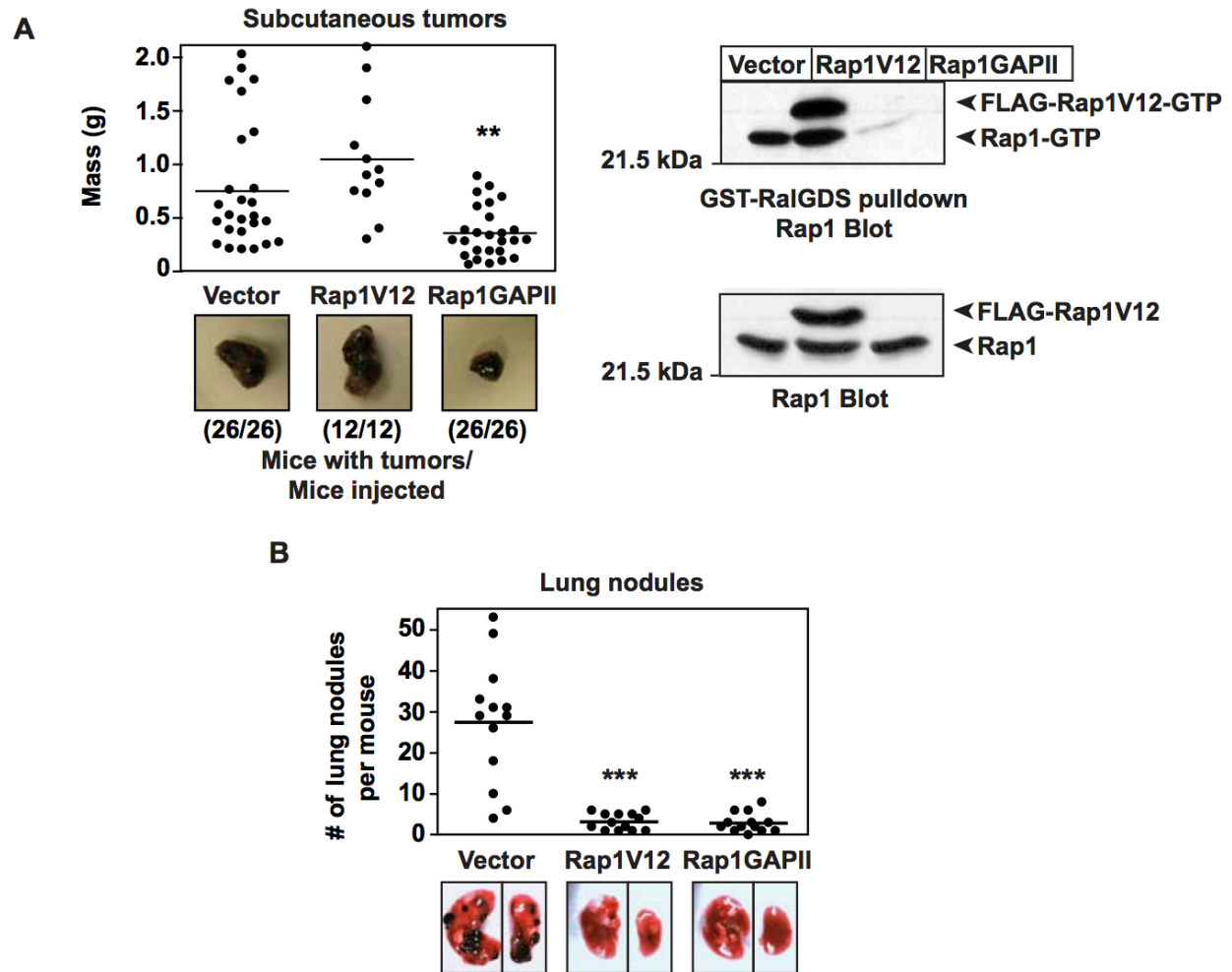


**Figure 4.1.** *Rap1 regulates focal adhesion formation.* *A*, B16F1 cells were maintained in suspension (-) or plated on fibronectin (FN) or laminin (LAM). Cell lysates were assayed for activated Rap1-GTP and total Rap1. *Right panel*, Rap1-GTP levels relative to suspension cells (mean +/- SD from 3 experiments). *B*, B16F1 cells stably transfected with the empty pIRM21-IRES-dsFP593 vector or derivatives encoding FLAG-Rap1V12 or FLAG-Rap1GAPII (see Supplementary Fig. S1) were plated on fibronectin for 4 h and then immunostained for  $\beta$ 1 integrin, paxillin, or phosphorylated FAK (pFAK). Representative confocal images of the cell-ECM interface are shown (Scale bar: 20  $\mu$ m). By setting the threshold for fluorescence detection such that only signals from protein clusters (putative adhesion complexes) were detected, the adhesion area per cell for each protein was determined (mean +/- SD for 50 cells from 3 experiments). *C*, B16F1 cells that were transiently co-transfected with talin-GFP plus the empty pIRM21-IRES-dsFP593 vector or derivatives encoding FLAG-Rap1V12 or FLAG-Rap1GAPII, were plated on fibronectin for 4 h and then imaged. Transfected cells were identified by GFP and dsFP593 (dsRed; inset) fluorescence. Adhesion area per cell for talin-GFP was determined as in *B*. *D*, The indicated tumor cell lines were transiently transfected with the indicated vectors and plated on fibronectin for 4 h. The cells were immunostained with anti-FLAG to identify transfected cells and with either a pan- $\beta$ 1 integrin antibody (murine K1735M1 cells) or the HUTS4 antibody, which recognizes only the active form of human  $\beta$ 1 integrin (human A375 and MDA-MB-231 cells). Representative confocal images of the cell-ECM interface (see Supplemental Fig. S3) were used to determine the  $\beta$ 1 integrin-containing adhesion area per cell, as in *B*. \*\*\* $P$ <0.001, \*\* $P$ <0.01 compared to control cells.

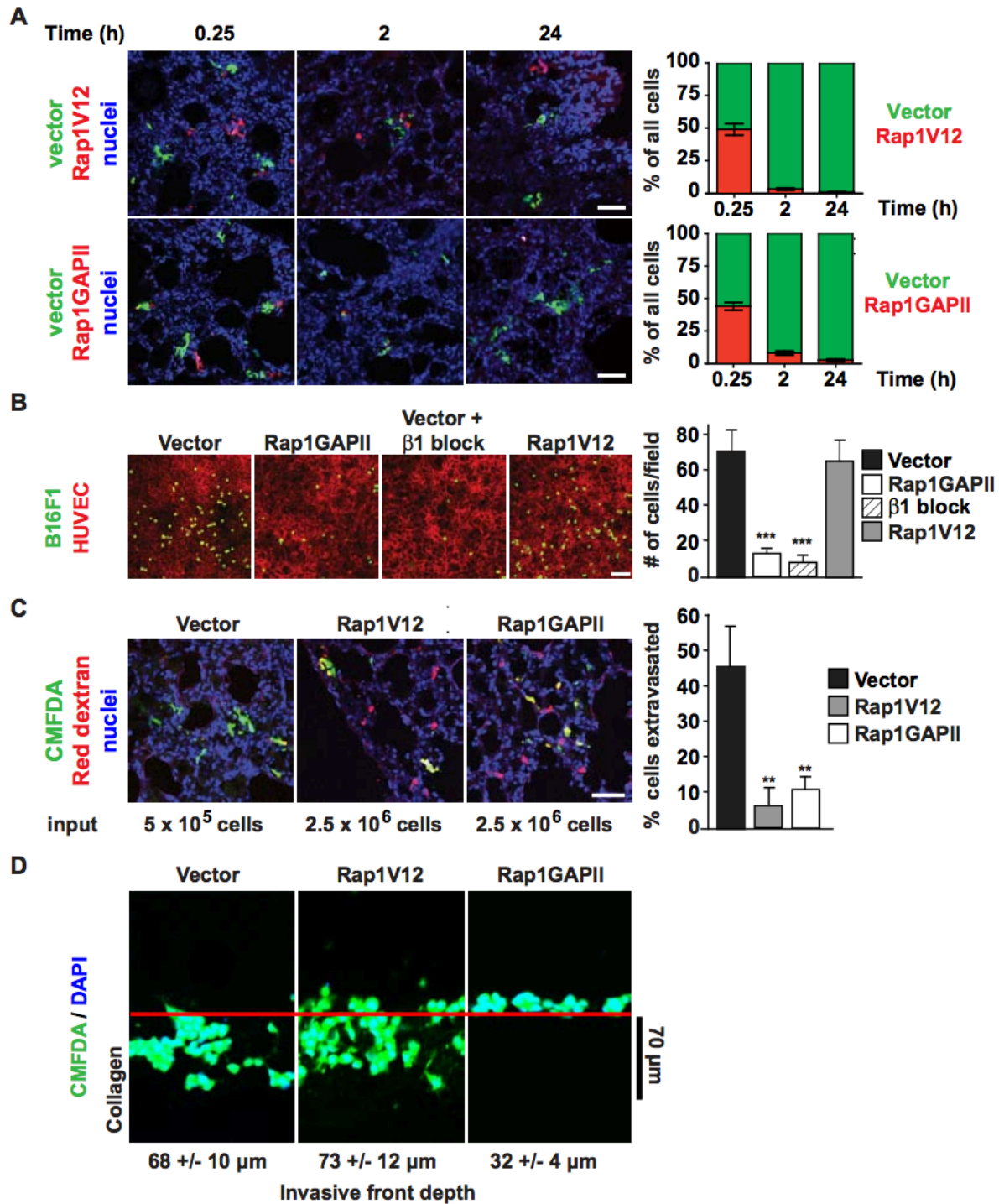


**Figure 4.2.** *Rap1* regulates adhesion and cytoskeletal dynamics, cell polarization, and tumor cell motility. *A*, Vector control, Rap1V12, and Rap1GAPII B16F1 cells expressing paxillin-GFP were plated on fibronectin for 4 h and then imaged continuously for 10 min. Focal adhesions in the first frame (0 min) were pseudocolored green and those in the final frame (10 min) were pseudocolored red before superimposing the two images to identify focal adhesions that were

newly-formed (red), disassembled (green), or stable (merge = yellow) over the 10-min period. Focal adhesion turnover (% either disassembled or newly assembled; mean +/- SD for 10-15 representative cells from 2 experiments) is graphed. *B*, The indicated cells co-expressing actin-GFP were plated on fibronectin for 4 h, and then imaged continuously for 5 min. *Upper panels*, representative still frames (Scale bars: 20  $\mu\text{m}$ ). *Lower panels*, composite images of pseudocolored frames collected at the indicated times. Stable localization of actin-GFP over the 5-min period appears white. The percent of the total actin-GFP in five equally divided regions of >25 cells from 3 experiments is graphed. *C*, Vector control, FLAG-Rap1V12-, FLAG-Rap1GAPII-, and Myc-Rap1N17-expressing B16F1 cells were plated for 16 h on fibronectin (2.5  $\mu\text{g}/\text{cm}^2$ ) that was overlaid with fluorescent microspheres. F-actin was visualized with Alexa488-phalloidin (green). Transfected cells were identified by immunostaining for FLAG or Myc (red). Representative confocal images are shown (Scale bar: 100  $\mu\text{m}$ ). The maximum distance from the edge of a cell to the edge of the area cleared of fluorescent beads (white arrows) for >50 cells from 3 experiments is graphed. The horizontal bar is the mean. \*\*\* $P < 0.001$  compared to vector control cells.

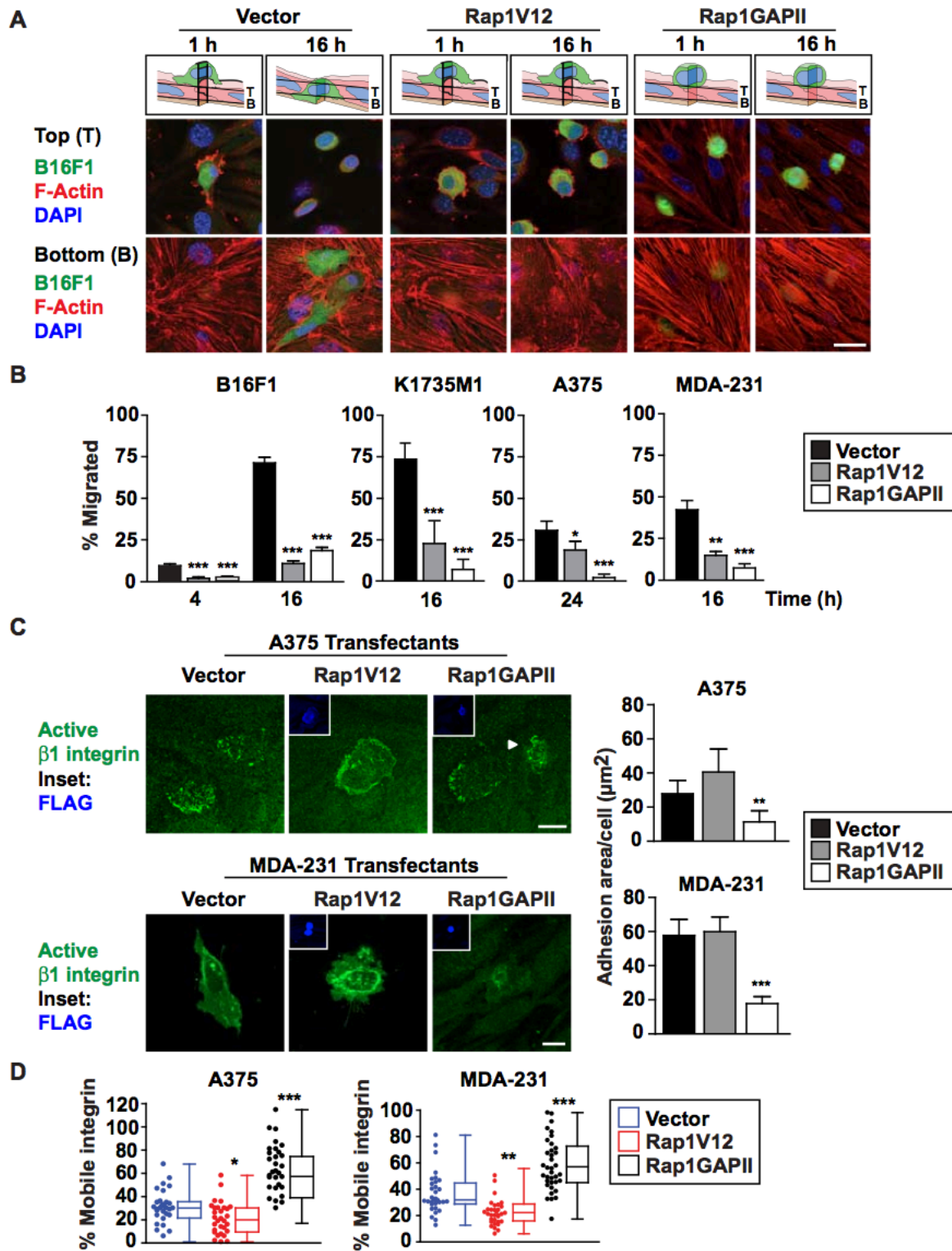


**Figure 4.3.** *Modulating Rap1 activity alters melanoma growth and metastasis in vivo.* *A*, Stably transfected B16F1 cells were injected subcutaneously into mice. All injections generated palpable tumors, which were excised and weighed after 14 days. Representative images of the tumors are shown. *Right panel*, Rap1-GTP (top) and total Rap1 (bottom) in lysates from excised subcutaneous tumors. *B*, Stably-transfected B16F1 cells were injected intravenously. After 21 days, lungs were removed, photographed, and visible colonies were counted. Horizontal bars represent the mean values. \*\*\* $P < 0.001$  compared to vector control cells.



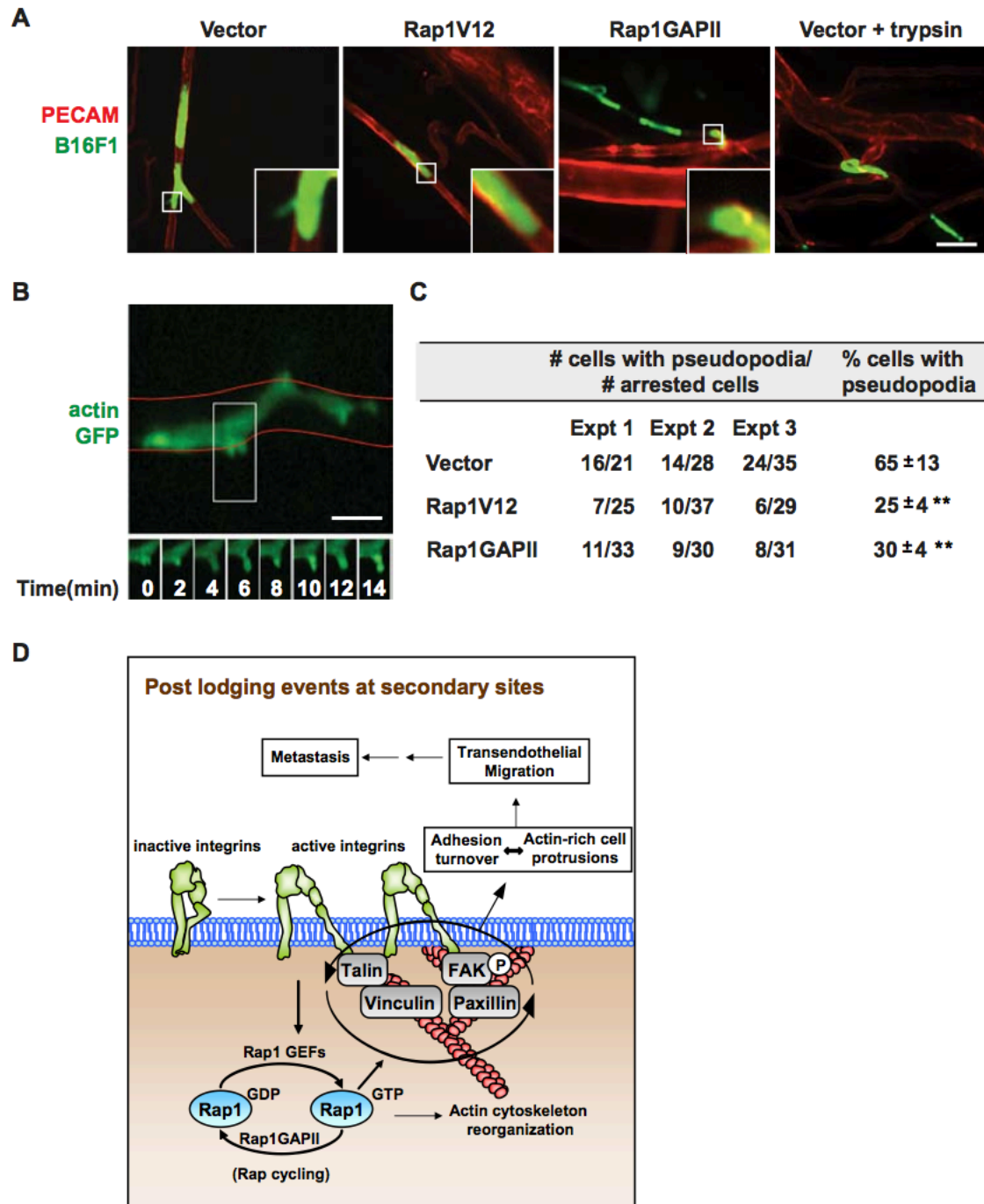
**Figure 4.4.** *Modulating Rap1 activity impairs melanoma cell extravasation.* *A*, For competitive lung arrest assays, equal numbers of fluorescently-labeled vector control B16F1 cells (green) and either Rap1V12- or Rap1GAPII-expressing (red) cells were co-injected intravenously into mice.

At the indicated times, lungs were removed, fixed, sectioned, stained with DAPI to mark all nuclei. Representative sections are shown. The relative number of the different cell populations in 10 to 30 500- $\mu\text{m}^2$  sections from 4 experiments (mean  $\pm$  SEM) is graphed. *B*, To assess tumor cell adhesion to endothelial cells under flow, fluorescently-labeled B16F1 cells (green) were perfused across a HUVEC monolayer (red) for 10 min in the absence or presence of a  $\beta$ 1 integrin blocking antibody. Representative images of tumor cells adhering to the monolayers are shown (Scale bars: 100  $\mu\text{m}$ ). The number of adherent cells per field is graphed (mean  $\pm$  SD for  $> 4$  fields in each of 3 experiments).  $***P < 0.001$  compared to control cells. *C*, For extravasation assays, fluorescently-labeled B16F1 cell populations (green) were injected intravenously together with fluorescent dextran (red) to label the lung microvasculature. After 4 h, lung sections were prepared and imaged as in *A* (Scale bar: 50  $\mu\text{m}$ ). Tumor cells that did not co-localize with the labeled dextran were considered to have extravasated (yellow = co-localized with dextran within the microvasculature; green = not co-localized, outside the microvasculature). For each cell type, the percent of imaged cells that had extravasated was determined and is expressed as mean  $\pm$  SD for 3 experiments.  $**P < 0.01$  compared to control cells. Because Rap1V12- and Rap1GAPII-expressing cells were poorly retained in the lungs, five times as many cells were injected (input) in order to visualize a sufficient number of cells. *D*, Stably-transfected CMFDA-labeled B16F1 cells were added to Transwell chambers in which the filters were coated with a collagen I gel. The lower chamber contained FCS and TGF- $\beta$  as chemoattractants. After 20 h, invasion of the cells into the 3D collagen ECM was imaged. Representative Z-axis images from one of three separate experiments with similar results are shown.



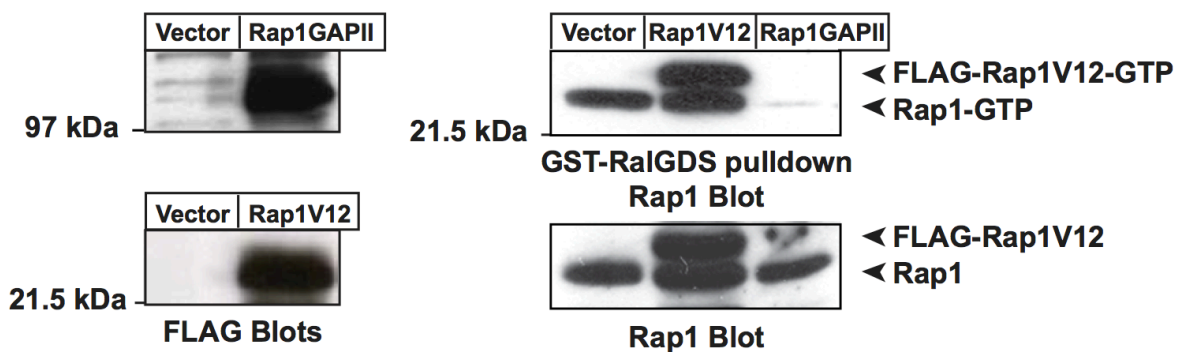
**Figure 4.5.** Modulating *Rap1* activity inhibits tumor cell TEM and alters adhesion dynamics in tumor cells interacting with endothelial cells. *A*, Fluorescently-labeled B16F1 cells (green) were

plated on monolayers of bEND.3 microvascular endothelial cells. After 4-24 hours the cells were stained for F-actin and imaged by confocal microscopy. Representative images of confocal slices of the 'bottom' ( $0\ \mu\text{m} = \text{B}$ ) and 'top' of the endothelial cells ( $4\text{-}5\ \mu\text{m} = \text{T}$ ), as in the schematics, are shown (Scale bar:  $20\ \mu\text{m}$ ). Cells that reached the bottom plane were scored as having undergone TEM. *B*, TEM by stably-transfected B16F1 cells, as well as transiently-transfected K1735M1, A375, and MDA-MB-231 cells, was analyzed as in *A*. The percent of imaged cells ( $>100$  per point) that underwent TEM is graphed as the mean  $\pm$  SEM for three experiments. *C*, Transiently-transfected A375 and MDA-MB-231 cells were plated on bEND.3 mouse endothelial cell monolayers. The HUTS4 antibody was used to detect active human  $\beta 1$  integrins (green). Anti-FLAG antibodies were used to detect transfected cells (insets - blue; arrowhead indicates transfected cell). Representative confocal images of the tumor cell-endothelial cell interface are shown (Scale bar:  $10\ \mu\text{m}$ ). The area per cell occupied by clustered active  $\beta 1$  integrins at the cell-cell interface was quantified as in Figure 1 (mean  $\pm$  SD for 30 cells). *D*, A375 and MDA-MB-231 cells transiently co-transfected with  $\beta 1$  integrin-GFP and the indicated vector were plated on endothelial cell monolayers. Transfected cells were identified by dsFP593 fluorescence. Regions containing integrin clusters were photobleached and fluorescence recovery was recorded in real time (see Supplementary Fig. S5). The maximal fluorescence recovery was taken as the percent of the  $\beta 1$  integrin-GFP that was mobile ( $n > 30$  adhesions per point). The horizontal bar is the mean.  $***P < 0.001$ ,  $**P < 0.01$ ,  $*P < 0.05$  compared to vector control cells.



**Figure 4.6.** *Modulating Rap1 activity reduces the ability of melanoma cells to form protrusions that cross capillary walls in vivo.* *A*, Stably-transfected B16F1 melanoma cells were labeled with CellTracker Green and injected into the femoral artery of mice along with AlexaFluor555-conjugated PECAM-1 antibodies to mark downstream capillaries (red). The cremaster muscle

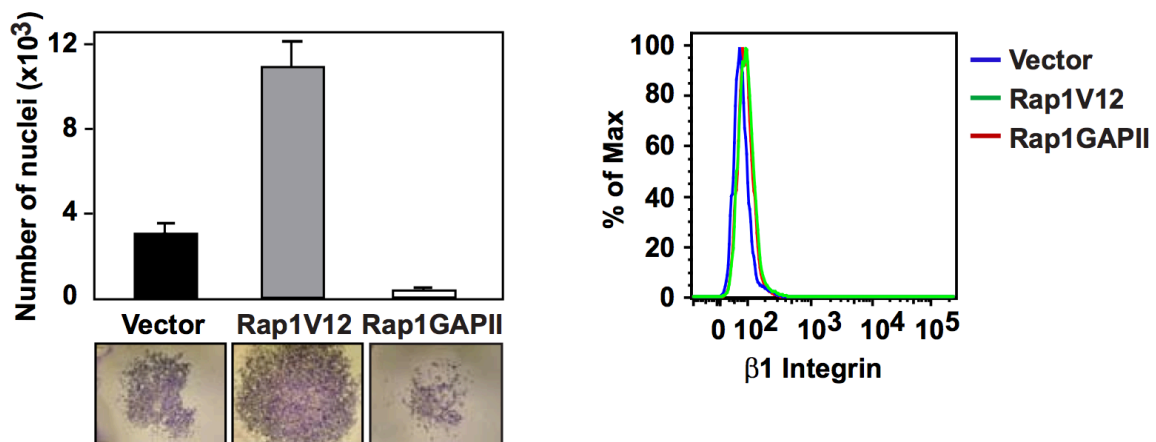
was exteriorized and imaged for 1-2 h after injection. Representative images of cells lodging in capillaries are shown (Scale bar: 50  $\mu\text{m}$ ). The higher magnification insets show a vector control cell with a protrusion that crosses the capillary wall as well as Rap1V12 and Rap1GAPII cells without such protrusions. In the right panel, a vector control cell that was treated with trypsin for 30 min prior to injection is shown lodged in a capillary. *B*, Actin-GFP-expressing vector control B16F1 cells were injected into the femoral artery along with labeled PECAM-1 antibodies to mark capillary walls (red). After 1 h, cells that lodged within capillaries were imaged continuously for 15 min. *Large image*, still frame from the start of the imaging period (0 min) showing actin-GFP within a protrusion that crossed the capillary wall. *Small images*, the same protrusion at 2-minute intervals from 0 to 14 min (Scale bars: 10  $\mu\text{m}$ ). *C*, Using images generated as in *A*, the percent of B16F1 cells with pseudopodial protrusions that penetrated the capillary wall was determined (mean  $\pm$  SD for three experiments in which  $>20$  cells were imaged per point).  $**P < 0.01$  compared to vector control cells. *D*, Model of how integrin-induced Rap1 activation and cycling contributes to the formation of protrusions that promote tumor cell extravasation and metastasis.



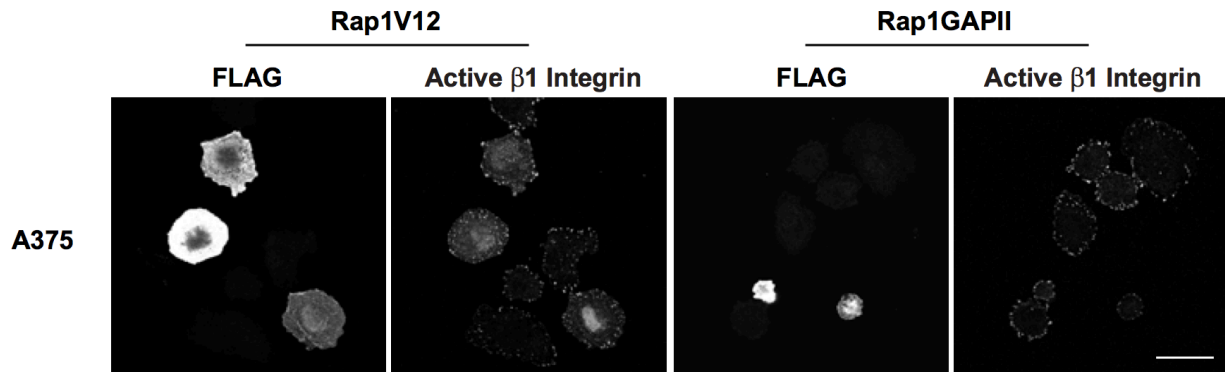
**Figure 4.7.** Expression of Rap1V12 and Rap1GAPII alters Rap1-GTP levels in B16F1

melanoma cells. B16F1 cells were stably transfected with the empty pIRM21 vector, pIRM21-

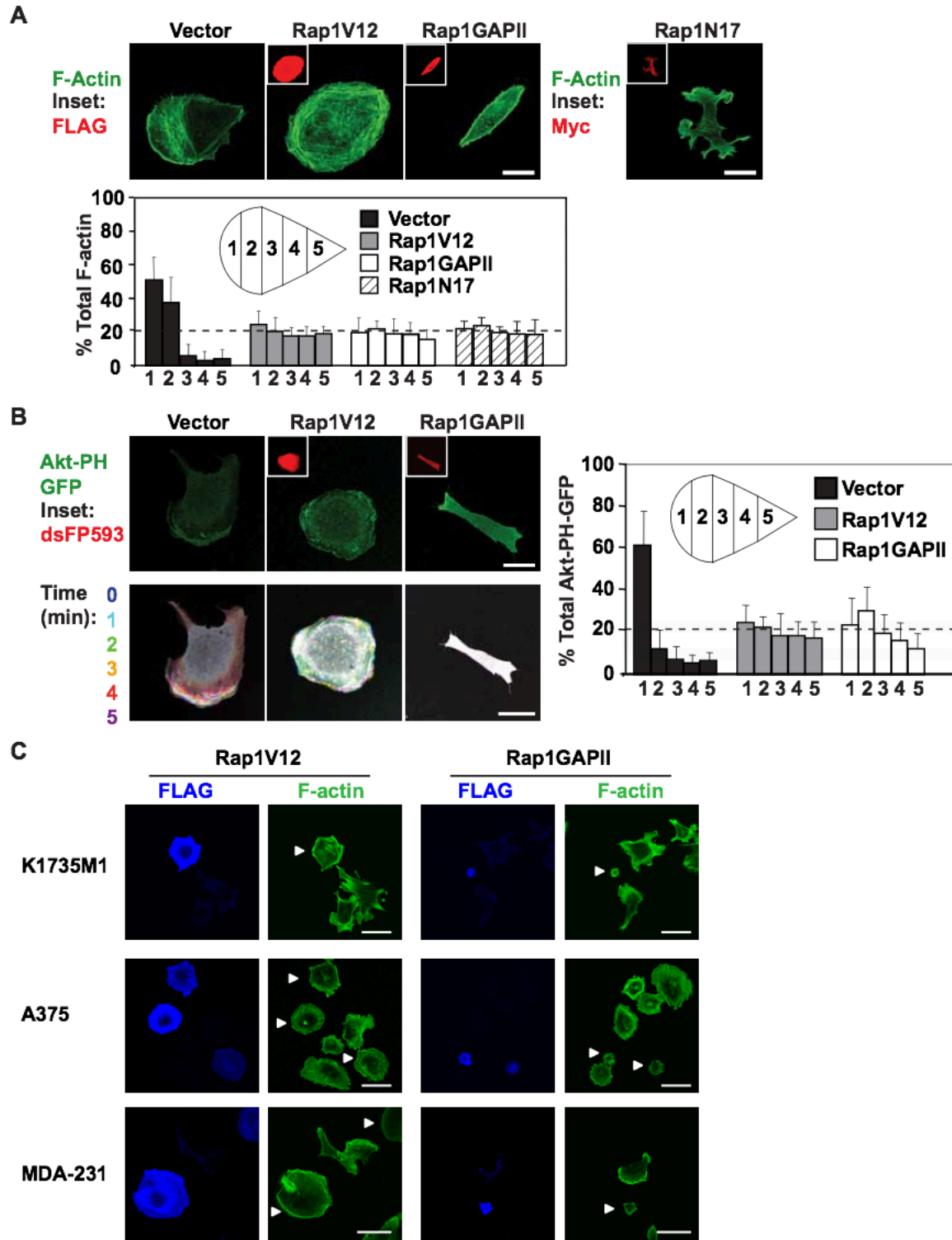
FLAG-Rap1V12, or pIRM21-FLAG-Rap1GAPII. Expression of the FLAG-tagged proteins was assessed by immunoblotting (left panels). Cells were plated on  $2 \mu\text{g}/\text{cm}^2$  fibronectin for 3 h and assayed for activated Rap1-GTP in the top right panel (see Materials and Methods for experimental details). The lower right panel shows total Rap1 in the cell lysates.



**Figure 4.8.** *Rap1-GTP levels regulate total adhesive strength.* Stably transfected B16F1 cells were cultured on rigid, serum-coated tissue plastic substrata overnight. They were then exposed to 0.04% EDTA for 5 min at 20°C to detach loosely adherent cells. The remaining well-attached cells were then stained with Hoechst 33342, fixed with 4% paraformaldehyde, and counted using an ArrayScan VTI imager (histogram). Alternatively, cells were fixed with methanol, stained with crystal violet, and photographed. Flow cytometry showed that the transfected cell populations all had similar levels of  $\beta 1$  integrins on the cell surface (right panel).

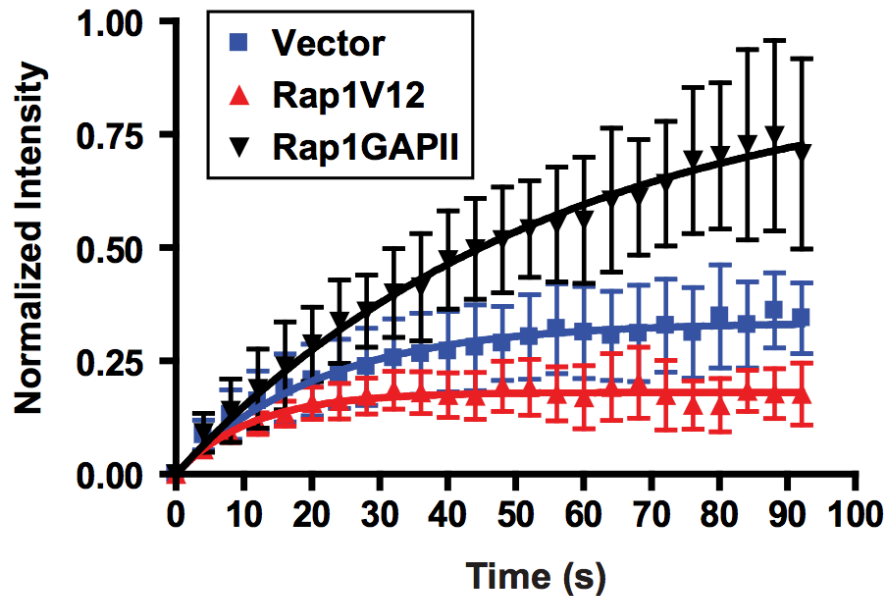
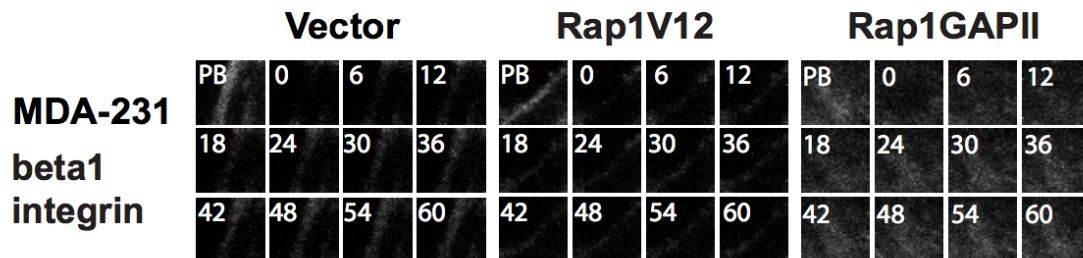


**Figure 4.9.** *Rap1-GTP* levels regulate the amount of active human  $\beta 1$  integrin in clusters at the cell-ECM interface (i.e. focal adhesions). A375 human melanoma cells were transiently transfected with the empty pIRM21-IRES-dsFP593 vector or derivatives encoding either FLAG-Rap1V12 or FLAG-Rap1GAPII. The cells were plated on FN for 4 h and stained with anti-FLAG antibodies to identify transfected cells. Active integrin was visualized by immunostaining using the HUTS4 antibody, which recognizes only the active form of human  $\beta 1$  integrin. Representative confocal images are shown. Arrows indicate transfected cells (Scale bar: 20  $\mu\text{m}$ ). The area occupied by the clustered active  $\beta 1$  integrin per cell is graphed in Fig. 1D, center panel.

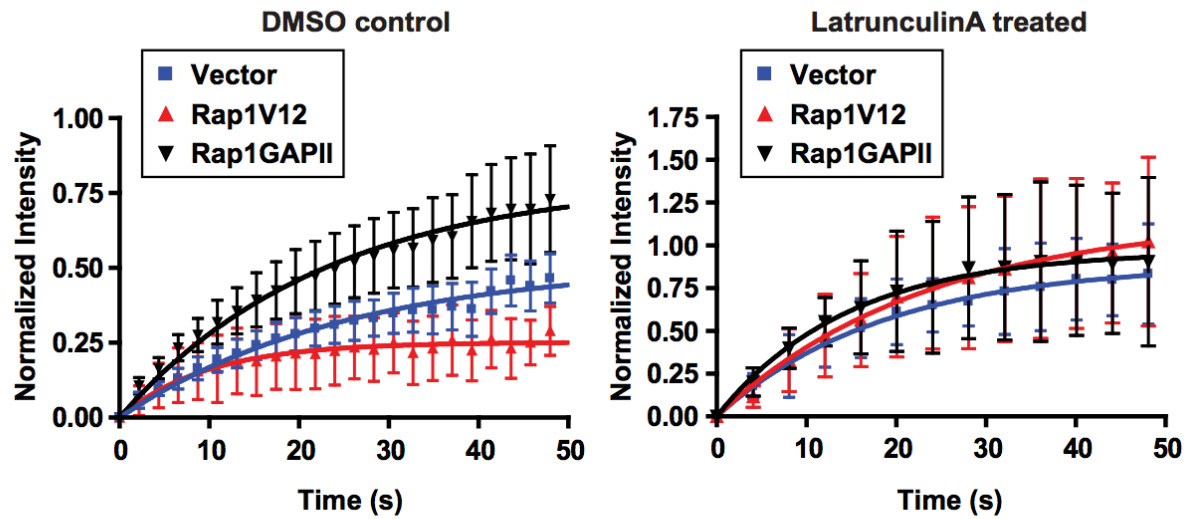


**Figure 4.10.** *Rap1* activation and cycling are required for establishing a polarized distribution of F-actin cytoskeleton and  $PIP_3$ . *A*, B16F1 cells were transiently transfected with the empty

pIRM21-IRES-dsFP593 vector or derivatives encoding FLAG-Rap1V12, FLAG-Rap1GAPII, or Myc-Rap1N17. After culturing the cells on  $2.5 \mu\text{g}/\text{cm}^2$  fibronectin for 2 h, transfected cells were identified using FLAG or Myc antibodies (inset; red). F-actin was visualized with Alexa488-phalloidin. Representative confocal images are shown (Scale bar:  $10 \mu\text{m}$ ). The percent of the total F-actin in five equally divided regions of  $>25$  cells from 3 experiments is graphed. *B*, B16F1 cells were transiently co-transfected with a vector encoding an Akt-PH-GFP fusion protein plus either the empty pIRM21-IRES-dsFP593 vector or derivatives encoding Rap1V12, or Rap1GAPII. The cells were cultured on fibronectin-coated chambers for 4 h, and then imaged. Representative still frames are shown (Scale bar:  $10 \mu\text{m}$ ). The distribution of Akt-PH-GFP is graphed, as in *A*, for  $>25$  cells from 3 experiments. *C*, K1735M1 murine melanoma cells, A375 human melanoma cells, and MDA-MB-231 human breast carcinoma cells were transiently transfected the empty pIRM21-IRES-dsFP593 vector or derivatives encoding FLAG-Rap1V12 or FLAG-Rap1GAPII. The cells were plated on FN for 4 h and stained with anti-FLAG antibodies to identify transfected cells (arrows) which facilitated comparison with untransfected cells in the same microscopic field. F-actin was visualized by staining with Alexa488-phalloidin. Representative confocal images are shown. (Scale bar:  $20 \mu\text{m}$ ).

**A****B**

**Figure 4.11.** FRAP analysis of  $\beta 1$  integrin-GFP exchange in adhesions. Regions of interest (ROIs) encompassing  $\beta 1$  integrin-GFP at the tumor cell-endothelial cell interfaces were photobleached in transiently-transfected vector control, Rap1V12-expressing, and Rap1GAPII-expressing MDA-MB-231 cells. The recovery of fluorescence within the ROI was then imaged every 6 s for 90 s. *A*, The recovery of fluorescence within the ROI is expressed as a fraction of the pre-bleach intensity (= 1.0). Each point is the mean  $\pm$  SD for 20 ROIs. *B*, Representative time-lapse sequences of  $\beta 1$  integrin-GFP fluorescence within these ROIs prior to bleaching (PB), and every 6 s thereafter, are shown.



	DMSO	LatA treated
<b>Mobile Fraction (YMAX)</b>		
Vector	0.51 ± 0.04	0.89 ± 0.03
Rap1V12	0.25 ± 0.01	1.16 ± 0.09
Rap1GAPII	0.80 ± 0.05	0.97 ± 0.04
<b>t1/2 (s)</b>		
Vector	17.6 ± 4.0	13.0 ± 1.2
Rap1V12	6.8 ± 1.6	16.2 ± 3.2
Rap1GAPII	16.0 ± 2.5	10.1 ± 1.3

**Figure 4.12.** *The exchange of  $\beta 1$  integrin-GFP in adhesions is limited by the actin cytoskeleton.* MDA-MB-231 cells transiently transfected with  $\beta 1$  integrin-GFP plus the empty pIRM21-IRES-dsFP593 vector or derivatives encoding Rap1V12 or Rap1GAPII were plated on a thin layer of collagen I (10  $\mu\text{g}/\text{mL}$ ) mixed with FN (10  $\mu\text{g}/\text{mL}$ ). The cells were then treated with DMSO or latrunculin A for 30 min before photobleaching ROIs and following the recovery of fluorescence intensity. The left panel shows the recovery of  $\beta 1$  integrin-GFP fluorescence in vehicle treated vector, Rap1V12, and Rap1GAPII transfected cells. The right panel shows the recovery of  $\beta 1$

integrin-GFP fluorescence in cells treated with latrunculin A (Lat A). Note that the curves in the two graphs are from the same experiments but that the curves are separated into a DMSO-treated set and a latrunculin A-treated set to clearly depict the effects of modulating Rap1 activation. Note also that the scales of the Y-axes are different for the two graphs given the significant increase in the recovery of all the cell types treated with latrunculin A. Each point represents the mean +/- SD for >20 ROIs in 2 experiments. The curves generated from these results were used to determine the percent of  $\beta 1$  integrin-GFP molecules that were mobile (mobile fraction = maximal recovery of fluorescence) and  $t_{1/2}$  (time to reach half maximal recovery), which are summarized in the table.

## **4.5 Experimental procedures**

### **4.5.1 Cells**

B16F1, A375, MDA-MB-231 (American Type Culture Collection; ATCC), K1735M1 (R. Nabi, University of British Columbia, Vancouver Canada) and bEND.3 cells (K. McNagny, University of British Columbia) were grown in DMEM with 8% FCS. HUVECs (ATCC) were grown in MCDB131 medium with 20% FCS, 16 U/mL heparin, and 20  $\mu$ g/mL endothelial cell growth supplement (Sigma-Aldrich).

### **4.5.2 Reagents**

Antibodies used were: FLAG (Sigma-Aldrich), Rap1 (Santa Cruz Biotechnology), HUTS4 (BD Pharmingen), paxillin (BD Biosciences), phosphor-Y397 FAK (pFAK, Invitrogen), and AlexaFluor555-anti-PECAM-1 (Research Diagnostics, Concord MA). Human fibronectin, laminin, and TNF- $\alpha$  were from Sigma-Aldrich. Fluorescently-labeled phalloidin, AlexaFluor568-dextran, and cell-labeling dyes were from Invitrogen. The pIRM21-IRES-dsFP593 vector and derivatives encoding FLAG-Rap1V12 or FLAG-Rap1GAPII were from M. Matsuda (Kyoto University, Kyoto, Japan). pEGFP-C1- $\beta$ 1-integrin was from V. Weaver (University of California, San Francisco, CA). pEGFP-C1- $\beta$ -actin and pEGFP-C1-paxillin were from R. Nabi (University of British Columbia). Cellular Lights<sup>TM</sup> talin-GFP was from Invitrogen.

### **4.5.3 Transfection**

To generate stable transfectants, expression vectors plus pMSCVpuro (BD Clontech) were transduced using calcium phosphate and cells were selected with 2  $\mu$ g/ml puromycin, followed by FACS sorting for dsFP593 expression. Transient transfections were performed using

Lipofectamine 2000 (Invitrogen).

#### **4.5.4 Rap1 activation**

Rap1-GTP was precipitated from cell lysates using a GST-RalGDS fusion protein and detected by immunoblotting with Rap1 antibodies [374].

#### **4.5.5 Immunofluorescence**

Cells on ECM-coated substrata were either fixed and stained with antibodies or imaged live in a chamber maintained at 37°C and 5% CO<sub>2</sub>. Images were acquired using the Uplan Apochromat 60X/1.35 NA objective on an Olympus FV1000 confocal microscope, captured with Olympus Fluoview v1.6 software, and analyzed using ImagePro (Media Cybernetics).

#### **4.5.6 Cell motility**

Cells were plated on coverslips coated with fibronectin and a lawn of 1- $\mu$ m fluorescent microspheres (FluoSpheres; Invitrogen). After 16 h, the maximum distance from the edge of the cell to the edge of the cleared area was determined using Fluoview v1.6 software.

#### **4.5.7 Tumor assays**

For subcutaneous tumor growth, 10<sup>5</sup> cells in 0.1 mL DMEM were injected into the hind flanks of C57BL/6 mice. Tumors were analyzed after 14 days. For metastasis assays, 2 x 10<sup>5</sup> cells in 0.1 mL DMEM were injected into the tail vein. After 21 days, the lungs were removed. Visible colonies were photographed and counted.

#### **4.5.8 Arrest and extravasation assays**

For competitive arrest experiments, tumor cell populations were differentially labeled with CellTracker Green or CellTrace Far Red dyes and equal numbers ( $5 \times 10^5$ ) were co-injected into the tail veins of C57BL/6 mice. For extravasation assays, labeled cells were co-injected with 5 mg/kg AlexaFluor568-dextran. At the indicated times, lungs were removed, fixed in paraformaldehyde, embedded in OCT, sectioned, stained with DAPI, and imaged using the Uplan Fluorite 20X/0.7 NA objective of an Olympus FV1000 confocal microscope.

#### **4.5.9 Adhesion under flow**

HUVECs were cultured as monolayers on flow chamber slides (IBIDI) and labeled with CellTrace Calcein Red. Tumor cells were labeled with CellTracker Green, mixed with mouse blood, and perfused across the HUVEC monolayer at  $2 \text{ dynes/cm}^2$ . After 10 min, the chamber was flushed and the cells were imaged.

#### **4.5.10 Transendothelial migration**

bEND.3 murine microvascular endothelial cells (25) were cultured as monolayers on chamber slides, activated with 50 ng/mL TNF- $\alpha$ , and overlaid with CellTracker Green-labeled tumor cells. After 1-24 h, cells were fixed and stained with rhodamine-phalloidin. Z-stacks were generated by confocal microscopy.

#### **4.5.11 Collagen invasion**

Collagen I (BD Biosciences; 2 mg/mL in PBS) was polymerized on Transwell filters (Falcon). The lower chamber contained DMEM with 55% FCS and 10 ng/mL TGF- $\beta$  (R&D Systems) and

$5 \times 10^5$  CMFDA-labeled B16F1 cells were added to the top chamber. After 20 h, filters were fixed with paraformaldehyde, embedded in OCT, sectioned vertically, and Z-axis images were acquired.

#### **4.5.12 Adhesion dynamics at tumor cell-endothelial cell interfaces**

Tumor cells were added to monolayers of TNF- $\alpha$ -activated bEND.3 cells. After fixation, cells were immunostained with the HUTS4 antibody and imaged by confocal microscopy using the 60X/1.35 NA objective. Fluorescence recovery after photobleaching (FRAP) was performed as described [413, 414] on  $\beta 1$  integrin-GFP-expressing cells. A circular region of interest (ROI) at the endothelial-tumor cell interface was photobleached using a 405 nm laser (100% intensity, 0.1 s). Fluorescence recovery was imaged until the intensity reached a plateau. The fluorescence signal was normalized to the pre-bleach intensity and single exponential fit curves of the data were generated using Prism 4 software (GraphPad).

#### **4.5.13 Intravital Microscopy**

Mice were anaesthetized and the cremaster muscle was exteriorized as described [415]. AlexaFluor555-conjugated anti-PECAM-1 (0.2 mg/mL) was injected into the femoral artery along with  $5 \times 10^5$  CMFDA dye-labeled B16F1 cells. The cremaster muscle microvasculature was imaged in real time using an Olympus BX51 upright spinning disk confocal microscope with an x20/0.95 XLUM Plan F1 objective.

#### **4.5.14 Statistical analysis**

P values were calculated using a two-tailed independent two-sample *t*-test.

## **5. Concluding chapter**

### **5.1 Summary of main findings**

#### **Chapter 2: TLR ligands increase the sensitivity of BCR signalling by increasing cytoskeletal dynamics and reducing BCR spatial confinement**

- TLR ligands prime B cells to respond to low densities of membrane-bound Ags by reducing BCR confinement and increasing BCR diffusion
- TLR signaling activates cofilin mediated severing of the membrane cytoskeleton to “open the gates” for BCR diffusion
- TLR ligands enhance BCR-BCR collisions and tonic signaling, possibly underlying their mitogenic nature for B cells
- Natural B cell populations show differences in cofilin activity and ability to form microclusters on low densities of membrane-bound Ags implicating cytoskeletal control as a mechanism for varied sensitivities of these cells

#### **Chapter 3: Cofilin-Mediated F-actin Severing is Regulated by the Rap GTPase and Controls the Cytoskeletal Dynamics that Drive Lymphocyte Spreading and BCR Microcluster Formation**

- F-actin networks in T and B cells are more dynamic on anti-CD3 + anti-CD28 or anti-BCR antibodies as compared to resting states (i.e. on FN)
- Increased actin dynamics are associated with increased barbed ends

- Increased actin dynamics are not a result of changes in G/F actin ratios and therefore must involve actin-binding proteins that accelerate F-actin turnover
- Ag receptor signaling induces cofilin mediated severing and dephosphorylation
- The activation of RapGTPases is required for cofilin mediated severing and dephosphorylation as well as increased actin dynamics in response to Ag receptor engagement
- The Rap/cofilin pathway mediates cortical cytoskeleton breakdown required for spreading on APC membranes, the formation of BCR microclusters, and resultant pTyr signaling
- The activation of cofilin independently controls microcluster formation from the inactivation of ezrin
- The Rap/cofilin pathway controls microcluster diffusion

**Chapter 4: Preventing the Activation or Cycling of the Rap1 GTPase Alters Adhesion and Cytoskeletal Dynamics and Blocks the Extravasation of Metastatic Melanoma Cells into the Lungs**

- Activating Rap in multiple murine and human melanoma cell lines as well as a breast cancer line increases the targeting of paxillin, FAK, Talin, and active integrins to 2D ECMs while blocking Rap activation limits targeting of focal adhesion components
- Rap activation and cycling are required for tumor cell polarization, actin dynamics, and cell migration on 2D ECMs
- Both Rap activation and cycling inhibit tumor cell extravasation *in vitro* and *in vivo*, preventing colonization of the lung

- The dynamic RapGDP-RapGTP cycle regulates integrin turnover of tumors cells on endothelia required for the zippering action of pseudopodia or leading edge structures to penetrate endothelial monolayers

## 5.2 Discussion

### 5.2.1 The Rap/cofilin pathway and receptor diffusion

In their 1972 seminal work describing the plasma membrane as a lipid bilayer, Singer and Nicholson wrote a final section on “Cooperative phenomena in membranes” [119]. This section described cooperative phenomena as any “effect which is initiated at one site on a complex structure and transmitted to another remote site by some structural coupling between the two sites”. They proposed these effects could act in a “cis” manner where “cooperative changes...may be produced over the entire membrane or at least large areas of it, as a consequence of some event or events occurring at only one or a few localized points on the membrane surface”. For receptor systems that require clustering to initiate signaling pathways like Ag receptors (e.g. BCR, integrins), altering receptor diffusion fits as a potential mechanism for cooperative phenomena.

An appreciation for barriers to receptor diffusion in the plasma membrane began soon after the seminal work by Singer and Nicholson when novel approaches to measure protein diffusion within membranes were developed. Early experiments using FRAP to measure protein diffusion in erythrocytes showed that disrupting spectrin and actin networks increased protein mobility by orders of magnitude [125]. Kusumi and colleagues have subsequently demonstrated that actin networks not only limit the diffusion of transmembrane proteins with cytoplasmic tails but also GPI-anchored outer leaflet proteins and even lipids [118, 122]. They have also demonstrated the interconnectivity and elasticity of these networks in elegant experiments where they showed that exerting force on spectrin at one site on a cell can alter receptor trajectories and shift receptor confinement zones at a distant site [127]. Upon release of spectrin, the receptors return close to their original position. Although Andrews *et al.* [416] and Treanor *et al.* [60]

have shown that the diffusion of immune cell receptors such as Fc receptors and the BCR, respectively, is controlled by the membrane-associated actin cytoskeleton (MSK), the biological contexts and signaling pathways that target the MSK are not well understood. For example, is the MSK dynamic and receptor diffusion altered in the presence of active infection?

In the first two data chapters of this thesis, I describe the activation of a Rap/cofilin pathway as a cooperative phenomenon underlying receptor diffusion. I first described how TLR ligands that would be present during an active infection prime the BCR to respond to lower densities of membrane-associated Ags by activating the Rap/cofilin pathway and thereby increasing BCR diffusion. This represents a novel mechanism for receptor crosstalk. TLR-primed B cells showed increased BCR-mediated tonic signaling, which may contribute to the ability of TLR ligands to drive B cell proliferation. The increased BCR mobility and microcluster formation in TLR-activated B cells was dependent on cofilin acting to dynamize the MSK by severing existing actin filaments. Photobleaching experiments indicated that TLR signaling in primary B cells made the F-actin network more dynamic and that this was dependent on activation of the Rap/cofilin pathway. In addition to making actin-based diffusion barriers more transient, TLR signaling resulted in reorganization of the actin cytoskeleton. Indeed, TLR signaling resulted in pronounced actin-based membrane ruffling but did not increase the total F-actin content of cells. This reorganization of the actin network was dependent on cofilin consistent with the observation that cofilin-mediated severing creates new barbed ends where the Arp2/3 complex can initiate branched actin polymerization. This branched actin polymerization likely drives the cell spreading that occurs when B cells encounter Ag-bearing surfaces. It is not known whether the transition from a cortical submembrane actin skeleton to a branched actin network also impacts the mobility of the BCR or other proteins in the plasma membrane. Highly

branched networks of F-actin may have less association with the plasma membrane than cortical actin networks, based on their orientation, however, and could therefore present less of a barrier to receptor diffusion.

Another possibility to explain increased BCR diffusion when cofilin is activated is that more dynamic and branched F-actin networks have decreased  $k_{on}$  and/or increased  $k_{off}$  rates for the cytoplasmic tails of transmembrane pickets or adaptors connecting F-actin to the membrane (e.g. ezrin). Cofilin loading on actin filaments results in a structural twist, a force that can be propagated through the filament [187]. If this twisting action were to dissociate the interaction of the filament from transmembrane pickets or intermediary scaffolding proteins (as it does for the Arp2/3 complex to cause debranching [191]), this could be a simple explanation for increased receptor diffusion. In this model, the major change in cells with activated cofilin is not a gross change in actin filaments or filament orientation, but less binding between filaments and transmembrane pickets. Still another possibility is that actin severing proteins can break long actin filaments into short polymers that can diffuse with the pickets. Little is known about how the diffusion of large protein complexes compares to single receptors and how this relates to the space between the MSK and cytoplasmic parts of the complex. For receptors with large cytoplasmic domains to “pass-over” filaments of the MSK, they may need to interact with lipids of the inner-leaflet. These interactions could involve polycationic stretches of the cytoplasmic tails that bind to negatively charged lipids like phosphoinositides. This could therefore be favored by increased PI3K activity [217]. Although the submembrane actin cytoskeleton may physically restrict receptor mobility by interacting with the cytoplasmic tails of proteins, barriers to protein diffusion in the plasma membrane exist even for proteins without cytoplasmic tails [118, 130].

In the case of the Fc receptor IIA, Jaumoullie and Grinstein have shown that truncating the ~30 amino acid cytoplasmic tail of the receptor, or adding GFP to the cytoplasmic tail, had no effect on diffusion (personal communication) despite a strong role for F-actin as a diffusion barrier for FcRIIA. These data suggest that the diffusion of FcRIIA may be controlled by the MSK through the intermediary network of transmembrane pickets. While protein crowding cannot explain ten- to twenty-fold decreases in diffusion of proteins in lipid bilayers versus cell membranes [118], transmembrane proteins that are immobilized by F-actin binding may restrict diffusion via their immobile extracellular domains. The extracellular domains of pickets may also be highly glycosylated and form lattices via interactions with galectin oligomers [417], however, there is little evidence that galectins decrease protein diffusion [418]. In any case, severing proteins that increase the diffusion of transmembrane pickets could control the diffusion of receptors with actin-interacting cytoplasmic tails and those without.

A final consideration relating to the control of receptor diffusion by F-actin networks and the role of Rap/cofilin is the possibility that actin maintains protein islands or clusters in an active way in resting cells. “Protein islands” have indeed been observed in resting T and B cells where actin not only corrals protein clusters but also directly associates with them [63, 66]. A model proposed by Madan Rao, Satyajit Mayor and colleagues describes a population of short, dynamic, polymerizing actin filaments that actively drive transient clusters [131]. How this population of actin is differently controlled from that observed by Kusumi and colleagues is unclear, however, both active clustering and corralled based diffusion barriers could co-exist in resting cells. If co-receptor complexes like CD19/CD21/CD81 associated with one pool of less dynamic F-actin while the BCR associated with another more dynamic pool, mixing of these

species would be achieved via homogenizing the cortical F-actin networks which could also involve the Rap/cofilin pathway.

### **5.2.2 Clearance of F-actin, a porous elastic solid material**

A major question for those working on the resting actin cytoskeleton is how do cells migrate and probe their extracellular environment (processes dependent on a dynamic actin cytoskeleton) while maintaining barriers to limit self-aggregation of receptors? Indeed, lymphocytes rapidly migrate through SLOs to maximize contacts with potential APCs. Rapid lymphocyte migration requires contraction of the elastic actin cytoskeleton and an amoeboid phenotype [419, 420]. Lymphocytes can also form large ‘invadopodia’ structures that dynamically probe potential APCs [421]. Throughout these processes, however, the cortical actin cytoskeleton remains dense even as it is remodeled. In fact, large decreases in cortical actin density only occur upon encounters with cognate Ag. In a step-wise manner, lymphocytes must first stop and spread on APCs before F-actin clearance occurs [195, 422, 423]. The stopping of lymphocytes requires an inactivation of myosin heavy chains (MyH9) [424] leading to the unbundling of actin filaments [425] while F-actin clearance is dependent on cofilin [195], hedgehog signaling [423], and PI3K. The severing and unbundling of actin filaments may lead to a decreased cortical rigidity such that lymphocytes can change their shape and spread on APCs [420]. It seems likely that multiple relevant biological inputs (e.g. cytokines, integrin ligands) may act on these pathways in order to switch lymphocyte motility from an amoeboid to an elongated type, preparing them for encounters with cognate Ag.

When an immune synapse begins to form, regions devoid of F-actin become a ‘sink’ for Ag receptor microclusters [422]. Conversely, regions cleared of F-actin exclude transmembrane

phosphatases like CD45 and CD148 [90]. While the size of these phosphatases is one mechanism for their exclusion (kinetic segregation), another possibility is that the binding of CD45 and CD148 to F-actin favors their movement to the periphery. In this model, a ring of F-actin initiating at the center of a synapse moving to the periphery could act like a zipper. Once established, F-actin, transmembrane phosphatases and integrins at the lamellipodia of the contact could maintain a diffusion barrier both extra- and intracellularly. Indeed, during immune synapse maturation, larger molecules like CD45 and integrin move to the periphery of the contact [426], however, both bind actin filaments via adaptor proteins (spectrin, ankyrin, Talin) making it challenging to dissect the kinetic segregation model from a zippering model. Another idea is that the delivery of new membrane to the IS that does not contain phosphatases is delivered, effectively decreasing the density of CD45 and CD148 at the center of the contact.

Though an F-actin ring forms at the outside of a synapse, F-actin flows towards the center of the IS in a retrograde direction. Despite retrograde flows of F-actin, molecules like CD4 and SLP-76 in T cells and monomeric G-actin can move in an anterograde fashion [427-429]. Krummel and colleagues have raised the intriguing possibility that actin, inter-connected through cytoplasm, can contract and displace the cytoplasmic medium to create hydrostatic pressure gradients at the IS [420]. Others have previously described the cytoplasm as a poroelastic material comprised of “porous elastic solid meshworks (cytoskeleton, organelles, macromolecules)” and “interstitial fluid (cytosol)” [430]. Given that the cytoplasm comprises a volumetric majority of most cells, the distribution of water plays a central role in cellular deformation (cell shape) and cell size [431-433]. If cytoplasm is displaced when cytoskeletal networks are contracted, a hydrostatic pressure will decrease, leading to fluid flow in the direction of the contraction. At the IS, Krummel and colleagues have described an opposing

fluid flow to the retrograde F-actin flow given this phenomenon [420]. How hydrostatic pressure gradients and fluid flow could differentially affect molecular diffusion in lymphocytes is not known and is challenging to assess. Initial work has used intracellular quantum dots to measure fluid dynamics in living cells [430]. Altering cell volume or co-assessing fluid flow and intracellular molecular diffusion are approaches that could begin to address these questions.

Of particular consideration in these questions for lymphocytes is the large volume occupied by the nucleus. In this regard, the nucleus may play a large buffering role for changes in hydrostatic pressure gradients. A major question is how the lymphocyte nucleus connects to the actin cytoskeleton and how these connections are regulated. While the linker of nucleoskeleton and cytoskeleton (LINC) complex is an area of investigation, the number of studies investigating these complexes and their regulation are miniscule compared to those investigating adhesion complexes at the plasma membrane. Given the importance for the elasticity of a cell's microenvironment and how it regulates differentiation via connections to the nucleus [434-436], an understanding of LINC is an important direction to pursue. In line with this idea, the IS of T cells is strongly implicated in the generation T cell memory. While much attention has been paid to adhesion at the IS as creating asymmetry of cell division, an alternative idea would be to explore mechanotransductive cues.

### **5.2.3 The IS as a diffusion barrier**

A 'sealed zone' formed during immune synapse formation has been determined in B cells as space between B cells and target particles is not accessible by antibodies [437]. Similar observations have been made in macrophages as they phagocytose particles [438]. In both B

cells [437] and macrophages (Sergio Grinstein, personal communication), LAMP-1 is enriched at persistent contacts, suggesting that inner leaflet proteins normally present at lysosomes begin to accumulate. In macrophages, the diffusion barrier function at these contacts become striking as PIP3 accumulates with the LAMP-1 while PIP2 remains on the outside of the contact. That phospholipids can form this discrete barrier in a continuous membrane requires either 1) a diffusion barrier and/or 2) a boundary of kinase and phosphatase activities controlling phosphoinositide phosphorylation. It will be interesting to determine the spatial nature of immune and phagocytic synapses to determine if the central region of the contact is sealed to exclude large phosphatases or if a diffusion barrier is formed by an outer actin-rich ring. This could be tested using micropatterning of ligand, FRAP, and single particle tracking.

#### **5.2.4 Immune cell populations, receptor organization and response thresholds**

The inter-relationship between F-actin dynamics, BCR mobility, and tonic BCR signaling may set response thresholds in B cell populations. I found that TLR ligands, for example, increase the level of tonic BCR signaling such that the cell achieves a “primed” state in which less Ag is required for its activation than for resting B cells. Such a primed state may be recapitulated *in vivo* in MZ B cells, which express high levels of TLRs. Within the MZ of the spleen, macrophages with high expression of receptors that bind polysaccharides (e.g. SIGN-R1) and scavenger receptors that bind both Gram (+)ve and (-)ve bacteria (e.g. MARCO), can trap microbial Ags. MZ B cells are specialized and localized for making rapid responses to these blood-borne microbial Ags [439, 440]. MZ B cells also rapidly respond to TLR ligands *in vitro* to proliferate and secrete Abs. I found that cytoskeletal dynamics were enhanced in MZ B cells, compared to follicular (FO) B cells, as illustrated by the observations that MZ B cells spread to a

greater degree than FO B cells when plated on anti-Ig Abs, gathered more Ag into microclusters when they encountered APCs, and had increased cofilin activation, as measured by its dephosphorylation. Based on these findings, I would predict that BCR mobility, as well as the kinetic segregation of bulky phosphatases away from the BCR should be greater in MZ B cells than in FO B cells. Although MZ B cells comprise only 5% of the B cells in mouse spleen, it should be possible to perform SPT of the BCR, CD45, CD148, etc. on these cells in order to compare their diffusion in MZ versus FO B cells. Increased diffusion could be one mechanism of enhanced sensitivity to membrane-associated Ags while pre-clustering of more BCRs within actin-based corrals or pre-assembling the BCR and CD19 co-receptor complex could be another.

In subsets of human diffuse large B cell lymphomas (DLBCLs), proliferation and survival requires the assembly of BCR microclusters that chronically activate BCR signaling pathways [441]. Hijacking of BCR signaling machinery for survival may require a number of mutations [442]. Two key mutations determined by work from Lou Staudt's group have been identified as those preventing normal endocytic trafficking of the BCR and activating mutations in the MyD88 signaling adaptor [441-443]. These mutations result in the maintenance of the BCR at the cell surface and the constitutive binding of MyD88 to the TIR domain of TLRs. While super resolution based imaging of the chronic BCR microclusters has yet to be done, Sue Pierce's group analyzed the mobility of these clusters using TIRF and determined them to be immobile [441]. This is similar to observations of signaling competent BCR microclusters formed on lipid bilayers. Cytoskeletal dynamics have not been investigated in these human lymphomas, however, my preliminary observations have in fact shown less cofilin activity in these cells and possibly decreased F-actin dynamics (data not shown). The relationship between F-actin and Ag receptor signaling may be biphasic. Remodeling of cortical F-actin is important

for corrals to be broken to increase diffusion in order to form signalosomes. Corrals may then reform in order to maintain signaling. Along these lines, upon Ag engagement by the BCR, ezrin seems to be temporarily inactivated resulting in the unbinding of F-actin. Within 1-2 min, ezrin is reactivated to rebind F-actin in order to corral a larger BCR microcluster containing CD19 [62, 63]. It may therefore be advantageous to locally limit F-actin severing in order to maintain newly clustered or pre-clustered receptor in the case of DLBCLs.

Increases in actin dynamics and receptor mobility may be a general mechanism of receptor crosstalk that primes cells to respond in an enhanced way (at lower ligand concentrations or more robustly) to other stimuli. For example, just as with memory B cells, memory T cells no longer require co-signaling and mount quicker and larger responses upon re-encounter with pMHC. The increased sensitivity of the BCR for Ag in memory B cells is largely due to increased affinity achieved via the germinal center reaction and somatic hypermutation. For T cells that do not undergo somatic hypermutation of the TCR genes, there must be other mechanisms for increased sensitivity of the TCR. Alarcon, van Santen and colleagues indeed found changes in the clustering of TCRs in the plasma membrane between T cell populations and coined this an “avidity” maturation mechanism of the TCR in memory T cells [444]. The authors found that while naïve T cells contained mostly monomeric TCRs (though a range from 1-13 TCRs per nanocluster was observed), activated T cell blasts and CD4<sup>+</sup> memory T cells sometimes had TCR oligomers of more than 15. TCR oligomerization may be mediated by a lateral association between CD3 $\zeta$  cytoplasmic tails as mutations in this region could disrupt TCR oligomerization [444]. Previous work has determined that TCR oligomerization in T cell blasts requires lipid rafts as extraction of cholesterol using methyl-beta-cyclo-dextran (M $\beta$ CD)

destroyed TCR oligomers [445]. In B cells, I did not observe changes in BCR diffusion upon treatment of cells with M $\beta$ CD, however, clustering of the BCR was not determined and there may be general differences between how the BCR and TCR interact with lipid domains. The cytoplasmic tail of CD3 $\epsilon$  and CD3 $\zeta$  may be embedded in the inner leaflet of the plasma membrane, mediated by polycationic stretches of the tails interacting with negatively charged lipids like PS [446], likely not observed for the BCR Ig $\alpha$  and Ig $\beta$  subunits. The retention and trafficking of PS may, in fact, require cholesterol (Jason Kay and Sergio Grinstein, personal communication), which could explain differences between the two antigen receptors and their responses to M $\beta$ CD. Increased TCR oligomerization in memory T cells may also be a result of epigenetic changes that alter the association between the TCR and the actin cytoskeleton/actin binding proteins and/or the MSK architecture. In addition to resting versus receptor-activated cells and naïve versus memory cells, different subsets of a given cell type may be imprinted with different cytoskeletal dynamics that affect receptor signaling and function. For examples, M1 macrophages have greater phagocytic activity than M2 macrophages, a property that could reflect differential mobility and confinement of Fc receptors or other receptors. Comparative analyses of the diffusive behaviours of Ag receptors in these cell populations would be useful.

### **5.2.5 Closing remarks**

The work in this thesis examines receptor organization and diffusion as it relates to signaling and responses thresholds. Early investigations of signaling pathways activated by Ag receptors largely used soluble cross-linking antibodies. These experiments shed light on how

aggregation of receptors in the membrane led to signal transduction resulting in lymphocyte activation and proliferation but did not yield spatial information. It is now appreciated that the majority of Ags seen by lymphocytes are either captured by receptors or processed and displayed at the plasma membrane of Ag presenting cells. Both Ag receptors as well as captured Ags do not diffuse as predicted by Brownian motion, rather, receptors are restricted by diffusion barriers including the membrane-associated cytoskeleton. This has led to intensive investigations of the spatial organization of Ag receptors (and some studies on Ag on APCs) in resting cells, cells forming contacts with APCs, memory cells, and transformed cells. While the surface expression of some molecules can change between these cell types, a major contribution to Ag receptor signaling is the ability for receptors to diffuse within the membrane. Increased diffusion of non-ligated receptors increases the chance of associating with coreceptors and recruiting and activating signaling enzymes.

The biological context in which lymphocytes encounter Ag are complex, involving cytokines, adhesion molecules, TLR ligands, etc. Recently, some studies have emerged describing cytokines as tuning T cell response thresholds. It has been established that integrin based adhesion lowers the threshold for T and B cell responses by providing traction for cell spreading and immune synapse formation on APCs. Interestingly, integrin signaling can also increase diffusion of Ag receptors, though this mechanism is not well understood (Valentin Jamoullie and Sergio Grinstein, personal communication). An understanding of the spatial organization and diffusion of immune receptors in different cell types and in different biological contexts will certainly be of great future interest.

## References

1. Beutler, B., *Innate immunity: an overview*. Molecular Immunology, 2004. **40**(12): p. 845-859.
2. Barrangou, R., et al., *CRISPR provides acquired resistance against viruses in prokaryotes*. Science, 2007. **315**(5819): p. 1709-1712.
3. Fincher, C.L., et al., *Pathogen prevalence predicts human cross-cultural variability in individualism/collectivism*. Proceedings of the Royal Society B-Biological Sciences, 2008. **275**(1640): p. 1279-1285.
4. Schaller, M. and D.R. Murray, *Pathogens, personality, and culture: Disease prevalence predicts worldwide variability in sociosexuality, extraversion, and openness to experience*. Journal of Personality and Social Psychology, 2008. **95**(1): p. 212-221.
5. Janeway, C., *Immunobiology : the immune system in health and disease*. 6th ed. 2005, New York: Garland Science. xxiii, 823 p.
6. Tolar, P., et al., *The molecular assembly and organization of signaling active B-cell receptor oligomers*. Immunological Reviews, 2009. **232**: p. 34-41.
7. Xu, Y.K., et al., *Lyn tyrosine kinase: Accentuating the positive and the negative*. Immunity, 2005. **22**(1): p. 9-18.
8. Janeway, C.A., *How the immune system works to protect the host from infection: A personal view*. Proceedings of the National Academy of Sciences of the United States of America, 2001. **98**(13): p. 7461-7468.
9. Takeuchi, O. and S. Akira, *Pattern Recognition Receptors and Inflammation*. Cell, 2010. **140**(6): p. 805-820.
10. Yipp, B.G. and P. Kubersky, *NETosis: how vital is it?* Blood, 2013. **122**(16): p. 2784-94.
11. Yipp, B.G., et al., *Infection-induced NETosis is a dynamic process involving neutrophil multitasking in vivo*. Nat Med, 2012. **18**(9): p. 1386-93.
12. Steinberg, B.E. and S. Grinstein, *Unconventional roles of the NADPH oxidase: signaling, ion homeostasis, and cell death*. Sci STKE, 2007. **2007**(379): p. pe11.
13. Cooper, M.D. and M.N. Alder, *The evolution of adaptive immune systems*. Cell, 2006. **124**(4): p. 815-822.
14. Rajewsky, K., *Clonal selection and learning in the antibody system*. Nature, 1996. **381**(6585): p. 751-758.
15. Kurosaki, T., *Regulation of B-cell signal transduction by adaptor proteins*. Nat Rev Immunol, 2002. **2**(5): p. 354-63.
16. Rolli, V., et al., *Amplification of B cell antigen receptor signaling by a Syk/ITAM positive feedback loop*. Molecular Cell, 2002. **10**(5): p. 1057-1069.
17. Gold, M.R., *To make antibodies or not: signaling by the B-cell antigen receptor*. Trends Pharmacol Sci, 2002. **23**(7): p. 316-24.
18. Gold, M.R., et al., *Targets of B-cell antigen receptor signaling: the phosphatidylinositol 3-kinase/Akt/glycogen synthase kinase-3 signaling pathway and the Rap1 GTPase*. Immunol Rev, 2000. **176**: p. 47-68.
19. Okada, T., et al., *BCAP: the tyrosine kinase substrate that connects B cell receptor to phosphoinositide 3-kinase activation*. Immunity, 2000. **13**(6): p. 817-27.
20. Nihiro, H. and E.A. Clark, *Regulation of B-cell fate by antigen-receptor signals*. Nat Rev Immunol, 2002. **2**(12): p. 945-56.

21. Cardone, M.H., et al., *Regulation of cell death protease caspase-9 by phosphorylation*. Science, 1998. **282**(5392): p. 1318-21.
22. Kane, L.P., et al., *Induction of NF-kappaB by the Akt/PKB kinase*. Curr Biol, 1999. **9**(11): p. 601-4.
23. Ma, Q., et al., *Impaired B-lymphopoiesis, myelopoiesis, and derailed cerebellar neuron migration in CXCR4- and SDF-1-deficient mice*. Proceedings of the National Academy of Sciences of the United States of America, 1998. **95**(16): p. 9448-9453.
24. D'Apuzzo, M., et al., *The chemokine SDF-1, stromal cell-derived factor 1, attracts early stage B cell precursors via the chemokine receptor CXCR4*. European Journal of Immunology, 1997. **27**(7): p. 1788-1793.
25. Brack, C., et al., *A complete immunoglobulin gene is created by somatic recombination*. Cell, 1978. **15**(1): p. 1-14.
26. Oettinger, M.A., et al., *RAG-1 and RAG-2, adjacent genes that synergistically activate V(D)J recombination*. Science, 1990. **248**(4962): p. 1517-23.
27. Schatz, D.G., M.A. Oettinger, and D. Baltimore, *The V(D)J recombination activating gene, RAG-1*. Cell, 1989. **59**(6): p. 1035-48.
28. Schatz, D.G. and Y. Ji, *Recombination centres and the orchestration of V(D)J recombination*. Nat Rev Immunol, 2011. **11**(4): p. 251-63.
29. Helmink, B.A. and B.P. Sleckman, *The response to and repair of RAG-mediated DNA double-strand breaks*. Annu Rev Immunol, 2012. **30**: p. 175-202.
30. Elantak, L., et al., *Structural Basis for Galectin-1-dependent Pre-B Cell Receptor (Pre-BCR) Activation*. Journal of Biological Chemistry, 2012. **287**(53): p. 44703-44713.
31. Gauthier, L., et al., *Galectin-1 is a stromal cell ligand of the pre-B cell receptor (BCR) implicated in synapse formation between pre-B and stromal cells and in pre-BCR triggering*. Proceedings of the National Academy of Sciences of the United States of America, 2002. **99**(20): p. 13014-13019.
32. Bankovich, A.J., et al., *Structural insight into pre-B cell receptor function*. Science, 2007. **316**(5822): p. 291-294.
33. Saijo, K., et al., *Essential role of Src-family protein tyrosine kinases in NF-kappa B activation during B cell development*. Nature Immunology, 2003. **4**(3): p. 274-279.
34. Otero, D.C. and R.C. Rickert, *CD19 function in early and late B cell development. II. CD19 facilitates the pro-B/pre-B transition*. Journal of Immunology, 2003. **171**(11): p. 5921-5930.
35. Wardemann, H., et al., *Predominant autoantibody production by early human B cell precursors*. Science, 2003. **301**(5638): p. 1374-1377.
36. Yarkoni, Y., A. Getahun, and J.C. Cambier, *Molecular underpinning of B-cell anergy*. Immunological Reviews, 2010. **237**: p. 249-263.
37. Lesley, R., et al., *Reduced competitiveness of autoantigen-engaged B cells due to increased dependence on BAFF*. Immunity, 2004. **20**(4): p. 441-453.
38. Monroe, J.G., *ITAM-mediated tonic signalling through pre-BCR and BCR complexes*. Nature Reviews Immunology, 2006. **6**(4): p. 283-294.
39. Lam, K.P., R. Kuhn, and K. Rajewsky, *In vivo ablation of surface immunoglobulin on mature B cells by inducible gene targeting results in rapid cell death*. Cell, 1997. **90**(6): p. 1073-1083.
40. Kraus, M., et al., *Survival of resting mature B lymphocytes depends on BCR signaling via the Ig alpha/beta heterodimer*. Cell, 2004. **117**(6): p. 787-800.

41. Shaffer, A.L. and M.S. Schlissel, *Truncated heavy chain protein relieves the requirement for surrogate light chains in early B cell development*. Journal of Immunology, 1997. **159**(3): p. 1265-1275.
42. Teh, Y.M. and M.S. Neuberger, *The immunoglobulin (Ig)alpha and Ig beta cytoplasmic domains are independently sufficient to signal B cell maturation and activation in transgenic mice*. Journal of Experimental Medicine, 1997. **185**(10): p. 1753-1758.
43. Meffre, E. and M.C. Nussenzweig, *Deletion of immunoglobulin ss in developing B cells leads to cell death*. Proceedings of the National Academy of Sciences of the United States of America, 2002. **99**(17): p. 11334-11339.
44. Wienands, J., O. Larbolette, and M. Reth, *Evidence for a preformed transducer complex organized by the B cell antigen receptor*. Proceedings of the National Academy of Sciences of the United States of America, 1996. **93**(15): p. 7865-7870.
45. Pani, G., et al., *Identification of the Tyrosine Phosphatase Ptp1c as a B-Cell Antigen Receptor-Associated Protein Involved in the Regulation of B-Cell Signaling*. Journal of Experimental Medicine, 1995. **181**(6): p. 2077-2084.
46. Pao, L.I., et al., *B cell-specific deletion of protein-tyrosine phosphatase Shp1 promotes B-1a cell development and causes systemic autoimmunity*. Immunity, 2007. **27**(1): p. 35-48.
47. Cyster, J.G. and C.C. Goodnow, *Protein-Tyrosine-Phosphatase 1c Negatively Regulates Antigen Receptor Signaling in B-Lymphocytes and Determines Thresholds for Negative Selection*. Immunity, 1995. **2**(1): p. 13-24.
48. Kurosaki, T., *Regulation of B cell fates by BCR signaling components*. Curr Opin Immunol, 2002. **14**(3): p. 341-7.
49. Chen, L., et al., *SYK-dependent tonic B-cell receptor signaling is a rational treatment target in diffuse large B-cell lymphoma*. Blood, 2008. **111**(4): p. 2230-7.
50. Smith, S.H. and M. Reth, *Perspectives on the nature of BCR-mediated survival signals*. Molecular Cell, 2004. **14**(6): p. 696-697.
51. Schweighoffer, E., et al., *The BAFF receptor transduces survival signals by co-opting the B cell receptor signaling pathway*. Immunity, 2013. **38**(3): p. 475-88.
52. Åström, K.J. and R.M. Murray, *Feedback systems : an introduction for scientists and engineers*. 2008, Princeton: Princeton University Press. xii, 396 p.
53. Yang, J.Y. and M. Reth, *The dissociation activation model of B cell antigen receptor triggering*. Febs Letters, 2010. **584**(24): p. 4872-4877.
54. Harwood, N.E. and F.D. Batista, *The Cytoskeleton Coordinates the Early Events of B-cell Activation*. Cold Spring Harbor Perspectives in Biology, 2011. **3**(2).
55. Pierce, S.K. and W.L. Liu, *The tipping points in the initiation of B cell signalling: how small changes make big differences*. Nature Reviews Immunology, 2010. **10**(11): p. 767-777.
56. Schamel, W.W.A. and M. Reth, *Monomeric and oligomeric complexes of the B cell antigen receptor*. Immunity, 2000. **13**(1): p. 5-14.
57. Tolar, P., H.W. Sohn, and S.K. Pierce, *The initiation of antigen-induced B cell antigen receptor signaling viewed in living cells by fluorescence resonance energy transfer*. Nature Immunology, 2005. **6**(11): p. 1168-1176.
58. Tolar, P., et al., *The constant region of the membrane immunoglobulin mediates B cell-receptor clustering and signaling in response to membrane antigens*. Immunity, 2009. **30**(1): p. 44-55.

59. Fuentes-Panana, E.M., et al., *Ig alpha/Ig ss complexes generate signals for B cell development independent of selective plasma membrane compartmentalization*. Journal of Immunology, 2005. **174**(3): p. 1245-1252.
60. Treanor, B., et al., *The membrane skeleton controls diffusion dynamics and signaling through the B cell receptor*. Immunity, 2010. **32**(2): p. 187-99.
61. Hao, S. and A. August, *Actin depolymerization transduces the strength of B-cell receptor stimulation*. Mol Biol Cell, 2005. **16**(5): p. 2275-84.
62. Treanor, B., et al., *Dynamic cortical actin remodeling by ERM proteins controls BCR microcluster organization and integrity*. J Exp Med, 2011. **208**(5): p. 1055-68.
63. Mattila, P.K., et al., *The actin and tetraspanin networks organize receptor nanoclusters to regulate B cell receptor-mediated signaling*. Immunity, 2013. **38**(3): p. 461-74.
64. Depoil, D., et al., *CD19 is essential for B cell activation by promoting B cell receptor-antigen microcluster formation in response to membrane-bound ligand*. Nature Immunology, 2008. **9**(1): p. 63-72.
65. Lillemeier, B.F., et al., *TCR and Lat are expressed on separate protein islands on T cell membranes and concatenate during activation*. Nat Immunol, 2010. **11**(1): p. 90-6.
66. Lillemeier, B.F., et al., *Plasma membrane-associated proteins are clustered into islands attached to the cytoskeleton*. Proceedings of the National Academy of Sciences of the United States of America, 2006. **103**(50): p. 18992-18997.
67. Srinivasan, L., et al., *PI3 Kinase Signals BCR-Dependent Mature B Cell Survival*. Cell, 2009. **139**(3): p. 573-586.
68. Diamant, E., Z. Keren, and D. Melamed, *CD19 regulates positive selection and maturation in B lymphopoiesis: lack of CD19 imposes developmental arrest of immature B cells and consequential stimulation of receptor editing*. Blood, 2005. **105**(8): p. 3247-3254.
69. Ng, L.G., C.R. Mackay, and F. Mackay, *The BAFF/APRIL system: life beyond B lymphocytes*. Molecular Immunology, 2005. **42**(7): p. 763-772.
70. Mackay, F., et al., *Mice transgenic for BAFF develop lymphocytic disorders along with autoimmune manifestations*. J Exp Med, 1999. **190**(11): p. 1697-710.
71. Batista, F.D. and N.E. Harwood, *The who, how and where of antigen presentation to B cells*. Nat Rev Immunol, 2009. **9**(1): p. 15-27.
72. Cyster, J.G., *B cell follicles and antigen encounters of the third kind*. Nat Immunol, 2010. **11**(11): p. 989-96.
73. Cyster, J.G., *Chemokines, sphingosine-1-phosphate, and cell migration in secondary lymphoid organs*. Annu Rev Immunol, 2005. **23**: p. 127-59.
74. Carrasco, Y.R. and F.D. Batista, *B cell recognition of membrane-bound antigen: an exquisite way of sensing ligands*. Curr Opin Immunol, 2006. **18**(3): p. 286-91.
75. Batista, F.D., D. Iber, and M.S. Neuberger, *B cells acquire antigen from target cells after synapse formation*. Nature, 2001. **411**(6836): p. 489-94.
76. Roozendaal, R., et al., *Conduits mediate transport of low-molecular-weight antigen to lymph node follicles*. Immunity, 2009. **30**(2): p. 264-76.
77. Junt, T., et al., *Subcapsular sinus macrophages in lymph nodes clear lymph-borne viruses and present them to antiviral B cells*. Nature, 2007. **450**(7166): p. 110-4.
78. Moseman, E.A., et al., *B cell maintenance of subcapsular sinus macrophages protects against a fatal viral infection independent of adaptive immunity*. Immunity, 2012. **36**(3): p. 415-26.

79. Barral, P., et al., *CD169(+) macrophages present lipid antigens to mediate early activation of iNKT cells in lymph nodes*. *Nat Immunol*, 2010. **11**(4): p. 303-12.
80. Heesters, B.A., et al., *Endocytosis and recycling of immune complexes by follicular dendritic cells enhances B cell antigen binding and activation*. *Immunity*, 2013. **38**(6): p. 1164-75.
81. Allen, C.D. and J.G. Cyster, *Follicular dendritic cell networks of primary follicles and germinal centers: phenotype and function*. *Semin Immunol*, 2008. **20**(1): p. 14-25.
82. Gonzalez, S.F., et al., *B cell acquisition of antigen in vivo*. *Curr Opin Immunol*, 2009. **21**(3): p. 251-7.
83. Harwood, N.E. and F.D. Batista, *Early events in B cell activation*. *Annu Rev Immunol*, 2010. **28**: p. 185-210.
84. Fleire, S.J., et al., *B cell ligand discrimination through a spreading and contraction response*. *Science*, 2006. **312**(5774): p. 738-741.
85. Natkanski, E., et al., *B cells use mechanical energy to discriminate antigen affinities*. *Science*, 2013. **340**(6140): p. 1587-90.
86. Hermiston, M.L., J. Zikherman, and J.W. Zhu, *CD45, CD148, and Lyp/Pep: critical phosphatases regulating Src family kinase signaling networks in immune cells*. *Immunol Rev*, 2009. **228**(1): p. 288-311.
87. Cordoba, S.P., et al., *The large ectodomains of CD45 and CD148 regulate their segregation from and inhibition of ligated T-cell receptor*. *Blood*, 2013. **121**(21): p. 4295-302.
88. Reth, M., *Matching cellular dimensions with molecular sizes*. *Nat Immunol*, 2013. **14**(8): p. 765-7.
89. Zhu, J.W., et al., *Structurally distinct phosphatases CD45 and CD148 both regulate B cell and macrophage immunoreceptor signaling*. *Immunity*, 2008. **28**(2): p. 183-96.
90. Davis, S.J. and P.A. van der Merwe, *The kinetic-segregation model: TCR triggering and beyond*. *Nat Immunol*, 2006. **7**(8): p. 803-9.
91. Varma, R., et al., *T cell receptor-proximal signals are sustained in peripheral microclusters and terminated in the central supramolecular activation cluster*. *Immunity*, 2006. **25**(1): p. 117-27.
92. Batista, F.D. and N.S. Neuberger, *B cells extract and present immobilized antigen: implications for affinity discrimination*. *Embo Journal*, 2000. **19**(4): p. 513-520.
93. Goodridge, H.S., et al., *Activation of the innate immune receptor Dectin-1 upon formation of a 'phagocytic synapse'*. *Nature*, 2011. **472**(7344): p. 471-5.
94. James, J.R. and R.D. Vale, *Biophysical mechanism of T-cell receptor triggering in a reconstituted system*. *Nature*, 2012. **487**(7405): p. 64-9.
95. Lin, K.B., et al., *The rap GTPases regulate B cell morphology, immune-synapse formation, and signaling by particulate B cell receptor ligands*. *Immunity*, 2008. **28**(1): p. 75-87.
96. Arana, E., et al., *Activation of the small GTPase Rac2 via the B cell receptor regulates B cell adhesion and immunological-synapse formation*. *Immunity*, 2008. **28**(1): p. 88-99.
97. Carrasco, Y.R., et al., *LFA-1/ICAM-1 interaction lowers the threshold of B cell activation by facilitating B cell adhesion and synapse formation*. *Immunity*, 2004. **20**(5): p. 589-599.
98. Dustin, M.L. and J.T. Groves, *Receptor Signaling Clusters in the Immune Synapse*. *Annual Review of Biophysics*, Vol 41, 2012. **41**: p. 543-556.

99. Scholer, A., et al., *Intercellular adhesion molecule-1-dependent stable interactions between T cells and dendritic cells determine CD8(+) T cell memory*. *Immunity*, 2008. **28**(2): p. 258-270.
100. Grakoui, A., et al., *The immunological synapse: A molecular machine controlling T cell activation*. *Science*, 1999. **285**(5425): p. 221-227.
101. Huse, M., et al., *T cells use two directionally distinct pathways for cytokine secretion*. *Nat Immunol*, 2006. **7**(3): p. 247-55.
102. Pan, C., N. Baumgarth, and J.R. Parnes, *CD72-deficient mice reveal nonredundant roles of CD72 in B cell development and activation*. *Immunity*, 1999. **11**(4): p. 495-506.
103. Rawlings, D.J., et al., *Integration of B cell responses through Toll-like receptors and antigen receptors*. *Nat Rev Immunol*, 2012. **12**(4): p. 282-94.
104. Reth, M., *Hydrogen peroxide as second messenger in lymphocyte activation*. *Nature Immunology*, 2002. **3**(12): p. 1129-1134.
105. Booth, J., et al., *Modulation of B cell responses by Toll-like receptors*. *Cell and Tissue Research*, 2011. **343**(1): p. 131-140.
106. Peng, S.L., *Signaling in B cells via toll-like receptors*. *Current Opinion in Immunology*, 2005. **17**(3): p. 230-236.
107. Hou, B.D., et al., *Selective Utilization of Toll-like Receptor and MyD88 Signaling in B Cells for Enhancement of the Antiviral Germinal Center Response*. *Immunity*, 2011. **34**(3): p. 375-384.
108. Pasare, C. and R. Medzhitov, *Control of B-cell responses by Toll-like receptors*. *Nature*, 2005. **438**(7066): p. 364-368.
109. Kasturi, S.P., et al., *Programming the magnitude and persistence of antibody responses with innate immunity*. *Nature*, 2011. **470**(7335): p. 543-U136.
110. Eckl-Dorna, J. and F.D. Batista, *BCR-mediated uptake of antigen linked to TLR9 ligand stimulates B-cell proliferation and antigen-specific plasma cell formation*. *Blood*, 2009. **113**(17): p. 3969-3977.
111. Gavin, A.L., et al., *Adjuvant-enhanced antibody responses in the absence of toll-like receptor signaling*. *Science*, 2006. **314**(5807): p. 1936-1938.
112. Krieg, A.M., et al., *Cpg Motifs in Bacterial-DNA Trigger Direct B-Cell Activation*. *Nature*, 1995. **374**(6522): p. 546-549.
113. Green, N.M. and A. Marshak-Rothstein, *Toll-like receptor driven B cell activation in the induction of systemic autoimmunity*. *Seminars in Immunology*, 2011. **23**(2): p. 106-112.
114. Leadbetter, E.A., et al., *Chromatin-IgG complexes activate B cells by dual engagement of IgM and Toll-like receptors*. *Nature*, 2002. **416**(6881): p. 603-607.
115. Romanczuk, P., et al., *Active Brownian particles From Individual to Collective Stochastic Dynamics*. *European Physical Journal-Special Topics*, 2012. **202**(1): p. 1-162.
116. Qian, H., M.P. Sheetz, and E.L. Elson, *Single-Particle Tracking - Analysis of Diffusion and Flow in 2-Dimensional Systems*. *Biophysical Journal*, 1991. **60**(4): p. 910-921.
117. Jaqaman, K., et al., *Robust single-particle tracking in live-cell time-lapse sequences*. *Nature Methods*, 2008. **5**(8): p. 695-702.
118. Kusumi, A., et al., *Dynamic organizing principles of the plasma membrane that regulate signal transduction: commemorating the fortieth anniversary of Singer and Nicolson's fluid-mosaic model*. *Annu Rev Cell Dev Biol*, 2012. **28**: p. 215-50.
119. Singer, S.J. and G.L. Nicolson, *Fluid Mosaic Model of Structure of Cell-Membranes*. *Science*, 1972. **175**(4023): p. 720-&.

120. Saxton, M.J. and K. Jacobson, *Single-particle tracking: Applications to membrane dynamics*. Annual Review of Biophysics and Biomolecular Structure, 1997. **26**: p. 373-399.
121. Fujiwara, T., et al., *Phospholipids undergo hop diffusion in compartmentalized cell membrane*. Journal of Cell Biology, 2002. **157**(6): p. 1071-1081.
122. Kusumi, A., et al., *Membrane mechanisms for signal transduction: the coupling of the meso-scale raft domains to membrane-skeleton-induced compartments and dynamic protein complexes*. Semin Cell Dev Biol, 2012. **23**(2): p. 126-44.
123. Lingwood, D. and K. Simons, *Lipid Rafts As a Membrane-Organizing Principle*. Science, 2010. **327**(5961): p. 46-50.
124. Frick, M., K. Schmidt, and B.J. Nichols, *Modulation of lateral diffusion in the plasma membrane by protein density*. Current Biology, 2007. **17**(5): p. 462-467.
125. Sheetz, M.P., M. Schindler, and D.E. Koppel, *Lateral Mobility of Integral Membrane-Proteins Is Increased in Spherocytic Erythrocytes*. Nature, 1980. **285**(5765): p. 510-512.
126. Baumgart, T., et al., *Large-scale fluid/fluid phase separation of proteins and lipids in giant plasma membrane vesicles*. Proceedings of the National Academy of Sciences of the United States of America, 2007. **104**(9): p. 3165-3170.
127. Tomishige, M., Y. Sako, and A. Kusumi, *Regulation mechanism of the lateral diffusion of band 3 in erythrocyte membranes by the membrane skeleton*. Journal of Cell Biology, 1998. **142**(4): p. 989-1000.
128. Morone, N., et al., *Three-dimensional reconstruction of the membrane skeleton at the plasma membrane interface by electron tomography*. Journal of Cell Biology, 2006. **174**(6): p. 851-862.
129. Eggeling, C., et al., *Direct observation of the nanoscale dynamics of membrane lipids in a living cell*. Nature, 2009. **457**(7233): p. 1159-U121.
130. Suzuki, K.G.N., et al., *GPI-anchored receptor clusters transiently recruit Lyn and G alpha for temporary cluster immobilization and Lyn activation: single-molecule tracking study I*. Journal of Cell Biology, 2007. **177**(4): p. 717-730.
131. Gowrishankar, K., et al., *Active Remodeling of Cortical Actin Regulates Spatiotemporal Organization of Cell Surface Molecules*. Cell, 2012. **149**(6): p. 1353-1367.
132. Hu, Q.C., et al., *A Septin Diffusion Barrier at the Base of the Primary Cilium Maintains Ciliary Membrane Protein Distribution*. Science, 2010. **329**(5990): p. 436-439.
133. Takizawa, P.A., et al., *Plasma membrane compartmentalization in yeast by messenger RNA transport and a septin diffusion barrier*. Science, 2000. **290**(5490): p. 341-344.
134. Luedeke, C., et al., *Septin-dependent compartmentalization of the endoplasmic reticulum during yeast polarized growth*. Journal of Cell Biology, 2005. **169**(6): p. 897-908.
135. Schlimpert, S., et al., *General Protein Diffusion Barriers Create Compartments within Bacterial Cells*. Cell, 2012. **151**(6): p. 1270-1282.
136. Banga I., S.-G.A., *Preparation and properties of myosin A and B*. Stud Inst Med Chem Univ Szeged, 1941-42. **I**: p. 6-15.
137. Szent-Gyorgyi, A.G., *The early history of the biochemistry of muscle contraction*. J Gen Physiol, 2004. **123**(6): p. 631-41.
138. Straub, F.B. and G. Feuer, *[Adenosine triphosphate, the functional group of actin]*. Kiserl Orvostud, 1950. **2**(2): p. 141-51.
139. Ingber, D.E., *Tensegrity I. Cell structure and hierarchical systems biology*. J Cell Sci, 2003. **116**(Pt 7): p. 1157-73.

140. Ingber, D.E., *Tensegrity II. How structural networks influence cellular information processing networks*. J Cell Sci, 2003. **116**(Pt 8): p. 1397-408.
141. Engqvist-Goldstein, A.E. and D.G. Drubin, *Actin assembly and endocytosis: from yeast to mammals*. Annu Rev Cell Dev Biol, 2003. **19**: p. 287-332.
142. Eggert, U.S., T.J. Mitchison, and C.M. Field, *Animal cytokinesis: from parts list to mechanisms*. Annu Rev Biochem, 2006. **75**: p. 543-66.
143. Hill, C.S., J. Wynne, and R. Treisman, *The Rho family GTPases RhoA, Rac1, and CDC42Hs regulate transcriptional activation by SRF*. Cell, 1995. **81**(7): p. 1159-70.
144. Pollard, T.D., *Rate constants for the reactions of ATP- and ADP-actin with the ends of actin filaments*. J Cell Biol, 1986. **103**(6 Pt 2): p. 2747-54.
145. Sept, D. and J.A. McCammon, *Thermodynamics and kinetics of actin filament nucleation*. Biophys J, 2001. **81**(2): p. 667-74.
146. Cooper, G.M., *The Cell: A Molecular Approach*, in *Structure and Organization of Actin Filaments*. 2000, Sunderland (MA): Sinauer Associates.
147. Bugyi, B. and M.F. Carrier, *Control of actin filament treadmilling in cell motility*. Annu Rev Biophys, 2010. **39**: p. 449-70.
148. Pollard, T.D. and G.G. Borisy, *Cellular motility driven by assembly and disassembly of actin filaments*. Cell, 2003. **112**(4): p. 453-65.
149. Machesky, L.M., et al., *Purification of a cortical complex containing two unconventional actins from Acanthamoeba by affinity chromatography on profilin-agarose*. J Cell Biol, 1994. **127**(1): p. 107-15.
150. Pollard, T.D., *Regulation of actin filament assembly by Arp2/3 complex and formins*. Annual Review of Biophysics and Biomolecular Structure, 2007. **36**: p. 451-477.
151. Mullins, R.D., J.A. Heuser, and T.D. Pollard, *The interaction of Arp2/3 complex with actin: nucleation, high affinity pointed end capping, and formation of branching networks of filaments*. Proc Natl Acad Sci U S A, 1998. **95**(11): p. 6181-6.
152. Firat-Karalar, E.N. and M.D. Welch, *New mechanisms and functions of actin nucleation*. Curr Opin Cell Biol, 2011. **23**(1): p. 4-13.
153. Andrianantoandro, E. and T.D. Pollard, *Mechanism of actin filament turnover by severing and nucleation at different concentrations of ADF/cofilin*. Molecular Cell, 2006. **24**(1): p. 13-23.
154. Sagot, I., et al., *An actin nucleation mechanism mediated by Bni1 and profilin*. Nat Cell Biol, 2002. **4**(8): p. 626-31.
155. Pruyne, D., et al., *Role of formins in actin assembly: nucleation and barbed-end association*. Science, 2002. **297**(5581): p. 612-5.
156. Chesarone, M.A., A.G. DuPage, and B.L. Goode, *Unleashing formins to remodel the actin and microtubule cytoskeletons*. Nat Rev Mol Cell Biol, 2010. **11**(1): p. 62-74.
157. Zigmond, S.H., et al., *Formin leaky cap allows elongation in the presence of tight capping proteins*. Curr Biol, 2003. **13**(20): p. 1820-3.
158. Quinlan, M.E., et al., *Drosophila Spire is an actin nucleation factor*. Nature, 2005. **433**(7024): p. 382-388.
159. Carrier, M.F., et al., *Control of actin assembly by the WH2 domains and their multifunctional tandem repeats in Spire and Cordon-Bleu*. Int Rev Cell Mol Biol, 2011. **290**: p. 55-85.
160. Quinlan, M.E., et al., *Regulatory interactions between two actin nucleators, Spire and Cappuccino*. J Cell Biol, 2007. **179**(1): p. 117-28.

161. Okada, K., et al., *Adenomatous polyposis coli protein nucleates actin assembly and synergizes with the formin mDia1*. J Cell Biol, 2010. **189**(7): p. 1087-96.
162. Carlier, M.F., J. Pernier, and B.S. Avvaru, *Control of actin filament dynamics at barbed ends by WH2 domains: From capping to permissive and processive assembly*. Cytoskeleton (Hoboken), 2013.
163. Ahuja, R., et al., *Cordon-bleu is an actin nucleation factor and controls neuronal morphology*. Cell, 2007. **131**(2): p. 337-50.
164. Husson, C., et al., *Cordon-Bleu uses WH2 domains as multifunctional dynamizers of actin filament assembly*. Mol Cell, 2011. **43**(3): p. 464-77.
165. Takenawa, T. and S. Suetsugu, *The WASP-WAVE protein network: connecting the membrane to the cytoskeleton*. Nat Rev Mol Cell Biol, 2007. **8**(1): p. 37-48.
166. Rotty, J.D., C. Wu, and J.E. Bear, *New insights into the regulation and cellular functions of the ARP2/3 complex*. Nat Rev Mol Cell Biol, 2013. **14**(1): p. 7-12.
167. Zhang, J., B. Dong, and K.A. Siminovitch, *Contributions of Wiskott-Aldrich syndrome family cytoskeletal regulatory adapters to immune regulation*. Immunol Rev, 2009. **232**(1): p. 175-94.
168. Aspenstrom, P., U. Lindberg, and A. Hall, *Two GTPases, Cdc42 and Rac, bind directly to a protein implicated in the immunodeficiency disorder Wiskott-Aldrich syndrome*. Curr Biol, 1996. **6**(1): p. 70-5.
169. Ridley, A.J. and A. Hall, *The small GTP-binding protein rho regulates the assembly of focal adhesions and actin stress fibers in response to growth factors*. Cell, 1992. **70**(3): p. 389-99.
170. Rohatgi, R., H.Y. Ho, and M.W. Kirschner, *Mechanism of N-WASP activation by CDC42 and phosphatidylinositol 4, 5-bisphosphate*. J Cell Biol, 2000. **150**(6): p. 1299-310.
171. Rohatgi, R., et al., *The interaction between N-WASP and the Arp2/3 complex links Cdc42-dependent signals to actin assembly*. Cell, 1999. **97**(2): p. 221-31.
172. Padrick, S.B. and M.K. Rosen, *Physical mechanisms of signal integration by WASP family proteins*. Annu Rev Biochem, 2010. **79**: p. 707-35.
173. Li, P., et al., *Phase transitions in the assembly of multivalent signalling proteins*. Nature, 2012. **483**(7389): p. 336-40.
174. Eden, S., et al., *Mechanism of regulation of WAVE1-induced actin nucleation by Rac1 and Nck*. Nature, 2002. **418**(6899): p. 790-3.
175. Oikawa, T., et al., *PtdIns(3,4,5)P3 binding is necessary for WAVE2-induced formation of lamellipodia*. Nat Cell Biol, 2004. **6**(5): p. 420-6.
176. Leng, Y., et al., *Abelson-interactor-1 promotes WAVE2 membrane translocation and Abelson-mediated tyrosine phosphorylation required for WAVE2 activation*. Proc Natl Acad Sci U S A, 2005. **102**(4): p. 1098-103.
177. Chen, Z., et al., *Structure and control of the actin regulatory WAVE complex*. Nature, 2010. **468**(7323): p. 533-8.
178. Linardopoulou, E.V., et al., *Human subtelomeric WASH genes encode a new subclass of the WASP family*. PLoS Genet, 2007. **3**(12): p. e237.
179. Gomez, T.S. and D.D. Billadeau, *A FAM21-containing WASH complex regulates retromer-dependent sorting*. Dev Cell, 2009. **17**(5): p. 699-711.
180. Harbour, M.E., S.Y. Breusegem, and M.N. Seaman, *Recruitment of the endosomal WASH complex is mediated by the extended 'tail' of Fam21 binding to the retromer protein Vps35*. Biochem J, 2012. **442**(1): p. 209-20.

181. Jia, D., et al., *Multiple repeat elements within the FAM21 tail link the WASH actin regulatory complex to the retromer*. Mol Biol Cell, 2012. **23**(12): p. 2352-61.
182. Hao, Y.H., et al., *Regulation of WASH-Dependent Actin Polymerization and Protein Trafficking by Ubiquitination*. Cell, 2013. **152**(5): p. 1051-1064.
183. Campellone, K.G., et al., *WHAMM is an Arp2/3 complex activator that binds microtubules and functions in ER to Golgi transport*. Cell, 2008. **134**(1): p. 148-161.
184. Gad, A.K., et al., *RhoD regulates cytoskeletal dynamics via the actin nucleation-promoting factor WASp homologue associated with actin Golgi membranes and microtubules*. Mol Biol Cell, 2012. **23**(24): p. 4807-19.
185. Haglund, C.M. and M.D. Welch, *Pathogens and polymers: microbe-host interactions illuminate the cytoskeleton*. J Cell Biol, 2011. **195**(1): p. 7-17.
186. Loisel, T.P., et al., *Reconstitution of actin-based motility of Listeria and Shigella using pure proteins*. Nature, 1999. **401**(6753): p. 613-6.
187. Bravo-Cordero, J.J., et al., *Functions of cofilin in cell locomotion and invasion*. Nat Rev Mol Cell Biol, 2013. **14**(7): p. 405-15.
188. Breitsprecher, D., et al., *Cofilin cooperates with fascin to disassemble filopodial actin filaments*. J Cell Sci, 2011. **124**(Pt 19): p. 3305-18.
189. Gandhi, M., et al., *Coronin switches roles in actin disassembly depending on the nucleotide state of actin*. Mol Cell, 2009. **34**(3): p. 364-74.
190. Kueh, H.Y., et al., *Actin disassembly by cofilin, coronin, and Aip1 occurs in bursts and is inhibited by barbed-end cappers*. J Cell Biol, 2008. **182**(2): p. 341-53.
191. Chan, C., C.C. Beltzner, and T.D. Pollard, *Cofilin dissociates Arp2/3 complex and branches from actin filaments*. Curr Biol, 2009. **19**(7): p. 537-45.
192. Wu, J.Q. and T.D. Pollard, *Counting cytokinesis proteins globally and locally in fission yeast*. Science, 2005. **310**(5746): p. 310-4.
193. Martin, A.C., M.D. Welch, and D.G. Drubin, *Arp2/3 ATP hydrolysis-catalysed branch dissociation is critical for endocytic force generation*. Nat Cell Biol, 2006. **8**(8): p. 826-33.
194. Ydenberg, C.A., et al., *GMF Severs Actin-Arp2/3 Complex Branch Junctions by a Cofilin-like Mechanism*. Current Biology, 2013. **23**(12): p. 1037-1045.
195. Freeman, S.A., et al., *Cofilin-mediated F-actin severing is regulated by the Rap GTPase and controls the cytoskeletal dynamics that drive lymphocyte spreading and BCR microcluster formation*. J Immunol, 2011. **187**(11): p. 5887-900.
196. Kiuchi, T., et al., *Cofilin promotes stimulus-induced lamellipodium formation by generating an abundant supply of actin monomers*. J Cell Biol, 2007. **177**(3): p. 465-76.
197. van Rheenen, J., J. Condeelis, and M. Glogauer, *A common cofilin activity cycle in invasive tumor cells and inflammatory cells*. J Cell Sci, 2009. **122**(Pt 3): p. 305-11.
198. Mizuno, K., *Signaling mechanisms and functional roles of cofilin phosphorylation and dephosphorylation*. Cellular Signalling, 2013. **25**(2): p. 457-469.
199. van Rheenen, J., et al., *EGF-induced PIP2 hydrolysis releases and activates cofilin locally in carcinoma cells*. J Cell Biol, 2007. **179**(6): p. 1247-59.
200. Oser, M., et al., *Cortactin regulates cofilin and N-WASp activities to control the stages of invadopodium assembly and maturation*. J Cell Biol, 2009. **186**(4): p. 571-87.
201. Yang, N., et al., *Cofilin phosphorylation by LIM-kinase 1 and its role in Rac-mediated actin reorganization*. Nature, 1998. **393**(6687): p. 809-12.

202. Frantz, C., et al., *Cofilin is a pH sensor for actin free barbed end formation: role of phosphoinositide binding*. J Cell Biol, 2008. **183**(5): p. 865-79.
203. Mader, C.C., et al., *An EGFR-Src-Arg-cortactin pathway mediates functional maturation of invadopodia and breast cancer cell invasion*. Cancer Res, 2011. **71**(5): p. 1730-41.
204. Kolsch, V., P.G. Charest, and R.A. Firtel, *The regulation of cell motility and chemotaxis by phospholipid signaling*. J Cell Sci, 2008. **121**(Pt 5): p. 551-9.
205. Sander, E.E., et al., *Rac downregulates Rho activity: reciprocal balance between both GTPases determines cellular morphology and migratory behavior*. J Cell Biol, 1999. **147**(5): p. 1009-22.
206. Martin, C., et al., *Intracellular pH gradients in migrating cells*. Am J Physiol Cell Physiol, 2011. **300**(3): p. C490-5.
207. Ghosh, M., et al., *Cofilin promotes actin polymerization and defines the direction of cell motility*. Science, 2004. **304**(5671): p. 743-6.
208. Bakal, C., et al., *Quantitative morphological signatures define local signaling networks regulating cell morphology*. Science, 2007. **316**(5832): p. 1753-6.
209. Kottling, C. and K. Gerwert, *The dynamics of the catalytic site in small GTPases, variations on a common motif*. FEBS Lett, 2013. **587**(13): p. 2025-7.
210. Raaijmakers, J.H. and J.L. Bos, *Specificity in Ras and Rap Signaling*. Journal of Biological Chemistry, 2009. **284**(17): p. 10995-10999.
211. Wright, L.P. and M.R. Philips, *Thematic review series: lipid posttranslational modifications. CAAX modification and membrane targeting of Ras*. J Lipid Res, 2006. **47**(5): p. 883-91.
212. Laude, A.J. and I.A. Prior, *Palmitoylation and localisation of RAS isoforms are modulated by the hypervariable linker domain*. J Cell Sci, 2008. **121**(Pt 4): p. 421-7.
213. Zhang, F.L. and P.J. Casey, *Protein prenylation: molecular mechanisms and functional consequences*. Annu Rev Biochem, 1996. **65**: p. 241-69.
214. Dovas, A. and J.R. Couchman, *RhoGDI: multiple functions in the regulation of Rho family GTPase activities*. Biochem J, 2005. **390**(Pt 1): p. 1-9.
215. Chandra, A., et al., *The GDI-like solubilizing factor PDEdelta sustains the spatial organization and signalling of Ras family proteins*. Nat Cell Biol, 2012. **14**(2): p. 148-58.
216. Hanzal-Bayer, M., et al., *The complex of Arl2-GTP and PDE delta: from structure to function*. EMBO J, 2002. **21**(9): p. 2095-106.
217. Bohdanowicz, M. and S. Grinstein, *Role of phospholipids in endocytosis, phagocytosis, and macropinocytosis*. Physiol Rev, 2013. **93**(1): p. 69-106.
218. Zimmermann, G., et al., *Small molecule inhibition of the KRAS-PDEdelta interaction impairs oncogenic KRAS signalling*. Nature, 2013. **497**(7451): p. 638-42.
219. Riou, P., et al., *14-3-3 Proteins Interact with a Hybrid Prenyl-Phosphorylation Motif to Inhibit G Proteins (vol 153, pg 640, 2013)*. Cell, 2013. **153**(5): p. 1164-1164.
220. Takahashi, M., et al., *PKA-dependent phosphorylation of Rap1 regulates its membrane localization and cell migration*. J Biol Chem, 2013.
221. Lee, R.H.K., et al., *XRab40 and XCullin5 form a ubiquitin ligase complex essential for the noncanonical Wnt pathway*. Embo Journal, 2007. **26**(15): p. 3592-3606.
222. Kawabe, H., et al., *Regulation of Rap2A by the ubiquitin ligase Nedd4-1 controls neurite development*. Neuron, 2010. **65**(3): p. 358-72.
223. Gloerich, M. and J.L. Bos, *Regulating Rap small G-proteins in time and space*. Trends in Cell Biology, 2011. **21**(10): p. 615-623.

224. Drubin, D.G. and W.J. Nelson, *Origins of cell polarity*. Cell, 1996. **84**(3): p. 335-44.
225. Park, H.O. and E. Bi, *Central roles of small GTPases in the development of cell polarity in yeast and beyond*. Microbiol Mol Biol Rev, 2007. **71**(1): p. 48-96.
226. Bender, A. and J.R. Pringle, *Multicopy suppression of the cdc24 budding defect in yeast by CDC42 and three newly identified genes including the ras-related gene RSR1*. Proc Natl Acad Sci U S A, 1989. **86**(24): p. 9976-80.
227. Chant, J. and I. Herskowitz, *Genetic control of bud site selection in yeast by a set of gene products that constitute a morphogenetic pathway*. Cell, 1991. **65**(7): p. 1203-12.
228. Drees, B.L., et al., *A protein interaction map for cell polarity development*. J Cell Biol, 2001. **154**(3): p. 549-71.
229. Ubersax, J.A., et al., *Targets of the cyclin-dependent kinase Cdk1*. Nature, 2003. **425**(6960): p. 859-64.
230. Xiong, Y., et al., *Cells navigate with a local-excitation, global-inhibition-biased excitable network*. Proc Natl Acad Sci U S A, 2010. **107**(40): p. 17079-86.
231. Lappalainen, P. and D.G. Drubin, *Cofilin promotes rapid actin filament turnover in vivo*. Nature, 1997. **388**(6637): p. 78-82.
232. Gerard, A., et al., *The Par polarity complex regulates Rap1- and chemokine-induced T cell polarization*. J Cell Biol, 2007. **176**(6): p. 863-75.
233. Bos, J.L., J. de Rooij, and K.A. Reedquist, *Rap1 signalling: adhering to new models*. Nat Rev Mol Cell Biol, 2001. **2**(5): p. 369-77.
234. Durand, C.A., et al., *The Rap GTPases mediate CXCL13- and sphingosine1-phosphate-induced chemotaxis, adhesion, and Pyk2 tyrosine phosphorylation in B lymphocytes*. Eur J Immunol, 2006. **36**(8): p. 2235-49.
235. McLeod, S.J., et al., *The Rap GTPases regulate B cell migration toward the chemokine stromal cell-derived factor-1 (CXCL12): potential role for Rap2 in promoting B cell migration*. J Immunol, 2002. **169**(3): p. 1365-71.
236. Sawada, Y., et al., *Force sensing by mechanical extension of the Src family kinase substrate p130Cas*. Cell, 2006. **127**(5): p. 1015-26.
237. Tamada, M., M.P. Sheetz, and Y. Sawada, *Activation of a signaling cascade by cytoskeleton stretch*. Dev Cell, 2004. **7**(5): p. 709-18.
238. Nolz, J.C., et al., *The WAVE2 complex regulates T cell receptor signaling to integrins via Abl- and CrkL-C3G-mediated activation of Rap1*. J Cell Biol, 2008. **182**(6): p. 1231-44.
239. Krause, M., et al., *Ena/VASP proteins: regulators of the actin cytoskeleton and cell migration*. Annu Rev Cell Dev Biol, 2003. **19**: p. 541-64.
240. Krugmann, S., et al., *ARAP3 is a PI3K- and rap-regulated GAP for RhoA*. Curr Biol, 2004. **14**(15): p. 1380-4.
241. Zhu, J., et al., *Structure of a complete integrin ectodomain in a physiologic resting state and activation and deactivation by applied forces*. Mol Cell, 2008. **32**(6): p. 849-61.
242. Alon, R. and K. Ley, *Cells on the run: shear-regulated integrin activation in leukocyte rolling and arrest on endothelial cells*. Curr Opin Cell Biol, 2008. **20**(5): p. 525-32.
243. Kim, C., F. Ye, and M.H. Ginsberg, *Regulation of integrin activation*. Annu Rev Cell Dev Biol, 2011. **27**: p. 321-45.
244. Katagiri, K., et al., *RAPL, a Rap1-binding molecule that mediates Rap1-induced adhesion through spatial regulation of LFA-1*. Nat Immunol, 2003. **4**(8): p. 741-8.
245. Calderwood, D.A., I.D. Campbell, and D.R. Critchley, *Talins and kindlins: partners in integrin-mediated adhesion*. Nat Rev Mol Cell Biol, 2013. **14**(8): p. 503-17.

246. Han, J., et al., *Reconstructing and deconstructing agonist-induced activation of integrin alphaIIb beta3*. *Curr Biol*, 2006. **16**(18): p. 1796-806.
247. Lee, H.S., et al., *RIAM activates integrins by linking talin to ras GTPase membrane-targeting sequences*. *J Biol Chem*, 2009. **284**(8): p. 5119-27.
248. Caron, E., A.J. Self, and A. Hall, *The GTPase Rap1 controls functional activation of macrophage integrin alphaM beta2 by LPS and other inflammatory mediators*. *Curr Biol*, 2000. **10**(16): p. 974-8.
249. Katagiri, K., et al., *Rap1 is a potent activation signal for leukocyte function-associated antigen 1 distinct from protein kinase C and phosphatidylinositol-3-OH kinase*. *Mol Cell Biol*, 2000. **20**(6): p. 1956-69.
250. Reedquist, K.A., et al., *The small GTPase, Rap1, mediates CD31-induced integrin adhesion*. *J Cell Biol*, 2000. **148**(6): p. 1151-8.
251. Li, Y., et al., *Rap1a null mice have altered myeloid cell functions suggesting distinct roles for the closely related Rap1a and 1b proteins*. *J Immunol*, 2007. **179**(12): p. 8322-31.
252. Chrzanowska-Wodnicka, M., et al., *Rap1b is required for normal platelet function and hemostasis in mice*. *J Clin Invest*, 2005. **115**(3): p. 680-7.
253. Bergmeier, W., et al., *Mice lacking the signaling molecule CalDAG-GEFI represent a model for leukocyte adhesion deficiency type III*. *J Clin Invest*, 2007. **117**(6): p. 1699-707.
254. Katagiri, K., et al., *Crucial functions of the Rap1 effector molecule RAPL in lymphocyte and dendritic cell trafficking*. *Nat Immunol*, 2004. **5**(10): p. 1045-51.
255. Batista, F.D., et al., *The role of integrins and coreceptors in refining thresholds for B-cell responses*. *Immunol Rev*, 2007. **218**: p. 197-213.
256. Carrasco, Y.R. and F.D. Batista, *B-cell activation by membrane-bound antigens is facilitated by the interaction of VLA-4 with VCAM-1*. *Embo Journal*, 2006. **25**(4): p. 889-899.
257. Dustin, M.L., *The Cellular Context of T Cell Signaling*. *Immunity*, 2009. **30**(4): p. 482-492.
258. Dustin, M.L., *Modular Design of Immunological Synapses and Kinapses*. *Cold Spring Harbor Perspectives in Biology*, 2009. **1**(1).
259. Gerard, A., et al., *Secondary T cell-T cell synaptic interactions drive the differentiation of protective CD8(+) T cells*. *Nature Immunology*, 2013. **14**(4): p. 356-363.
260. Nguyen, D.X., P.D. Bos, and J. Massague, *Metastasis: from dissemination to organ-specific colonization*. *Nat Rev Cancer*, 2009. **9**(4): p. 274-84.
261. Chambers, A.F., A.C. Groom, and I.C. MacDonald, *Dissemination and growth of cancer cells in metastatic sites*. *Nat Rev Cancer*, 2002. **2**(8): p. 563-72.
262. Valastyan, S. and R.A. Weinberg, *Tumor Metastasis: Molecular Insights and Evolving Paradigms*. *Cell*, 2011. **147**(2): p. 275-292.
263. Plaks, V., C.D. Koopman, and Z. Werb, *Cancer. Circulating tumor cells*. *Science*, 2013. **341**(6151): p. 1186-8.
264. Nagrath, S., et al., *Isolation of rare circulating tumour cells in cancer patients by microchip technology*. *Nature*, 2007. **450**(7173): p. 1235-9.
265. Yu, M., et al., *Circulating tumor cells: approaches to isolation and characterization*. *J Cell Biol*, 2011. **192**(3): p. 373-82.

266. Baccelli, I., et al., *Identification of a population of blood circulating tumor cells from breast cancer patients that initiates metastasis in a xenograft assay*. Nat Biotechnol, 2013. **31**(6): p. 539-44.
267. Pantel, K., et al., *Circulating epithelial cells in patients with benign colon diseases*. Clin Chem, 2012. **58**(5): p. 936-40.
268. Cohen, S.J., et al., *Relationship of circulating tumor cells to tumor response, progression-free survival, and overall survival in patients with metastatic colorectal cancer*. J Clin Oncol, 2008. **26**(19): p. 3213-21.
269. Cristofanilli, M., et al., *Circulating tumor cells, disease progression, and survival in metastatic breast cancer*. N Engl J Med, 2004. **351**(8): p. 781-91.
270. Rhim, A.D., et al., *EMT and dissemination precede pancreatic tumor formation*. Cell, 2012. **148**(1-2): p. 349-61.
271. Freeman, S.A., et al., *Preventing the Activation or Cycling of the Rap1 GTPase Alters Adhesion and Cytoskeletal Dynamics and Blocks Metastatic Melanoma Cell Extravasation into the Lungs*. Cancer Research, 2010. **70**(11): p. 4590-4601.
272. Luzzi, K.J., et al., *Multistep nature of metastatic inefficiency: dormancy of solitary cells after successful extravasation and limited survival of early micrometastases*. Am J Pathol, 1998. **153**(3): p. 865-73.
273. Ghajar, C.M., et al., *The perivascular niche regulates breast tumour dormancy*. Nat Cell Biol, 2013. **15**(7): p. 807-17.
274. Hanahan, D. and R.A. Weinberg, *The hallmarks of cancer*. Cell, 2000. **100**(1): p. 57-70.
275. Nelson, C.M. and M.J. Bissell, *Of extracellular matrix, scaffolds, and signaling: Tissue architecture regulates development, homeostasis, and cancer*. Annual Review of Cell and Developmental Biology, 2006. **22**: p. 287-309.
276. Qian, B.Z. and J.W. Pollard, *Macrophage diversity enhances tumor progression and metastasis*. Cell, 2010. **141**(1): p. 39-51.
277. Hanahan, D. and L.M. Coussens, *Accessories to the Crime: Functions of Cells Recruited to the Tumor Microenvironment*. Cancer Cell, 2012. **21**(3): p. 309-322.
278. Hanahan, D. and R.A. Weinberg, *Hallmarks of Cancer: The Next Generation*. Cell, 2011. **144**(5): p. 646-674.
279. Kim, J., et al., *Tumor initiating but differentiated luminal-like breast cancer cells are highly invasive in the absence of basal-like activity*. Proc Natl Acad Sci U S A, 2012. **109**(16): p. 6124-9.
280. Quintana, E., et al., *Efficient tumour formation by single human melanoma cells*. Nature, 2008. **456**(7222): p. 593-8.
281. Nguyen, L.V., et al., *Cancer stem cells: an evolving concept*. Nature Reviews Cancer, 2012. **12**(2): p. 133-143.
282. Eaves, C.J., *CANCER STEM CELLS Here, there, everywhere?* Nature, 2008. **456**(7222): p. 581-582.
283. Wang, J.C.Y. and J.E. Dick, *Cancer stem cells: lessons from leukemia*. Trends in Cell Biology, 2005. **15**(9): p. 494-501.
284. Grivnikov, S.I., F.R. Greten, and M. Karin, *Immunity, Inflammation, and Cancer*. Cell, 2010. **140**(6): p. 883-899.
285. Parkin, D.M., *The global health burden of infection -associated cancers in the year 2002*. International Journal of Cancer, 2006. **118**(12): p. 3030-3044.

286. Chen, Q., X.H.F. Zhang, and J. Massague, *Macrophage Binding to Receptor VCAM-1 Transmits Survival Signals in Breast Cancer Cells that Invade the Lungs*. *Cancer Cell*, 2011. **20**(4): p. 538-549.
287. Joyce, J.A. and J.W. Pollard, *Microenvironmental regulation of metastasis*. *Nature Reviews Cancer*, 2009. **9**(4): p. 239-252.
288. DeNardo, D.G., et al., *CD4(+) T Cells Regulate Pulmonary Metastasis of Mammary Carcinomas by Enhancing Protumor Properties of Macrophages*. *Cancer Cell*, 2009. **16**(2): p. 91-102.
289. Taranova, A.G., et al., *Allergic Pulmonary Inflammation Promotes the Recruitment of Circulating Tumor Cells to the Lung*. *Cancer Research*, 2008. **68**(20): p. 8582-8589.
290. Kim, S., et al., *Carcinoma-produced factors activate myeloid cells through TLR2 to stimulate metastasis*. *Nature*, 2009. **457**(7225): p. 102-U108.
291. Hirose, Y., et al., *Inhibition of Stabilin-2 elevates circulating hyaluronic acid levels and prevents tumor metastasis*. *Proceedings of the National Academy of Sciences of the United States of America*, 2012. **109**(11): p. 4263-4268.
292. Itano, N., et al., *Relationship between hyaluronan production and metastatic potential of mouse mammary carcinoma cells*. *Cancer Research*, 1999. **59**(10): p. 2499-2504.
293. Oskarsson, T., et al., *Breast cancer cells produce tenascin C as a metastatic niche component to colonize the lungs*. *Nature Medicine*, 2011. **17**(7): p. 867-U256.
294. Levental, K.R., et al., *Matrix Crosslinking Forces Tumor Progression by Enhancing Integrin Signaling*. *Cell*, 2009. **139**(5): p. 891-906.
295. Paszek, M.J., et al., *Tensional homeostasis and the malignant phenotype*. *Cancer Cell*, 2005. **8**(3): p. 241-254.
296. Lu, P.F., V.M. Weaver, and Z. Werb, *The extracellular matrix: A dynamic niche in cancer progression*. *Journal of Cell Biology*, 2012. **196**(4): p. 395-406.
297. DuFort, C.C., M.J. Paszek, and V.M. Weaver, *Balancing forces: architectural control of mechanotransduction*. *Nature Reviews Molecular Cell Biology*, 2011. **12**(5): p. 308-319.
298. Wang, N., J.D. Tytell, and D.E. Ingber, *Mechanotransduction at a distance: mechanically coupling the extracellular matrix with the nucleus*. *Nature Reviews Molecular Cell Biology*, 2009. **10**(1): p. 75-82.
299. Halder, G., S. Dupont, and S. Piccolo, *Transduction of mechanical and cytoskeletal cues by YAP and TAZ*. *Nature Reviews Molecular Cell Biology*, 2012. **13**(9): p. 591-600.
300. Thery, M. and M. Bornens, *Cell shape and cell division*. *Current Opinion in Cell Biology*, 2006. **18**(6): p. 648-657.
301. Thery, M., et al., *The extracellular matrix guides the orientation of the cell division axis*. *Nature Cell Biology*, 2005. **7**(10): p. 947-U29.
302. Arnadottir, J. and M. Chalfie, *Eukaryotic mechanosensitive channels*. *Annu Rev Biophys*, 2010. **39**: p. 111-37.
303. Parsons, J.T., A.R. Horwitz, and M.A. Schwartz, *Cell adhesion: integrating cytoskeletal dynamics and cellular tension*. *Nature Reviews Molecular Cell Biology*, 2010. **11**(9): p. 633-643.
304. Gauthier, N.C., T.A. Masters, and M.P. Sheetz, *Mechanical feedback between membrane tension and dynamics*. *Trends in Cell Biology*, 2012. **22**(10): p. 527-535.
305. Roca-Cusachs, P., T. Iskratsch, and M.P. Sheetz, *Finding the weakest link - exploring integrin-mediated mechanical molecular pathways*. *Journal of Cell Science*, 2012. **125**(13): p. 3025-3038.

306. Moore, S.W., P. Roca-Cusachs, and M.P. Sheetz, *Stretchy Proteins on Stretchy Substrates: The Important Elements of Integrin-Mediated Rigidity Sensing*. Developmental Cell, 2010. **19**(2): p. 194-206.
307. Mammoto, A., T. Mammoto, and D.E. Ingber, *Mechanosensitive mechanisms in transcriptional regulation*. Journal of Cell Science, 2012. **125**(13): p. 3061-3073.
308. Jaqaman, K. and S. Grinstein, *Regulation from within: the cytoskeleton in transmembrane signaling*. Trends Cell Biol, 2012. **22**(10): p. 515-26.
309. Song, W., C. Liu, and A. Upadhyaya, *The pivotal position of the actin cytoskeleton in the initiation and regulation of B cell receptor activation*. Biochim Biophys Acta, 2013.
310. Ishii, K.J. and S. Akira, *Toll or toll-free adjuvant path toward the optimal vaccine development*. J Clin Immunol, 2007. **27**(4): p. 363-71.
311. Klinman, D.M., K.M. Barnhart, and J. Conover, *CpG motifs as immune adjuvants*. Vaccine, 1999. **17**(1): p. 19-25.
312. Palm, N.W. and R. Medzhitov, *Pattern recognition receptors and control of adaptive immunity*. Immunol Rev, 2009. **227**(1): p. 221-33.
313. Kawai, T. and S. Akira, *Toll-like Receptors and Their Crosstalk with Other Innate Receptors in Infection and Immunity*. Immunity, 2011. **34**(5): p. 637-650.
314. Kumar, H., T. Kawai, and S. Akira, *Pathogen recognition by the innate immune system*. Int Rev Immunol, 2011. **30**(1): p. 16-34.
315. Hou, B., et al., *Selective utilization of Toll-like receptor and MyD88 signaling in B cells for enhancement of the antiviral germinal center response*. Immunity, 2011. **34**(3): p. 375-84.
316. DeFranco, A.L., D.C. Rookhuizen, and B. Hou, *Contribution of Toll-like receptor signaling to germinal center antibody responses*. Immunol Rev, 2012. **247**(1): p. 64-72.
317. Weber, M., et al., *Phospholipase C-gamma2 and Vav cooperate within signaling microclusters to propagate B cell spreading in response to membrane-bound antigen*. J Exp Med, 2008. **205**(4): p. 853-68.
318. Depoil, D., et al., *CD19 is essential for B cell activation by promoting B cell receptor-antigen microcluster formation in response to membrane-bound ligand*. Nat Immunol, 2008. **9**(1): p. 63-72.
319. Tolar, P., et al., *The molecular assembly and organization of signaling active B-cell receptor oligomers*. Immunol Rev, 2009. **232**(1): p. 34-41.
320. Treanor, B., N.E. Harwood, and F.D. Batista, *Microsignalosomes: spatially resolved receptor signalling*. Biochem Soc Trans, 2009. **37**(Pt 5): p. 1014-8.
321. Carrasco, Y.R. and F.D. Batista, *B-cell activation by membrane-bound antigens is facilitated by the interaction of VLA-4 with VCAM-1*. EMBO J, 2006. **25**(4): p. 889-99.
322. Harwood, N.E. and F.D. Batista, *The cytoskeleton coordinates the early events of B-cell activation*. Cold Spring Harb Perspect Biol, 2011. **3**(2).
323. Lam, K.P., R. Kuhn, and K. Rajewsky, *In vivo ablation of surface immunoglobulin on mature B cells by inducible gene targeting results in rapid cell death*. Cell, 1997. **90**(6): p. 1073-83.
324. Liu, C., et al., *Actin reorganization is required for the formation of polarized B cell receptor signalosomes in response to both soluble and membrane-associated antigens*. J Immunol, 2012. **188**(7): p. 3237-46.
325. Jaqaman, K., et al., *Robust single-particle tracking in live-cell time-lapse sequences*. Nat Methods, 2008. **5**(8): p. 695-702.

326. Das, R., C.W. Cairo, and D. Coombs, *A hidden Markov model for single particle tracks quantifies dynamic interactions between LFA-1 and the actin cytoskeleton*. PLoS Comput Biol, 2009. **5**(11): p. e1000556.
327. Kusumi, A., Y. Sako, and M. Yamamoto, *Confined lateral diffusion of membrane receptors as studied by single particle tracking (nanovid microscopy). Effects of calcium-induced differentiation in cultured epithelial cells*. Biophys J, 1993. **65**(5): p. 2021-40.
328. Ferrari, R., A.J. Manfoi, and W.R. Young, *Strongly and weakly self-similar diffusion*. Physica D, 2001. **154**: p. 111-137.
329. Ewers, H., et al., *Single-particle tracking of murine polyoma virus-like particles on live cells and artificial membranes*. Proc Natl Acad Sci U S A, 2005. **102**(42): p. 15110-5.
330. Jaqaman, K., et al., *Cytoskeletal Control of CD36 Diffusion Promotes Its Receptor and Signaling Function*. Cell, 2011. **146**(4): p. 593-606.
331. Akira, S. and K. Takeda, *Toll-like receptor signalling*. Nat Rev Immunol, 2004. **4**(7): p. 499-511.
332. Spiering, D. and L. Hodgson, *Dynamics of the Rho-family small GTPases in actin regulation and motility*. Cell Adh Migr, 2011. **5**(2): p. 170-80.
333. Ichetovkin, I., W. Grant, and J. Condeelis, *Cofilin produces newly polymerized actin filaments that are preferred for dendritic nucleation by the Arp2/3 complex*. Curr Biol, 2002. **12**(1): p. 79-84.
334. Van Troys, M., et al., *Ins and outs of ADF/cofilin activity and regulation*. Eur J Cell Biol, 2008. **87**(8-9): p. 649-67.
335. Eibert, S.M., et al., *Cofilin peptide homologs interfere with immunological synapse formation and T cell activation*. Proc Natl Acad Sci U S A, 2004. **101**(7): p. 1957-62.
336. Schmidt, G., et al., *Gln 63 of Rho is deamidated by Escherichia coli cytotoxic necrotizing factor-1*. Nature, 1997. **387**(6634): p. 725-9.
337. Flatau, G., et al., *Toxin-induced activation of the G protein p21 Rho by deamidation of glutamine*. Nature, 1997. **387**(6634): p. 729-33.
338. Maekawa, M., et al., *Signaling from Rho to the actin cytoskeleton through protein kinases ROCK and LIM-kinase*. Science, 1999. **285**(5429): p. 895-8.
339. Monroe, J.G., *Ligand-independent tonic signaling in B-cell receptor function*. Curr Opin Immunol, 2004. **16**(3): p. 288-95.
340. Treanor, B. and F.D. Batista, *Organisation and dynamics of antigen receptors: implications for lymphocyte signalling*. Curr Opin Immunol, 2010. **22**(3): p. 299-307.
341. Pierce, S.K. and W. Liu, *The tipping points in the initiation of B cell signalling: how small changes make big differences*. Nat Rev Immunol, 2010. **10**(11): p. 767-77.
342. Martin, F. and J.F. Kearney, *Marginal-zone B cells*. Nat Rev Immunol, 2002. **2**(5): p. 323-35.
343. Cerutti, A., M. Cols, and I. Puga, *Marginal zone B cells: virtues of innate-like antibody-producing lymphocytes*. Nat Rev Immunol, 2013. **13**(2): p. 118-32.
344. Cairo, C.W., et al., *Dynamic regulation of CD45 lateral mobility by the spectrin-ankyrin cytoskeleton of T cells*. J Biol Chem, 2010. **285**(15): p. 11392-401.
345. Jabara, H.H., et al., *DOCK8 functions as an adaptor that links TLR-MyD88 signaling to B cell activation*. Nature Immunology, 2012. **13**(6): p. 612-+.
346. Sullivan, K.E., et al., *A Multiinstitutional Survey of the Wiskott-Aldrich Syndrome*. Journal of Pediatrics, 1994. **125**(6): p. 876-885.

347. Dupuis-Girod, S., et al., *Autoimmunity in Wiskott-Aldrich syndrome: Risk factors, clinical features, and outcome in a single-center cohort of 55 patients*. *Pediatrics*, 2003. **111**(5): p. E622-E627.
348. Becker-Herman, S., et al., *WASp-deficient B cells play a critical, cell-intrinsic role in triggering autoimmunity*. *Journal of Experimental Medicine*, 2011. **208**(10): p. 2033-2042.
349. Ngo, V.N., et al., *Oncogenically active MYD88 mutations in human lymphoma*. *Nature*, 2011. **470**(7332): p. 115-U133.
350. Davis, R.E., et al., *Chronic active B-cell-receptor signalling in diffuse large B-cell lymphoma*. *Nature*, 2010. **463**(7277): p. 88-U97.
351. Kusumi, A., et al., *Hierarchical mesoscale domain organization of the plasma membrane*. *Trends Biochem Sci*, 2011. **36**(11): p. 604-15.
352. Goodridge, H.S., et al., *Activation of the innate immune receptor Dectin-1 upon formation of a 'phagocytic synapse'*. *Nature*, 2011. **472**(7344): p. 471-U541.
353. Davis, S.J. and P.A. van der Merwe, *The kinetic-segregation model: TCR triggering and beyond*. *Nature Immunology*, 2006. **7**(8): p. 803-809.
354. Durand, C.A., et al., *Phosphoinositide 3-kinase p110 delta regulates natural antibody production, marginal zone and B-1 B cell function, and autoantibody responses*. *J Immunol*, 2009. **183**(9): p. 5673-84.
355. Ait-Azzouzene, D., et al., *An immunoglobulin C kappa-reactive single chain antibody fusion protein induces tolerance through receptor editing in a normal polyclonal immune system*. *J Exp Med*, 2005. **201**(5): p. 817-28.
356. Huet, S., et al., *Analysis of transient behavior in complex trajectories: application to secretory vesicle dynamics*. *Biophys J*, 2006. **91**(9): p. 3542-59.
357. Moriyama, K., et al., *Mutational analysis of an actin-binding site of cofilin and characterization of chimeric proteins between cofilin and destrin*. *J Biol Chem*, 1992. **267**(11): p. 7240-4.
358. Grakoui, A., et al., *The immunological synapse: a molecular machine controlling T cell activation*. *Science*, 1999. **285**(5425): p. 221-7.
359. Campi, G., R. Varma, and M.L. Dustin, *Actin and agonist MHC-peptide complex-dependent T cell receptor microclusters as scaffolds for signaling*. *J Exp Med*, 2005. **202**(8): p. 1031-6.
360. Lee, K.H., et al., *The immunological synapse balances T cell receptor signaling and degradation*. *Science*, 2003. **302**(5648): p. 1218-22.
361. Harwood, N.E. and F.D. Batista, *Visualizing the molecular and cellular events underlying the initiation of B-cell activation*. *Curr Top Microbiol Immunol*, 2009. **334**: p. 153-77.
362. Batista, F.D., B. Treanor, and N.E. Harwood, *Visualizing a role for the actin cytoskeleton in the regulation of B-cell activation*. *Immunol Rev*, 2010. **237**(1): p. 191-204.
363. Arana, E., et al., *Activation of the small GTPase Rac2 via the B cell receptor regulates B cell adhesion and immunological-synapse formation*. *Immunity*, 2008. **28**(1): p. 88-99.
364. Bos, J.L., *Linking Rap to cell adhesion*. *Curr. Opin. Cell Biol.*, 2005. **17**(2): p. 123-8.
365. Gupta, N., et al., *Quantitative proteomic analysis of B cell lipid rafts reveals that ezrin regulates antigen receptor-mediated lipid raft dynamics*. *Nat Immunol*, 2006. **7**(6): p. 625-33.

366. Bretscher, A., K. Edwards, and R.G. Fehon, *ERM proteins and merlin: integrators at the cell cortex*. Nat Rev Mol Cell Biol, 2002. **3**(8): p. 586-99.
367. Condeelis, J., *How is actin polymerization nucleated in vivo?* Trends Cell Biol, 2001. **11**(7): p. 288-93.
368. Chan, A.Y., et al., *Role of cofilin in epidermal growth factor-stimulated actin polymerization and lamellipod protrusion*. J Cell Biol, 2000. **148**(3): p. 531-42.
369. Burkel, B.M., G. von Dassow, and W.M. Bement, *Versatile fluorescent probes for actin filaments based on the actin-binding domain of utrophin*. Cell Motil Cytoskeleton, 2007. **64**(11): p. 822-32.
370. Nishita, M., et al., *Spatial and temporal regulation of cofilin activity by LIM kinase and Slingshot is critical for directional cell migration*. J Cell Biol, 2005. **171**(2): p. 349-59.
371. Faure, S., et al., *ERM proteins regulate cytoskeleton relaxation promoting T cell-APC conjugation*. Nat Immunol, 2004. **5**(3): p. 272-9.
372. Davey, E.J., et al., *Regulation of cell morphology in B lymphocytes by IL-4: evidence for induced cytoskeletal changes*. J Immunol, 1998. **160**(11): p. 5366-73.
373. Bernstein, B.W. and J.R. Bamburg, *ADF/cofilin: a functional node in cell biology*. Trends Cell Biol, 2010. **20**(4): p. 187-95.
374. McLeod, S.J., et al., *The Rap GTPases regulate integrin-mediated adhesion, cell spreading, actin polymerization, and Pyk2 tyrosine phosphorylation in B lymphocytes*. J Biol Chem, 2004. **279**(13): p. 12009-19.
375. Lankar, D., et al., *Dynamics of major histocompatibility complex class II compartments during B cell receptor-mediated cell activation*. J Exp Med, 2002. **195**(4): p. 461-72.
376. Algrain, M., et al., *Ezrin contains cytoskeleton and membrane binding domains accounting for its proposed role as a membrane-cytoskeletal linker*. J Cell Biol, 1993. **120**(1): p. 129-39.
377. June, C.H., et al., *T-cell proliferation involving the CD28 pathway is associated with cyclosporine-resistant interleukin 2 gene expression*. Mol Cell Biol, 1987. **7**(12): p. 4472-81.
378. Freeman, S.A., et al., *Preventing the activation or cycling of the Rap1 GTPase alters adhesion and cytoskeletal dynamics and blocks metastatic melanoma cell extravasation into the lungs*. Cancer Res, 2010. **70**(11): p. 4590-601.
379. Lorenz, M., et al., *Measurement of barbed ends, actin polymerization, and motility in live carcinoma cells after growth factor stimulation*. Cell Motil Cytoskeleton, 2004. **57**(4): p. 207-17.
380. Chudakov, D.M., et al., *Photoswitchable cyan fluorescent protein for protein tracking*. Nat Biotechnol, 2004. **22**(11): p. 1435-9.
381. Chambers, A.F., A.C. Groom, and I.C. MacDonald, *Dissemination and growth of cancer cells in metastatic sites*. Nature Reviews Cancer, 2002. **2**(8): p. 563-572.
382. Christofori, G., *New signals from the invasive front*. Nature, 2006. **441**(7092): p. 444-450.
383. Friedl, P. and K. Wolf, *Tumour-cell invasion and migration: Diversity and escape mechanisms*. Nature Reviews Cancer, 2003. **3**(5): p. 362-374.
384. Condeelis, J., R.H. Singer, and J.E. Segall, *The great escape: When cancer cells hijack the genes for chemotaxis and motility*. Annual Review of Cell and Developmental Biology, 2005. **21**: p. 695-718.

385. Zijlstra, A., et al., *The inhibition of tumor cell intravasation and subsequent metastasis via regulation of in vivo tumor cell motility by the tetraspanin CD151*. *Cancer Cell*, 2008. **13**(3): p. 221-234.
386. Sanz-Moreno, V., et al., *Rac Activation and Inactivation Control Plasticity of Tumor Cell Movement*. *Cell*, 2008. **135**(3): p. 510-523.
387. Bos, J.L., *Linking Rap to cell adhesion*. *Current Opinion in Cell Biology*, 2005. **17**(2): p. 123-128.
388. Lyle, K.S., et al., *cAMP-induced Epac-Rap activation inhibits epithelial cell migration by modulating focal adhesion and leading edge dynamics*. *Cellular Signalling*, 2008. **20**(6): p. 1104-1116.
389. Schwamborn, J.C., et al., *Ubiquitination of the GTPase Rap1B by the ubiquitin ligase Smurf2 is required for the establishment of neuronal polarity*. *Embo Journal*, 2007. **26**(5): p. 1410-1422.
390. Arthur, W.T., L.A. Quilliam, and J.A. Cooper, *Rap1 promotes cell spreading by localizing Rac guanine nucleotide exchange factors*. *Journal of Cell Biology*, 2004. **167**(1): p. 111-122.
391. Lafuente, E.M., et al., *RIAM, an Ena/VASP and Profilin ligand, interacts with Rap1-GTP and mediates Rap1-induced adhesion*. *Dev Cell*, 2004. **7**(4): p. 585-95.
392. Jeon, T.J., et al., *Rap1 controls cell adhesion and cell motility through the regulation of myosin II*. *Journal of Cell Biology*, 2007. **176**(7): p. 1021-1033.
393. Zhang, L.Z., et al., *Identification of a putative tumor suppressor gene Rap1GAP in pancreatic cancer*. *Cancer Research*, 2006. **66**(2): p. 898-906.
394. Zhang, Z.C., et al., *Rap1 GAP inhibits tumor growth in oropharyngeal squamous cell carcinoma*. *American Journal of Pathology*, 2006. **168**(2): p. 585-596.
395. Yajnik, V., et al., *DOCK4, a GTPase activator, is disrupted during tumorigenesis*. *Cell*, 2003. **112**(5): p. 673-684.
396. Gao, L., et al., *Ras-associated protein-1 regulates extracellular signal-regulated kinase activation and migration in melanoma cells: Two processes important to melanoma tumorigenesis and metastasis*. *Cancer Research*, 2006. **66**(16): p. 7880-7888.
397. Crawford, N.P.S., et al., *Germline polymorphisms in SIPA1 are associated with metastasis and other indicators of poor prognosis in breast cancer*. *Breast Cancer Research*, 2006. **8**(2).
398. Zuo, H., et al., *Downregulation of Rap1GAP through Epigenetic Silencing and Loss of Heterozygosity Promotes Invasion and Progression of Thyroid Tumors*. *Cancer Research*, 2010. **70**(4): p. 1389-1397.
399. Bailey, C.L., P. Kelly, and P.J. Casey, *Activation of Rap1 Promotes Prostate Cancer Metastasis*. *Cancer Research*, 2009. **69**(12): p. 4962-4968.
400. Itoh, M., et al., *Rap1 integrates tissue polarity, lumen formation, and tumorigenic potential in human breast epithelial cells*. *Cancer Research*, 2007. **67**(10): p. 4759-4766.
401. Fidler, I.J., *Biological Behavior of Malignant-Melanoma Cells Correlated to Their Survival In vivo*. *Cancer Research*, 1975. **35**(1): p. 218-224.
402. Ballestrem, C., et al., *Actin-dependent lamellipodia formation and microtubule-dependent tail retraction control-directed cell migration*. *Molecular Biology of the Cell*, 2000. **11**(9): p. 2999-3012.

403. Mould, A.P., et al., *Conformational changes in the integrin beta A domain provide a mechanism for signal transduction via hybrid domain movement*. J Biol Chem, 2003. **278**(19): p. 17028-35.
404. Chambers, A.F., et al., *Early steps in hematogenous metastasis of B16F1 melanoma cells in chick embryos studied by high-resolution intravital videomicroscopy*. J Natl Cancer Inst, 1992. **84**(10): p. 797-803.
405. Crissman, J.D., et al., *Morphological study of the interaction of intravascular tumor cells with endothelial cells and subendothelial matrix*. Cancer Res, 1988. **48**(14): p. 4065-72.
406. Zheng, H., et al., *Down-regulation of Rap1GAP via promoter hypermethylation promotes melanoma cell proliferation, survival, and migration*. Cancer Res, 2009. **69**(2): p. 449-57.
407. Olson, M.F. and E. Sahai, *The actin cytoskeleton in cancer cell motility*. Clin Exp Metastasis, 2009. **26**(4): p. 273-87.
408. Koop, S., et al., *Independence of metastatic ability and extravasation: metastatic ras-transformed and control fibroblasts extravasate equally well*. Proc Natl Acad Sci U S A, 1996. **93**(20): p. 11080-4.
409. Koop, S., et al., *Fate of melanoma cells entering the microcirculation: over 80% survive and extravasate*. Cancer Res, 1995. **55**(12): p. 2520-3.
410. Morris, V.L., et al., *Mammary carcinoma cell lines of high and low metastatic potential differ not in extravasation but in subsequent migration and growth*. Clin Exp Metastasis, 1994. **12**(6): p. 357-67.
411. Wylie, S., et al., *The matrix metalloproteinase inhibitor batimastat inhibits angiogenesis in liver metastases of B16F1 melanoma cells*. Clin Exp Metastasis, 1999. **17**(2): p. 111-7.
412. Koop, S., et al., *Overexpression of metalloproteinase inhibitor in B16F10 cells does not affect extravasation but reduces tumor growth*. Cancer Res, 1994. **54**(17): p. 4791-7.
413. Hamadi, A., et al., *Regulation of focal adhesion dynamics and disassembly by phosphorylation of FAK at tyrosine 397*. J Cell Sci, 2005. **118**(Pt 19): p. 4415-25.
414. Goetz, J.G., et al., *Concerted regulation of focal adhesion dynamics by galectin-3 and tyrosine-phosphorylated caveolin-1*. J Cell Biol, 2008. **180**(6): p. 1261-75.
415. Cara, D.C. and P. Kubes, *Intravital microscopy as a tool for studying recruitment and chemotaxis*. Methods Mol Biol, 2004. **239**: p. 123-32.
416. Andrews, N.L., et al., *Actin restricts Fc epsilon RI diffusion and facilitates antigen-induced receptor immobilization*. Nature Cell Biology, 2008. **10**(8): p. 955-963.
417. Lajoie, P., et al., *Lattices, rafts, and scaffolds: domain regulation of receptor signaling at the plasma membrane*. Journal of Cell Biology, 2009. **185**(3): p. 381-385.
418. Boscher, C., et al., *Galectin-3 protein regulates mobility of N-cadherin and GM1 ganglioside at cell-cell junctions of mammary carcinoma cells*. J Biol Chem, 2012. **287**(39): p. 32940-52.
419. Jacobelli, J., et al., *Confinement-optimized three-dimensional T cell amoeboid motility is modulated via myosin IIA-regulated adhesions*. Nat Immunol, 2010. **11**(10): p. 953-61.
420. Beemiller, P. and M.F. Krummel, *Regulation of T-cell receptor signaling by the actin cytoskeleton and poroelastic cytoplasm*. Immunol Rev, 2013. **256**(1): p. 148-59.
421. Ueda, H., et al., *CD4+ T-cell synapses involve multiple distinct stages*. Proc Natl Acad Sci U S A, 2011. **108**(41): p. 17099-104.
422. Beemiller, P., J. Jacobelli, and M.F. Krummel, *Integration of the movement of signaling microclusters with cellular motility in immunological synapses*. Nat Immunol, 2012. **13**(8): p. 787-95.

423. de la Roche, M., et al., *Hedgehog signaling controls T cell killing at the immunological synapse*. Science, 2013. **342**(6163): p. 1247-50.
424. Jacobelli, J., et al., *A single class II myosin modulates T cell motility and stopping, but not synapse formation*. Nat Immunol, 2004. **5**(5): p. 531-8.
425. Egelhoff, T.T., R.J. Lee, and J.A. Spudich, *Dictyostelium myosin heavy chain phosphorylation sites regulate myosin filament assembly and localization in vivo*. Cell, 1993. **75**(2): p. 363-71.
426. Lee, K.H., et al., *T cell receptor signaling precedes immunological synapse formation*. Science, 2002. **295**(5559): p. 1539-42.
427. Zicha, D., et al., *Rapid actin transport during cell protrusion*. Science, 2003. **300**(5616): p. 142-5.
428. Kaizuka, Y., et al., *Mechanisms for segregating T cell receptor and adhesion molecules during immunological synapse formation in Jurkat T cells*. Proc Natl Acad Sci U S A, 2007. **104**(51): p. 20296-301.
429. Krummel, M.F., et al., *Differential clustering of CD4 and CD3zeta during T cell recognition*. Science, 2000. **289**(5483): p. 1349-52.
430. Moeendarbary, E., et al., *The cytoplasm of living cells behaves as a poroelastic material*. Nat Mater, 2013. **12**(3): p. 253-61.
431. Keren, K., et al., *Intracellular fluid flow in rapidly moving cells*. Nat Cell Biol, 2009. **11**(10): p. 1219-24.
432. Mitchison, T.J., G.T. Charras, and L. Mahadevan, *Implications of a poroelastic cytoplasm for the dynamics of animal cell shape*. Semin Cell Dev Biol, 2008. **19**(3): p. 215-23.
433. Charras, G.T., T.J. Mitchison, and L. Mahadevan, *Animal cell hydraulics*. J Cell Sci, 2009. **122**(Pt 18): p. 3233-41.
434. Buxboim, A. and D.E. Discher, *Stem cells feel the difference*. Nat Methods, 2010. **7**(9): p. 695-7.
435. Pajerowski, J.D., et al., *Physical plasticity of the nucleus in stem cell differentiation*. Proc Natl Acad Sci U S A, 2007. **104**(40): p. 15619-24.
436. Engler, A.J., et al., *Matrix elasticity directs stem cell lineage specification*. Cell, 2006. **126**(4): p. 677-89.
437. Yuseff, M.I., et al., *Polarized secretion of lysosomes at the B cell synapse couples antigen extraction to processing and presentation*. Immunity, 2011. **35**(3): p. 361-74.
438. Sarantis, H. and S. Grinstein, *Subversion of phagocytosis for pathogen survival*. Cell Host Microbe, 2012. **12**(4): p. 419-31.
439. You, Y., et al., *Marginal zone B cells regulate antigen capture by marginal zone macrophages*. J Immunol, 2011. **186**(4): p. 2172-81.
440. Pillai, S., A. Cariappa, and S.T. Moran, *Marginal zone B cells*. Annu Rev Immunol, 2005. **23**: p. 161-96.
441. Davis, R.E., et al., *Chronic active B-cell-receptor signalling in diffuse large B-cell lymphoma*. Nature, 2010. **463**(7277): p. 88-92.
442. Shaffer, A.L., 3rd, R.M. Young, and L.M. Staudt, *Pathogenesis of human B cell lymphomas*. Annu Rev Immunol, 2012. **30**: p. 565-610.
443. Ngo, V.N., et al., *Oncogenically active MYD88 mutations in human lymphoma*. Nature, 2011. **470**(7332): p. 115-9.

444. Kumar, R., et al., *Increased sensitivity of antigen-experienced T cells through the enrichment of oligomeric T cell receptor complexes*. *Immunity*, 2011. **35**(3): p. 375-87.
445. Schamel, W.W., et al., *Coexistence of multivalent and monovalent TCRs explains high sensitivity and wide range of response*. *J Exp Med*, 2005. **202**(4): p. 493-503.
446. Xu, C., et al., *Regulation of T cell receptor activation by dynamic membrane binding of the CD3epsilon cytoplasmic tyrosine-based motif*. *Cell*, 2008. **135**(4): p. 702-13.
447. Arnadottir, J. and M. Chalfie, *Eukaryotic Mechanosensitive Channels*. *Annual Review of Biophysics*, Vol 39, 2010. **39**: p. 111-137.
448. Margadant, F., et al., *Mechanotransduction in vivo by repeated talin stretch-relaxation events depends upon vinculin*. *PLoS Biol*, 2011. **9**(12): p. e1001223.
449. de Bruyn, K.M.T., et al., *The small GTPase Rap1 is activated by turbulence and is involved in integrin alpha(IIb)beta(3)-mediated cell adhesion in human megakaryocytes*. *Journal of Biological Chemistry*, 2003. **278**(25): p. 22412-22417.
450. Psaila, B. and D. Lyden, *The metastatic niche: adapting the foreign soil*. *Nat Rev Cancer*, 2009. **9**(4): p. 285-93.
451. Joyce, J.A. and J.W. Pollard, *Microenvironmental regulation of metastasis*. *Nat Rev Cancer*, 2009. **9**(4): p. 239-52.
452. Hanahan, D. and L.M. Coussens, *Accessories to the crime: functions of cells recruited to the tumor microenvironment*. *Cancer Cell*, 2012. **21**(3): p. 309-22.
453. Chen, Q., X.H. Zhang, and J. Massague, *Macrophage binding to receptor VCAM-1 transmits survival signals in breast cancer cells that invade the lungs*. *Cancer Cell*, 2011. **20**(4): p. 538-49.
454. Wyckoff, J., et al., *A paracrine loop between tumor cells and macrophages is required for tumor cell migration in mammary tumors*. *Cancer Research*, 2004. **64**(19): p. 7022-7029.
455. Qian, B.Z., et al., *CCL2 recruits inflammatory monocytes to facilitate breast-tumour metastasis*. *Nature*, 2011. **475**(7355): p. 222-5.
456. Kaplan, R.N., et al., *VEGFR1-positive haematopoietic bone marrow progenitors initiate the pre-metastatic niche*. *Nature*, 2005. **438**(7069): p. 820-827.
457. Blanchet, M.R., et al., *CD34 is required for dendritic cell trafficking and pathology in murine hypersensitivity pneumonitis*. *Am J Respir Crit Care Med*, 2011. **184**(6): p. 687-98.
458. Blanchet, M.R., et al., *CD34 facilitates the development of allergic asthma*. *Blood*, 2007. **110**(6): p. 2005-12.

## **Appendix A: Force activation of Rap GTPases regulates adhesion dynamics**

### **A.1 Introduction**

A major factor in tumorigenesis is the loss of tissue homeostasis (tissue dysplasia) and disrupted tissue architecture, described as the tensional or “mechanical” phenotype [294, 295]. Tissue stiffness, measured by an elastic modulus, is a poor prognostic indicator in different cancers, and drives invasion and growth [296]. The tensional phenotype has a reciprocal relationship between tumor cells/stromal cells, neighbouring cells, and the surrounding ECM where forces exerted by cells pull and remodel matrices while the ECM and tissue has an opposing elastic resistance [296, 297]. The net of this relationship governs mechanotransduction at the plasma membrane: mechanical signals converted to intracellular biochemical signals that impact transcription and growth [294, 298, 299]. The tensional phenotype determines the maturation of focal adhesions and migratory capacity of cells [295], cell division axis orientation [300, 301], the action of a number of mechanosensitive channels [447], and more direct connections with the nucleus via the linker of nucleoskeleton and cytoskeleton (LINC) complex [298]. Regulators of the mechanical phenotype are therefore of great interest.

In mechanotransduction initiated at the plasma membrane, force exertion by extracellular and intracellular matrices or physical stimuli results in conformational changes of proteins which can effect their function by revealing cryptic binding sites with the protein [303-306, 447]. Cryptic sites are found within focal adhesion associated proteins that bear forces including talin [448] and p130Cas [236, 237]. Upon stretch, p130Cas can be phosphorylated at an otherwise cryptic tyrosine (Y165) to then recruit the adaptor Crk and Rap GEF, C3G [236].

Rap1 is indeed activated upon stretch applied to fibroblasts [237] and shear applied to hematopoietic cell lines [449].

In this work, we determine that Rap1 is activated upon stretch in tumor cells adhered to stretchable silicone rubber and that its inducible activity is required for appropriate adhesive responses to tension applied through 2 and 3D ECMs. Upon changing tension in uniaxial or equibiaxial directions, focal adhesions recruited vinculin in a Rap dependent manner. Activating Rap1 resulted in phenotypes normally observed under higher tension conditions suggesting that Rap activation may act as a “tensional rheostat”. Along these lines, the turnover of focal adhesion proteins were altered by activating Rap1 similarly as applying shear to the cells. Specifically, both Rap activation and shear stabilized  $\alpha 5$  integrin and accelerated the turnover of the focal adhesion adaptor protein paxillin. Tumor cells unable to calibrate intracellular tension to extracellular tension should have dysregulated mechanotransduction, potentially acting on the malignant phenotype of tumors. Indeed, we observed that constitutively activating Rap1 elevated the phosphorylation of p130Cas and increased cell contractility and invasion in 3D collagen gels. Conversely, blocking Rap activation reduced invasion in 3D collagen gels and growth *in vivo*. These data suggest that Rap indeed acts as a sensor of tension and feeds back on mechanotransductive pathways by remodeling focal adhesions. Disrupting the tensional rheostat results in abnormal tensional phenotypes.

## A.2 Figures

### Figure 1

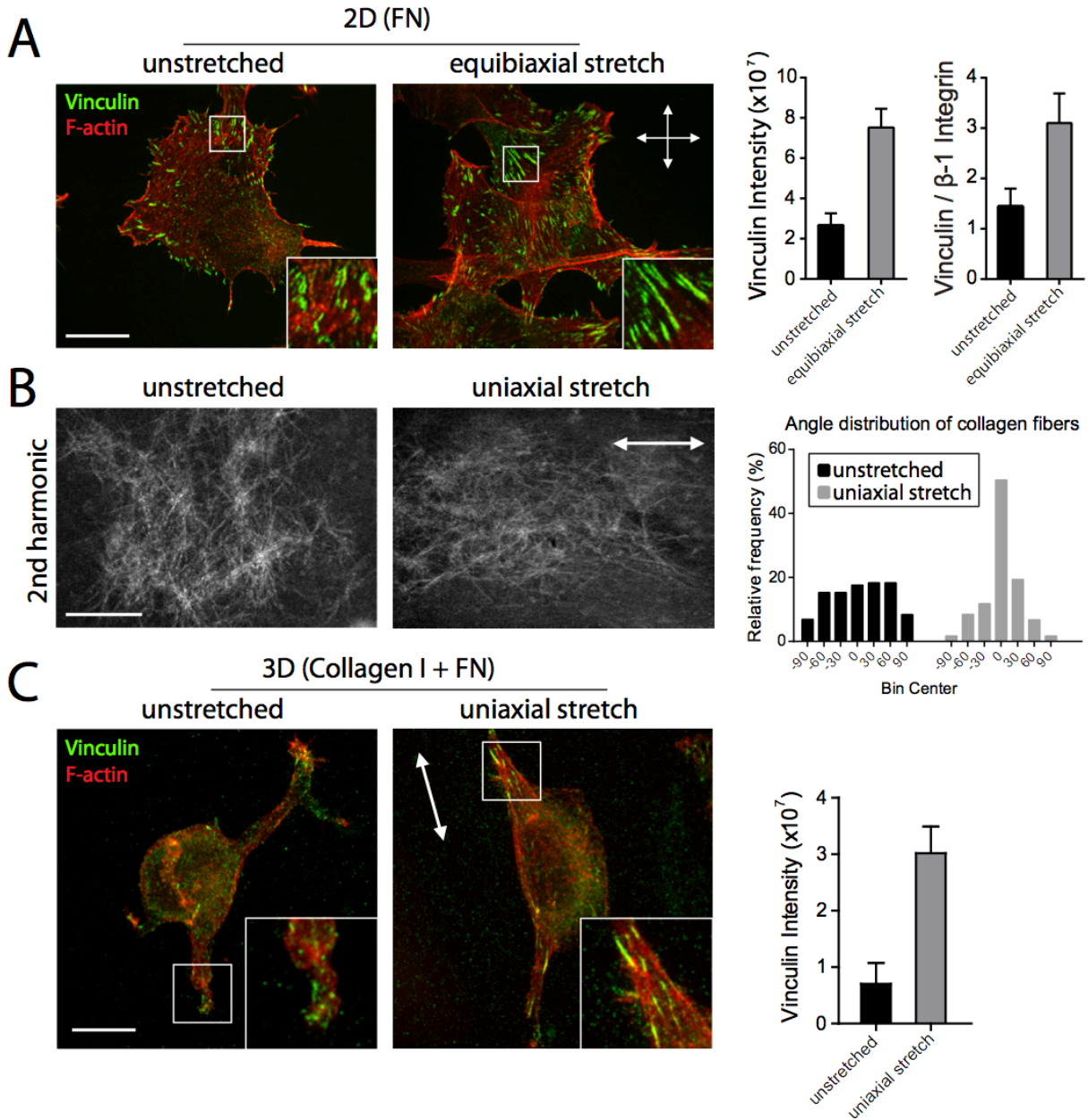


**Figure 1. Applied stretch induces vinculin binding at focal adhesions in B16F1 cells.** A) B16F1 cells were seeded onto FN ( $5 \mu\text{g}/\text{cm}^2$ ) coated silicone rubber plates overnight before applying 10% equibiaxial stretch to the substrata for 4 h. Cells were stained using vinculin

antibodies and Rhodamine phalloidin to visualize f-actin, left panels. Vinculin intensity was quantitated for unstretched control and stretched cells (left graph) and normalized to beta-1 integrin intensity (right graph). B) Collagen I (2.17 mg/mL) + FN (5 ug/mL) 3D gels were polymerized and either left unstretched or uniaxially stretched for 24 h then imaged by second harmonics. Fiber orientation is quantified by measuring >100 fibers from 2 experiments and graphed (right). C) B16F1 cells were seeded within 3D Collagen I + FN gels and stretched for 24 h. Vinculin fluorescence is shown (left) and quantified (right). All scale bars, 10 um. White arrows indicate the direction of applied stretch.

**Figure 2**

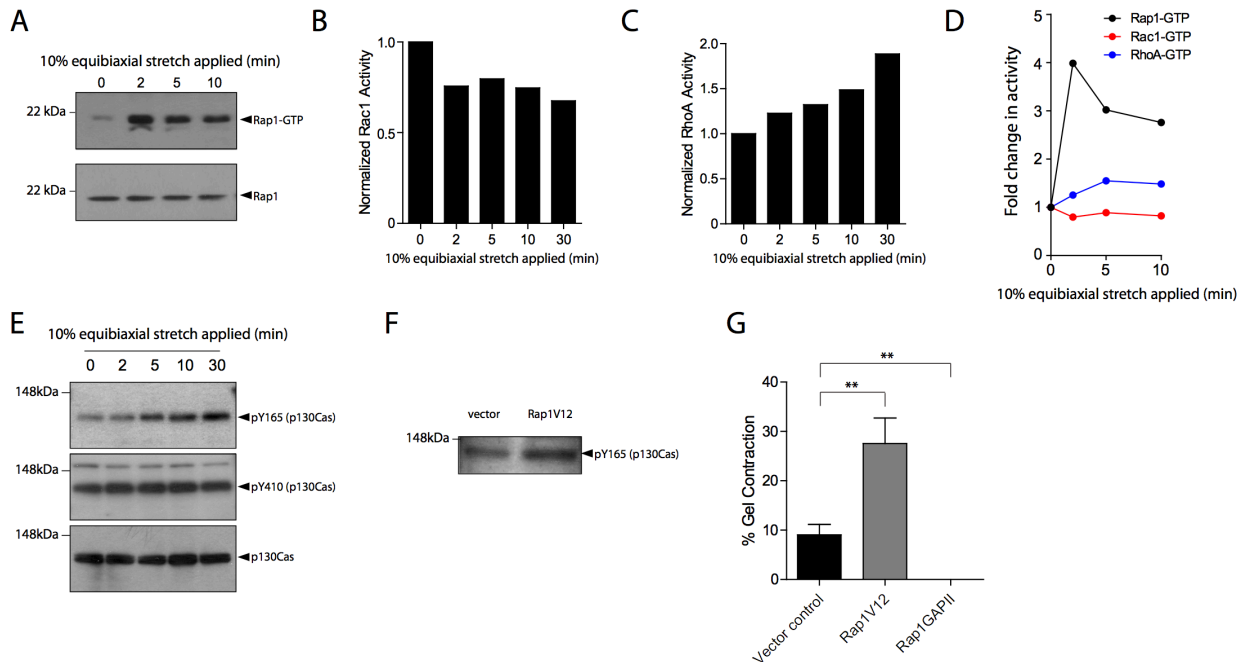


**Figure 2. Applied stretch activates Rap1 and results in phosphorylation of the p130Cas cryptic tyrosine in tumor cells in a positive feedback loop.** A-E) B16F1 cells were seeded onto FN (5 ug/cm<sup>2</sup>) coated silicone rubber plates overnight before applying 10% equibiaxial stretch to the substrata for indicated times. A) Active Rap1 (Rap1-GTP) was determined using a Ral-GDS-GST pulldown and probing with anti-Rap1 antibodies. Total Rap1 from a fraction of

the lysates is shown below. B-C) Rac1 and RhoA activities were determined using GLISA assays. D) Rap1, Rac1, and RhoA activities were normalized and graphed. E) Phosphorylation of cryptic (Y165) and non-cryptic (Y410) tyrosines in p130Cas were probed for using phosphor-specific antibodies. Total p130Cas is shown below. F) B16F1 cells stably expressing vector control or Rap1V12 were lysed and probed for phosphoY165 p130Cas. G) B16F1 cells stably expressing vector, Rap1V12, or Rap1GAPII were cultured in collagen gels and released to determine the % contraction compared to gels without cells added.

Figure 3

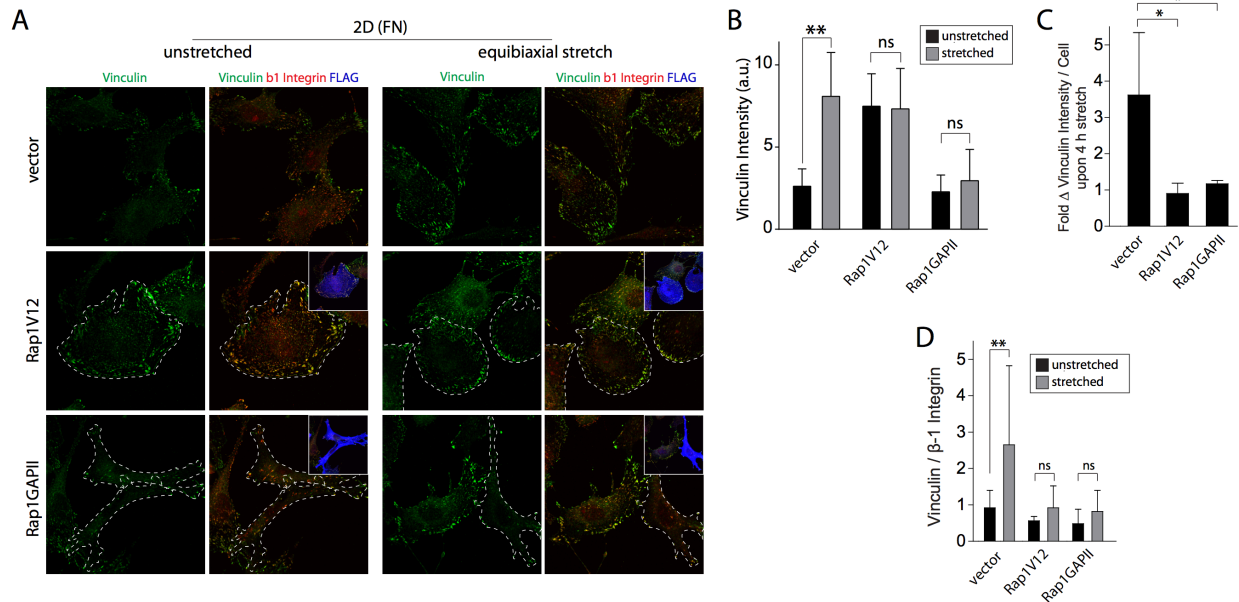


**Figure 3. Vinculin enrichment at focal adhesions in response to stretch in 2-D requires Rap activation and cycling.** A) B16F1 cells transiently expressing vector, Rap1V12-FLAG, or Rap1GAPII-FLAG were seeded onto FN coated silicone rubber plates overnight before applying 10% equibiaxial stretch to the substrata for 4 h. Cells were fixed and stained for Vinculin and  $\beta$ 1-integrin. B-D) Vinculin and  $\beta$ 1-integrin intensities per cell were quantified for >30 cells from 3 experiments in stretched and unstretched conditions. Vinculin intensity is expressed in arbitrary

units (a.u.) (B) or in fold change upon post-stretch (C). D) The ratio of Vinculin to  $\beta$ 1-integrin per cell is shown. In all case, the mean  $\pm$  the SEM is graphed.

**Figure 4**

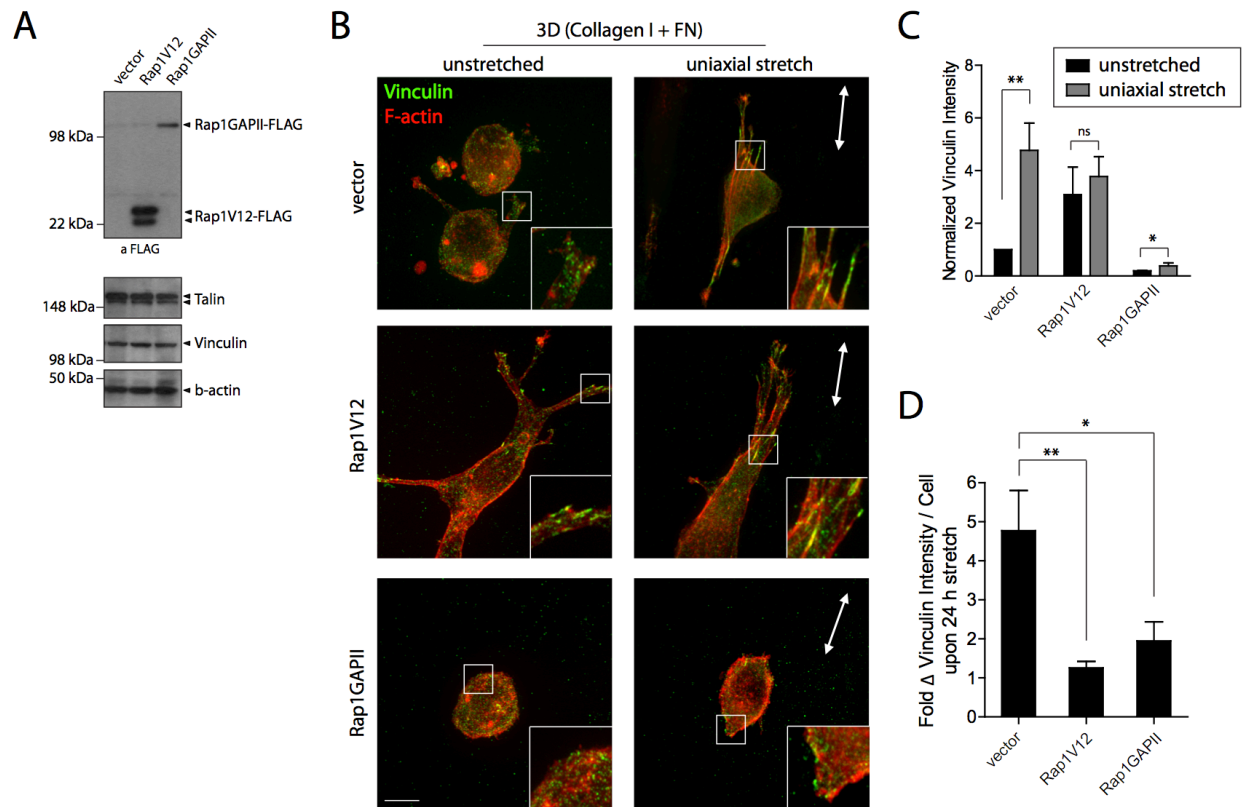


**Figure 4. Vinculin enrichment at focal adhesions in 3-D requires Rap activation and cycling.** A) B16F1 cells stably expressing vector, Rap1V12, and Rap1GAPII were probed for Talin, Vinculin, and  $\beta$ -actin expression. B) Stable cells were seeded in 3-D Collagen I + FN gels overnight, stretched uniaxially for 4 h, and stained for Vinculin and F-actin. Images shown are from z-stacks projected through the xy plane. C-D) Vinculin intensity was calculated per cell from z-stacks and shown in either arbitrary units (a.u.) (C) or as fold change in intensity between unstretched and stretched conditions (D).

Figure 5

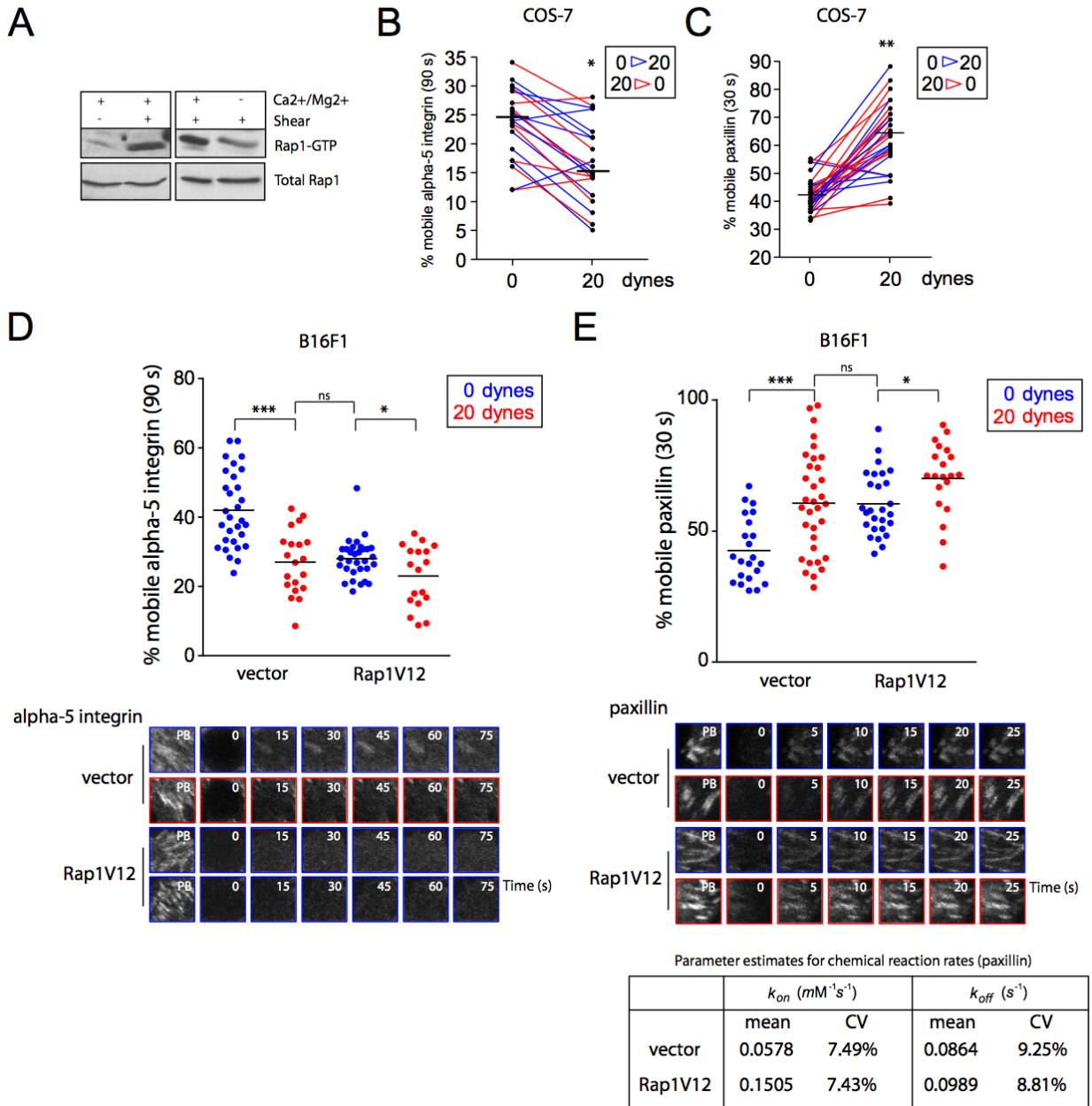


**Figure 5. Shear flow activates Rap1 to stabilize integrin and increase turnover of paxillin at established focal adhesions.** A) B16F1 cells were lifted from plates using a cell dissociation buffer, washed and resuspended in DMEM with or without Ca<sup>2+</sup> and Mg<sup>2+</sup>. Cells were either lysed or run through a 28G needle for 2 minutes before lysing and probing for Rap1-GTP. B-C) COS-7 fibroblasts were transfected with  $\alpha$ 5-integrin-GFP or paxillin-GFP and seeded onto FN

coated flow chamber slides. A syringe was used to draw media from end of the chamber, creating a 20 dyne shear force to the cells that could be acutely turned on or off. Adhesions within cells were bleached and allowed to recover for the indicated times either under shear or not. Shear was then applied (blue lines) or terminated (red lines) for 1 min and proximal adhesions were subsequently bleached and allowed to recover. D-E) B16F1 cells were transfected with  $\alpha 5$ -integrin-GFP or paxillin-GFP and focal adhesions were bleached under 20 dynes of shear or not. The mobile fraction for indicated times are plotted. Each dot represents an individual ROI. Examples of fluorescence recovery are shown (below). The  $k_{on}$  and  $k_{off}$  values for conditions without shear applied were estimated from mobile fraction curves.

Figure 6

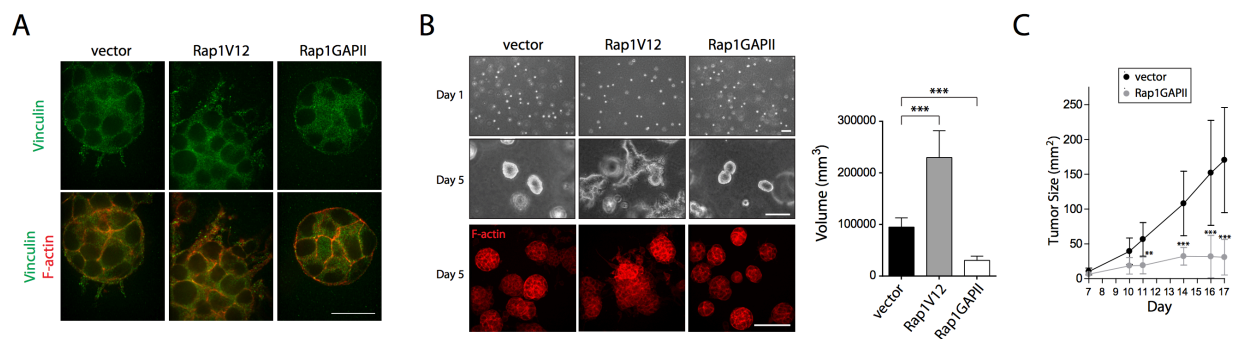


**Figure 6. Rap1-GTP regulates growth in 3D and *in vivo*.** A-B) Single B16F1 cells stably expressing a control vector, Rap1V12, or Rap1GAPII were seeded into Collagen + FN gels and grown for 5 days. A) Vinculin and F-actin were stained and the border of individual colonies with the matrix is shown. B) Phase contrast and F-actin imaging of individual fields at days 1 and 5 (left). F-actin staining was used to determine colony volume (right). C)  $1 \times 10^5$  cells were injected subcutaneously into C57Bl6 mice and tumor size quantified at indicated days.

### A.3 Conclusions

In this study, we have shown that applied tension through matrices in 2- and 3-D can alter focal adhesion phenotypes in B16F1 cells by activating the Rap1GTPase. In 2D, applied stretch increased fibrillar adhesions and the amount of Vinculin per  $\beta$ 1-integrin at these adhesions that were Rap dependent processes. Stretch applied through 3D matrices realigned collagen fibers in the direction of stretch and resulted in focal adhesion complexes that were largely absent in unstretched 3D gels. Activating Rap using a Rap1V12 form alone was able to reproduce this force induced adhesion phenotype while blocking Rap activation prevented focal adhesion formation under stretch. These data suggested that Rap is activated upon stretch to form focal adhesions in 3D and boost Vinculin at adhesions in 2D.

Indeed, Rap1 was activated upon stretch in 2D more rapidly and robustly than small Rho GTPases Rac1 and RhoA. A cryptic tyrosine residue of p130Cas that can only be phosphorylated by Src family kinases when tension is applied through the protein was inducibly phosphorylated in B16F1 cells upon stretch. This phosphorylation could be induced by activating Rap1. Activating Rap1 also resulted in increased contractility of 3D gels. Rap is therefore activated in response to tension, but also feeds back on mechanoresponsive signaling pathways at focal adhesions. We have referred to Rap1-GTP as a tensional rheostat based on these findings.

In order to determine how Rap1-GTP alters focal adhesions in response to exogenous force, we used applied shear to cells where we took advantage of being able to FRAP individual adhesions before and after shear. We found that on FN, 25% of the  $\alpha$ 5-integrin at focal adhesions was mobile while 15% was mobile under shear. This was interpreted as a stabilization of the engaged integrin under flow. Interestingly, we found paxillin showed an opposite trend where it was more mobile under shear flow. This trend was observed in fibroblasts as well as

B16F1 cells. In line with our findings where activating Rap1 was sufficient to induce focal adhesion phenotypes normally observed under exogenous force, we found that expressing Rap1V12 in B16F1 cells led to the stabilization of integrins and the increased turnover of paxillin.

Tissue stiffness leads to the growth and invasion of tumor cells mediated partly by integrin signaling. ECM crosslinking that increases tissue stiffness can occur over the natural history of a tumor where both stromal and tumor cells deposit and remodel the ECM over time. Throughout the metastatic cascade, there may also be abrupt changes in the microenvironmental tissue stiffness experienced by tumor cells. For example, upon seeding secondary organs tumor cells may go from a stiff environment at the primary tumor to a compliant matrix at the perivascular niche. The accumulation of mutations that lead to an intrinsic activation of mechanotransductive pathways may therefore augment late steps in metastasis. In several cancer types, Rap1 activation is indeed increased via multiple mechanisms. Going forward it will be interesting to determine if the dysregulation of tensional rheostats is commonly selected for in tumor cells which colonize secondary organs and if these correspond to the elastic modulus of the distant site.

## **A.4 Experimental procedures**

### **A.4.1 Cell lines**

B16F1 melanoma cells obtained from American Type Culture Collection (ATCC) were stably co-transfected with either the pIRM21-IRES-dsFP593 empty vector or vectors driving the expression of FLAG-Rap1V12 or FLAG-Rap1GAPII constructs from Michiyuki Matsuda (Kyoto University, Kyoto, Japan) and pMSCVpuro (BD Clontech, California, USA) using

calcium phosphate. Cells were selected for by using 2  $\mu\text{g/ml}$  of puromycin and sorted by a fluorescence-activated cell sorter for dsFP593 expression. Cells were cultured in Dulbecco's Modified Eagle Medium (DMEM) supplemented with 8% fetal bovine serum (FBS) at 5%  $\text{CO}_2$  and 37°C.

#### **A.4.2 Plasmids, transfections, FRAP**

B16F1 transient transfections were done using Lipofectamine 2000 (Invitrogen). Paxillin-GFP and alpha-5 integrin-GFP were from Robert Nabi (UBC). FRAP was carried out as previously described [271].

#### **A.4.3 Collagen gel contraction assays**

Collagen was pre-assembled on ice 1 hour prior to the start of the experiment by mixing 1 part 10x DMEM with 10 parts rat collagen 1 (4.0mg/ml, BD Biosciences) and neutralized using 1N NaOH to obtain a pH of 7. Stably transfected B16F1 melanoma cells were mixed 1:1 with pre-assembled collagen (1.77mg/ml final collagen concentration,  $1.05 \times 10^6$  cells/ml final cell concentration). Fibronectin (Sigma, 50 $\mu\text{g/ml}$  final concentration) was also mixed into the cell/collagen mixture and (total volume 200 $\mu\text{l}$ ) added to 12-well cell culture inserts (BD Falcon) with regular growth media and incubated for 2 days prior to lifting the gel. Lifted gels were allowed to contract overnight and gel diameters were quantified the next day.

#### **A.4.4 3D Collagen growth assay**

Pre-assembled collagen was prepared 1 hour on ice prior to the start of the experiment by mixing 10x DMEM and rat collagen I (5.0 mg/ml, Trevigen) in a 1:9 ratio and neutralized to a pH of 7

using 1N NaOH. Stably transfected B16F1 cells were mixed 1:1 with pre-assembled collagen (2.17 mg/ml final collagen concentration,  $1 \times 10^5$  cells/ml final cell concentration). Fibronectin (Sigma, 5  $\mu\text{g/ml}$  final concentration) was added in with the collagen/cell mixture and seeded onto glass coverslips in regular growth media. Cells were left in culture for 5 days before fixing. Cells were visualized using the 20x objective lens on a Zeiss 200M Axiovert microscope. Focal adhesion and actin staining were visualized using the 100x / 1.45 lens. Volumetric analysis was performed using Slidebook v5.5 (3i Intelligent Imaging Innovations).

#### **A.4.5 Equibiaxial stretch of cells in 2D**

Transiently transfected B16F1 cells (vector control, Rap1V12 and Rap1GAPII) were lifted using cell dissociation buffer and  $6.4 \times 10^4$  cells were seeded in a monolayer onto a 6-well flexible silicone-bottom BioFlex® Culture Plate (Flexcell International Corporation) coated with 5  $\mu\text{g/cm}^2$  of fibronectin (Sigma). Cells were allowed to adhere for 4 hours prior to the induction of stretch using the Flexcell Tension System (Flexcell International Corporation). The Flexcell Tension System utilizes a computer-regulated vacuum that deforms the flexible membrane culture plates. In brief, monolayer of cells seeded on the flexible membrane culture plates were placed on the Bioflex 25 mm loading post. The vacuum pressure applied through the bottom of the loading post created a mechanical equibiaxial elongation on the monolayer of cells adhered to the flexible membrane by pulling down on the flexible-bottom culture plates surrounding the post. In order to obtain a 10% elongation of the membrane, a vacuum pressure of 42.5 kPa was applied. Stretch was applied for 4 hours before fixing. Focal adhesion and actin staining were visualized using the UPLAN Apochromat 60x/1.35 numerical aperture (NA) objective on the Olympus FV1000 confocal microscope and processed using the Olympus FluoView v1.6

software. Quantifications of vinculin and  $\beta$ 1-integrin intensity were analyzed on the Image-Pro software (Media Cybernetics).

#### **A.4.6 Uniaxial stretch of cells in 3D collagen**

Collagen was pre-assembled on ice 1 hour prior to the start of the experiment by mixing 10x DMEM with rat collagen I (5 mg/ml; BD Biosciences) at a ratio of 1:9 and neutralized using 1N NaOH to pH 7. Fibronectin (Sigma, 50  $\mu$ g/ml final concentration) was added to pre-assembled collagen and mixed 1:1 with B16F1 stables ( $5.0 \times 10^4$  cells/ml final cell concentration, 2.17mg/ml final collagen concentration). Tissue Train® Culture Plates (Flexcell International Corporation) were loaded onto Tissue Train® Linear Trough Loaders under 15% vacuum to create a linear trough. Collagen/fibronectin and cell mixtures (120  $\mu$ l) were loaded into the troughs and left in the incubator for 2 hours at 37°C to polymerize creating a strip of cell-embedded collagen/fibronectin gel attached to anchor meshes on two opposing sides of the membrane. Regular growth media (3 ml) was added to each well and cells were left overnight prior to stretching. Tissue Train Culture Plates containing the strip of cell-embedded collagen/fibronectin gel were placed onto Arctangle® Loading Posts. A 46.55 kPa pressure was applied through the vacuum pulling down the flexible-membrane at where the mesh was connected to the gel to create an uniaxial 10% elongation on two opposing ends of the strip of collagen gel. Cells were fixed after 24 h stretch. Control cells were left in the incubator with no stretch applied. Cells were visualized using a 100x / 1.45 objective on a Zeiss 200M Axiovert microscope. Vinculin intensity was analyzed using Slidebook v5.5 (3i Intelligent Imaging Innovations).

#### **A.4.7 Immunofluorescence staining in 2D/3D**

Cells were fixed in 4% paraformaldehyde for 15 minutes, permeabilized with 0.1% Triton X-100 for 10 minutes and blocked with 10% normal goat serum (Jackson ImmunoResearch) in 1% BSA for half an hour for 2D stains. For 3D stains, cells were permeabilized with 0.5% Triton-X for one hour and blocked with 10% normal goat serum (Jackson ImmunoResearch) in 1% BSA for one hour. After blocking, cells were probed with monoclonal anti-vinculin (mouse) primary antibody (1:100; cat. no. V4505, Sigma), anti-FLAG (rabbit) primary antibody (1:200; cat. no. F7425, Sigma), and monoclonal anti-mouse CD29 (Integrin,  $\beta$ 1 chain) primary antibody (1:100; cat. no. 553715, BD Biosciences) in 1% BSA for 1 hour at room temperature for 2D stains and overnight at 4°C for 3D stains. Cells were subsequently incubated with Alexa Fluor 488 goat anti-mouse (1:100; cat. no. A11029, Invitrogen), Alexa Fluor 568 goat anti-rabbit (1:100; cat. no. A11011, Invitrogen), Alexa fluor 647 goat anti-rat (1:100; cat. no. A21247, Invitrogen) secondary antibodies and rhodamine phalloidin (1:200, cat. no. R415, Invitrogen) in 1% BSA for 1 hour in 2D stains and 2 hours for 3D stains. Cells were then mounted onto coverslips using ProLong Gold anti-fade reagent containing DAPI (Molecular Probes).

#### **A.4.8 Rac1/RhoA activation assays and phospho-p130cas**

B16F1 parentals were seeded at a density of  $1.5 \times 10^5$  cells per well overnight in 6-well silicone rubber BioFlex<sup>®</sup> Culture Plates (Flexcell International Corporation, Hillsborough, CA) coated with  $5 \mu\text{g}/\text{cm}^2$  of fibronectin (Sigma). Cell lysates were collected and prepared following 30, 10, 5 and 2 minutes of 10% equibiaxial mechanical stretch using the Flexcell Tension System (Flexcell, International corporation). A G-LISA was used to determine Rac1 and RhoA activity and all procedures including cell lysate collection and preparation were performed according to

the manufacturer's instructions (Cytoskeleton). Cells were lysed in RIPA lysis buffer containing protease and phosphatase inhibitors and collected for western blot quantification of pY165-p130cas and pY410-p130cas.

#### **A.4.9 Western blotting and antibodies**

Protein lysates were separated by sodium dodecyl sulfate polyacrylamide gel electrophoresis and transferred to polyvinylidene fluoride membranes. Membranes were blocked with 5% BSA for 1 hour at room temperature and incubated overnight at 4°C with primary antibodies diluted in 1% BSA (anti-talin, Santa Cruz, cat. no. sc-7534; anti-vinculin, Sigma, cat. no. V4505; anti-FLAG, Sigma, cat. no. F7425; anti-pY165-p130cas, Cell Signaling, cat. no. 4015; anti-pY410-p130cas, Cell Signaling, cat. no. 4011, anti- $\beta$ -actin, Sigma, cat. no. A4700). Membranes were then incubated with their respective HRP-conjugated secondary antibody diluted in 1% BSA for 1 hour at room temperature. Membranes were developed by Immobilon Western Chemiluminescent HRP Substrate (Millipore).

## **Appendix B: Inflammation in the lung primes the premetastatic niche via hyaluronic acid**

### **B.1 Introduction**

Coopting the immune system is a general strategy used by tumor cells throughout the metastatic cascade. While immune cells promote growth, invasion and intravasation at primary tumors, the relative influence on these steps at secondary sites is not well understood. We used two very different models of inflammation in the lung, hypersensitivity pneumonitis and asthma, and found that both significantly increased metastasis of normally weakly metastatic melanoma. Tumor cell extravasation could be enhanced *in vitro* under inflammatory conditions, but this was not observed *in vivo*. Differences in the development of micrometastases associated with hyaluronic acid (HA) were observed in both models of inflammation where HA was highly present in the tissue. Expression of the HA receptor, CD44, was similar across melanoma lines and did not correlate with HA binding, however, the ability to bind HA correlated with metastases. These findings posit HA as a critical regulator of inflammation enhanced metastasis in the lung.

Priming of the metastatic niche occurs through multiple mechanisms including the alteration or recruitment of stromal cells, remodeling of vasculature and extracellular matrices, and increasing the availability of growth factors [450]. The immune response/inflammation can play a major role in these mechanisms, though the complex etiologies of inflammation and tumor cell metastasis have made these studies challenging. For example, crippling the immune system using NOD/SCID/IL2R $\gamma$  mice results in hugely enhanced tumor initiating potential of single tumor cells [280] while blocking the infiltration of immune cells to secondary tumor lesions can

limit their establishment and growth [276, 451]. Indeed, the ability to evade immune detection while harnessing immune cells to promote growth are emerging hallmarks of malignancy [278, 452].

A selection for intrinsic tumor cell features that augment metastatic colonization of secondary organs converges on metastatic niche priming mechanisms. For example, breast cancer cells that colonize the lung have high levels of surface VCAM in order to bridge their interaction with resident macrophages that express the integrin VLA-4 [453]. VCAM signalling in tumor cells or, alternatively, growth factors produced by macrophages, in turn enhance proliferation and invasion of the tumor cells [453, 454]. Similarly, the recruitment of inflammatory monocytes expressing CCR2 that differentiate into the metastases-associated macrophages is achieved by the secretion of CCL2 from tumor cells seeding the lung [455]. Blocking tumor cell-monocyte/macrophage interactions using CCL2 antibodies or knocking down VCAM reduces metastasis of the lung [453, 455, 456]. VLA-4+/VEGFR1+ bone marrow-derived cells are essential cellular components of the premetastatic niche in the lung for Lewis Lung carcinoma (LLC) and melanoma, interacting with tumor cells at fibronectin-rich sites [456]. Some tumor cells may also secrete their own extracellular matrix proteins to mediate interactions with immune cells. Versican is secreted by LLCs to potently activate macrophages via TLR2 and TLR6 [290]. Activated macrophages then secrete TNF $\alpha$ , required for LLC metastasis [290]. Versican also binds hyaluronic acid (HA), another ECM component implicated in metastasis [291, 292]. Collectively, the intrinsic ability to produce ECM or find resident macrophages, appears to be largely pro-tumorigenic at the metastatic niche.

In order to investigate mechanistic commonalities where inflammation may augment metastasis, we used established models of hypersensitivity pneumonitis [457], resulting in a

Th1/Th17 skewed cytokine response, and asthma [458], resulting in a Th2 response. We then introduced a relatively non-metastatic melanoma cell line, B16F0, into circulation to determine how inflammation of the target organ affected late steps of the metastatic cascade. We found that both models of inflammation dramatically enhanced the metastasis of the lung without affecting tumor cell extravasation. Instead, the presence of hyaluronic acid (HA) in inflamed lungs created platforms of tumor cell growth where early cell divisions occurred. The ability of melanoma cells to bind HA *in vitro* correlated with metastatic potential *in vivo* and accounted for some of the increased metastasis observed in inflammatory conditions. Our findings lend to the emerging hypothesis that inflammation primes the metastatic niche and identifies HA as a common contribution in this therapeutically pertinent relationship.

## B.2 Figures

Figure 1

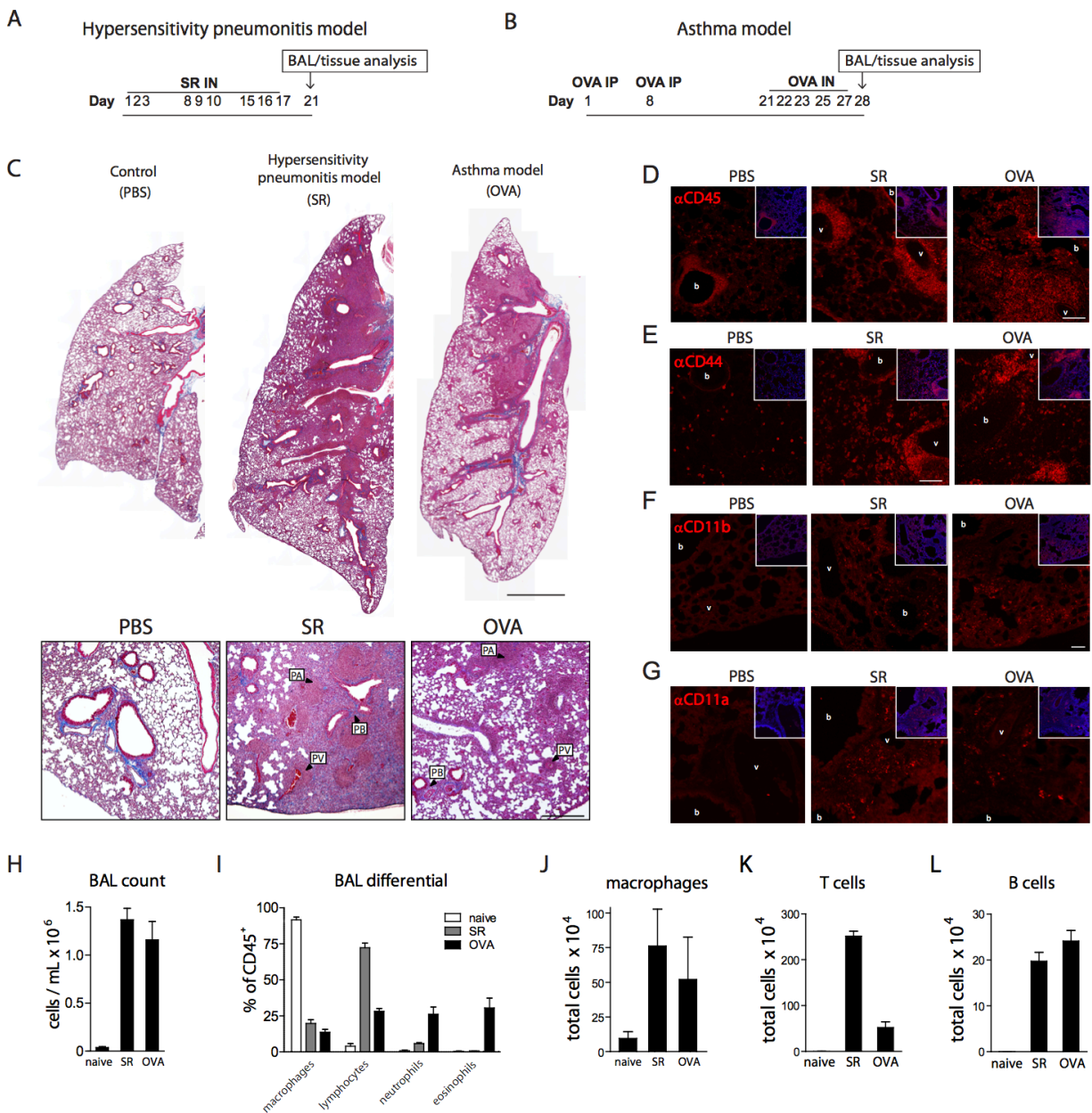


**Figure 1.** Hypersensitivity pneumonitis and asthma models of inflammation in the lung. A) A model of hypersensitivity pneumonitis was established by intranasal (IN) delivery of *Saccharopolyspora rectivirgula* (SR) antigen on days indicated. B) A model of asthma was established by intraperitoneal delivery of chicken ovalbumin coupled to Alum to allow for the

development of OVA-specific IgEs. OVA was then administered IN. C) Masson's Trichrome staining for collagen fibers and cellular infiltrates of control and inflamed lungs showing either whole lung sections (above) where images have been stitched together or higher magnification images (below) with labelled parenchymal infiltrates (PA), peribronchial infiltrates (PB), or perivascular infiltrates (PV). Scale bars 1 mm (above) and 250  $\mu$ m (below). D-G) Immunofluorescent staining of cellular infiltrates in control and inflamed lungs using CD45 (D), CD44 (E), CD11b (F), and CD11a (G) antibodies with bronchii (b) and vasculature (v) identified using DAPI (merged in insets). H-J) BAL fluid was assessed by FACS. H) Total CD45+ cells/mL in 3 mL total volume. I) CD45+ cells were categorized as macrophages (autofluorescence+, SiglecF+, CD11c+), lymphocytes (CD3 $\epsilon$  or B220+), neutrophils (7/4+), and eosinophils (SiglecF+, CD11c-). J-L) Total number of macrophages, T cells (CD3 $\epsilon$ +), and B cells (B220+) in BAL fluid isolated from control and inflamed lungs.

# Figure 2

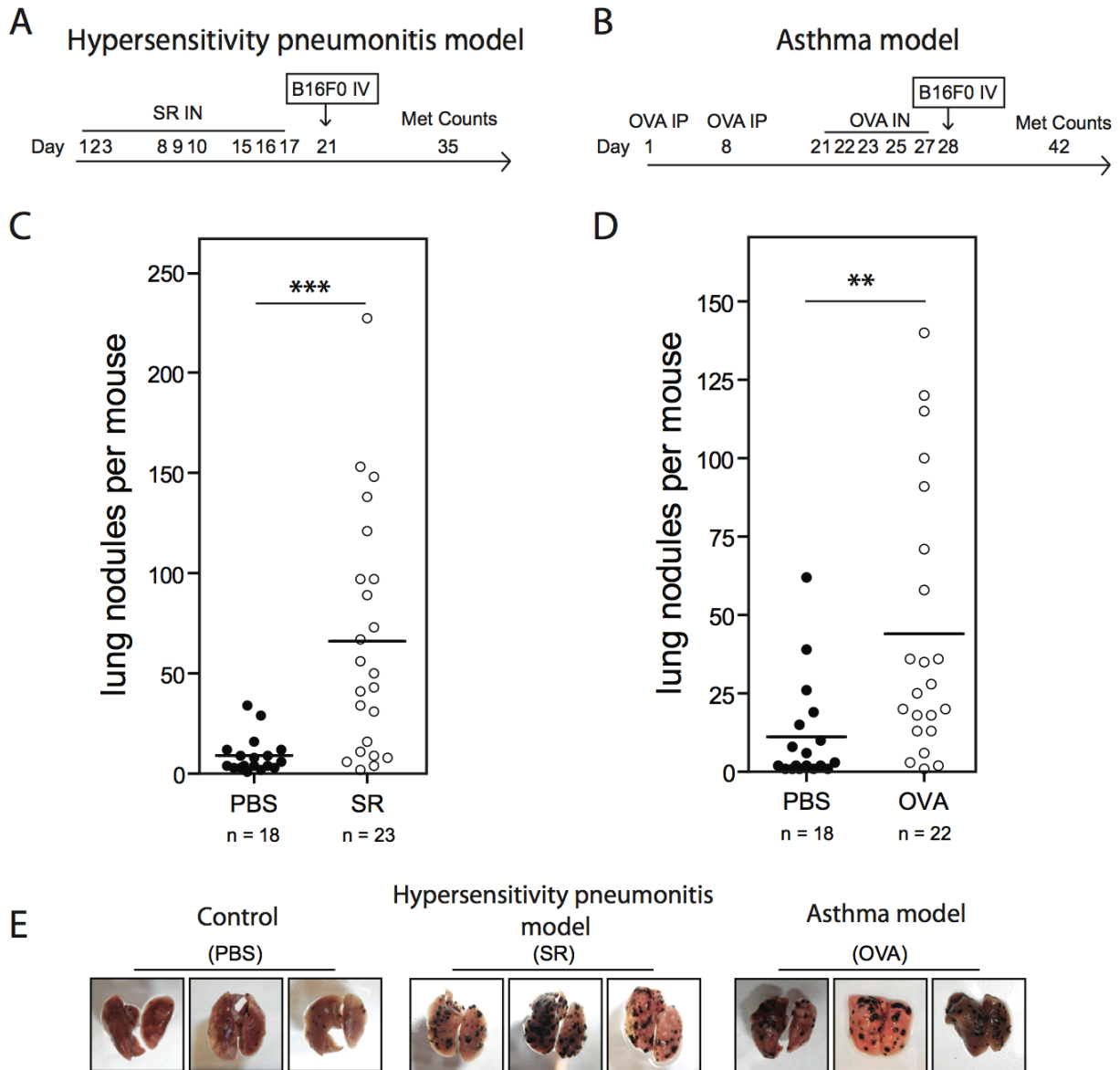


**Figure 2.** *Hypersensitivity pneumonitis and asthma models of inflammation increase pulmonary metastasis.* A-B) Models for Hypersensitivity pneumonitis and asthma with indicated day of introducing B16F0 cells into circulation via tail vein injection and final metastases count. C-D) Quantitation of nodules at days 35 and 42, 2 weeks after B16F0 injection. E) Representative intact lungs from (C) and (D).

**Figure 3**

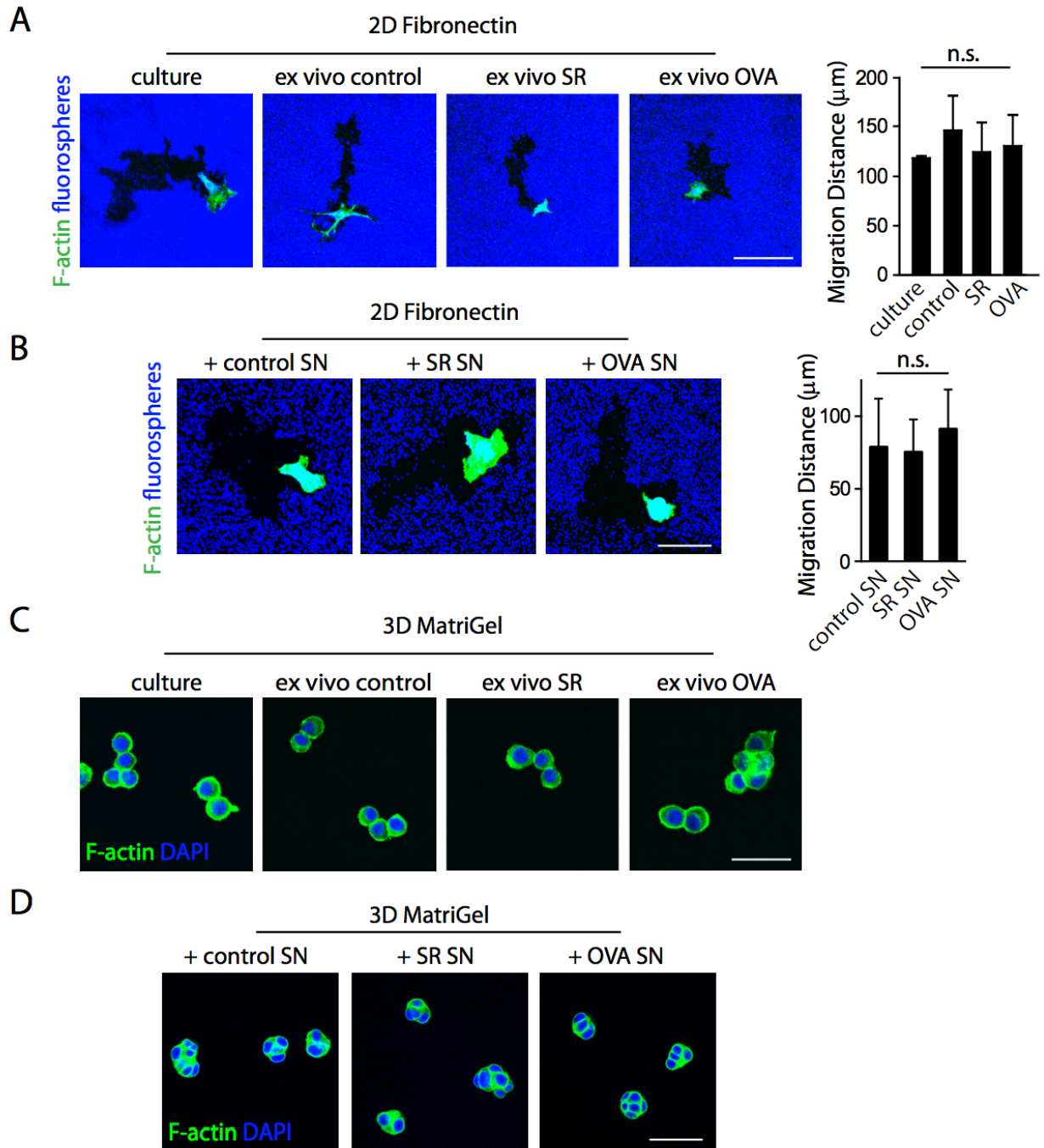


**Figure 3.** *The inflammatory niche does not alter or select for enhanced tumor cell motility. A-D) B16F0 cells from culture or pulmonary metastases isolated from control, SR challenged, or OVA challenged mice after 16 h migration on 2D Fibronectin and fluorescent beads (A-B), 16 h in 3D*

MatriGel (C), or 36 h in MatriGel (D) with or without supernatants (SN) collected from whole lung cultures. Cells were stained as indicated. For (A-B) the mean migration distance  $\pm$  the SEM is quantified from 3 experiments and  $>50$  cells. Scale bars, 100  $\mu\text{m}$  (A) and 50  $\mu\text{m}$  (B). For (C-D), representative images of tumor cells from 3 experiments are shown. Scale bar, 50  $\mu\text{m}$  (C) and 100 $\mu\text{m}$  (D).

Figure 4

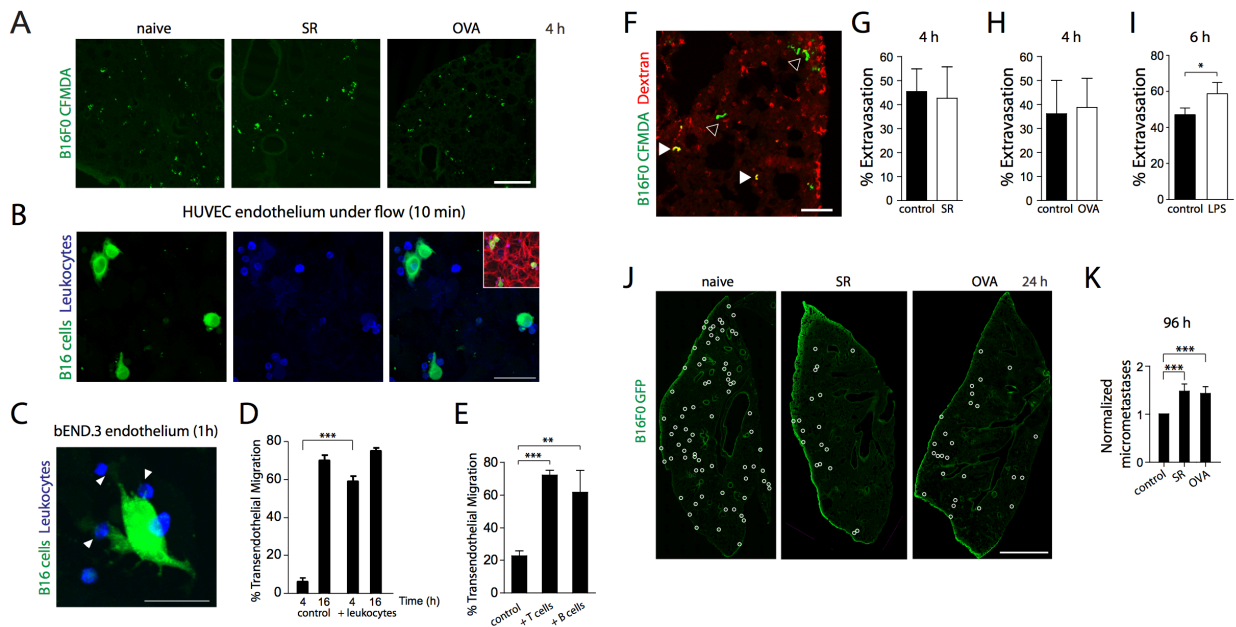


**Figure 4.** *B16F0* cells show enhanced extravasation under inflammatory conditions *in vitro* but *not in vivo*. A) *B16F0* cells labelled with CMFDA in lungs at 4 h. Scale bar, 200  $\mu\text{m}$ . B) HUVEC endothelial monolayers perfused with leukocytes (blue) mixed with *B16F1* tumor cells (green). Inset is a merged imaged with F-actin (red). Scale bar, 50  $\mu\text{m}$ . C) bEND.3 endothelial monolayers with leukocytes (blue) and *B16F1* cells (green) added. Arrows indicate leukocyte-tumor cell interactions at sites of tumor cell protrusions. Scale bar, 40  $\mu\text{m}$ . D-E) %TEM of *B16F1* cells at 4 and 16 h (D) and 4 h (E) on bEND.3 endothelial monolayers with or without leukocytes from peripheral blood or purified T or B cells added. G) %TEM at 4 h on bEND.3

endothelial monolayers as in (D). In all experiments, leukocytes, T cells, or B cells were at a 10:1 ratio to tumor cells. F-H) B16F0 cells labelled with Cell Tracker Green co-delivered with high molecular weight Alexa647-dextran via tail vein in order to visualize the vasculature in lung. Lungs were sectioned and imaged after 4 h. F) Closed arrows indicate tumor cells remaining in the vasculature which appear yellow and open arrows indicate tumor cells that have extravasated. Scale bar, 100  $\mu$ m. G and H) Percent extravasation quantified as described in (F). I) Extravasation of CMFDA labelled B16F0 cells injected tail vein 6 h after intratracheal administration of LPS or PBS control. Lungs were sectioned and imaged for quantification after 6 h. Means are graphed from >5 mice and >100 sections. J) B16F0 GFP expressing cells in lungs at 24 h. Scale bar, 1 mm.

## Figure 5

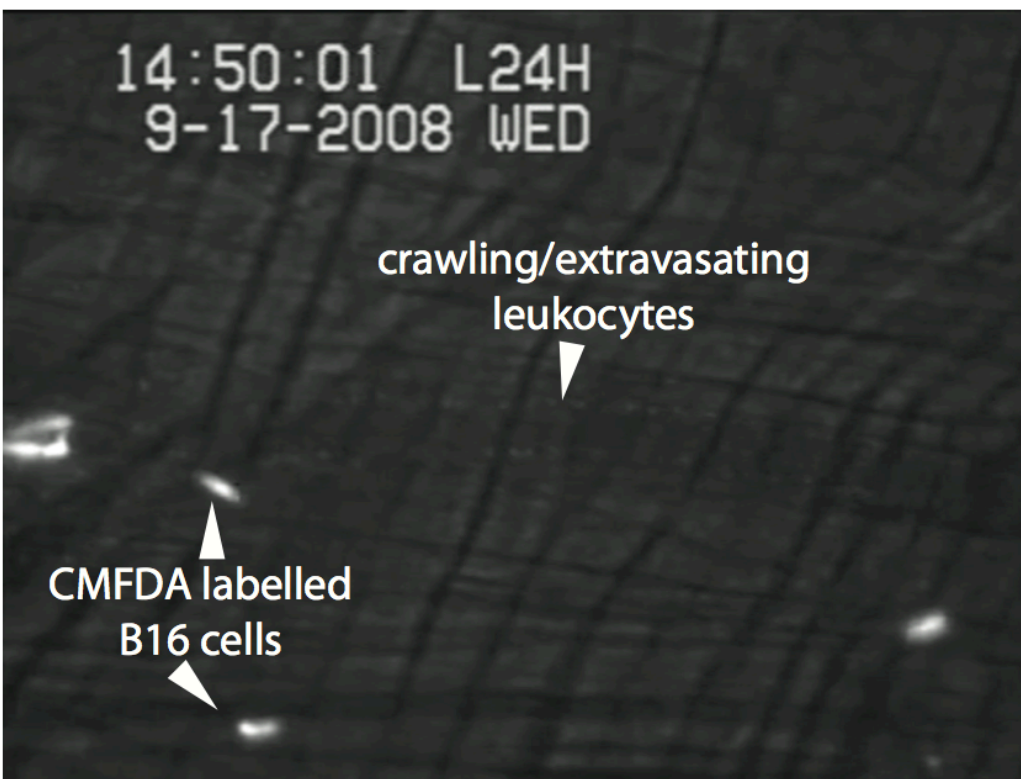


**Figure 5.** *B16 cells arrest in small capillaries of the closed vasculature in the cremaster muscle.*

CMFDA labelled B16F1 cells were visualized in mice given TNF $\alpha$  by IP 4 h previously where extensive leukocyte firm adhesion and crawling are observed in the large venules of the cremaster. Still image is representative of 3 experiments and taken from Video 1.

## Figure 6

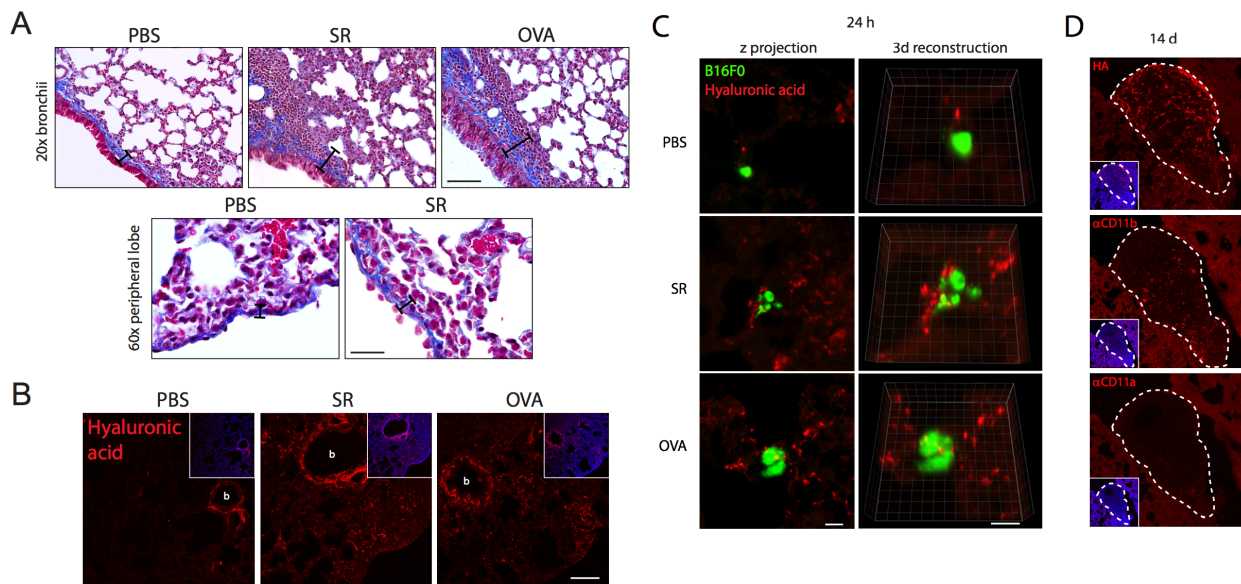


**Figure 6.** *Initial cell divisions and metastases show close association with hyaluronic acid more*

*abundant in inflamed lungs.* A) Masson's Trichrome staining of control and inflamed lungs.

Brochial regions (above), where metastases rarely form, show thickening of collagen (blue).

Peripheral lobe regions, where metastases form, show similar collagen thickness. Scale bars 100

$\mu\text{m}$  and 50  $\mu\text{m}$ . B) Immunofluorescent staining of hyaluronic acid (HA) using biotinylated HA

binding protein followed by Alexa647-steptavidin (shown in red) with bronchii (b) and

vasculature (v) identified using DAPI (merged in insets). C) Single B16F0 GFP expressing cells

(PBS control) or those undergone cell division (SR and OVA treated) shown in lung tissue

stained for HA as in (B). Scale bars, 25  $\mu$ m. D) Established metastases at 14 days stained for HA, CD11b, and CD11a.

**Figure 7**

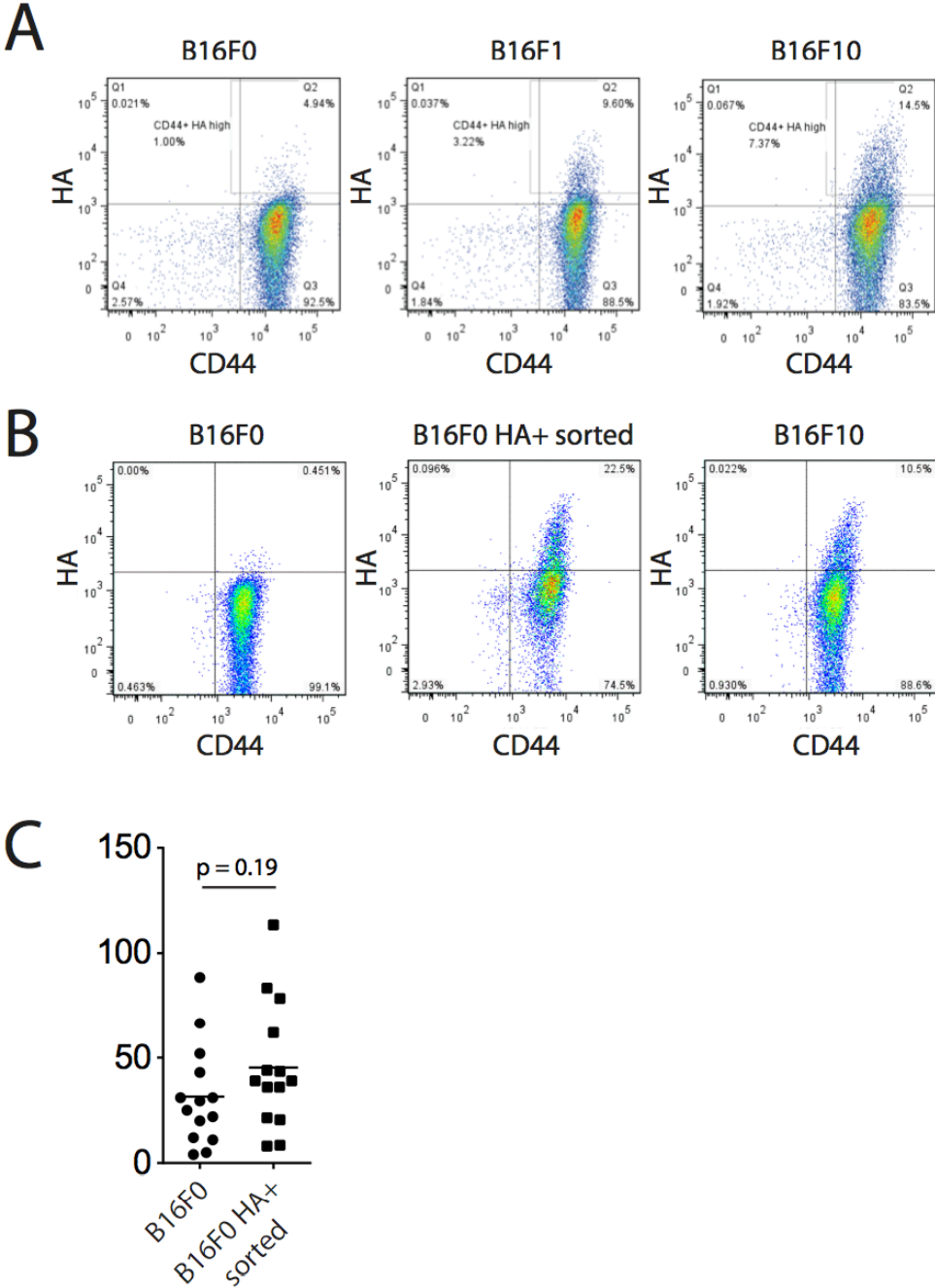


**Figure 7.** *The intrinsic ability of tumor cells to bind HA augments lung metastases.* A) B16F0, F1, and F10 cell lines incubated with CD44 antibodies plus APC conjugated HA and assessed by FACS. B) FACS analysis of B16F0, B16F0 HA<sup>+</sup> sorted cells, and B16F10 cells used as a positive control incubated with CD44 antibodies plus APC conjugated HA. C) Metastases counted from lungs of mice 14 days post tail vein injection of parental B16F0 and sorted B16F0 HA<sup>+</sup> cells.

### **B.3 Conclusions**

In this study, we used established models for hypersensitivity pneumonitis and asthma in order to broadly assess a role for inflammation in the premetastatic niche of the lung. We introduced the B16F0 melanoma line i.v. in a model of metastasis where CTCs do not readily colonize the lung. We found that both models of inflammation increased metastases by ~3-5 fold and tumor cells isolated from colonies did not show intrinsic difference in migration, invasion or growth. We therefore investigated steps of metastatic colonization that an inflammatory microenvironment could enhance. We found that homing, arrest and extravasation were not enhanced in inflamed lungs *in vivo*, even though forcing interactions between leukocytes and tumor cells *in vitro* could indeed increase tumor cell extravasation. The lack of apparent enhanced TEM *in vivo* may be the result of tumor cells largely arresting in the small capillaries of the lung where leukocytes more readily extravasate from larger vasculature.

Once tumor cells extravasate, most will remain dormant in the perivascular niche. Given that tumor cell dormancy is a major rate-limiting step in metastasis, we next investigated the growth of tumor cells within inflamed versus naïve lungs. We found that micrometases were more present in inflamed lungs. We therefore investigated microenvironmental niche elements

altered in inflammation that associated with micrometastases. We found that hyaluronic acid, an ECM component highly deposited in the lungs in both hypersensitivity pneumonitis and asthma, associated with micrometastases. A small fraction of B16F0 cells were able to bind HA in vitro while the more metastatic B16F1 and B16F10 cell lines showed a much higher fraction of HA binding suggesting a selection for HA binding in the series. We then sorted B16F0 cells for HA binding and found that these cells formed more metastases even in the absence of inflammation. These data suggest that inflammation in the lungs can augment tumor cell metastasis that may involve the production of HA. Future studies should investigate targeting HA or HA binding by tumor cells in the presence of inflammation.

## **B.4 Experimental procedures**

### **B.4.1 Induction of asthma and assessment of alveolar inflammation**

Asthma was induced in C57BL/6 mice as previously described with minor modifications. Briefly, mice were sensitized intraperitoneally with 0.2% chicken ovalbumin (OVA) in Al(OH)<sub>3</sub> (both from Sigma, St Louis, MO) on days 1 and 8. Mice were subsequently intranasally challenged on days 21, 22, 23, 25, and 27 with 50  $\mu$ L 2% OVA. To assess inflammation of the lung on day 28, mice were anaesthetized with 200 mg/kg ketamine/10 mg/kg xylazine and bronchoalveolar lavages (BALs) were performed by 3 subsequent introductions and aspirations of 1.0 mL sterile PBS to determine cell infiltration and lungs were also fixed with either 4% PFA or formalin for histologic studies. BAL fluid was analyzed by FACS.

#### **B.4.2 Induction of HP and assessment of lung inflammation**

HP was induced as previously described by injecting 50  $\mu$ l of 4 mg/ml endotoxin-free *Saccharopolyspora rectivirgula* antigen intranasally three times a week for 3 weeks. Four days after the last intranasal instillation (day 21), inflammation of the lung was assessed by analyzing BAL fluid and lung tissue as described above.

#### **B.4.3 Cells**

B16F0 melanoma cells (American Type Culture Collection) were cultured in DMEM supplemented with 10% fetal bovine serum and 1% penicillin/streptomycin. Stably expressing B16F0 EGFP cells were generated by transfection of the EGFP-C1 vector (Clontech) using Lipofectamine 2000 (Invitrogen), selection in 1.2 mg/ml G418 (Gibco), and 2 x fluorescence-activated cell sorting for high expressing (top 10%) EGFP positive cells. Primary murine T cells, B cells, and neutrophils were isolated from the lymph nodes and spleens (T and B cells) or whole blood (neutrophils) of 6 to 8 wk by depletion of non-B cells, non-T cells, and non-neutrophils using kits from Stemcell Technologies. For white blood cell cultures, whole blood was taken by cardiac puncture and erythrocytes were lysed with Tris-buffered  $\text{NH}_4\text{Cl}$ .

#### **B.4.4 FACS of bronchoalveolar lavage fluid and tumor cells**

Bronchoalveolar lavage (BAL) was performed by three subsequent introductions and collections of 1 ml sterile phosphate-buffered saline (PBS). BAL fluid was stained with antibodies in PBS containing 2% FCS and 2mM EDTA. Samples were first blocked in buffer containing 5 $\mu$ g/mL anti-CD16/32 (2.4G2) to block non-specific antibody binding. PE-Cy7 conjugated CD3 $\epsilon$  (2C11)

and APC-eFluor780 conjugated CD45R/B220 (RA3-6B2) antibodies were from eBioscience. PE conjugated Siglec-F (E50-2440) antibody was from BD Biosciences. FITC conjugated anti-Neutrophil (7/4) antibody was from Abcam. Pacific Blue conjugated CD45 (I3/2) and Alexa-647 conjugated CD11c (N418) antibodies were made and conjugated in house. Autofluorescence +ve, SiglecF+, CD11c+ were considered macrophages. Autofluorescence -ve, SiglecF-, CD11c+ were considered Dendritic cells. SiglecF+, CD11c- were considered eosinophils. Cells +ve for 7/4 antibody were considered neutrophils. CD3ε+ and B220+ cells were considered lymphocytes. Samples were acquired on a BD LSRII and data analysis was performed using Flowjo.

#### **B.4.5 Tracking B16F0 colonization of the lung**

For lung metastasis experiments,  $2.5 \times 10^5$  B16F0 cells were injected into the tail vein of mice in 100 μL volume of DMEM and lungs were removed and imaged after 14 days. For homing, extravasation, and initial colonization experiments,  $1 \times 10^6$  B16F0-GFP cells were injected with or without 5 mg/kg AlexaFluor647-dextran (Molecular Probes) in 100 μL volume of DMEM. At the indicated times, lungs were removed, fixed in 4% PFA, embedded in OCT, sectioned at 35 μm, and stained.

#### **B.4.6 Immunostaining**

OCT embedded tissue was sectioned at 18 μm, fixed with 4% PFA on slides (Fisher Scientific), permeabilized with 0.5% Tween-20 in PBS or Acetone for 5 minutes and blocked in 1% BSA/PBS solution. For tissue permeabilized in 0.5% Tween-20, anti-CD45 (30-F11) and anti-

CD44 were from BD Biosciences, anti-CD11b (M1/70) was from Abcam, and anti-HABP was from Calbiochem. For tissue permeabilized in Acetone, anti-CD11a (M17/4) was from Abcam.

#### **B.4.7 *In vitro* transendothelial migration**

HUVECs were cultured as monolayers on m slide VI(0.4) chamber slides (ibidi) and tumor cells were labeled with CellTracker Green CMFDA (Molecular Probes), mixed with murine peripheral blood leukocytes labelled with CellTrace FarRed DDAO (Molecular Probes), and perfused across the HUVEC monolayer at 2 dynes/cm<sup>2</sup>. After 10 minutes, the chamber was flushed, fixed with 4% paraformaldehyde and stained for F-actin with Rhodamine phalloidin. bEND.3 murine microvascular endothelial cells were cultured as monolayers on m slide 8 well chamber slides (ibidi) and activated with 50 ng/mL TNF- $\alpha$  for 4 hours. Monolayers were overlaid with CellTrace FarRed DDAO (Molecular Probes) primary leukocyte populations and CellTracker Green CMFDA-labeled B16F1 cells. After 4 or 8 hours, cells were imaged by confocal microscopy through the z-axis to determine TEM as previously described.

#### **B.4.8 2D fibronectin migration**

Cells were plated on coverslips coated with 2.5 mg/cm<sup>2</sup> fibronectin and a lawn of 1- $\mu$ m fluorescent microspheres at a 1:10 dilution (FluoSpheres, Invitrogen). After 16 hours, the maximum distance from the edge of the cell to the edge of the cleared area was determined using FluoView v1.6 software.

#### **B.4.9 MatriGel invasion**

For MatriGel invasion assays, tumors were separated from lung tissue, mechanically disrupted, and passed through 40  $\mu\text{m}$  filters. Red blood cells were lysed (155 mM  $\text{NH}_4\text{Cl}$ , 12mM  $\text{NaHCO}_3$ , 0.1mM EDTA) for 3 min at 37 degrees. Cells were resuspended in a 50:50 mixture of MatriGel (BD Biosciences) and DMEM containing 20% FCS and set to polymerize on coverslips for 30 min at 37 degrees before adding DMEM containing 10% FCS. After 20 hours coverslips were fixed with paraformaldehyde, stained with Phalloidin and imaged.

#### **B.4.10 Intravital microscopy**

TNF- $\alpha$  (25  $\mu\text{g}/\text{kg}$ ) was administered intraperitoneally to C57/B6 mice before analysis. Mice were anesthetized and the cremaster muscle was exteriorized as described previously [271].  $5 \times 10^5$  CMFDA dye-labeled B16F1 cells were injected into the femoral artery and visualized by epi-illumination. Images were recorded as described previously [271].

#### **B.4.11 Statistics**

All statistical analyses were done using GraphPad Prism Software. Results are presented as mean  $\pm$  SEM. Statistical analysis was performed using paired t tests where \* =  $P < 0.05$ , \*\* =  $P < 0.01$ , \*\*\* =  $P < 0.001$ .